The University of Sheffield

Department of Physics & Astronomy

Doctoral Thesis

Optical Characterisation of Hybrid Perovskites for Photovoltaic Applications

---

Submitted for the degree of Doctor of Philosophy

on October 9, 2020

by

Claire Greenland

under the supervision of Prof. David Lidzey

EPSRC CENTRE FOR DOCTORAL TRAINING
NEW AND SUSTAINABLE
PHOTOVOLTAICS

This thesis is dedicated to my wonderful Nannie, who sadly passed away before she got to see its completion. I know she's up there cheering me on.

Abstract

Research interest in hybrid perovskites for photovoltaic applications has accelerated rapidly over the past 10 years. Hybrid metal halide perovskites are a family of materials of the form ABX_3, where A is either an organic cation or a mix of organic and inorganic cations, B is a divalent metal cation and X is a halide anion. Hybrid perovskites are promising candidates for absorbers for photovoltaic cells, as they exhibit many favourable properties such as long charge carrier lifetimes, long diffusion lengths and high charge carrier mobilities. Furthermore, the ability to fabricate thin films of such materials via solution processing means that fabricating photovoltaic cells based on hybrid perovskite is relatively inexpensive, low temperature and facile, and can be adapted for deposition on flexible substrates and for roll-to-roll processing.

Hybrid perovskites which are composed of mixed A-site cations and mixed X-site halides are of particular interest due to the ability to tune the optical properties of the material through compositional engineering. The double cation, mixed halide perovskite $(FAPbI_3)_{0.85}(MAPbBr_3)_{0.15}$ and the triple cation, mixed halide perovskite $Cs_{0.05}$ $FA_{0.76}MA_{0.19}PbI_{2.55}Br_{0.45}$ are both excellent candidates for solar cell absorbers. In this thesis, the optical properties of these materials are investigated through a combination of spectroscopic techniques, and their crystal structure is probed through X-ray diffraction measurements.

In Chapter 4, proof of concept is presented for a time-resolved PL mapping system, designed and built during this PhD project for the correlation of surface morphology with local fluorescence lifetimes in hybrid perovskite thin films. In Chapter 5, the TRPL mapping system is utilised to investigate the relationship between surface morphology and fluorescence lifetimes in $(FAPbI_3)_{0.85}(MAPbBr_3)_{0.15}$ and $Cs_{0.05}$ $FA_{0.76}MA_{0.19}PbI_{2.55}Br_{0.45}$ thin films. It is found that both types of films exhibit wrinkled morphology as a result

of processing conditions, and these wrinkles correlate with local variations in PL intensity and PL lifetime. The effect of vacuum-assisted solution processing (VASP) on the morphology of spray-cast triple cation perovskites is also explored. The TRPL mapping system reveals a significant increase in surface uniformity as a result of the vacuum treatment, accompanied by lengthened fluorescence lifetimes and increased spatial homogeneity of lifetimes. These findings correlated with enhanced device performance in PV cells based on VASP-treated films.

In Chapter 6, absorbance and photoluminescence spectroscopy are employed to investigate the temperature dependence of the optical properties of $(FAPbI_3)_{0.85}(MAPbBr_3)_{0.15}$, and variable temperature X-ray diffraction measurements are taken to determine the phase behaviour of the material. Two phase transitions were identified for this material: a high temperature transition from a pseudo-cubic phase to a pseudo-tetragonal phase at $\sim$ 260 K (-13°C), and a low temperature phase transition at $\sim$ 80 K (-193°C) to a lower symmetry variation on the tetragonal phase. This material exhibits phase-specific optoelectronic properties, such as the discontinuity in the temperature-dependent blueshift in the optical band gap observed to correlate with the high temperature phase transition. A correlation between the size and shape of the lattice unit cell and the resulting recombination rates in the material is found, speculated to be linked to polaron formation in the material.

Chapter 7 extends these investigations into the Cs-containing triple cation perovskite family of materials. In this chapter, varying amounts of Cs were added to $(FAPbI_3)_{0.85}(MAPbBr_3)_{0.15}$ to determine the effect of Cs incorporation on the phase behaviour and optoelectronic properties of mixed cation perovskites. It is shown that the phase behaviour of Cs-containing triple cation perovskites is largely the same as that of $(FAPbI_3)_{0.85}(MAPbBr_3)_{0.15}$, but that the high temperature cubic-tetragonal phase transition shifts to higher temperatures as Cs content is increased. The band gap of these Cs-containing perovskites widens with increasing temperature, and it is speculated that this widening is driven by the lengthening of the lattice parameter c with increasing temperature.

Acknowledgements

First and foremost, from the bottom of my heart I would like to thank David, my excellent supervisor. Not only are you the best academic mentor I could have hoped for, but in EPMM you have created a brilliant group, of not only colleagues but friends.

Thank you to Onkar Game and Joel Smith, who have made so many samples for me over the years and were always willing to use their excellent scientific minds to help me. Thank you to Chris Bracher, who helped me get the ball rolling with my TRPL setup way back when. Thank you to Rahul Jayaprakash and Dave Coles, who always took the time to help me in the optics lab and share their boundless knowledge and expertise of all things optics with me. Thank you to Samuele Lilliu, who wrote my TRPL mapping software and laid the foundation for everything I now know about coding.

When I first started my PhD, I joined a research group of which I was the only female member. Now I'm leaving it in the capable hands of some excellent female physicists: Rachel, Mary, Emma, Elena and Kirsty. To them, and to the all other great friends I've made in EPMM, past (Dave, Jon, Theo, Chris, Mike, Ben *et al.*) and present (James, Tom, Kyriacos, Joel, Onkar, Rahul *et al.*)—thanks for all the good times. The Friday night antics, the hundreds of hours spent in the Uni Arms, the games nights, the beer festivals, the pub quizzes, the curries, and so on... this lot made life during my PhD not only bearable but so much fun.

To my parents: I am eternally grateful to you, for your emotional and financial support over the past 9 years as I have progressed through my physics education.

To my boyfriend Will: you've been by my side through the whole thing, the good times, the bad times and the downright ugly times. I am forever grateful for your unwavering support and encouragement.

Publications

1. J. A. Smith, O. S. Game, J. E. Bishop, E. L. K. Spooner, R. C. Kilbride, C. Greenland, R. Jayaprakash, T. I. Alanazi, E. J. Cassella, A. Tejada, G. Chistiakova, M. Wong-Stringer, T. J. Routledge, A. Parnell, D. B. Hammond, D. G. Lidzey, *Rapid scalable processing of tin oxide transport layers for perovskite solar cells*, *ACS Appl. Energy Mater.*, **2020**, **3**, 6, 5552–5562

2. C. Greenland, A. Shnier, S. K. Rajendran, J. A. Smith, O. S. Game, D. Wamwangi, G. A. Turnbull, I. D. W. Samuel, D. G. Billing, D. G. Lidzey, *Correlating Phase Behaviour with Photophysical Properties in Mixed-Cation Mixed-Halide Perovskite Thin Films*, *Adv. Energy. Mater.*, **2020**, *10*, 4, 1901350 (This publication constitutes **Chapter 6** of this thesis.)

3. J. E. Bishop, J. A. Smith, C. Greenland, V. Kumar, N. Vaenas, O. S. Game, T. J. Routledge, M. Wong-Stringer, C. Rodenburg, D. G. Lidzey, *High-Efficiency Spray-Coated Perovskite Solar Cells Utilizing Vacuum-Assisted Solution Processing*, *ACS Appl. Mater. Interfaces*, **2018**, *10*, 39428-39434.

4. M. Alsari, O. Bikondoa, J. Bishop, M. Abdi-Jalebi, L. Y. Ozer, M. Hampton, P. Thompson, M. T. Hörantner, S. Mahesh, C. Greenland, J. E. Macdonald, G. Palmisano, H. J. Snaith, D. G. Lidzey, S. D. Stranks, R. H. Friend, S. Lilliu, *In Situ Simultaneous Photovoltaic and Structural Evolution of Perovskite Solar Cells During Film Formation*, *Energy Environ. Sci.*, **2018**, *11*, 383.

5. C. Greenland, S. Lilliu, O. S. Game, J. A. Smith, D. G. Lidzey, *Fluorescence Lifetime Imaging of Mixed Cation Perovskite Thin Films for Solar Cell Applications*, **in preparation**.

Contents

Chapter 1

Introduction

As the global population soars past 7.5 billion,[1] global energy demand is steadily increasing with it. In 1920, global energy consumption was approximately 18,000 TWh, but over the past 100 years it has increased and is now at an estimated 160,000 TWh,[2] and is projected to increase by another 50% before 2050 as the global population continues to rise and the energy demand of developing countries continues to rise.[3] This demand is currently met largely by fossil fuels such as coal, natural gas and crude oil. As of 2019, coal still provided $\sim$ 27% of the total global energy supply, while natural gas met $\sim$ 24% of supply and crude oil $\sim$ 33%.[2] Fossil fuels such as coal, oil and gas are not only a finite resource, but they are also an environmental catastrophe. The burning of fossil fuels emits greenhouse gases such as carbon dioxide (CO_2), which trap heat in the atmosphere and re-radiate it towards the Earth, causing warming of the Earth's surface.

For some time now it has been undeniable that global warming is happening—the global average surface temperature having already risen by 1°C, compared to pre-industrial levels, by 2015.[4] Some of the highest temperatures since records began have been recorded in the past two years, including a temperature of 54.4°C in Death Valley in California in August 2020[5] and a high of 38.7°C in Cambridge, UK in July 2019.[6] It is now the scientific consensus that global warming is not happening of its own accord—rising atmospheric CO_2 levels due to excessive burning of fossil fuels for human needs is the main driving force.[7,8] Atmospheric CO_2 concentrations have risen from $\sim$ 310 parts per million (ppm) in 1960 to $\sim$ 415 ppm as of 2019.[9]

Preventing further global temperature increases is of paramount importance, as even a 2°C increase would have a devastating impact on the world as we know it. The effects of a 2°C rise include: a 56 cm sea level rise by 2100;[10] habitat loss for hundreds of thousands of animal species;[11] and forced migration of human populations due to extreme temperatures.[12,13] In order to limit the global temperature increase to 1.5°C, atmospheric CO_2 levels must not rise above 450 ppm.[14] Achieving this ambitious target will involve actions by individuals, governments and corporations, including but not limited to: switching away from land- and emission-intensive animal agriculture for food production; electrifying transport; and developing 'green infrastructure', for example as building green roofs (the roof of a building that is wholly or partially covered in vegetation).[12] But perhaps most importantly, our reliance on fossil fuels for energy generation must rapidly decline, to be replaced by renewable, low-carbon energy sources.

Renewable, low-carbon energy sources such as wind, hydroelectric and solar power only provide $\sim$ 11% of the global energy demand.[2] The Sun is an abundant renewable energy source, and the immense amount of power transmitted to the Earth by the Sun ($\sim$ 1000 W/m^2)[15] could provide the entire global electricity supply if it could be harnessed efficiently with the appropriate infrastructure. For example: the Sahara Desert in Africa is ideal for solar energy harvesting, with at least 12 hours of sunlight every day. It has an area of 9.2 million km^2 [16], therefore the global energy demand of $\sim$ 18.5 TW could be met with an area of just 1.1% of the total area of the Sahara desert (assuming 18% solar energy conversion efficency). In reality, this is impractical due to the huge power losses incurred in transporting this electricity around the globe. Additionally, the global energy demand cannot be entirely met by electricity with the current technology—solar-powered aircraft are a long way from commercialisation, for example. However, the vast majority of energy demands can be met by electricity, including domestic transport (electric vehicles) and most domestic and commercial applications. We can even harness the Sun's power for water heating, which is known as solar heating or solar thermal.[17] As it stands however, solar energy provides only 1.1% of total energy consumed worldwide,[2] a figure that is increasing rapidly as the technology advances and the costs come down.

The basis of solar energy generation is the photovoltaic effect, which is the physical

process by which energy from solar radiation is converted to electrical energy. It was first demonstrated experimentally by Edmond Becquerel in 1839, who created an electric current by immersing two plates of either platinum or gold in an acid, neutral or base solution and exposing them to sunlight.[18] A solar cell, or photovoltaic (PV) cell, is an electrical device which is configured to convert solar radiation into an electrical current through the photovoltaic effect. When multiple cells are connected together in a circuit, this is known as a module, and the solar panels seen on rooftops and in solar farms are made up of modules.

The first commercially available PV cells were fabricated from crystalline silicon (c-Si)—these are the so-called 'first generation' of solar cells. The 'second generation' of solar cells encompasses the more advanced 'thin film' technologies, some of which are currently commercially available. A thin film solar cell is one where the absorber layer is typically on the order of a few nm, up to a few μm.[19] Second generation thin film technologies include cadmium telluride (CdTe),[20] copper indium gallium diselenide (CIGS) and amorphous silicon (a-Si).[21] The thin film nature of such cells means that they can be deployed in flexible and building-integrated applications[19] and are much lighter than c-Si cells, which generally use silicon wafers up to 200 μm in thickness.[22]

When discussing solar cells, the proportion of incoming solar radiation that can be converted by the cell into electricity, in other words the efficiency, is an important parameter. The chart in Figure 1.1 shows the cell efficiency of a wide variety of solar cell technologies as a function of time since the 1970s. The cells in this chart are those fabricated in the laboratory as opposed to solar modules, and will therefore exhibit higher efficiencies than modules due to the comparatively small illuminated area and the losses involved when connecting cells together in a module. The chart nevertheless gives an idea of the progression of solar cell technology over the past 50 years. When comparing solar cell technologies, the costs involved in producing solar panels must also be considered, along with the carbon footprint of the production—after all, a key reason for implementing solar energy technology is to mitigate carbon emissions. Another important metric to consider is the energy payback time (EPBT), which is defined as the time taken for the cell to produce enough energy to offset the energy used to produce

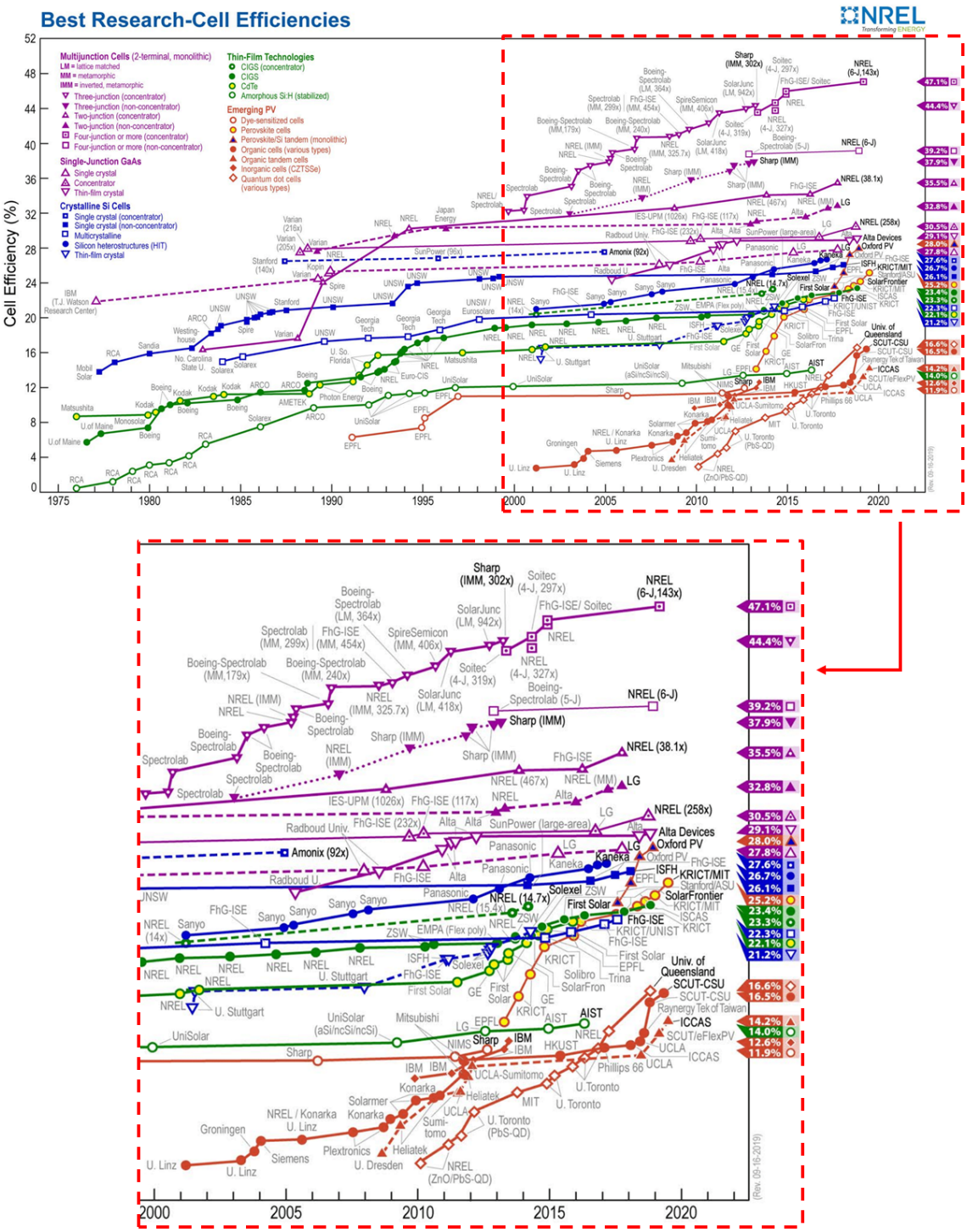

Figure 1.1: Chart made by the National Renewable Energy Laboratory (NREL), which is updated regularly to reflect the highest confirmed cell efficiency for the whole range of photovoltaic technologies, with data going back to 1976. [23]

it. Table 1.1 summarises these key parameters for three of the most commonly used commercial PV technologies: c-Si, CdTe and CIGS. Over the past 30 years, the payback time for c-Si cells has reduced from just under 3.5 years to only around 1.5 years. [22] As shown in Table 1.1, thin film cells are cheaper to produce than silicon, which is largely due to significantly less semiconductor material being used and lower processing costs.

Table 1.1: Comparison of the 3 main commercialised solar PV technologies (c-Si, CdTe, CIGS) and perovskite solar cells, in terms of some key parameters: the minimum sustainable price (MSP), which quantifies the price of producing solar cells that produces the minimum return necessary for a sustainable business; the energy payback time (EPBT); the carbon footprint of producing the cell, given in grams of CO_2 equivalent per watt of solar enegry produced (i.e. the effect of greenhouses gases other than CO_2 is quantified by how much CO_2 it is equivalent to in creating the greenhouse effect); and the maximum recorded efficiency of solar modules.

Technology	c-Si (mono)	CdTe	CIGS	Perovskite
MSP ($/Wp)	0.64–0.76 [24,25]	0.60 [26]	0.67 [27]	0.41 [26]
EPBT (years)	1.5 [22]	0.7-1.1 [28,29]	1.02 [29]	0.19-0.26 [30]
Carbon footprint (g CO_2-eq/kWh)	38.06 [29]	15.83 [29]	21.44 [29]	60-83 [30]
Module efficiency (%)	24.4 [31]	19.0 [31]	19.2 [31]	16.1 [31]

However, as shown in Table 1.1, they are also less efficient. These factors lead to a trade-off which means that the payback time for thin film technologies is comparable to c-Si, at around 1 year on average, as shown in Table 1.1. Although c-Si still dominates the PV market today, thin film technologies such as CdTe and CIGS have a $\sim 5\%$ market share. [22]

Beyond the second generation of solar cells, there is also a third generation which consists of emerging technologies that are still in the research stages and have little to no commercial availability. These include organic photovoltaics (OPV), copper zinc tin sulphide (CZTS), quantum dot solar cells, dye-sensitised solar cells (DSSCs) and perovskite solar cells (PSCs). Solar cells based on metal halide perovskites (MHPs) have garnered much research attention since their advent in 2009. [32] MHPs are perovskites consisting of metals (usually lead) at the B-site and halogens at the X-site, and this family of semiconductor materials exhibit a range of properties that make them promising candidates for solar cell absorber materials. Their high dielectric permittivity and low binding energies [33] make charge dissociation and transport relatively easily, which is complemented by their long charge carrier lifetimes [34,35] and diffusion lengths. [36] They also exhibit strong absorption and their band gap is tunable by compositional modifications. [37] These properties will be discussed in more depth in Section 2.2.

In addition to their favourable optoelectronic properties, MHPs can be processed from solution, which means that PSCs are cost-effective to fabricate, do not require

high temperatures and can be fabricated in high-throughput roll-to-roll processes.[38] As a result of these factors, it has been predicted that the energy payback time for PSCs could be as little as a few months.[30] As Table 1.1 shows, perovskite solar cells are cheaper to produce than c-Si, CIGS and CdTe cells, and have a shorter EPBT. Currently, the record efficiency for a perovskite solar module stands at 16.1%, and given the rapid rise in PSC efficiency over the past 10 years as shown in Figure 1.1, this can only be expected to further grow as the research continues. This gives PSCs the potential to be a strong competitor for silicon on the solar PV market.

However, the biggest hurdle to this is the stability of perovskite solar cells. While c-Si solar modules generally have a predicted lifespan of 25-35 years,[39] perovskite solar cells are notoriously unstable. Laboratory tests have shown that cells based on the prototypical $MAPbI_3$ perovskite can degrade over as little as 24 hours.[40,41] This is due to the fact that certain types of MHPs exhibit fundamental structural instability on exposure to moisture and light.[42–45] A tenfold improvement in cell lifespan compared to $MAPbI_3$ has been demonstrated in recent years,[46] and such improvements have been achieved through compositional engineering in hybrid perovskites.[47,48]

It is a combination of several factors which will hopefully bring PSCs to commercial viability: rapid efficiency improvements; enhancing stability through compositional engineering and encapsulation techniques;[49] breaking theoretical efficiency limits through incorporation of perovskites into tandem solar cells;[50–52] and the lowering of PSC fabrication costs through optimisation of cheap, scalable processing methods such as spray-coating[53–55] and other roll-to-roll processes.[38] This thesis will explore some of the fundamental physics underpinning the stability and photovoltaic performance of hybrid perovskite materials, bringing further understanding to the optimisation process which will eventually lead to the commercialisation of perovskite solar cells.

1.1 Thesis Motivation

The original aim of this PhD project was to develop an experimental system for time-resolved photoluminescence mapping of hybrid lead halide perovskites, in order to investigate the relationship between thin film surface morphology and fluorescence lifetime

homogeneity in such perovskites. At the time that the system was first being tested, mixed cation MHPs based on combinations of Cs, formamidinium (FA) and methylammonium (MA) at the A-site were just emerging as a more thermally stable and efficient alternative to the prototypical hybrid perovskite $MAPbI_3$ for photovoltaic applications. This was due to the exclusion or only minimal inclusion of MA in these perovskites, which is a particularly thermally unstable molecule. It was therefore decided that the TRPL mapping system would be used to investigate the correlation between thin film morphology and charge carrier lifetimes in mixed cation MHPs. These investigations opened up many questions about the optoelectronic properties of mixed cation perovskite systems, and at this time there was very little investigation into the temperature-dependent properties of such systems, which is undoubtedly a key factor in their enhanced thermal stability compared to $MAPbI_3$. Therefore subsequent investigations for this thesis employed temperature-dependent X-ray diffraction to investigate the phase behaviour of mixed cation perovskites, with the aim of drawing links between the phase behaviour and the temperature dependence of optoelectronic properties. Later, these investigations were extended to the Cs-containing triple cation perovskite, which was first demonstrated in solar cells in 2016 [46] and was shown to further improve the performance and stability of mixed cation perovskites as solar cell absorbers.

1.2 Thesis Overview

Chapter 2 details the theoretical and experimental background behind the work presented in this thesis. In **Chapter 3**, all experimental methods utilised in this thesis are discussed, and the contribution of collaborators to this experimental work and the parts of the thesis where certain techniques are used is highlighted.

As part of this PhD project, a time-resolved photoluminescence (TRPL) mapping system was designed, developed and built for the characterisation of hybrid perovskites. The system was designed to allow the direct comparison of surface morphology with local variations in fluorescence lifetime on hybrid perovskite thin films. The development and experimental realisation of this system is detailed in **Chapter 4**. In **Chapter 5**, the TRPL mapping system is utilised to investigate the relationship between surface morphology and

fluorescence lifetimes in $(FAPbI_3)_{0.85}(MAPbBr_3)_{0.15}$ and $Cs_{0.05}FA_{0.76}MA_{0.19}PbI_{2.55}Br_{0.45}$ thin films.

In **Chapter 6**, absorbance and photoluminescence spectroscopy are employed to investigate the temperature dependence of the optical properties of $(FAPbI_3)_{0.85}$ $(MAPbBr_3)_{0.15}$, and variable temperature X-ray diffraction measurements are taken to determine the phase behaviour of the material.

In **Chapter 7**, small amounts of Cs are added to the A-site in $(FAPbI_3)_{0.85}$ $(MAPbBr_3)_{0.15}$, to form the triple cation perovskite $Cs_zFA_xMA_yPbI_{2.55}Br_{0.45}$, where $z = 1 - x - y$. The effects of varying z between 0.03 and 0.15 on the phase behaviour and temperature-dependent optical properties of the perovskite are investigated through absorbance and photoluminescence spectroscopy combined with X-ray diffraction.

Chapter 8 summarises the main conclusions of the work and their implications for the research field, along with discussing some future directions in which the work presented in this thesis could be taken.

References

[1] Population, total, https://data.worldbank.org/indicator/SP.POP.TOTL?end=2019&start=1960, accessed on 2020-10-08.

[2] H. Ritchie, *Our World In Data* **2014**.

[3] International Energy Outlook 2019, https://www.eia.gov/outlooks/ieo/, accessed on 2020-09-30.

[4] E. Hawkins, P. Ortega, E. Suckling, A. Schurer, G. Hegerl, P. Jones, M. Joshi, T. J. Osborn, V. Masson-Delmotte, J. Mignot, P. Thorne, G. J. Van Oldenborgh, *Bulletin of the American Meteorological Society* **2017**, *98*, 1841.

[5] C. de León, J. Schwartz, *The New York Times* **2020**.

[6] UK Climate Extremes - Met Office, https://www.metoffice.gov.uk/research/climate/maps-and-data/uk-climate-extremes, accessed on 2020-10-07.

[7] N. Oreskes, in *Climate Modelling: Philosophical and Conceptual Issues*, Springer International Publishing, **2018**, pp. 31–64.

[8] P. Zhai, B. Zhou, Y. Chen, *Journal of Meteorological Research* **2018**, *32*, 671.

[9] Global Monitoring Laboratory - Carbon Cycle Greenhouse Gases, https://www.esrl.noaa.gov/gmd/ccgg/trends/mlo.html, accessed on 2020-10-08.

[10] D. J. Rasmussen, K. Bittermann, M. K. Buchanan, S. Kulp, B. H. Strauss, R. E. Kopp, M. Oppenheimer, *Environmental Research Letters* **2018**, *13*, 034040.

[11] R. Warren, J. Price, E. Graham, N. Forstenhaeusler, J. VanDerWal, *Science* **2018**, *360*, 791.

[12] V. Masson-Delmotte, P. Zhai, H.-O. Pörtner, D. Roberts, J. Skea, P. R. Shukla, A. Pirani, W. Moufouma-Okia, C. Péan, R. Pidcock, S. Connors, J. B. R. Matthews, Y. Chen, X. Zhou, M. I. Gomis, E. Lonnoy, T. Maycock, M. Tignor, T. Waterfield, Global warming of 1.5C, Tech. rep., Intergovernmental Panel on Climate Change, **2018**.

[13] V. V. Kharin, G. M. Flato, X. Zhang, N. P. Gillett, F. Zwiers, K. J. Anderson, *Earth's Future* **2018**, *6*, 704.

[14] V. Marchal, R. Dellink, D. V. Vuuren, C. Clapp, J. Château, E. Lanzi, B. Magné, J. V. Vliet, OECD Environmental Outlook to 2050 - Chapter 3: Climate Change, Tech. Rep. November, Organisation for Economic Co-operation and Development, **2011**.

[15] C. Fröhlich, J. Lean, *Astronomy and Astrophysics Review* **2004**, *12*, 273.

[16] Largest Desert in the World, http://geology.com/records/largest-desert.shtml, accessed on 2020-10-08.

[17] B. Norton, *Green* **2011**, *1*, 189.

[18] A. E. Becquerel, *Comptes Rendus L'Academie Des Sci* **1839**, *9*, 561.

[19] K. L. Chopra, P. D. Paulson, V. Dutta, *Progress in Photovoltaics: Research and Applications* **2004**, *12*, 69.

[20] Z. Fang, X. C. Wang, H. C. Wu, C. Z. Zhao, Achievements and challenges of CdS/CdTe solar cells, **2011**.

[21] T. D. Lee, A. U. Ebong, A review of thin film solar cell technologies and challenges, **2017**.

[22] B. Burger, K. Kiefer, C. Kost, S. Nold, S. Philipps, R. Preu, J. Rentsch, T. Schlegl, G. Stryi-Hipp, H. Wirth, W. Warmuth, Photovoltaics Report, Tech. rep., Fraunhofer Institute for Solar Energy Systems, Freiburg, **2020**.

[23] NREL: Best Research-Cell Efficiencies Chart, https://pvdpc.nrel.gov/, accessed on 2020-08-04.

[24] D. M. Powell, M. T. Winkler, H. J. Choi, C. B. Simmons, D. B. Needleman, T. Buonassisi, Crystalline silicon photovoltaics: A cost analysis framework for determining technology pathways to reach baseload electricity costs, **2012**.

[25] D. M. Powell, R. Fu, K. Horowitz, P. A. Basore, M. Woodhouse, T. Buonassisi, *Energy and Environmental Science* **2015**, *8*, 3395.

[26] Z. Song, C. L. McElvany, A. B. Phillips, I. Celik, P. W. Krantz, S. C. Watthage, G. K. Liyanage, D. Apul, M. J. Heben, *Energy and Environmental Science* **2017**, *10*, 1297.

[27] K. A. Horowitz, R. Fu, M. Woodhouse, *Solar Energy Materials and Solar Cells* **2016**, *154*, 1.

[28] M. Held, R. Ilg, *Progress in Photovoltaics: Research and Applications* **2011**, *19*, 614.

[29] M. J. De Wild-Scholten, *Solar Energy Materials and Solar Cells* **2013**, *119*, 296.

[30] J. Gong, S. B. Darling, F. You, *Energy and Environmental Science* **2015**, *8*, 1953.

[31] M. A. Green, E. D. Dunlop, J. Hohl-Ebinger, M. Yoshita, N. Kopidakis, A. W. Ho-Baillie, *Progress in Photovoltaics: Research and Applications* **2020**, *28*, 3.

[32] A. Kojima, K. Teshima, Y. Shirai, T. Miyasaka, *Journal of the American Chemical Society* **2009**, *131*, 6050.

[33] A. Miyata, A. Mitioglu, P. Plochocka, O. Portugall, J. T.-W. Wang, S. D. Stranks, H. J. Snaith, R. J. Nicholas, *Nature Physics* **2015**, *11*, 582.

[34] C. Wehrenfennig, G. E. Eperon, M. B. Johnston, H. J. Snaith, L. M. Herz, *Advanced Materials* **2014**, *26*, 1584.

[35] M. Zhang, H. Yu, M. Lyu, Q. Wang, J.-H. Yun, L. Wang, *Chemical Communications* **2014**, *50*, 11727.

[36] S. D. Stranks, G. E. Eperon, G. Grancini, C. Menelaou, M. J. P. Alcocer, T. Leijtens, L. M. Herz, A. Petrozza, H. J. Snaith, *Science (New York, N.Y.)* **2014**, *342*, 341.

[37] J. H. Noh, S. H. Im, J. H. Heo, T. N. Mandal, S. I. Seok, *Nano letters* **2013**, *13*, 1764.

[38] N. L. Chang, A. W. Y. Ho-Baillie, D. Vak, M. Gao, M. A. Green, R. J. Egan, *Solar Energy Materials and Solar Cells* **2018**, *174*, 314.

[39] What Is the Lifespan of a Solar Panel?, https://www.engineering.com/DesignerEdge/DesignerEdgeArticles/ArticleID/7475/What-Is-the-Lifespan-of-a-Solar-Panel.aspx, accessed on 2020-10-09.

[40] H. Zhou, Q. Chen, G. Li, S. Luo, T. B. Song, H. S. Duan, Z. Hong, J. You, Y. Liu, Y. Yang, *Science* **2014**, *345*, 542.

[41] J. Yang, B. D. Siempelkamp, D. Liu, T. L. Kelly, *ACS Nano* **2015**, *9*, 1955.

[42] T. Leijtens, G. E. Eperon, N. K. Noel, S. N. Habisreutinger, A. Petrozza, H. J. Snaith, *Advanced Energy Materials* **2015**, *5*, 1500963.

[43] G. E. Eperon, S. N. Habisreutinger, T. Leijtens, B. J. Bruijnaers, J. J. van Franeker, D. W. DeQuilettes, S. Pathak, R. J. Sutton, G. Grancini, D. S. Ginger, R. A. J. Janssen, A. Petrozza, H. J. Snaith, *ACS Nano* **2015**, *9*, 9380.

[44] A. J. Pearson, G. E. Eperon, P. E. Hopkinson, S. N. Habisreutinger, J. T.-W. Wang, H. J. Snaith, N. C. Greenham, *Advanced Energy Materials* **2016**, *6*, 1600014.

[45] M. L. Petrus, Y. Hu, D. Moia, P. Calado, A. M. A. Leguy, P. R. F. Barnes, P. Docampo, *ChemSusChem* **2016**, *9*, 2699.

[46] M. Saliba, T. Matsui, J.-Y. Seo, K. Domanski, J.-P. Correa-Baena, M. K. Nazeeruddin, S. M. Zakeeruddin, W. Tress, A. Abate, A. Hagfeldt, M. Grätzel, *Energy & Environmental Science* **2016**, *9*, 1989.

[47] N. J. Jeon, J. H. Noh, W. S. Yang, Y. C. Kim, S. Ryu, J. Seo, S. I. Seok, *Nature* **2015**, *517*, 476.

[48] W. Rehman, D. P. McMeekin, J. B. Patel, R. L. Milot, M. B. Johnston, H. J. Snaith, L. M. Herz, *Energy & Environmental Science* **2017**, *10*, 361.

[49] S. N. Habisreutinger, D. P. McMeekin, H. J. Snaith, R. J. Nicholas, *APL Materials* **2016**, *4*.

[50] P. Mantilla-Perez, T. Feurer, J. P. Correa-Baena, Q. Liu, S. Colodrero, J. Toudert, M. Saliba, S. Buecheler, A. Hagfeldt, A. N. Tiwari, J. Martorell, *ACS Photonics* **2017**, *4*, 861.

[51] Q. Xu, Y. Zhao, X. Zhang, *Solar RRL* **2019**, 1900206.

[52] J. Zheng, H. Mehrvarz, C. Liao, J. Bing, X. Cui, Y. Li, V. R. Gonçales, C. F. J. Lau, D. S. Lee, Y. Li, M. Zhang, J. Kim, Y. Cho, L. G. Caro, S. Tang, C. Chen, S. Huang, A. W. Ho-Baillie, *ACS Energy Letters* **2019**, *4*, 2623.

[53] A. T. Barrows, A. J. Pearson, C. K. Kwak, A. D. F. Dunbar, A. R. Buckley, D. G. Lidzey, *Energy & Environmental Science* **2014**, *7*, 2944.

[54] J. E. Bishop, D. K. Mohamad, M. Wong-Stringer, A. Smith, D. G. Lidzey, *Scientific Reports* **2017**, *7*, 7962.

[55] J. E. Bishop, J. A. Smith, C. Greenland, V. Kumar, N. Vaenas, O. S. Game, T. J. Routledge, M. Wong-Stringer, C. Rodenburg, D. G. Lidzey, *ACS Applied Materials & Interfaces* **2018**, *10*, 39428.

Chapter 2

Background

2.1 Hybrid Perovskites

The term perovskite refers to materials with the perovskite structure, which is classed as any crystal structure of the same type as that of calcium titanate ($CaTiO_3$).[1] The mineral perovskite is formed of $CaTiO_3$, and was first discovered by Gustav Rose in the Ural mountains in 1839 and named after the Russian mineralogist L. Perovski.[2]

The general chemical formula for perovskites is ABX_3, where A and B are cations of different sizes with A being larger than B, and X is an anion.[3] In this thesis, the perovskites being discussed are hybrid lead halide perovskites: 'hybrid' means that they contain both organic and inorganic compounds; 'lead' denotes that the B-cation is lead (Pb); and 'halide' describes that the X anion is taken from the halogens group of the periodic table. In hybrid lead halide perovskites, the A-cation can be made up of one or more organic molecules, or a mixture of organic and inorganic compounds. Whether it is lead or not, the B cation must be a large divalent metal cation, and sometimes tin (Sn) is used instead of Pb. The X anion is a halide, which can be a single halide or a mixture of two halides.[4] Despite the fact that the lattice contains organic molecules, defining these perovskites as hybrid organic-inorganic, the material is crystalline and therefore I will here describe the basic principles of solid state crystal structure.

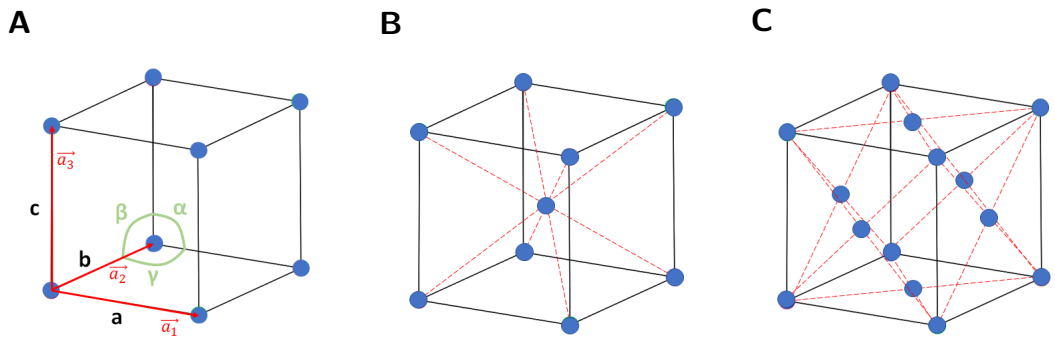

Figure 2.1: Schematics of a cubic crystal structure. **A** Simple cubic, **B** body-centred cubic (BCC) and **C** face-centred cubic (FCC) Bravais lattices.

2.1.1 Physics of Crystals: An Overview

Crystals are periodically repeating units made up of atoms or molecules, and the arrangement of the atoms or molecules in the crystal is known as the crystal structure. A crystal structure is made up of a basis, which is the system of atoms or molecules needed to make up the crystal, and a lattice, which is an infinitely repeating pattern of points arranged in a a particular way. Placing the basis at each lattice point creates the crystal. All lattice points can be located using the lattice vector $\boldsymbol{T}$, which is defined as

$$\boldsymbol{T} = n_1\boldsymbol{a}_1 + n_2\boldsymbol{a}_2 + n_3\boldsymbol{a}_3 \tag{2.1}$$

where $\boldsymbol{a}_1$, $\boldsymbol{a}_2$ and $\boldsymbol{a}_3$ are the primitive translation vectors, which are defined by the pattern of the lattice. The size of the integer coefficients n_i depends on the lattice point being located. A lattice which can be defined using Equation (2.1) is known as a Bravais lattice.[5]

Another key concept in crystallography is the reciprocal lattice. Mathematically speaking, the reciprocal lattice is the Fourier transform of the Bravais lattice. The reciprocal lattice can be defined, in a similar way to the real-space lattice, by the vector

$$\boldsymbol{G} = m_1\boldsymbol{b}_1 + m_2\boldsymbol{b}_2 + m_3\boldsymbol{b}_3 \tag{2.2}$$

where $\boldsymbol{b}_i$ are the primitive translation vectors for the reciprocal lattice, and m_i is a set of integer coefficients defined by the position in the reciprocal lattice.[6]

The smallest possible unit of atoms or molecules which can be repeated across all of space to produce the crystal is known as the unit cell. The physical dimensions of the

Table 2.1: Relationships between lattice constants and interaxial angles for the 7 crystal systems.

Crystal system	Lattice constants	Interaxial angles
cubic	$a = b = c$	$\alpha = \beta = \gamma = 90°$
trigonal	$a = b = c$	$\alpha = \beta = \gamma < 120°, \neq 90°$
hexagonal	$a = b \neq c$	$\alpha = \beta = 90°, \gamma = 120°$
tetragonal	$a = b \neq c$	$\alpha = \beta = \gamma = 90°$
orthorhombic	$a \neq b \neq c$	$\alpha = \beta = \gamma = 90°$
monoclinic	$a \neq b \neq c$	$\alpha = \beta = 90° \neq \gamma$
triclinic	$a \neq b \neq c$	$\alpha \neq \beta \neq \gamma$

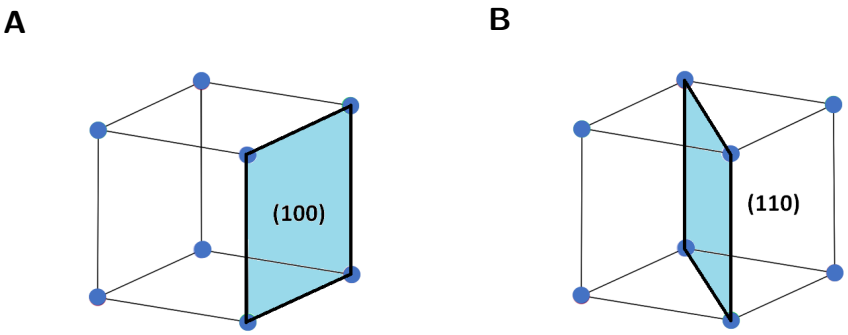

Figure 2.2: Diagram of a simple cubic structure, with the **A** (100) and **B** (110) crystal planes labelled.

unit cell are known as the lattice constants or lattice parameters. In three dimensions, there are three lattice constants: a, b and c.

There are 14 different Bravais lattices in total, which can be classified as one of 7 different crystal systems. These systems are differentiated by: the relative size of a, b and c; and the angles between the dimensions of the unit cell (denoted as α, β and γ). The definitions of the 7 crystal systems are summarised in Table 2.1.[6]

Planes whose intersections with the lattice are periodic, i.e. planes that would form 2-dimensional Bravais lattices, are known as lattice planes or crystal planes of a 3-dimensional Bravais lattice. Crystal planes are characterised by their Miller indices. The Miller index $(hk\ell)$ denotes a plane that is orthogonal to the reciprocal lattice vector $h\boldsymbol{b}_1 + k\boldsymbol{b}_2 + \ell\boldsymbol{b}_3$. In simpler terms, the Miller index is made up of the reciprocal axis intercepts of each axis by the plane in question. Examples of lattice planes with the Miller indices (100) and (110) in a cubic crystal are shown in Figure 2.2.

The spacing between lattice planes depends on the values of h, k and ℓ, and can be calculated for a cubic lattice in the following way,

$$d_{hkl} = \frac{a}{\sqrt{h^2 + k^2 + \ell^2}} \tag{2.3}$$

where a is the lattice constant.[5]

Bragg Diffraction

Lattice planes in a crystalline solid, and by extension its crystal structure, can be characterised using X-ray diffraction. The way in which electromagnetic waves, specifically X-rays, interact with crystalline solids holds the key to this. When X-rays are incident on a crystal, the waves will be reflected by planes within the crystal. The diffraction pattern obtained from this will depend on the spacing between the planes, which is the interplanar spacing d as defined in Equation (2.3). Constructive interference will be at its strongest when the condition

$$2d \sin\theta = n\lambda \tag{2.4}$$

is met, where d is the interplanar spacing between the reflecting planes, θ is the angle of incidence of the X-rays (defined as a glancing angle to the plane, not to the normal of the plane), n is a positive integer and λ is the wavelength of the incident X-rays.[7]

This condition can be used to 'index' crystal planes (i.e. identify the Miller indices) in a crystalline material, based on the interference pattern created by X-rays after being incident on the crystal.

2.1.2 Crystal Structure of Hybrid Metal Halide Perovskites

The perovskite crystal structure is depicted in Figure 2.3 in its cubic form. In the cubic perovskite structure, the A cation takes the corner positions of the cubic structure. The Pb atoms (the B cations) occupy the body-centred position and are bonded to 6 halide ions (the X anions) which are at the face-centred postions, forming PbX_6 octahedra as shown in Figure 2.3. The lead octahedra are corner-connected to form a three-dimensional framework.[9] Despite the crystalline nature of hybrid perovskites, it must be noted that hybrid perovskites have more of a "soft" crystal structure,[10] meaning

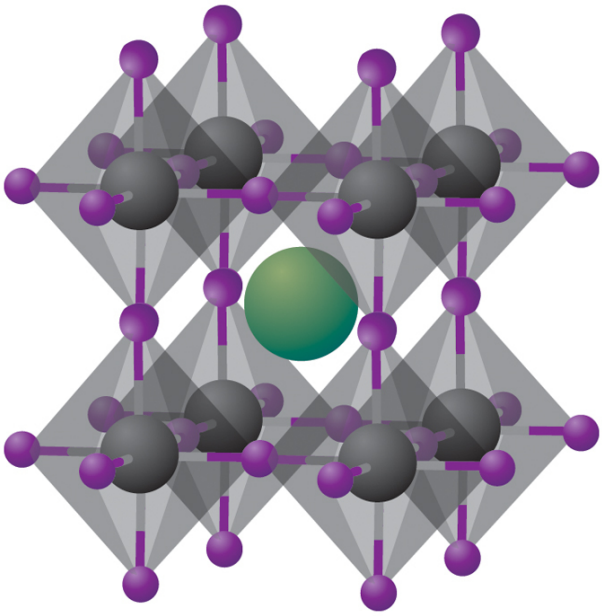

Figure 2.3: Perovskite crystal structure in the cubic phase. *Green:* organic or inorganic cations (A); *Grey:* metal cations (B); *Purple:* halide anions (X).[8].

that the constituents of the lattice have additional degrees of freedom compared to a solid state crystal.

The size and electronic properties of A, B and X will determine the probable structure and the inherent stability of that structure. The structure and its stability are determined by two variables, t and μ: t is the tolerance factor ($t = (R_A + R_X)/[\sqrt{2}(R_B + R_X)]$),[4] where R_A, R_B and R_X are the ionic radii of the corresponding ions, and μ is defined as the ratio R_B/R_X.[11]

The hybrid lead halide perovskite which has been the most studied to date is methylammonium lead triiodide, $CH_3NH_3PbI_3$. Methylammonium is an organic molecule, abbreviated as MA. $MAPbI_3$ has been found to adopt a $Pm\bar{3}m$ cubic crystal structure at temperatures above $\sim 57°C$ (330 K).[12] For the cubic unit cell at 60°C, the lattice parameter a has been reported to be 6.276 Å, as determined from powder X-ray diffraction measurements.[13]

In crystallography, a material of the same chemical composition but with a different crystal structure is known as a polymorph. $MAPbI_3$ has several polymorphs it can assume, and the polymorph it takes depends on material temperature. Below $\sim 57°C$, $MAPbI_3$ transforms to a tetragonal polymorph belonging to the $I4/mcm$ space group, with closer packing within the ab-plane. The lattice parameters of the tetragonal unit cell at 55°C have been reported as $a = b = 8.864$ Å and $c = 12.497$ Å.[13] The transition

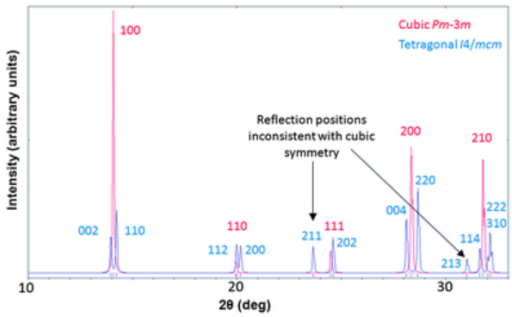

Figure 2.4: Calculated x-ray diffraction patterns for the cubic and tetragonal polymorphs of $MAPbI_3$. Figure reproduced from Baikie *et al. J. Mater. Chem. A* **2013** *1*, 5628.[13]

Table 2.2: Key crystal planes for cubic and tetragonal polymorphs of $MAPbI_3$, along with the 2θ value that would identify the plane in an X-ray diffraction pattern and the interplanar spacing d for each plane.[17]

Cubic			Tetragonal		
Miller Index	$2\theta(^\circ)$	d-spacing (Å)	Miller Index	$2\theta(^\circ)$	d-spacing (Å)
(100)	13.845	6.391	(002)	13.951	6.343
(110)	19.628	4.519	(110)	14.222	6.223
(111)	24.099	3.690	(112)	19.973	4.442
(200)	27.897	3.196	(200)	20.165	4.400
(210)	31.270	2.858	(211)	23.651	3.759
			(202)	24.601	3.615
			(004)	28.115	3.171
			(220)	28.668	3.111
			(213)	31.018	2.881
			(114)	31.641	2.826
			(222)	32.015	2.793
			(310)	32.139	2.783

to the tetragonal phase involves a collective rotation of the PbI_6 octahedra around the c axis.[14,15] $MAPbI_3$ can also form an orthorhombic crystal structure at temperatures below $\sim$ 160 K,[15,16] which is characterised by a tilting of the PbI_6 octahedra out of the ab-plane.[13] Figure 2.4 shows calculated x-ray diffraction patterns for both the pseudo-cubic and tetragonal polymorphs of $MAPbI_3$. Some of the key crystal planes are listed in Table 2.2, along with the 2θ value and interplanar spacings d (from Bragg's law, Equation (2.4)) of each plane.

Another commonly studied perovskite structure is that of $HC(NH_2)_2PbI_3$, where $HC(NH_2)_2$ is the organic molecule formamidinium (abbreviated as FA). $FAPbI_3$ forms two polymorphs at room temperature: a cubic perovskite phase (α-$FAPbI_3$), and δ-$FAPbI_3$, a yellow (not photo-active) hexagonal phase. The α-$FAPbI_3$ phase needed for

photovoltaic applications can be synthesised at temperatures about 60 °C but is not as stable as the δ-phase. A transition to a tetragonal unit cell (β-$FAPbI_3$) occurs just below room temperature at 285 K. A further phase transition occurs at 140 K to a low temperature phase known as γ-$FAPbI_3$, which is characterised by a set of weak Bragg scattering peaks.[18]

In $MAPbI_3$ and $FAPbI_3$, X-ray diffraction measurements only in fact represent a time-averaged picture of what is actually a fluctuation between different perovskite structures on a sub-ps timescale.[19] These different structures are characterised by different possible orientations of the organic cation and rotations of the octahedra.[20,21] In $MAPbI_3$, the organic cation has additional rotational degrees of freedom with respect to the octahedral framework in the tetragonal and cubic phases, as revealed by vibrational infrared (IR) spectroscopy and nuclear magnetic resonance (NMR) measurements.[14,16] Leguy and coworkers[22] used quasi-elastic neutron scattering (QENS) measurements to reveal that dipolar methylammonium ions reorientate between the faces, corners or edges of the pseudo-cubic lattice cages in $MAPbI_3$ crystals. Similarly, it has been found in formamidinium lead triiodide ($FAPbI_3$) that the organic formamidinium molecules rotate preferentially around the direction parallel to the line connecting its two nitrogen atoms.[10]

There are several sets of possible rotations of the lead octahedra, known as tilt transitions, which lead to symmetry reduction of the cubic phase and result in phase transitions to tetragonal and orthorhombic phases.[9,23,24] The rotational behaviour of the organic cation in $MAPbI_3$ is also phase-dependent. In the tetragonal phase, the organic cations are kept oriented along specific directions resulting in less freedom of rotation, whereas in the cubic phase there is nearly-free rotational motion of the organic cation within the octahedral framework.[16,25] Similarly, in $FAPbI_3$ the cubic phase is characterised by 'tumbling' motion of the FA cation[26] whereas in the tetragonal phase the FA cation has only a few preferred orientations in the A-site cage.[18]

This dynamic disorder in hybrid metal halide perovskites influences their electronic properties. Molecular dynamics simulations have suggested that it causes a spatial separation of the valence and conduction bands, leading to localisation of electronic

states.[21,27] This was previously speculated to be the origin of the easy exciton dissociation and low electron-hole recombination rates in hybrid lead halide perovskites. However, recent research has shown that this is unlikely to be the case, as discussed in Section 2.2.3 and Section 2.2.5.

2.2 Optoelectronic Properties of Hybrid Perovskites

As discussed in Section 2.1.2, hybrid perovskites are crystalline semiconductors. In periodic crystals, the allowed electronic energy levels form into bands. The highest occupied band, containing the valence electrons, is known as the valence band, while the lowest unoccupied band is known as the conduction band. In semiconductor materials, the valence and conduction bands are separated by an energy gap, generally referred to as the band gap.[28] The Fermi level, which is defined as the highest occupied single particle state at T = 0 K, usually lies within the band gap of a semiconductor. This means that all electrons in the material will remain in the valence band unless supplied with enough energy to surpass the energy gap.[6] The absorption of a photon of energy greater than the band gap causes the excitation of an electron-hole pair across the band gap. This allows for conduction of electrons in a process known as photoconductivity, and these conducting electrons can then be exploited to generate an electric current in a photovoltaic cell,[29] a process which will be discussed in more detail in Section 2.3.1.

If we consider the valence and conduction bands of a semiconductor as a basic two-level system with energies E_v and E_c, respectively, where $E_c > E_v$, we have three distinct events which can occur in this system. These are: the absorption of a photon to promote an electron from E_v to E_c, the relaxation of an electron from E_c to E_v, causing emission of a photon (spontaneous emission), and relaxation of an electron to E_v from E_c having been stimulated by an incident photon, causing emission of a second photon (stimulated emission). In a solar cell, the absorption process of interest is one which promotes an electron from E_v to E_c.[30]

Photoluminescence (PL) is strictly defined as light emission from a material caused by absorption of photons into the material. Given that certain additional conditions are required to cause stimulated emission, PL emission in solar cells is generally a result

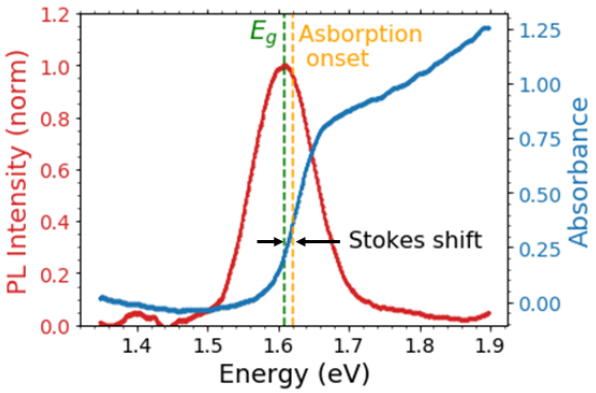

Figure 2.5: Example of PL and absorbance traces typical of hybrid perovskites, showing the optical band gap E_g as determined by the PL peak energy, the absorption onset and the Stokes shift.

of spontaneous emission. Fluorescence is a sub-process of PL in which the re-emission happens on "fast" timescales i.e. on the order of nanoseconds, in contrast to phosporescence, where the photoluminescence occurs over longer timescales such as hours or days. In the context of photovoltaics, it is fluorescence that is the key process of interest.[31] Examples of absorbance and PL emission spectra for a typical perovskite are shown in Figure 2.5. Generally, the peak of the PL emission curve quantifies the optical band gap, E_g, of the perovskite. The absorbance spectrum also gives a measure of the band edge, via the absorption onset. In an ideal system, we would expect the optical band gap determined from the PL emissions to be at the same energy as the absorption onset, but often this is not the case due to energetic disorder in the material. The difference between these quantities is known as the Stokes shift, as shown in Figure 2.5.[32]

2.2.1 Generation and Recombination

In a solar cell, generation is the process by which electrons excited by absorption of a photon become free charge carriers, and recombination is the process by which these electrons relax back to their original state. The generation process of interest in a PV cell is the creation of an electron-hole pair, also known as an exciton, caused by a photon absorption event. There are several relevant recombination processes, but generally these can be simplified to the relaxation of the electron back into the valence band rendering it no longer a free charge carrier, in a spontaneous emission event. It is the rates of both these processes, combined with the charge carrier transport properties

of the semiconductor material, which are the driving forces of PV cell performance.

We can derive the photogeneration rate, i.e. the rate at which mobile electrons and holes are generated by photon absorption, if we consider not only the incident photon flux, but also how well the material absorbs photons. The latter is facilitated by introducing some sort of absorption coefficient. The full derivation is not necessary here, but the result is that the total generation rate $G(x)$ at a given depth x into an absorber material is given by

$$G(x) = \int g(E, x) dE \tag{2.5}$$

where the spectral generation rate $g(E, x)$ is given by

$$g(E, x) = (1 - R(E))\alpha(E) b_s(E) e^{-\int_0^x \alpha(E, x') dx'} \tag{2.6}$$

where $R(E)$ is the reflectivity of the surface, $\alpha(E)$ is the macroscopic absorption coefficient and b_s(E) is the incident photon flux. We need only to perform the integral over energies where photon absorption primarily results in free carrier generation, where $E \geq E_g$, where E_g is the band gap of the material.[33]

In cases where $E > E_g$, the excess energy is generally unable to be put to use as it is lost in thermalisation. This is the process whereby the electron is excited to a higher energy level in the conduction band, but relaxes back to the band edge via repeated collisions with the lattice which cause it to lose kinetic energy. This generally happens on the order of picoseconds due the high density of states near the band edge, and therefore in a PV cell it is one of the main sources of energy loss as it far outpaces any generation process. It is a combination of this and other more complex thermodynamic processes which result in a fundamental thermodynamic limit on the efficiency of a single-junction solar cell of $\sim 33.7\%$.[34]

Recombination refers to any loss of mobile electrons in a semiconductor, and such mechanisms fall into two broad categories - radiative and non-radiative. In PV cells,

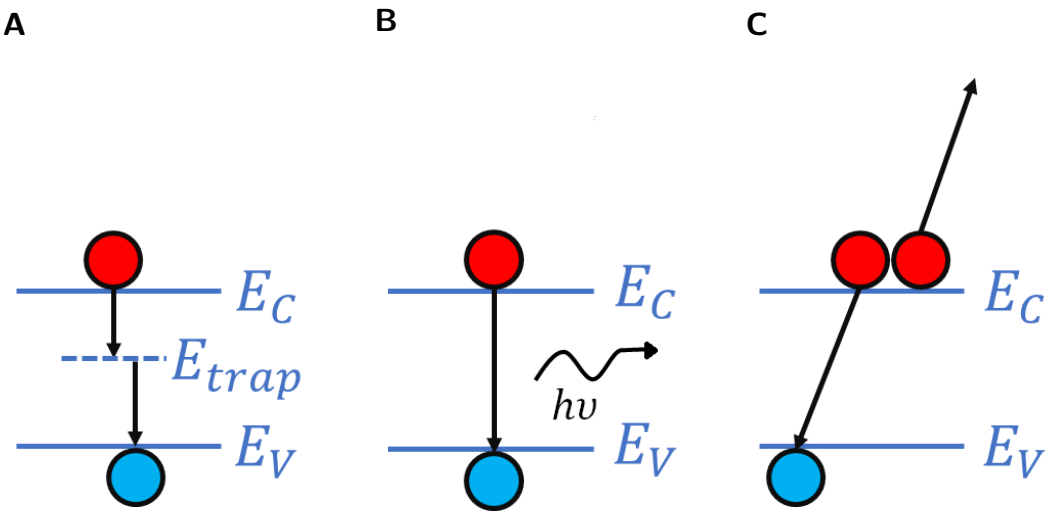

Figure 2.6: Simplified energy band schematics showing the mechanisms of **A** monomolecular trap-assisted recombination, **B** bimolecular recombination through spontaneous emission, and **C** Auger recombination, which may happen through an interaction with another charge carrier in the conduction band, as shown here, or with a phonon.

radiative recombination occurs through spontaneous emission. There are two primary mechanisms for non-radiative recombination. The first is Auger recombination, where the interaction of an electron (or hole) with a second similar carrier leads to the decay of the carrier across the band gap and the increase in kinetic energy of the second carrier. Non-radiative recombination can also occur by way of relaxation via localised trap states, which are present due to defects in the crystalline structure; this is known as Shockley-Read-Hall recombination.[33]

Recombination in semiconductors is generally governed by the following rate equation:

$$\frac{dn}{dt} = -k_3 n^3 - k_2 n^2 - k_1 n \tag{2.7}$$

where n is the charge carrier density, k_1 is the monomolecular recombination rate, k_2 is the bimolecular recombination rate and k_3 is the third order recombination rate. In other words, k_1 describes the rate of recombination processes involving only one charge carrier, such as non-radiative Shockley-Read-Hall recombination. k_2 describes recombination processes involving two charge carriers, such as direct-electron hole recombination via spontaneous emission. k_3 describes recombination involving three particles, which are usually Auger recombination processes.

From this, the total recombination rate is derived as follows:[35]

$$R_{TOT} = -\frac{1}{n}\frac{dn}{dt} = k_3 n^2 + k_2 n + k_1 \tag{2.8}$$

The carrier lifetime is a measure of the average time photoexcited electrons can exist in the material before recombining with holes in the conduction band, and therefore is a key parameter affecting performance in solar cells.

Photoluminescence Quantum Yield

The photoluminescence quantum yield (PLQY) (sometimes called photoluminescence quantum efficiency [PLQE]) is a measure of the output photoluminescence as a proportion of absorbed photons. It is defined as

$$PLQY = \frac{photons \quad out}{photons \quad in} \tag{2.9}$$

Alternatively it can be expressed in terms of recombination rates, as

$$PLQY = \frac{k_r}{k_{nr} + k_r} \tag{2.10}$$

where $k_{nr} = k_1 + k_3 n^2$ is the non-radiative recombination rate and $k_r = nk_2$ is the radiative recombination rate, as dictated by Equation (2.8). The PLQY therefore gives a measure of the proportion of the recombination in the material which is radiative, which varies depending on the charge carrier density n.[31] This is an important parameter to quantify in solar cells, as a high proportion of recombination occurring through non-radiative pathways is detrimental for solar cell performance.

2.2.2 Band Structure

Density functional theory calculations have revealed the electronic band structure of hybrid lead halide perovskites.[36–40] A schematic diagram of the band structure for $MAPbI_3$ at room temperature (tetragonal polymorph), is shown in Figure 2.7**A**. The valence band maximum (VBM) is formed of antibonding states derived from hybridizations of the atomic $5p$ orbitals of iodine and $6s$ orbitals of lead. The conduction band minimum (CBM) is mainly formed of empty $6p$ orbitals of lead[36,38]. Due to the presence of the

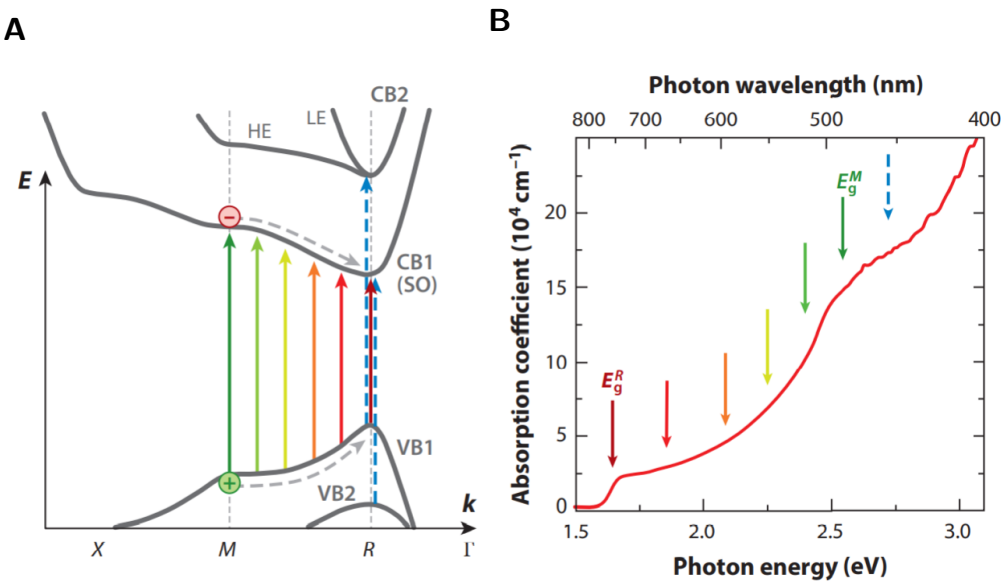

Figure 2.7: **A** Schematic of the electronic band structure of $MAPbI_3$ at room temperature, as calculated by density-functional theory calculations.[40,41] Coloured arrows represent photo-induced electronic transitions which are allowed by selection rules. The dashed blue arrows indicate partly dipole-allowed transitions (VB2 → CB1 and VB1 → CB2). **B** Absorption spectrum for $MAPbI_3$, showing the absorption continuum which is a result of a continuum of electronic transitions between the R and M high-symmetry points.[42]Figures reproduced from Herz *Annu. Rev. Phys. Chem.* **2016** *67*, 65.[43]

heavy ions lead and iodine, spin-orbit coupling leads to splitting of the conduction band. The lower conduction band (CB1) is the spin-orbit (SO) band, whereas the higher band (CB2) comprises heavy- and light-electron states.[40,41] The lower SO band forms the conduction band minimum (CBM).[38]

The points Γ, *M*, *R* and *X* marked in Figure 2.7A are known as high-symmetry points, which are points in *k*-space corresponding to certain positions on the Brillouin zone: the Brillouin zone is effectively the unit cell for the reciprocal lattice of the crystal. Optically allowed transitions of electrons from the VBM to the CBM at the R-point correspond to the band-gap energy E_g, which is observed in the absorption spectrum in Figure 2.7**B** as the absorption onset at $\sim$ 1.6 eV. Optical transitions at *k*-values between the *M*- and *R*-points (coloured arrows in Figure 2.7**A**) lead to the absorption continuum at photon energies above E_g, as shown by the coloured arrows in Figure 2.7**B**. The band structure of $MAPbI_3$ therefore allows for the photogeneration of electron-hole pairs across a wide range of visible wavelengths.[44] Subsequent relaxation of electrons gives rise to a photoluminescence (PL) peak at $\sim$ 1.6 eV, which arises from CB1 → VB1 transitions at the R-point.

2.2.3 Charge Carriers: Excitons or Free Carriers?

Absorption of photons near the band edge creates electron–hole pairs in hybrid metal halide perovskites (MHPs). The bound electron-hole pair, also known as an exciton, has a binding energy E_B, and has to be separated in order for electrons and holes to contribute to the photocurrent. If $E_B < k_B T$, where $k_B T$ is the thermal energy at temperature T (k_B is the Boltzmann constant), the thermal energy will be sufficient to dissociate the electron-hole pair, creating free charge carriers which can conduct electricity. The question of whether the dominant carrier species after photo-excitation in MHPs is excitons or free charge carriers has long been hotly debated.[45–55]

The exciton binding energy for $MAPbI_3$ has been investigated through optical absorption by various groups.[41,49,53,55,56] D'Innocenzo *et al.*[48] reported a technique for estimating the binding energy of a material by analysing the absorption spectra near the absorption onset, based on the assumption that the absorption onset contains contributions from both homogeneous excitonic broadening mechanisms and inhomogeneous broadening resulting from disorder. By extracting the width of the absorption onset feature as a function of temperature, they found a binding energy of 55 $\pm$ 20 meV for $MAPbI_3$.

The exciton binding energy can also be calculated from the absorption onset using Elliott's theory,[57] which describes the shape of the absorption onset, taking into account excitonic and continuum absorption. In the absence of excitonic effects, the absorption coefficient α for photons with energy E incident on a material is $\alpha \propto E - E_g$ near the absorption onset, where the valence and conduction bands can be approximated as parabolic. Coulombic interactions lead to additional absorption features below the absorption onset, but will also enhance the absorption in the continuum states.[57,58] Figure 2.8 demonstrates how the absorption spectrum of hybrid perovskites can be modelled using Elliott's theory, with contributions from excitonic and continuum absorption fitted with blue and red dashed lines, respectively.[59]

Several groups have taken this approach[49,53,55,59] and found room temperature exciton binding energies varying from 5 meV[41] to 25 meV.[49] The Elliott's theory method was also able to elucidate the temperature-dependent exciton binding energy of per-

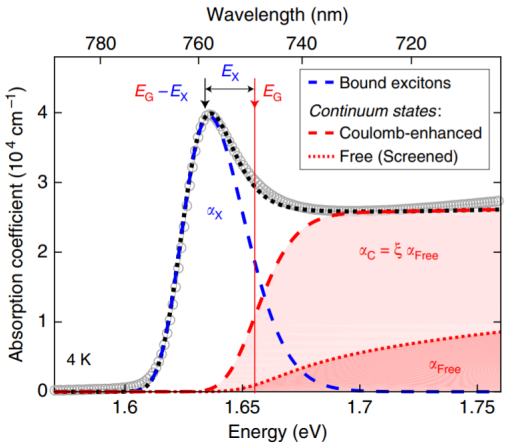

Figure 2.8: Absorption spectrum of $MAPbI_3$ at $T = 4$ K. The black dotted line is a fit to the data based on Elliott's theory, which allows the separation of the contributions to the total absorption coefficient arising from bound excitonic states (blue dashed line α_X) and electron-hole continuum states (red dashed line α_C). The red dotted line α_{Free} represents the free charge carrier states, and the absorption from these is enhanced by Coulombic interactions by the Coulomb enhancement factor ξ, resulting in α_C. Arrows indicate the position of the band gap (E_g) and the value of the exciton binding energy (here denoted E_X). Figure obtained from Davies *et al.*, *Nat. Comms* **2018** *9*, 293.[59]

ovskites, and unsurprisingly there were found to be variations in E_B depending on the structural phase. As discussed in Section 2.1.2, the phase transitions in perovskite are characterised by changes in the rotation of the MA cation with respect to the $C - N$ axis, and the polarity of the MA cation along the $C - N$ axis modifies the dielectric function, therefore significant changes in the exciton binding energy are expected at the phase transitions.[38,39] Even and coworkers[41] found that E_B remained relatively constant at 5 meV in the tetragonal (room temperature) phase of $MAPbI_3$, whereas in the orthorhombic (low temperature) phase E_B reached 15 meV with a relatively abrupt change between phases. Contrastingly, Yamada and coworkers[53] found a much more gradual increase in binding energy, increasing from $\sim$ 6 meV at room temperature to 30 meV at 13 K.

This large variation in E_B values found for $MAPbI_3$ may be due to the fact that the excitonic absorption peak is not clearly separated from the continuum absporption in $MAPbI_3$.[54] Therefore an alternative method was used by Sestu and colleagues,[54] which was based on fits to the temperature dependence of the integrated absorption near the onset, a method which should be less sensitive to lineshape broadening. Using this method, Sestu *et al.* reported an exciton binding energy of 29 meV at room temperature, which underwent a discontinuous change to 34 meV at the transition to the orthorhombic

phase.

Another way of obtaining the exciton binding energy is by carrying out absorption measurements under a strong magnetic field in a technique known as magneto-absorption. When a magnetic field is applied to a material, its absorption feature may shift in energy, known as the diamagnetic shift. By measuring the diamagnetic shift as a function of applied magnetic field, the diamagnetic coefficient c_0 can be derived. Excitons are formed due to the interaction of the dielectric function $\epsilon(\omega)$ of the solid with the electric field of an incident electromagnetic wave. The exciton binding energy can be found from c_0 via the following relation,

$$\frac{E_B}{Ry} = \left(\frac{1}{\epsilon^4(c_0/c_H)}\right)^{1/3} \tag{2.11}$$

by taking ϵ as the high-frequency value of $\epsilon(\omega)$, i.e. the value in the optical region of the energy dispersion. Ry and c_H are the Rydberg constant and diamagnetic constant, respectively, for a hydroden atom. Using this method, values of E_B of 37 meV[45] and 50 meV[36] have been reported for the orthorhombic $MAPbI_3$ phase.

However, due to the large variation in values of dielectric function ϵ for $MAPbI_3$, not only with frequency[46,60] but also with temperature,[15,61] there is a large variation in the exciton binding energy calculated from diamagnetic shifts from magneto-absorption.[41,46,52] An accurate choice of ϵ relies on prior knowledge of E_B in this method, therefore this approach is not self-consistent.

There is a way to use the diamagnetic shift to find E_B without the dielectric function, which Miyata and colleagues demonstrated, observing the absorption features originating from both $1s$ and $2s$ exciton states in their magneto-absorption measurements.[52] In this way they found an exciton binding energy of 16 meV in the orthorhombic phase. However, this method did not allow for high temperature (tetragonal phase) measurements of $MAPbI_3$'s exciton binding energy due to thermal broadening, therefore this method still had its limitations.

E_B for hybrid perovskites has also been found from temperature-dependent photoluminescence (PL) intensities[50,51,62,63] In all such studies, a decrease in PL intensity with increasing temperature was attributed to thermally-activated exciton dissociation, and a

Boltzman activaton law was applied to the temperature dependence of the PL intensity, to extract an activation energy which represents the exciton binding energy. These investigations led to reports of $E_B = 19$ meV[50] and 32 meV[51] for $MAPbI_3$, and 62 meV for $MAPbI_{3-x}Cl_x$.[47] In these investigations, the change in luminescence efficiency at the orthorhombic phase transition was not discontinuous. This suggests that, unlike the Elliott theory-derived results of Even *et al.*[41] and Sestu *et al.*,[54] the E_B value does not undergo an abrupt change at the phase transition. Similarly to the magneto-absorption and optical absorption methods, this method has yielded a wide variation in E_B values. This is suspected to be due to the complex temperature dependence of the PL emission even in the absence of excitonic effects, which will make it difficult to disentangle the exciton binding energy from such methods.

Despite the large variation in reported E_B values and discrepancies in temperature dependence of E_B, there nevertheless clearly is a temperature dependence of the exciton binding energy, therefore there is no global value of E_B for hybrid lead halide perovskites.

As discussed above, reported values of E_B for $MAPbI_3$ at room temperature range between 5 meV[41] and $\sim$ 50 meV.[36] These values are comparable to the room temperature thermal energy of $k_B T \sim 25$ meV, which suggests that the dominant species of charge carrier in hybrid perovskites at room temperature is free carriers as opposed to excitons. To confirm this, numerous studies focussed on $MAPbI_3$ have reported that the dominant photo-excited species in this material is free charge carriers,[64–67] as revealed by time-resolved spectroscopic experiments on solution-processed thin films. Wehrenfennig and coworkers found through transient terahertz (THz) pump-probe spectroscopy on $MAPbI_3$ and $MAPbI_{3-x}Cl_x$ that only one type of charge carrier species appeared to contribute to the THz photo-conductivity, and the Drude-like conductivity spectrum suggested that this species was free charge carriers.[64] Ponseca *et al.*[67] also measured the photo-induced terahertz conductivity of $MAPbI_3$ and, correlating it with band-edge absorption behaviour, suggested that there was only one species of charge carrier present at room temperature.

Further to this, Yamada and coworkers[66] used time-resolved PL spectroscopy and transient absorption (TA) spectroscopy (a technique which measures absorption as a

function of wavelength and time after excitation) to study the carrier relaxation and recombination dynamics in $MAPbI_3$ thin films. They found that the PL intensity just after excitation was dependent on the square of the excitation intensity, indicating that the dominant recombination process was radiative recombination of free electrons and holes. The finding that the dominant charge carrier species at room temperature in $MAPbI_3$ was free carriers was great news for $MAPbI_3$ as a promising solar cell absorber, as photovoltaic action relies on the presence of free charge carriers to conduct electricity.

2.2.4 Early Time Charge Carrier Relaxation

Initial creation of electron-hole pairs in hybrid perovkites is followed by relaxation of some charge carriers back to the band edge, as a significant portion of the photo-excited charge carriers will have an energy much larger than the band gap. Inorganic semiconductors such as GaAs (gallium arsenide), whose charge carrier dynamics are much more well-established than those of hybrid perovskites,[58,68,69] undergo several processes in the early timescales after photo-excitation. The first of these is the loss of the coherence of photo-excited states generated by excitation by a laser source through scattering events such as collisions with other charge carriers or phonons.[69] Electronic coherence after photo-excitation in $MAPbI_3$ or other hybrid perovskites has not yet been widely explored, however ultrafast pump-probe spectroscopy has suggested a dephasing time of approximately 1 ps for $MAPbI_3$ perovskite.[70]

As described in Section 2.3.2, photo-excited electrons with energy much larger than the band gap of the material will undergo a process called thermalisation. Collisions with the lattice cause such electrons to rapidly lose energy, on the timescale of picoseconds or faster. This will lead to the charge carriers within the electronic bands conforming to a thermalised Maxwell distribution with a characteristic carrier temperature T_c.[69] At this stage, $T_c > T_L$, where T_L is the temperature of a lattice, and the charge carriers are described as 'hot'. Subsequently, carrier cooling occurs via interactions with the lattice. For traditional inorganic semiconductors such as GaAs, carrier cooling at this stage originates from interactions between the electron and hole populations and the longitudinal optical (LO) phonon population.[71,72] This may be followed by a

slower cooling process involving a thermal equilibrium being reached between LO and acoustic phonons. However, if the charge carrier density n is high, the LO phonon mode occupation may increase, elevating acoustic phonon temperature closer to T_c and therefore allowing carriers to stay hot for longer timescales, in a phenomenon known as a phonon bottleneck.[72,73] It is clearly important to understand these early-time carrier cooling mechanisms in hybrid perovskite absorbers, as the excess energy of hot carriers could be potentially be utilised in photovoltaic cells to achieve higher open circuit voltages and power conversion efficiencies, especially if sustained for extended timescales due to a phonon bottleneck.

The initial charge carrier relaxation processes discussed have been widely studied in hybrid perovskites, with most investigations focussing on $MAPbI_3$.[74–82] The most commonly used technique to investigate such processes has been transient absorption spectroscopy, where laser pulses on the order of 100s of femtoseconds can be used to probe early time dynamics of hybrid perovskites by interpreting the transient absorption spectra. Early investigations were based on the shape of the TA spectrum near the band edge,[74,76,78,80] with some investigations also focussing the observation of a high energy absorption peak near 2.6 eV.[74,76] This high energy absorption feature has been attributed by some groups to a VB2 $\rightarrow$ CB1 (dipole-allowed) transition[74,75,79,82] and by others to charge transfer between different lead halide complexes in the lattice.[76,81,83]

With regards to the spectral shape near the band edge ($\sim$ 1.6 eV), some researchers attribute it to a combination of excitonic and free carrier effects,[55,78] while others showed that it originates solely from free carrier effects and refractive index modulations.[80] Despite the complex time evolution of the near-band-edge absorption spectrum, originating from the interplay of several different charge relaxation mechanisms, studies have brought the research field to a general consensus that absorption features above the band edge ($\gtrsim$ 1.7 eV) are a result of hot carriers. Hot carrier cooling dynamics have been reported by multiple groups as being on sub-picosecond timescales.[74,82,84] Through DFT calculations, it has been postulated that this sub-picosecond cooling process is facilitated by coupling to LO phonon modes associated with the lead halide octahedral framework.[79] Lead halide vibrational modes have been shown to couple to

the photo-excited charge carrier density,[64,85] a finding that is in agreement with this mechanism for hot carrier cooling. Cooling processes on longer timescales (≤ 1 ns) have also been reported for carriers with energies significantly above the band edge.[74–76] For higher excitation densities, these carrier cooling processes have been shown to slow down, which has been attributed to a phonon bottleneck.[55,80] However, the harvesting of these hot carriers in solar cells must be investigated further, as the excitation densities needed for the phonon bottleneck effect are close to $n \sim 10^{17}$ cm^{-3},[80] whereas 1 Sun illumination at AM1.5 leads to a lower carrier density of $n \sim 10^{15}$ cm^{-3}.[35]

2.2.5 Charge Carrier Recombination Dynamics

The dynamics and recombination of photo-excited charge carriers is of paramount importance to the functionality of solar cells. The charge carrier lifetime is the total time that photo-excited charge carriers exist in the material before recombination occurs. Therefore the carrier lifetime is a measure of the time available for charge carrier extraction into selective contact layers to occur. Hybrid perovskites have been shown to not only have long charge carrier lifetimes but also high-charge carrier mobilities, a combination which makes them ideal absorber materials for solar cells.

As discussed in Section 2.2.1, once the free charge carrier density n has been generated in a semiconductor, its subsequent decay can be described through Equation (2.7) (the rate equation). There are three separate decay rates which arise from different physical processes which contribute to the decay of the charge carrier density. k_1 is the monomolecular rate constant, associated either with excitonic recombination or trap-assisted recombination involving a single carrier (an electron or a hole) being trapped in a sub-bandgap defect state, as shown in Figure 2.6**A**. As discussed in Section 2.2.3, previous studies on hybrid perovskites suggests that excitonic effects are largely absent at room temperature, therefore k_1 is likely to be associated with predominantly non-radiative recombination.

The rate k_2 is the bimolecular recombination rate, which is the rate of intrinsic electron-hole recombination—the mechanism for this is shown in Figure 2.6**B**. This rate depends on n_e, the electron density and n_h, the hole density due to the relation $n_e n_h = n^2$.

Bimolecular recombination is likely to be predominantly radiative in hybrid perovskites as they are direct band gap semiconductors. Wetzalaer and coworkers used electroluminescence to investigate the recombination pathways in perovskite. Electroluminescence is the resulting light emission when a semiconductor material is driven at a bias voltage, creating conduction electrons which are then free to recombine with the valence band holes, and the electroluminescence quantum efficiency is the number of photons emitted per driving currrent electron, therefore allowing for differentiation between radiative and non-radiative recombination pathways. Wetzalaer and coworkers found, by combining electroluminescence quantum efficiency measurements with investigations of the diode ideality factor of perovskite solar cells (see Equation (2.15) in Section 2.3.1), that trap-assisted recombination was mainly nonradiative, while bimolecular recombination was mostly radiative.[86]

The rate k_3 is the rate of Auger recombination processes, which are many-body processes involving recombination of an electron with a hole which is accompanied by energy and momentum transfer to a third body, which is either an electron (or hole) in the conduction band (or valence band), or a phonon. Auger recombination is inherently non-radiative due to the loss of energy and momentum to the third body in the interaction.

Mobility and Diffusion

The recombination dynamics influence other optoelectronic properties such as diffusion length. The diffusion length is the average distance a photo-excited carrier can travel before recombining. It is given by[64,85]

$$L_D(n) = \sqrt{\frac{\mu k_B T}{R_{TOT}(n) e}} \tag{2.12}$$

where μ is the electron mobility, T is the temperature (of the thin film), e is the elementary charge and R_{TOT} is the total recombination rate, as given by Equation (2.8) in Section 2.2.1. The charge carrier mobility is related to the photoconductivity σ by $\sigma = ne\mu$, where n is the charge carrier density as in Equations (2.7) and (2.8), and therefore is a key parameter to characterise in solar cell absorbers.

Wehrenfennig and coworkers[64] determined charge carrier mobilities in the per-

ovskites $MAPbI_3$ and $MAPbI_{3-x}Cl_x$, using THz pump-probe spectroscopy to find the mobility from the change in THz electric field transmission. Here the charge carrier mobilities were determined to be 11.6 $cm^2V^{-1}s^{-1}$ for $MAPbI_{3-x}Cl_x$ and ~ 8 $cm^2V^{-1}s^{-1}$ for $MAPbI_3$, values which are extremely high for solution-processed films. Other reports confirm this, with mobility values between 20 and 70 $cm^2V^{-1}s^{-1}$ being reported for $MAPbI_3$ and $MAPbI_{3-x}Cl_x$ films.[85,87,88] For comparison, mesoporous TiO_2 (titanium dioxide, often used as a charge-selective layer in perovskite solar cells) has a mobility in the range $\sim 10^{-4} - 10^{-3}$ $cm^2V^{-1}s^{-1}$ [89] and organic semiconductors typically have mobilities on the order of 10^{-4}.[90–92]

Transient optical spectroscopy techniques such as TA spectroscopy, THz pump-probe spectroscopy and time-resolved photoluminescence (TRPL) spectroscopy can be used to probe electron and hole diffusion in these materials, by investigating solution-processed hybrid perovskites deposited with an electron- or hole-selective contact for quenching of PL.[65,74,93] Long-range electron–hole diffusion lengths of $\gtrsim 100$ nm have been found for solution processed $MAPbI_3$.[65,93–97] The mixed halide $MAPbI_{3-x}Cl_x$ has been found to have diffusion lengths one order longer than this, exceeding 1 μm,[65] demonstrating the scope of compositional engineering in hybrid perovskites to improve device performance through tuning of optoelectronic properties.

Long diffusion lengths in hybrid perovskites can be attributed to the ideal combination of low charge carrier recombination rates and high charge carrier mobilities in these materials. It has been reported that both monomolecular and bimolecular carrier recombination rates in $MAPbI_3$ are fairly low considering the organic components of the crystal, as will be discussed in detail below.

Trap-Assisted Recombination

For solar cells under 1 Sun illumination at AM1.5, typical resulting charge-carrier densities are in the range $n \sim 10^{15}$–10^{16} cm^3.[35] At such low values of n, the monomolecular recombination k_1 dominates the decay of the charge carrier population. This allows the decay rate to be modelled by the simple relation $n = n_0 \exp(-k_1 t)$ from which k_1 can be extracted.

As the monomolecular rate is likely to be dominated by trap-assisted processes in hybrid perovskites, this rate will be highly dependent on the density of defects and the nature of defect states in the material. Hence a wide range of values for the monomolecular charge-carrier lifetime $\tau_1 = k_1^{-1}$ have been reported for $MAPbI_3$ and $MAPbI_{3-x}Cl_x$, from 4 ns to 1 μs ($k_1 = 1\text{–}250 \times 10^6$ s^{-1}).[49,65,66,88,98–100] The nature and density of traps will also vary with material composition, therefore there is a large variation in τ_1 when elemental substitutions are made. In the mixed halide perovskite systems $MAPbBr_yI_{3-y}$ and $FAPbBr_yI_{3-y}$, the value of k_1 increased significantly as the y-value converged inwards towards the range $y/3 = 0.3\text{–}0.5$.[101,102] This was attributed to poor crystallinity in this compositional range, due to changes in crystal structure.[103] Mixing the A-site cation as well as the halide has been shown to improve this.[104]

Due to the strong dependence of the nature and density of defects on processing conditions in solution-processed thin films, the k_1 rate can be effectively reduced through the modification of processing conditions.[65,97,99,100,105] It follows from Equations (2.8) and (2.12) that a decrease in k_1 will increase the diffusion length L_D, which would be advantageous for the operation of solar cells.

Defects in Hybrid Perovskites

The nature of defect states in hybrid perovskites is essential understanding for the optimisation of perovskite solar cells due to its effect on the trap-assisted recombination rate, which dominates the charge carrier recombination dynamics at 1 Sun illumination. DFT simulations have revealed that defect states in $MAPbI_3$ are predominantly shallow traps, which would go some way to explaining the excellent transport properties of this material.[106,107] Shallow traps, with depths as small as 10 meV have also been experimentally observed, using modelling of photoconductivity spectra.[88] Yin and colleagues postulated that shallow traps are likely to originate from elemental vacancies, such as lead, iodine or MA ions missing from the lattice, with trap depths below 50 meV.[107] The current consensus is that iodide vacancies, also known as iodine interstitials, are the most common defects in hybrid perovskites.[108–114] The migration of iodine ions leads to current-voltage hysteresis in perovskite solar cell devices, i.e. a difference in the

current-voltage behaviour when driving the solar cell under opposite biases.[115,116]

The extent of energetic disorder in a material can shed light on the underlying nature of trap states. Energetic disorder can be investigated through the Urbach tail of the absorption spectrum, which is the exponential drop-off of the absorption onset below the band edge. A quantity known as the Urbach energy can be extracted from the slope of the exponential, which gives a measure of the energetic disorder. Urbach energies have been found for perovskite in the range 15 meV, further indicating that trap states are predominantly shallow as this denotes a very low level of energetic disorder.[117,118] The temperature dependence of the Urbach energy has also been investigated and the results suggest that there is some thermal activation process for shallow traps,[119] an idea that has been postulated previously by Milot *et al.* when studying the temperature dependence of k_1.[120] In this study, Milot and colleagues observed an increase in k_1 with increasing temperature, and attributed this to the explanation that shallow traps in perovskite originated from ionized impurities, which will be effectively passivated below the ionisation energy of the impurity and therefore will begin to become active as the temperature is increased. The activation energy of such impurities revealed an effective trap depth of $\sim$ 20 meV in the tetragonal phase of $MAPbI_3$, which increased to $\sim$ 200 meV in the cubic phase,[120] suggesting that the trap depth is related to crystal structure.

The density of traps in hybrid perovskites has also been investigated experimentally with a variety of techniques, with values in the range 10^{16}–10^{17} cm^{-3} being reported.[76,121–123] This value appears to increase near perovskite grain boundaries and at interfaces with hole- or electron-extracting layers,[100,105,123] which means that trap-assisted recombination rates are not only dependent on crystallite size but also vary spatially. The spatial variation of trap states means that the rate equation (Equation (2.7)) must also include a charge carrier diffusion term such as $D\nabla^2 n(x, y, z, t)$ where D is the diffusion coefficient, which means that k_1 rates extracted without this consideration may not be completely accurate. This is often accounted for in experimental work by modelling the trap-assisted decay dynamics with a stretched exponential e.g. $n = n_0 \exp(-t/\tau)^{\beta}$, instead of a single exponential ($n = n_0 \exp(-k_1 t)$).[65,100,124]

Bimolecular Recombination

The bimolecular recombination rate has been shown to dominate in hybrid perovskites in the charge carrier density range $10^{17} - 10^{18}$ cm^{-3},[64] and this was consolidated by Saba and colleagues,[49] who found that the photoluminescence quantum yield peaked near a charge-carrier density of $\sim 10^{18}$ cm^{-3}.

The bimolecular recombination rate can be determined using a range of spectroscopic techniques, and values in the range ~ 0.8–20×10^{-10} cm^3s^{-1} have been reported for $MAPbI_3$ and $MAPbI_{3-x}Cl_x$.[51,64,66,76,82,85,98,120,125] This is a much smaller variation in values than those for the trap-assisted rate, which may be due to the fact that bimolecular recombination is more intrinsic to the material composition and less sensitive to processing conditions. Davies *et al.* showed theroetically and experimentally that bimolecular recombination is an inverse light absorption process in hybrid perovskite, which shows that it is an intrinsic property of the material and intrinsically linked to band structure.[59]

The mixing of cations in the A-site and halides in the X-site has the potential to modify the bimolecular recombination rate. The mixed-cation, mixed-halide perovskite system $FA_{1-x}MA_xPbI_{3-y}Br_y$ has been shown to exhibit k_2 rates across the wide range $0.2 - 6 \times 10^{-10}$ cm^3s^{-1}.[126,127] In the Cs-containing mixed-cation, mixed halide perovskite $Cs_{0.17}FA_{0.83}Pb(I_{0.6}Br_{0.4})_3$, values of $k_2 = 0.2 - 0.4 \times 10^{-10}$ cm^3s^{-1} have been reported,[104,128] with Rehman and colleagues[128] reporting an increasing in k_2 with an increase in bromide content at the X-site. When the perovskite $FA_{0.83}MA_{0.17}Pb(I_{0.83}Br_{0.17})_3$ is further alloyed to incorporate 5% Cs into the A-site cation, the bimolecular rate has been reported as 4.2×10^{-10} cm^3s^{-1}, and as 3.5×10^{-10} cm^3s^{-1} when 5% Rb is substituted instead.[127] These studies show the potential of mixing halides and cations to modify the optoelectronic properties of hybrid perovskites, and further supports the idea that the bimolecular recombination rates are an intrinsic property tied to the band structure of the material.

Interestingly, the measured bimolecular recombination rates in hybrid MHPs have been shown to be orders of magnitude lower than those which would be predicted by the Langevin recombination model. Within the framework of the Langevin model, the

recombination rate k_2 can be expressed as:

$$k_2 = \frac{e}{\epsilon}\mu \tag{2.13}$$

where e is the elementary charge, ϵ is the dielectric constant and μ is the charge carrier mobility.[129] This model assumes that recombination will occur once an electron and hole move inside their joint capture radius.[130,131] Wehrenfennig and colleagues used transient THz spectroscopy to find k_2 and μ for $MAPbI_3$ and $MAPbI_{3-x}Cl_x$, and found a ratio k_2/μ which was over four orders of magnitude lower than expected by Equation (2.13).[64] Several other groups have also found non-Langevin bimolecular recombination rates in $MAPbI_3$ and $MAPbI_{3-x}Cl_x$.[51,81,85,132] Non-Langevin bimolecular rates have also been found for the formamidinium (FA)-based system $FAPbI_{3-y}Br_y$,[102] which suggests that this is a general property of hybrid lead halide perovskites which makes them extremely promising as solar cell asborbers.

A low k_2/μ ratio is extremely advantageous for solar cell applications, as it will extend diffusion lengths in accordance with Equation (2.12). This has indeed been shown in $MAPbI_{3-x}Cl_x$—the Langevin model would have predicted $L_D \sim 100$ nm, whereas experiments have revealed diffusion lengths of > 1 μm.[65]

The temperature dependence of the bimolecular recombination rate was investigated by Savenije *et al.* through transient microwave conductivity measurements.[51] This study shows that k_2 decreased with decreasing temperature, however this has since been contradicted by Milot *et al.* who found an increasing k_2 with decreasing temperature using transient THz conductivity measurements.[120] Milot *et al.* postulated that this increase in k_2 was a result of the increasing charge carrier mobility with decreasing temperature which they also observed (previously attributed to reduced electron-phonon scattering with decreasing temperature[51,88]). They suggested that increasing mobility increases the probability of electrons and holes moving inside their joint Coulomb capture radius, therefore increasing the probability of bimolecular recombination. However, more recently it has been proposed that the thermal broadening of the Fermi-Dirac distribution with increasing temperature decreases band-to-band recombination and therefore k_2, in line with the Shockley-van Rooesbroeck theory.[59,133]

Although the low bimolecular rates in hybrid perovskites have positive consequences for photovoltaic performance due to increasing the diffusion length, it should be noted that the radiative recombination process itself is not necessarily detrimental for photovoltaic cells, as a high radiative efficiency increases the efficiency of solar energy conversion.

Auger Recombination

Auger recombination rates in hybrid lead halide perovskites have been less widely studied, possibly due to the fact that Auger recombination is unlikely to operate in photovoltaic devices under 1 Sun illumination, as it dominates the recombination only at charge carrier densities above 10^{18} cm^{-3}.[134] However it would be relevant for lasing[135–137] or solar concentrator applications,[138–140] where such high charge-carrier densities are necessary for functionality. Furthermore, the Auger recombination rate sets a fundamental limit on the radiative efficiency of the solar cell,[141] therefore it is still an important parameter to quantify in hybrid perovskites.

Auger recombination rate constants k_3 have been reported in the range $0.2–10 \times 10^{28}$ cm^6s^{-1} for $MAPbI_3$ and $MAPbI_{3-x}Cl_x$.[64,82,85,120,125] These values of k_3 are unexpectedly high, being comparable to those of strongly confined colloidal quantum dots[142] and two orders larger than those reported for highly-doped bulk silicon wafers.[143]

The Auger recombination rate is strongly dependent on the material band structure[144,145] due to the very specific energetic requirements for a many-body process which conserves momentum and energy.[146] Auger recombination will also be affected by phonons and impurities, which can be involved in momentum transfer during the Auger process.[147,148]

The dependence of Auger rates on band structure has been experimentally demonstrated by Milot and coworkers[120], who found strong phase specificity for Auger recombination rates in $MAPbI_3$. The researchers found that the Auger rate decreased with increasing temperature in the orthorhombic phase, but began to rise with increasing temperature in the tetragonal phase, a trend which then reversed again in the cubic phase. For the FA-based perovskite $FAPbI_{3-y}Br_y$, Rehman and colleagues[102] showed that the

Auger recombination rate increased monotonously by an order of magnitude when the bromide fraction $y/3$ was increased from 0 to 1, coinciding with gradual changes in the lattice parameter.[103] This dependence of the Auger rate on crystal structure confirms that it is influenced by electronic band structure and therefore suggests that engineering of the band structure through compositional changes, such as A-site cation alloying/replacement or halide substitution, could effectively tune this recombination rate.

2.3 Photovoltaic cells

2.3.1 Principles of Solar Cell Operation

The photovoltaic (PV) cell is a device which converts solar energy into electricity. Under the right conditions, the interaction of light with matter causes the absorption of a photon resulting in the promotion of an electron to a higher energy level in an atom. In order for photovoltaic cells to generate an electrical current from the excited electrons, there must be mechanisms for the separation and extraction of charge. In a conventional inorganic solar cell, this is achieved by the creation of a p-n junction, which is a heterojunction of p- and n-type semiconductors. A p-type semiconductor is one which favourably accepts electrons (or donates holes) and an n-type semiconductor is one which favourably donates electrons.[29] As discussed in Section 2.2, the Fermi level, μ, is the highest occupied electron state at $T = 0$ K. The Fermi level can be conceptualised as the electrochemical potential of electrons, in other words the change in free energy when one electron is added to the system. In a p-type semiconductor, μ lies closer to the valence band than the conduction band, whereas in an n-type semiconductor it is closer to the conduction band. When a p-n junction is formed, band-bending occurs in both types of material to balance the electrochemical potential.[149] This results in a diffusion of electrons from the n-type material (and holes from the p-type region), leaving behind fixed ions and creating a layer at the interface known as the depletion region. In this region there is a potential difference for electrons in the conduction band, leading to an in-built electric field across the depletion region. It is this electric field which causes dissociation of excitons, because it causes charge flow in a direction such as to oppose and, ultimately,

balance out the diffusion current - in other words, it creates a diode.[150]

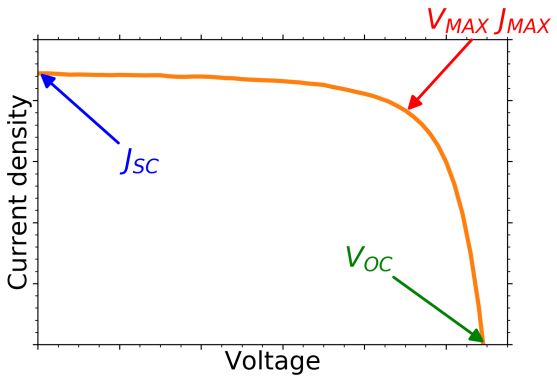

Figure 2.9: Example of a measured $J-V$ curve for an illuminated solar cell.

The current-voltage relationship in a PV device can be best described by the Shockley ideal photodiode equation:

$$J(V) = J_{ph} - J_0 \left[\exp\left(\frac{qV}{\eta k_B T} \right) - 1 \right] \tag{2.14}$$

where J_{ph} is the photocurrent provided by the photoactive absorbing layer and the second term is the diode current. J_0 denotes the saturation current density (the diode reverse saturation current), η is the ideality factor, k_B the Boltzmann constant and T is the temperature. The diode current (which opposes the photocurrent) exponentially increases as the applied voltage V increases.[150]

The ideality factor η is a measure of the slope of the J–V characteristics on a semi-logarithmic plot and can be determined by differentiation according to:[33]

$$\eta = \left(\frac{k_B T}{q} \frac{\partial \ln J}{\partial V} \right)^{-1} \tag{2.15}$$

Photovoltaic cell performance is measured using four key metrics. The first of these is the J_{SC}, which is known as the short-circuit current. Strictly speaking, the J_{SC} is the current density in the device under illumination with no external load. In practical terms, it quantifies the photocurrent in the device. When testing solar cells we also measure the open circuit voltage (V_{OC}), which quantifies the voltage across the device under illumination when it is 'open', in other words when the resistance across the two electrodes of the cell is infinite. In practical terms it is therefore the maximum voltage achievable in the device. The short-circuit current decreases with increasing

band gap, whereas the open-circuit voltage increases, therefore placing a limit on the overall efficiency of the cell. Another important metric to consider is the fill factor, which is essentially the fraction of the maximum theoretical power that is actually being reached in the cell. It is given by

$$FF = \frac{P_{MAX}}{P_T} = \frac{J_{MAX} \cdot \mathrm{V}_{MAX}}{J_{SC} \cdot V_{OC}} \tag{2.16}$$

where J_{MAX} and V_{MAX} are the values of voltage and current at the maximum power point.[151] This metric quantifies the quality of the device. When testing a solar cell, the device is driven at a sweep of bias voltages and the current density at each voltage is measured, resulting in a $J - V$ curve as shown in Figure 2.9. On this curve, V_{OC}, J_{SC}, V_{MAX} and J_{MAX} are marked. The final metric to consider is the power conversion efficiency (PCE), which is the ratio of the output power of the device to the input power, namely the power of the light source. This gives a direct indication of the cell's ability to convert energy from the sun to electrical energy and is therefore ultimately the most important metric.

2.3.2 Solar Energy Harvesting

To understand how best to optimise solar cells, we must first know the wavelength and intensity of photons which will be incident on the cell. For this we need to quantify the solar spectrum, but this will vary depending on our location on the Earth's surface. Definitions of the solar spectrum are therefore based on the air mass coefficient (abbreviated as AM), which is a measure of the optical path length of solar radiation through the Earth's atmosphere relative to the path length when the sun is directly overhead. Within this convention, AM0 denotes the solar spectrum before entering the Earth's atmosphere, and AM1 denotes the solar spectrum at sea level having passed through the atmosphere at the solar zenith. At mid-latitudes, such as here in the UK, the air mass coefficient is 1.5, which is the relative optical path length after passing through the atmosphere at a solar zenith angle of $z = 48.2^{\circ}$.[152,153] Therefore the reference solar spectrum mid-latitudes is known as AM1.5G (the 'G' stands for 'global', and it denotes

that the spectrum applies to any PV application that is operating at 1 Sun, in other

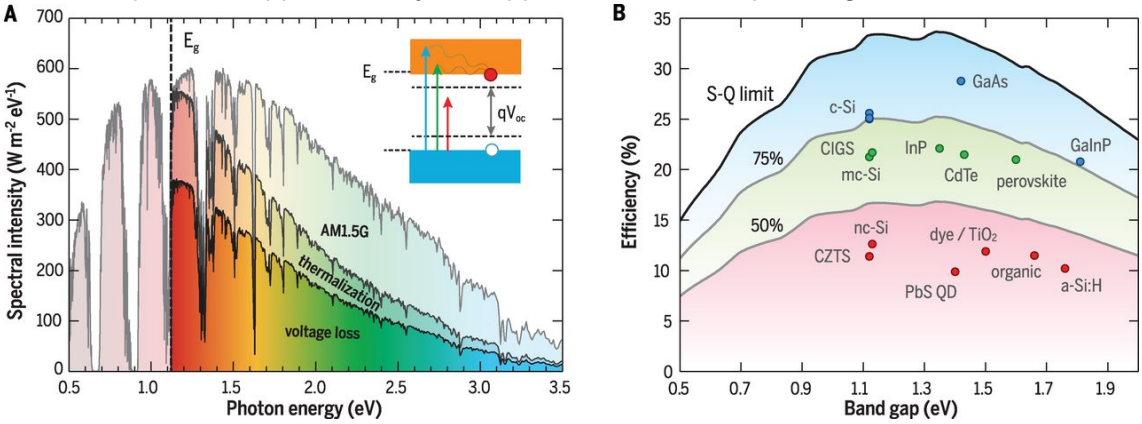

Figure 2.10: **A** The AM1.5 solar spectrum. E_g denotes the band gap of silicon, and the greyed out areas show portions of the solar spectrum which are lost to thermalisation, as well as those which are inaccessible due to being below the band gap energy. *Inset:* Electronic band structure of a semiconductor, annotated to show how the quasi-Fermi levels determine the open-circuit voltage V_{OC}. **B** Theoretical Shockley-Queisser efficiency limit as a function of band gap (black line). The areas under the grey lines represent 75% and 50% of the limit. Labelled circles mark the record efficiencies for the majority of PV technologies, as of 2016. Figure obtained from Polman *et al.*, *Science* **2016** *352*, 6283.

words with no solar concentrators). In reality, the spectrum varies with the season and time of day, but AM1.5 can be used as a realistic measure of the average irradiation in the UK (and other mid-latitude countries) over the course of a year.[154] The AM1.5G spectrum is not measured, but rather is calculated from the reference AM0 spectrum, under geometric and atmospheric conditions that are generally representative of mid-latitudes. The average power density of solar irradiance at the Earth's atmosphere is $\sim$ 1.36 kWm^{-2}, and the solar irradiation on a horizontal surface at ground level is $\sim$ 1.12 kWm^{-2}.[155] The power density at Earth's surface is approximated as 1 kWm^{-2} when simulating solar irradiation in the lab for testing of PV cells, and this condition is known as 1 Sun illumination.

Figure 2.10 shows the AM1.5G solar spectrum before and after losses due to thermalisation. The dips in the spectrum are due to molecular absorption in Earth's atmosphere. Now we have spectral information about the incident radiation, we need to know the fundamental limits on the efficiency of converting this radiation into electrical energy. Shockley and Queisser completed this analysis in 1961, using the principle of detailed balance to determine the theoretical maximum efficiency of a solar cell under real-life operating conditions.[34] The detailed balance limit takes into account all photons going in and coming out, and considers thermodynamic principles along with a number of geometric considerations such as angle subtended by the sun on the solar panel. The limit

also assumes that every photon absorption event promotes a photon to the conduction band. However, this limit varies depending on the band gap of the semiconductor material. Photons with energies below the band gap of the material cannot be absorbed by it, therefore it should follow that it is desirable to have as small a band gap as possible. However, if a photon with more energy than the band gap is absorbed, it is very unlikely to be converted to electrical energy due to the process of thermalisation. During thermalisation, charge carriers excited above the band gap will rapidly lose energy through collisions with the lattice and drop back to the bottom of the conduction band. This process results in huge energy losses in narrow band gap solar cells, as shown in Figure 2.10**A**, because it takes place on a much shorter timescale than the charge carrier extraction processes in the cell.

Figure 2.10**B** shows the variation of the Shockley-Queisser limit with band gap, for a single-junction solar cell under 1 Sun illumination with the standard AM1.5G solar spectrum. The maximum efficiency occurs for a semiconductor with a band gap of 1.34 eV and is 33.7%. The maximum achievable efficiency for a perovskite solar cell, within this framework, is $\sim$30%, and the current record efficiency for a single-junction perovskite solar cell is 25.2% (as of 2020; the plot in Figure 2.10**B** is from 2016).[156]

2.4 Perovskite Solar Cells

The general architecture of a perovskite solar cell consists of a perovskite absorber layer, interfaced with a hole-transporting medium (HTM) and an electron-transporting medium (ETM), deposited on a transparent conducting layer in order to allow sunlight to reach the absorber layer without losing conductivity. These layers must be carefully selected in terms of their electron affinities, to enable the diode functionality of the cell as described in Section 2.3.1. Figure 2.11 shows the resultant energy band diagram for a PSC based on a TiO_2 ETM, with FTO (fluorine-doped tin oxide) as a transparent conducting oxide.

The perovskite solar cell (PSC) field is a fast-moving one, whose origins can be traced back to the dye-sensitised solar cell. A photovoltaic response in a lead halide perovskite absorber was first realised by Kojima and coworkers in 2006, who reported a cell with a 2.2% power conversion efficiency (PCE) when perovskite nanoparticles were incorporated

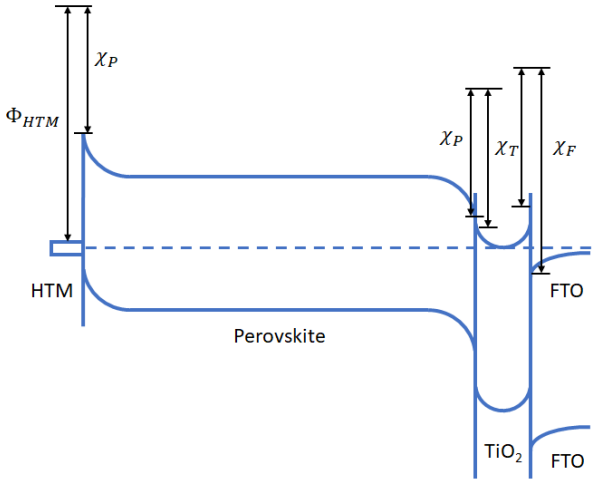

Figure 2.11: Energy band diagram for a typical PSC with compact TiO_2 as the ETM and FTO as the transparent conducting oxide. χ_P,χ_T and χ_F are the electron affinities of the perovskite, TiO_2 and FTO, respectively. Φ_{HTM} is the work function of the HTM.

into the nanoporous TiO_2 layer of a dye-sensitised solar cell.[157] By switching from $CH_3NH_3PbBr_3$ to $CH_3NH_3PbI_3$ (commonly shortened to MAPI, as the organic compound CH_3NH_3 is known as methylammonium (MA)), the same group improved this efficiency to 3.8% in 2009.[158] In these early stages, an organic electrolyte containing lithium halide and the corresponding halogen was employed as the hole-transporting medium (HTM), but a major breakthrough in 2012 was the replacement of this electrolyte with a solid state HTM by Kim *et al.*[159] This HTM was the organic compound spiro-MeOTAD and allowed them to reach an efficiency of 9.7%.

Concurrently, it was Snaith and coworkers[160] who made three major divergences from the status quo in PSC fabrication. The first was moving away from perovskite nanoparticles, to instead coat mesoporous TiO_2 structures with a thin layer of perovskite, in a cell known as a meso-superstructured cell (LHS in Figure 2.12A). The second was to replace the iodine with a mixed halide ($I_{3-x}Cl_x$) to the benefit of the stability and carrier transport in the cells. The third was to replace the TiO_2 matrix with a similar, but non-conducting, Al_2O_3 network, which served to show that the perovskites were able to efficiently transport both electrons and holes to the cell terminals. This development was seminal as it showed that simple planar cells with no mesoporous scaffolding were a possibility.

Since this discovery, several groups have demonstrated high efficiencies in planar cells with inorganic transporting media, such as when Liu and Kelly[162] replaced the TiO_2

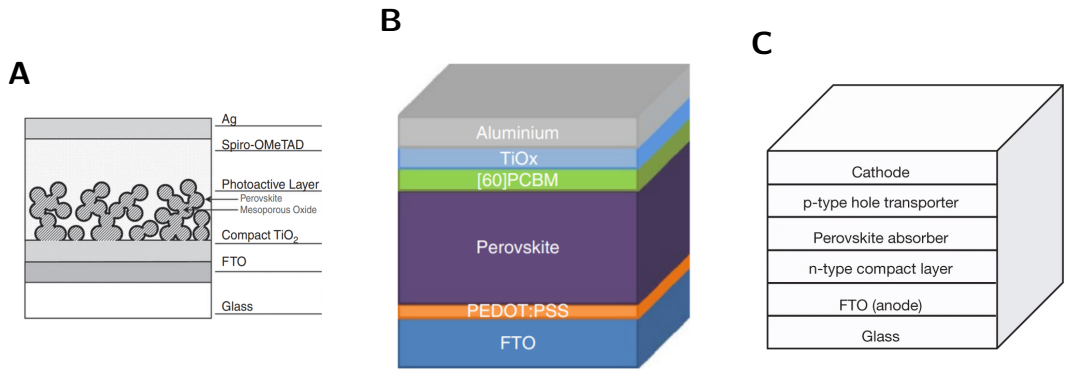

Figure 2.12: **A** Perovskite device architecture with mesoporous scaffold. **B** An example structure for the planar heterojunction hybrid PSC in the inverted architecture. **C** Generic structure for the planar heterojunction hybrid PSC in the standard architecture. **A** is taken from Lee *et al.*[160] **B** is taken from Docampo *et al.*[161] **C** is taken from Liu *et al.*[162]

mesoporous layer with a ZnO-nanoparticle layer, yielding a 15.7% PCE. However, efficiencies of up to 12% have also been achieved using organic electron-transporting mediums (ETMs) and HTMs,[163] namely with PEDOT:PSS (poly(2,3-dihydrothieno-1,4-dioxin)-poly(styrenesulphonate)) as the HTM and PC_61BM ((6,6)-phenyl C_61-butyric acid methyl ester) as the ETM. Docampo *et al.* found in 2013 via PL studies that the photoluminescence quenching efficiency (PLQE) of PEDOT:PSS was just as high as that of spiro-MeOTAD and for PCBM it was almost twice as high as that of TiO_2.[161] However, they were still only able to achieve a PCE of 9.8% for their inverted architecture planar devices (see Figure 2.12**B** for the generic structure) with $CH_3NH_3PbI_{3-x}Cl_x$ as the absorber and PEDOT:PSS and PCBM as the HTM and ETM respectively. This reduction in efficiency from their standard architecture (demonstrated in Figure 2.12C) devices (which exhibited 11.8% PCE) was attributed to their slightly lower J_{SC}, V_{OC} and fill factor.

2.4.1 Compositional Engineering

By 2014, $MAPbI_3$-based solar cells had reached a PCE of $\sim$ 17%,[164] which had increased to 19.19% by 2017.[165] However, this material is far from ideal as a solar cell absorber. It has been demonstrated to be extremely unstable under ambient conditions[166–169] and its band gap, reported at various values between 1.5 and 1.6 eV[84,170,171] is well above the ideal solar cell band gap as dictated by the Shockley-Quiesser model, which is the range 1.1 - 1.4 eV.[34] Hybrid perovskites can be synthesised with a large number

of different organic and inorganic A-cations and a variety of different halides, therefore there is much potential for compositional engineering for tuning of the band gap, stability and device performance.

The perovskite $MAPbBr_3$ has a much wider band gap than $MAPbI_3$, generally reported to be 2.3 eV[172]. This is far from ideal for high efficiency PV devices due to its limited ability to absorb light from the solar spectrum, and sure enough, $MAPbBr_3$-based devices have not exceeded $\sim 8\%$ PCE to date.[173,174] However, the partial substitution of I^- by Br^- ions has been proven to tune the band gap of hybrid perovskites, with a widening of the band gap demonstrated with increasing Br content in $MAPbI_{1-x}Br_x$[175] and $FAPbI_{1-x}Br_x$[103] (where FA is the organic molecule formamidinium with chemical formula $HC(NH_2)_2$). This is supported by first-principles calculations, which have suggested that a decrease in band gap occurs with increasing atomic size of the halide anion ($R_{A_{Cl}} < R_{A_{Br}} < R_{A_I}$).[36,176]

Mixed halide perovskites of the form $MAPbI_{1-x}Br_x$ ($x = 0.1$ - 0.15) have been widely implemented in PV devices, with PCEs of up to 18.02% reported.[164,177] At $x = 0.13$, a structural phase transition occurs to a pseudo-cubic phase from the tetragonal phase characteristic of $MAPbI_3$, leading to elevated moisture stability at $x > 0.13$ but a slightly lower efficiency due to the wider band gap. The mixing of perovskite crystals in this way should follow Vegard's law,[178] from which we should expect a linear dependence of the lattice parameter, and therefore the band gap E_g on the inclusion of Br^- ions into the lattice. However a quadratic dependence of E_g on Br inclusion is observed, suggesting some compositional disorder in these mixed halide perovskites.[179] Extensive work has also been done on doping the X-site with small amounts of chlorine (Cl).[180–182] Docampo and coworkers found that the doping of $MAPbI_3$ with a small amount of Cl increases light absorption at the band edge and lengthens the carrier lifetime.[183] In addition, Stranks and colleagues found a tenfold increase in the charge carrier diffusion length of $MAPbI_{1-x}Cl_x$ compared to $MAPbI_3$. This is consistent lengthening of the carrier lifetime observed when Cl is added in small quantities to the perovskite precursor solution:[65] this added Cl is thought to aid the crystallisation process but is not included in the resulting perovskites lattice.

Alloying of cations in the A-site, i.e. substitution of MA^+ by other cations such as FA^+, Cs^+, Rb^+, has been shown to enhance the optoelectronic properties of $MAPbI_3$, leading to rapid increases in PCE and improvements in material stability over the past few years.[184,185] It has been demonstrated that the size of the organic cation in hybrid perovskites influences the optical band gap by changing the size of the B-X-B tilt angle.[186] Substituting MA with FA shifts the band gap to $\sim$ 1.45 eV, however but the problem with $FAPbI_3$ is that is does not assume a stable black perovskite phase at room temperature. Therefore it was Pellet *et al.* who first synthesised perovskite solar cells from mixed FA/MA-cation perovskites of the form $FA_{1-x}MA_xPbI_3$. They found that the composition $FA_{0.4}MA_{0.6}PbI_3$ exhibited the best solar cell performance, reaching a PCE of 13.7%.[187]

It was later found that mixing both the cations and the halides in mixed perovskites helped to improve device performance and stability even further. Jeon and coworkers investigated the compositional parameter space $(FAPbI_3)_{1-x}(MAPbBr_3)_x$,[188] finding that the ideal composition had $x = 0.15$, resulting in devices with an efficiency of 17.9%. In 2016, Jacobsson and coworkers[184] explored the full $(FAPbI_3)_{1-x}(MAPbBr_3)_x$ parameter space with respect to PL and absorption properties, device performance and stability. They found a broad range of PCE values, demonstrating how small changes in composition can have a major impact on device performance. They found the lowest PCEs for mixed halide perovskites with high bromide content, due to a large amount of sub-bandgap emission. The highest PCE of 20.7% was found for devices with $FA_{2/3}MA_{1/3}Pb(I_{5/6}Br_{1/6})_3$. Their work was an excellent illustration of the importance of composition in making high efficiency perovskite devices.

Adding Cs to A-site cation in addition to FA and MA has been shown to not only enhance power conversion efficiency compared to $(FAPbI_3)_{1-x}(MAPbBr_3)_x$ but also to increase device stability.[189,190] Saliba *et al.* demonstrated cells based on $Cs_{0.05}(FA_{0.83}MA_{0.17})_{0.95}Pb(I_{0.83}Br_{0.17})_3$ with a stabilised PCE of 21.1%, which dropped to 18% after a few hours but stayed at this value for another 250 hours.[189] The addition of Cs has also been shown to suppress halide segregation.[191] In 2020, Zheng and coworkers achieved a stabilised PCE of 22.3% in the triple cation perovskite $Cs_{0.05}(FA_{0.92}MA_{0.08})_{0.95}Pb(I_{0.92}Br_{0.08})_3$.[192]

References

[1] H.-R. Wenk, A. Bulakh, *Minerals: Their Constitution and Origin*, Cambridge University Press, Cambridge, UK, **2004**.

[2] Perovskite Mineral Data, http://webmineral.com/data/Perovskite.shtml#.X4BEsWhKg2w, accessed on 2020-10-09.

[3] M. Johnsson, P. Lemmens, in *Handbook of Magnetism and Advanced Magnetic Materials*, John Wiley & Sons, Ltd, Chichester, UK, **2007**.

[4] M. A. Green, A. Ho-Baillie, H. J. Snaith, *Nature Photonics* **2014**, *8*, 506.

[5] N. Ashcroft, N. Mermin, *Solid State Physics*, Brooks Cole, 1st edn., **1976**.

[6] C. Kittel, *Introduction to Solid State Physics*, Wiley, 8th edn., **2004**.

[7] J. R. Hook, H. E. Hall, *Solid State Physics*, Wiley, 2nd edn., **1991**.

[8] M. Grätzel, *Nature Materials* **2014**, *13*, 838.

[9] A. M. Glazer, *Acta Crystallographica Section B Structural Crystallography and Crystal Chemistry* **1972**, *28*, 3384.

[10] M. A. Carignano, Y. Saeed, S. A. Aravindh, I. S. Roqan, J. Even, C. Katan, *Physical Chemistry Chemical Physics* **2016**, *18*, 27109.

[11] C. Li, X. Lu, W. Ding, L. Feng, Y. Gao, Z. Guo, *Acta Crystallographica Section B: Structural Science* **2008**, *64*, 702.

[12] Y. Kawamura, H. Mashiyama, K. Hasebe, *Journal of the Physical Society of Japan* **2002**, *71*, 1694.

[13] T. Baikie, Y. Fang, J. M. Kadro, M. Schreyer, F. Wei, S. G. Mhaisalkar, M. Graetzel, T. J. White, *Journal of Materials Chemistry A* **2013**, *1*, 5628.

[14] R. E. Wasylishen, O. Knop, J. B. Macdonald, *Solid State Communications* **1985**, *56*, 581.

[15] A. Poglitsch, D. Weber, *The Journal of Chemical Physics* **1987**, *87*, 6373.

[16] N. Onoda-Yamamuro, T. Matsuo, H. Suga, *Journal of Physics and Chemistry of Solids* **1990**, *51*, 1383.

[17] T. Oku, in Leonid A. Kosyachenko (Ed.), *Solar Cells - New Approaches and Reviews*, IntechOpen, chap. 3, **2015**.

[18] O. J. Weber, D. Ghosh, S. Gaines, P. F. Henry, A. B. Walker, M. S. Islam, M. T. Weller, *Chemistry of Materials* **2018**, *30*, 3768.

[19] E. Mosconi, C. Quarti, T. Ivanovska, G. Ruani, F. De Angelis, *Physical Chemistry Chemical Physics* **2014**, *16*, 16137.

[20] F. Brivio, J. M. Frost, J. M. Skelton, A. J. Jackson, O. J. Weber, M. T. Weller, A. R. Goñi, A. M. Leguy, P. R. Barnes, A. Walsh, *Physical Review B - Condensed Matter and Materials Physics* **2015**, *92*, 144308.

[21] C. Quarti, E. Mosconi, F. De Angelis, Structural and electronic properties of organo-halide hybrid perovskites from ab initio molecular dynamics, **2015**.

[22] A. M. Leguy, J. M. Frost, A. P. McMahon, V. G. Sakai, W. Kochelmann, C. Law, X. Li, F. Foglia, A. Walsh, B. C. O'Regan, J. Nelson, J. T. Cabral, P. R. Barnes, *Nature Communications* **2015**, *6*, 1.

[23] A. M. Glazer, *Acta Crystallographica Section A* **1975**, *31*, 756.

[24] C. J. Howard, H. T. Stokes, *Acta Crystallographica Section B Structural Science* **1998**, *54*, 782.

[25] O. Knop, R. E. Wasylishen, M. A. White, T. S. Cameron, M. J. M. V. Oort, *Canadian Journal of Chemistry* **1990**, *68*, 412.

[26] M. T. Weller, O. J. Weber, J. M. Frost, A. Walsh, *The Journal of Physical Chemistry Letters* **2015**, *6*, 3209.

[27] J. Ma, L. W. Wang, *Nano Letters* **2015**, *15*, 248.

[28] P. Y. Yu, M. Cardona, in *Fundamentals of Semiconductors*, Springer-Verlag Berlin Heidelberg, 4th edn., **2010**, pp. 17–106.

[29] S. Sze, K. K. Ng, *Physics of Semiconductor Devices*, John Wiley & Sons, Inc., Hoboken, NJ, USA, **2006**.

[30] P. A. M. Dirac, *Proceedings of the Royal Society of London* **1927**, *114*, 243.

[31] J. R. Lakowicz (Ed.), *Principles of Fluorescence Spectroscopy*, Springer US, Boston, MA, 3rd edn., **2006**.

[32] J. R. Gispert, *Coordination Chemistry*, Wiley-VCH, **2008**.

[33] J. Nelson, *The Physics of Solar Cells*, Imperial College Press, **2004**.

[34] W. Shockley, H. J. Queisser, *Journal of Applied Physics* **1961**, *32*, 510.

[35] M. B. Johnston, L. M. Herz, *Accounts of Chemical Research* **2016**, *49*, 146.

[36] K. Tanaka, T. Takahashi, T. Ban, T. Kondo, K. Uchida, N. Miura, *Solid State Communications* **2003**, *127*, 619.

[37] J. Even, L. Pedesseau, J. M. Jancu, C. Katan, *Journal of Physical Chemistry Letters* **2013**, *4*, 2999.

[38] F. Brivio, A. B. Walker, A. Walsh, *APL Materials* **2013**, *1*, 042111.

[39] J. M. Frost, K. T. Butler, F. Brivio, C. H. Hendon, M. Van Schilfgaarde, A. Walsh, *Nano Letters* **2014**, *14*, 2584.

[40] J. Even, L. Pedesseau, C. Katan, M. Kepenekian, J. S. Lauret, D. Sapori, E. Deleporte, *Journal of Physical Chemistry C* **2015**, *119*, 10161.

[41] J. Even, L. Pedesseau, C. Katan, *Journal of Physical Chemistry C* **2014**, *118*, 11566.

[42] C. Wehrenfennig, M. Liu, H. J. Snaith, M. B. Johnston, L. M. Herz, *Journal of Physical Chemistry Letters* **2014**, *5*, 1300.

[43] L. M. Herz, *Annual Review of Physical Chemistry* **2016**, *67*, 65.

[44] J. Even, L. Pedesseau, J. M. Jancu, C. Katan, *Physica Status Solidi - Rapid Research Letters* **2014**, *8*, 31.

[45] M. Hirasawa, T. Ishihara, T. Goto, K. Uchida, N. Miura, *Physica B: Physics of Condensed Matter* **1994**, *201*, 427.

[46] Q. Lin, A. Armin, R. C. R. Nagiri, P. L. Burn, P. Meredith, *Nature Photonics* **2014**, *9*, 106.

[47] K. Wu, A. Bera, C. Ma, Y. Du, Y. Yang, L. Li, T. Wu, *Physical chemistry chemical physics : PCCP* **2014**, *16*, 22476.

[48] V. D'Innocenzo, G. Grancini, M. J. P. Alcocer, A. R. S. Kandada, S. D. Stranks, M. M. Lee, G. Lanzani, H. J. Snaith, A. Petrozza, *Nature Communications* **2014**, *5*, 3586.

[49] M. Saba, M. Cadelano, D. Marongiu, F. Chen, V. Sarritzu, N. Sestu, C. Figus, M. Aresti, R. Piras, A. Geddo Lehmann, C. Cannas, A. Musinu, F. Quochi, A. Mura, G. Bongiovanni, *Nature Communications* **2014**, *5*.

[50] S. Sun, T. Salim, N. Mathews, M. Duchamp, C. Boothroyd, G. Xing, T. C. Sum, Y. M. Lam, *Energy Environ. Sci.* **2014**, *7*, 399.

[51] T. J. Savenije, C. S. Ponseca, L. Kunneman, M. Abdellah, K. Zheng, Y. Tian, Q. Zhu, S. E. Canton, I. G. Scheblykin, T. Pullerits, A. Yartsev, V. Sundström, *Journal of Physical Chemistry Letters* **2014**, *5*, 2189.

[52] A. Miyata, A. Mitioglu, P. Plochocka, O. Portugall, J. T.-W. Wang, S. D. Stranks, H. J. Snaith, R. J. Nicholas, *Nature Physics* **2015**, *11*, 582.

[53] Y. Yamada, T. Nakamura, M. Endo, A. Wakamiya, Y. Kanemitsu, *IEEE Journal of Photovoltaics* **2015**, *5*, 401.

[54] N. Sestu, M. Cadelano, V. Sarritzu, F. Chen, D. Marongiu, R. Piras, M. Mainas, F. Quochi, M. Saba, A. Mura, G. Bongiovanni, *Journal of Physical Chemistry Letters* **2015**, *6*, 4566.

[55] Y. Yang, D. P. Ostrowski, R. M. France, K. Zhu, J. Van De Lagemaat, J. M. Luther, M. C. Beard, *Nature Photonics* **2016**, *10*, 53.

[56] I. B. Koutselas, L. Ducasse, G. C. Papavassiliou, *Journal of Physics: Condensed Matter* **1996**, *8*, 1217.

[57] R. J. Elliott, *Physical Review* **1957**, *108*, 1384.

[58] P. Y. Yu, M. Cardona, in *Fundamentals of Semiconductors*, Springer-Verlag Berlin Heidelberg, 4th edn., **2010**, pp. 243–344.

[59] C. L. Davies, M. R. Filip, J. B. Patel, T. W. Crothers, C. Verdi, A. D. Wright, R. L. Milot, F. Giustino, M. B. Johnston, L. M. Herz, *Nature Communications* **2018**, *9*, 293.

[60] E. J. Juarez-Perez, R. S. Sanchez, L. Badia, G. Garcia-Belmonte, Y. S. Kang, I. Mora-Sero, J. Bisquert, *Journal of Physical Chemistry Letters* **2014**, *5*, 2390.

[61] N. Onoda-Yamamuro, T. Matsuo, H. Suga, *Journal of Physics and Chemistry of Solids* **1992**, *53*, 935.

[62] T. Ishihara, *Journal of Luminescence* **1994**, *60-61*, 269.

[63] H. Zheng, J. Dai, J. Duan, F. Chen, G. Zhu, F. Wang, C. Xu, *Journal of Materials Chemistry C* **2017**, *5*, 12057.

[64] C. Wehrenfennig, G. E. Eperon, M. B. Johnston, H. J. Snaith, L. M. Herz, *Advanced Materials* **2014**, *26*, 1584.

[65] S. D. Stranks, G. E. Eperon, G. Grancini, C. Menelaou, M. J. P. Alcocer, T. Leijtens, L. M. Herz, A. Petrozza, H. J. Snaith, *Science (New York, N.Y.)* **2014**, *342*, 341.

[66] Y. Yamada, T. Nakamura, M. Endo, A. Wakamiya, Y. Kanemitsu, *J. Am. Chem. Soc* **2014**, *16*, 52.

[67] C. S. Ponseca, T. J. Savenije, M. Abdellah, K. Zheng, A. Yartsev, T. Pascher, T. Harlang, P. Chabera, T. Pullerits, A. Stepanov, J. P. Wolf, V. Sundström, *Journal of the American Chemical Society* **2014**, *136*, 5189.

[68] C. F. Klingshirn, *Semiconductor Optics*, Springer-Verlag Berlin Heidelberg, **1995**.

[69] J. Shah, *Ultrafast Spectroscopy of Semiconductors and Semiconductor Nanostructures*, Springer, New York, 1st edn., **1999**.

[70] L. Luo, L. Men, Z. Liu, Y. Mudryk, X. Zhao, Y. Yao, J. M. Park, R. Shinar, J. Shinar, K. M. Ho, I. E. Perakis, J. Vela, J. Wang, *Nature Communications* **2017**, *8*, 1.

[71] D. Von Der Linde, R. Lambrich, *Physical Review Letters* **1979**, *42*, 1090.

[72] V. Klimov, P. Haring Bolivar, H. Kurz, *Physical Review B* **1995**, *52*, 4728.

[73] C. K. Yong, J. Wong-Leung, H. J. Joyce, J. Lloyd-Hughes, Q. Gao, H. H. Tan, C. Jagadish, M. B. Johnston, L. M. Herz, *Nano Letters* **2013**, *13*, 4280.

[74] G. Xing, N. Mathews, S. Sun, S. S. Lim, Y. M. Lam, M. Grätzel, S. Mhaisalkar, T. C. Sum, *Science (New York, N.Y.)* **2013**, *342*, 344.

[75] H.-Y. Hsu, C.-Y. Wang, A. Fathi, J.-W. Shiu, C.-C. Chung, P.-S. Shen, T.-F. Guo, P. Chen, Y.-P. Lee, E. W.-G. Diau, *Angewandte Chemie* **2014**, *126*, 9493.

[76] J. S. Manser, P. V. Kamat, *Nature Photonics* **2014**, *8*, 737.

[77] L. Wang, C. McCleese, A. Kovalsky, Y. Zhao, C. Burda, *Journal of the American Chemical Society* **2014**, *136*, 12205.

[78] G. Grancini, A. R. Srimath Kandada, J. M. Frost, A. J. Barker, M. De Bastiani, M. Gandini, S. Marras, G. Lanzani, A. Walsh, A. Petrozza, *Nature Photonics* **2015**, *9*, 695.

[79] H. Kawai, G. Giorgi, A. Marini, K. Yamashita, *Nano Letters* **2015**, *15*, 3103.

[80] M. B. Price, J. Butkus, T. C. Jellicoe, A. Sadhanala, A. Briane, J. E. Halpert, K. Broch, J. M. Hodgkiss, R. H. Friend, F. Deschler, *Nature Communications* **2015**, *6*, 1.

[81] K. G. Stamplecoskie, J. S. Manser, P. V. Kamat, *Energy and Environmental Science* **2015**, *8*, 208.

[82] M. T. Trinh, X. Wu, D. Niesner, X. Y. Zhu, *Journal of Materials Chemistry A* **2015**, *3*, 9285.

[83] J. A. Christians, J. S. Manser, P. V. Kamat, *Journal of Physical Chemistry Letters* **2015**, *6*, 2086.

[84] Q. Chen, N. De Marco, Y. Yang, T. B. Song, C. C. Chen, H. Zhao, Z. Hong, H. Zhou, Y. Yang, Under the spotlight: The organic-inorganic hybrid halide perovskite for optoelectronic applications, **2015**.

[85] C. Wehrenfennig, M. Liu, H. J. Snaith, M. B. Johnston, L. M. Herz, *Energy and Environmental Science* **2014**, *7*, 2269.

[86] G. J. A. Wetzelaer, M. Scheepers, A. M. Sempere, C. Momblona, J. Ávila, H. J. Bolink, *Advanced Materials* **2015**, *27*, 1837.

[87] C. C. Stoumpos, C. D. Malliakas, M. G. Kanatzidis, *Inorganic Chemistry* **2013**, *52*, 9019.

[88] H. Oga, A. Saeki, Y. Ogomi, S. Hayase, S. Seki, *Journal of the American Chemical Society* **2014**, *136*, 13818.

[89] T. Leijtens, J. Lim, J. Teuscher, T. Park, H. J. Snaith, *Advanced Materials* **2013**, *25*, 3227.

[90] M. Lonergan, *Annual Review of Physical Chemistry* **2004**, *55*, 257.

[91] A. Pivrikas, N. S. Sariciftci, G. Juška, R. Österbacka, *Progress in Photovoltaics: Research and Applications* **2007**, *15*, 677.

[92] J. V. Li, A. M. Nardes, Z. Liang, S. E. Shaheen, B. A. Gregg, D. H. Levi, *Organic Electronics* **2011**, *12*, 1879.

[93] T. C. Sum, N. Mathews, *Energy Environ. Sci.* **2014**, *7*, 2518.

[94] E. Edri, S. Kirmayer, S. Mukhopadhyay, K. Gartsman, G. Hodes, D. Cahen, *Nature communications* **2014**, *5*, 3461.

[95] E. Edri, S. Kirmayer, A. Henning, S. Mukhopadhyay, K. Gartsman, Y. Rosenwaks, G. Hodes, D. Cahen, *Nano Letters* **2014**, *14*, 1000.

[96] C. Wehrenfennig, M. Liu, H. J. Snaith, M. B. Johnston, L. M. Herz, *APL Materials* **2014**, *2*, 081513.

[97] D. Shi, V. Adinolfi, R. Comin, M. Yuan, E. Alarousu, A. Buin, Y. Chen, S. Hoogland, A. Rothenberger, K. Katsiev, Y. Losovyj, X. Zhang, P. A. Dowben, O. F. Mohammed, E. H. Sargent, O. M. Bakr, *Science* **2015**, *347*, 519.

[98] V. D'Innocenzo, A. R. Srimath Kandada, M. De Bastiani, M. Gandini, A. Petrozza, *Journal of the American Chemical Society* **2014**, *136*, 17730.

[99] H. Zhou, Q. Chen, G. Li, S. Luo, T. B. Song, H. S. Duan, Z. Hong, J. You, Y. Liu, Y. Yang, *Science* **2014**, *345*, 542.

[100] D. W. de Quilettes, S. M. Vorpahl, S. D. Stranks, H. Nagaoka, G. E. Eperon, M. E. Ziffer, H. J. Snaith, D. S. Ginger, *Science* **2015**, *348*, 683.

[101] A. Sadhanala, F. Deschler, T. H. Thomas, S. E. Dutton, K. C. Goedel, F. C. Hanusch, M. L. Lai, U. Steiner, T. Bein, P. Docampo, D. Cahen, R. H. Friend, *Journal of Physical Chemistry Letters* **2014**, *5*, 2501.

[102] W. Rehman, R. L. Milot, G. E. Eperon, C. Wehrenfennig, J. L. Boland, H. J. Snaith, M. B. Johnston, L. M. Herz, *Advanced Materials* **2015**, *27*, 7938.

[103] G. E. Eperon, S. D. Stranks, C. Menelaou, M. B. Johnston, L. M. Herz, H. J. Snaith, *Energy & Environmental Science* **2014**, *7*, 982.

[104] D. P. McMeekin, G. Sadoughi, W. Rehman, G. E. Eperon, M. Saliba, M. T. Hörantner, A. Haghighirad, N. Sakai, L. Korte, B. Rech, M. B. Johnston, L. M. Herz, H. J. Snaith, *Science (New York, N.Y.)* **2016**, *351*, 151.

[105] W. Nie, H. Tsai, R. Asadpour, J. C. Blancon, A. J. Neukirch, G. Gupta, J. J. Crochet, M. Chhowalla, S. Tretiak, M. A. Alam, H. L. Wang, A. D. Mohite, *Science* **2015**, *347*, 522.

[106] J. Kim, S. H. Lee, J. H. Lee, K. H. Hong, *Journal of Physical Chemistry Letters* **2014**, *5*, 1312.

[107] W. J. Yin, T. Shi, Y. Yan, *Applied Physics Letters* **2014**, *104*, 063903.

[108] C. Eames, J. M. Frost, P. R. Barnes, B. C. O'Regan, A. Walsh, M. S. Islam, *Nature Communications* **2015**, *6*, 1.

[109] J. Haruyama, K. Sodeyama, L. Han, Y. Tateyama, *Journal of the American Chemical Society* **2015**, *137*, 10048.

[110] T.-Y. Yang, G. Gregori, N. Pellet, M. Grätzel, J. Maier, *Angewandte Chemie* **2015**, *127*, 8016.

[111] C. Li, S. Tscheuschner, F. Paulus, P. E. Hopkinson, J. Kießling, A. Köhler, Y. Vaynzof, S. Huettner, *Advanced Materials* **2016**, *28*, 2446.

[112] D. Yang, W. Ming, H. Shi, L. Zhang, M. H. Du, *Chemistry of Materials* **2016**, *28*, 4349.

[113] O. S. Game, G. J. Buchsbaum, Y. Zhou, N. P. Padture, A. I. Kingon, *Advanced Functional Materials* **2017**, *27*, 1606584.

[114] A. Senocrate, I. Moudrakovski, G. Y. Kim, T. Y. Yang, G. Gregori, M. Grätzel, J. Maier, *Angewandte Chemie - International Edition* **2017**, *56*, 7755.

[115] A. Dualeh, T. Moehl, N. Tétreault, J. Teuscher, P. Gao, M. K. Nazeeruddin, M. Grätzel, *ACS Nano* **2014**, *8*, 362.

[116] W. Tress, J. P. Correa Baena, M. Saliba, A. Abate, M. Graetzel, *Advanced Energy Materials* **2016**, *6*, 1600396.

[117] S. De Wolf, J. Holovsky, S. J. Moon, P. Löper, B. Niesen, M. Ledinsky, F. J. Haug, J. H. Yum, C. Ballif, *Journal of Physical Chemistry Letters* **2014**, *5*, 1035.

[118] E. T. Hoke, D. J. Slotcavage, E. R. Dohner, A. R. Bowring, H. I. Karunadasa, M. D. McGehee, *Chemical Science* **2015**, *6*, 613.

[119] M. Ledinsky, T. Schönfeldová, J. Holovský, E. Aydin, Z. Hájková, L. Landová, N. Neyková, A. Fejfar, S. De Wolf, *Journal of Physical Chemistry Letters* **2019**, *10*, 1368.

[120] R. L. Milot, G. E. Eperon, H. J. Snaith, M. B. Johnston, L. M. Herz, *Advanced Functional Materials* **2015**, *25*, 6218.

[121] M. Samiee, S. Konduri, B. Ganapathy, R. Kottokkaran, H. A. Abbas, A. Kitahara, P. Joshi, L. Zhang, M. Noack, V. Dalal, *Applied Physics Letters* **2014**, *105*, 153502.

[122] S. D. Stranks, V. M. Burlakov, T. Leijtens, J. M. Ball, A. Goriely, H. J. Snaith, *Physical Review Applied* **2014**, *2*, 034007.

[123] G. Xing, N. Mathews, S. S. Lim, N. Yantara, X. Liu, D. Sabba, M. Grätzel, S. Mhaisalkar, T. C. Sum, *Nature Materials* **2014**, *13*, 476.

[124] L. M. Herz, C. Silva, A. C. Grimsdale, K. Müllen, R. T. Phillips, *Physical Review B - Condensed Matter and Materials Physics* **2004**, *70*, 1.

[125] Z. Guo, J. S. Manser, Y. Wan, P. V. Kamat, L. Huang, *Nature Communications* **2015**, *6*, 1.

[126] D. Bi, W. Tress, M. I. Dar, P. Gao, J. Luo, C. Renevier, K. Schenk, A. Abate, F. Giordano, J.-P. Correa Baena, J.-D. Decoppet, S. M. Zakeeruddin, M. K. Nazeeruddin, M. Gra tzel, A. Hagfeldt, *Science Advances* **2016**, *2*, e1501170.

[127] Y. Hu, E. M. Hutter, P. Rieder, I. Grill, J. Hanisch, M. F. Aygüler, A. G. Hufnagel, M. Handloser, T. Bein, A. Hartschuh, K. Tvingstedt, V. Dyakonov, A. Baumann, T. J. Savenije, M. L. Petrus, P. Docampo, *Advanced Energy Materials* **2018**, *8*, 1703057.

[128] W. Rehman, D. P. McMeekin, J. B. Patel, R. L. Milot, M. B. Johnston, H. J. Snaith, L. M. Herz, *Energy & Environmental Science* **2017**, *10*, 361.

[129] J. J. Van Der Holst, F. W. Van Oost, R. Coehoorn, P. A. Bobbert, *Physical Review B - Condensed Matter and Materials Physics* **2009**, *80*, 235202.

[130] C. E. Swenberg, M. Pope, *Electronic processes in organic crystals and polymers*, Oxford University Press, New York, 2nd edn., **1999**.

[131] P. Langevin, *Ann. Chim. Phys* **1903**, *28*, 433.

[132] D. Li, C. Liang, H. Zhang, C. Zhang, F. You, Z. He, *Journal of Applied Physics* **2015**, *117*, 074901.

[133] A. Filippetti, P. Delugas, A. Mattoni, *The Journal of Physical Chemistry C* **2014**, *118*, 24843.

[134] X. Zhang, J. Shen, C. G. Van de Walle, *Advanced Energy Materials* **2020**, *10*, 1902830.

[135] F. Deschler, M. Price, S. Pathak, L. E. Klintberg, D.-D. Jarausch, R. Higler, S. Hu, T. Leijtens, S. D. Stranks, H. J. Snaith, M. Atatu, R. T. Phillips, R. H. Friend, *J. Phys. Chem. Lett* **2014**, *5*, 1421.

[136] K. Chen, A. J. Barker, F. L. Morgan, J. E. Halpert, J. M. Hodgkiss, *Journal of Physical Chemistry Letters* **2015**, *6*, 153.

[137] S. D. Stranks, S. M. Wood, K. Wojciechowski, F. Deschler, M. Saliba, H. Khandelwal, J. B. Patel, S. J. Elston, L. M. Herz, M. B. Johnston, A. P. Schenning, M. G. Debije, M. K. Riede, S. M. Morris, H. J. Snaith, *Nano Letters* **2015**, *15*, 4935.

[138] F. Meinardi, Q. A. Akkerman, F. Bruni, S. Park, M. Mauri, Z. Dang, L. Manna, S. Brovelli, *ACS Energy Letters* **2017**, *2*, 2368.

[139] H. Zhao, Y. Zhou, D. Benetti, D. Ma, F. Rosei, *Nano Energy* **2017**, *37*, 214.

[140] Q. Lin, Z. Wang, H. J. Snaith, M. B. Johnston, L. M. Herz, *Advanced Science* **2018**, *5*, 1700792.

[141] L. M. Pazos-Outón, T. P. Xiao, E. Yablonovitch, *The Journal of Physical Chemistry Letters* **2018**, *9*, 1703.

[142] V. I. Klimov, A. A. Mikhailovsky, D. W. McBranch, C. A. Leatherdale, M. G. Bawendi, *Science* **2000**, *287*, 1011.

[143] J. Dziewior, W. Schmid, *Applied Physics Letters* **1977**, *31*, 346.

[144] A. Haug, *Journal of Physics C: Solid State Physics* **1983**, *16*, 4159.

[145] A. Haug, *Journal of Physics and Chemistry of Solids* **1988**, *49*, 599.

[146] A. R. Beattie, P. T. Landsberg, *Proceedings of the Royal Society A: Mathematical, Physical and Engineering Sciences* **1959**, *249*, 16.

[147] M. Takeshima, *Physical Review B* **1982**, *25*, 5390.

[148] P. T. Landsberg, *Solid State Electronics* **1987**, *30*, 1107.

[149] E. W. Lorenz, M. E. Fernandez, R. Zilles, J. Minano, G. L. Araujo, A. Cuevas, *Solar Electricity: Engineering of Photovoltaic Systems*, Promotora General de Estudios, S.A., **1994**.

[150] W. Shockley, *Bell System Technical Journal* **1949**, *28*, 435.

[151] M. A. Green, *Solid State Electronics* **1981**, *24*, 788.

[152] F. Kasten, A. T. Young, *Applied Optics* **1989**, *28*, 4735.

[153] C. A. Gueymard, D. Myers, K. Emery, *Solar Energy* **2002**, *73*, 443.

[154] R. C. Willson, H. S. Hudson, *Nature* **1991**, *351*, 42.

[155] O. Coddington, J. L. Lean, P. Pilewskie, M. Snow, D. Lindholm, *Bulletin of the American Meteorological Society* **2016**, *97*, 1265.

[156] NREL: Best Research-Cell Efficiencies Chart, https://pvdpc.nrel.gov/, accessed on 2020-08-04.

[157] A. Kojima, K. Teshima, Y. Shirai, T. Miyasaka, Y. Shirai, T. Miyasaka, *ECS* **2006**, *MA2006-02*, 397.

[158] A. Kojima, K. Teshima, Y. Shirai, T. Miyasaka, *Journal of the American Chemical Society* **2009**, *131*, 6050.

[159] H.-S. Kim, C.-R. Lee, J.-H. Im, K.-B. Lee, T. Moehl, A. Marchioro, S.-J. Moon, R. Humphry-Baker, J.-H. Yum, J. E. Moser, M. Grätzel, N.-G. Park, *Scientific Reports* **2012**, *2*, 583.

[160] M. M. Lee, J. Teuscher, T. Miyasaka, T. N. Murakami, H. J. Snaith, *Science (New York, N.Y.)* **2012**, *338*, 643.

[161] P. Docampo, J. M. Ball, M. Darwich, G. E. Eperon, H. J. Snaith, *Nature Communications* **2013**, *4*, 2761.

[162] M. Liu, M. B. Johnston, H. J. Snaith, *Nature* **2013**, *501*, 395.

[163] O. Malinkiewicz, A. Yella, Y. H. Lee, G. M. M. Espallargas, M. Graetzel, M. K. Nazeeruddin, H. J. Bolink, *Nature Photonics* **2014**, *8*, 128.

[164] N. J. Jeon, H. G. Lee, Y. C. Kim, J. Seo, J. H. Noh, J. Lee, S. I. Seok, *Journal of the American Chemical Society* **2014**, *136*, 7837.

[165] Y. Wu, F. Xie, H. Chen, X. Yang, H. Su, M. Cai, Z. Zhou, T. Noda, L. Han, *Advanced Materials* **2017**, *29*.

[166] G. E. Eperon, S. N. Habisreutinger, T. Leijtens, B. J. Bruijnaers, J. J. van Franeker, D. W. DeQuilettes, S. Pathak, R. J. Sutton, G. Grancini, D. S. Ginger, R. A. J. Janssen, A. Petrozza, H. J. Snaith, *ACS Nano* **2015**, *9*, 9380.

[167] T. Leijtens, G. E. Eperon, N. K. Noel, S. N. Habisreutinger, A. Petrozza, H. J. Snaith, *Advanced Energy Materials* **2015**, *5*, 1500963.

[168] J. Yang, B. D. Siempelkamp, D. Liu, T. L. Kelly, *ACS Nano* **2015**, *9*, 1955.

[169] S. N. Habisreutinger, D. P. McMeekin, H. J. Snaith, R. J. Nicholas, *APL Materials* **2016**, *4*.

[170] W. J. Yin, J. H. Yang, J. Kang, Y. Yan, S. H. Wei, *Journal of Materials Chemistry A* **2015**, *3*, 8926.

[171] M. Shirayama, H. Kadowaki, T. Miyadera, T. Sugita, M. Tamakoshi, M. Kato, T. Fujiseki, D. Murata, S. Hara, T. N. Murakami, S. Fujimoto, M. Chikamatsu, H. Fujiwara, *Physical Review Applied* **2016**, *5*, 014012.

[172] N. Kitazawa, Y. Watanabe, Y. Nakamura, *Journal of Materials Science* **2002**, *37*, 3585.

[173] S. Ryu, J. H. Noh, N. J. Jeon, Y. Chan Kim, W. S. Yang, J. Seo, S. I. Seok, *Energy and Environmental Science* **2014**, *7*, 2614.

[174] L. M. Falk, K. P. Goetz, V. Lami, Q. An, P. Fassl, J. Herkel, F. Thome, A. D. Taylor, F. Paulus, Y. Vaynzof, *Energy Technology* **2020**, *8*, 1900737.

[175] J. H. Noh, S. H. Im, J. H. Heo, T. N. Mandal, S. I. Seok, *Nano letters* **2013**, *13*, 1764.

[176] E. Mosconi, A. Amat, M. K. Nazeeruddin, M. Grätzel, F. De Angelis, *Journal of Physical Chemistry C* **2013**, *117*, 13902.

[177] Y. Tu, J. Wu, Z. Lan, X. He, J. Dong, J. Jia, P. Guo, J. Lin, M. Huang, Y. Huang, *Scientific Reports* **2017**, *7*, 1.

[178] L. Vegard, *Zeitschrift für Physik* **1921**, *5*, 17.

[179] L. K. Ono, E. J. Juarez-Perez, Y. Qi, *ACS Applied Materials & Interfaces* **2017**, *9*, 30197.

[180] S. Colella, E. Mosconi, P. Fedeli, A. Listorti, F. Gazza, F. Orlandi, P. Ferro, T. Besagni, A. Rizzo, G. Calestani, G. Gigli, F. De Angelis, R. Mosca, *Chemistry of Materials* **2013**, *25*, 4613.

[181] S. Colella, E. Mosconi, G. Pellegrino, A. Alberti, V. L. Guerra, S. Masi, A. Listorti, A. Rizzo, G. G. Condorelli, F. De Angelis, G. Gigli, *Journal of Physical Chemistry Letters* **2014**, *5*, 3532.

[182] H. Yu, F. Wang, F. Xie, W. Li, J. Chen, N. Zhao, *Advanced Functional Materials* **2014**, *24*, 7102.

[183] P. Docampo, F. C. Hanusch, S. D. Stranks, M. Döblinger, J. M. Feckl, M. Ehrensperger, N. K. Minar, M. B. Johnston, H. J. Snaith, T. Bein, *Advanced Energy Materials* **2014**, *4*, 1400355.

[184] T. Jesper Jacobsson, J.-P. Correa-Baena, M. Pazoki, M. Saliba, K. Schenk, M. Grätzel, A. Hagfeldt, *Energy & Environmental Science* **2016**, *9*, 1706.

[185] F. Xu, T. Zhang, G. Li, Y. Zhao, Mixed cation hybrid lead halide perovskites with enhanced performance and stability, **2017**.

[186] I. Borriello, G. Cantele, D. Ninno, *Physical Review B - Condensed Matter and Materials Physics* **2008**, *77*, 235214.

[187] N. Pellet, P. Gao, G. Gregori, T.-Y. Yang, M. K. Nazeeruddin, J. Maier, M. Grätzel, *Angewandte Chemie* **2014**, *126*, 3215.

[188] N. J. Jeon, J. H. Noh, W. S. Yang, Y. C. Kim, S. Ryu, J. Seo, S. I. Seok, *Nature* **2015**, *517*, 476.

[189] M. Saliba, T. Matsui, J.-Y. Seo, K. Domanski, J.-P. Correa-Baena, M. K. Nazeeruddin, S. M. Zakeeruddin, W. Tress, A. Abate, A. Hagfeldt, M. Grätzel, *Energy & Environmental Science* **2016**, *9*, 1989.

[190] T. Matsui, J.-Y. Seo, M. Saliba, S. M. Zakeeruddin, M. Grätzel, *Advanced Materials* **2017**, *29*, 1606258.

[191] M. Deepa, M. Salado, L. Calio, S. Kazim, S. M. Shivaprasad, S. Ahmad, *Physical Chemistry Chemical Physics* **2017**, *19*, 4069.

[192] X. Zheng, Y. Hou, C. Bao, J. Yin, F. Yuan, Z. Huang, K. Song, J. Liu, J. Troughton, N. Gasparini, C. Zhou, Y. Lin, D.-J. Xue, B. Chen, A. K. Johnston, N. Wei, M. N. Hedhili, M. Wei, A. Y. Alsalloum, P. Maity, B. Turedi, C. Yang, D. Baran, T. D. Anthopoulos, Y. Han, Z.-H. Lu, O. F. Mohammed, F. Gao, E. H. Sargent, O. M. Bakr, *Nature Energy* **2020**, *5*, 131.

Chapter 3

Experimental Methods

3.1 Perovskite Fabrication Methods

3.1.1 Double Cation Perovskite Fabrication

Thin films of the double cation, mixed halide perovskite $(FAPbI_3)_{0.85}(MAPbBr_3)_{0.15}$ were fabricated for fluorescence lifetime mapping studies in Chapter 5, and for powder X-ray diffraction (PXRD), photoluminescence and absorbance measurements in Chapter 6. All of the double cation perovskite films used in this thesis were fabricated for me by Joel Smith and Dr. Onkar Game, my colleagues in the Electronic and Photonic Molecular Materials (EPMM) group.

Precursor Preparation: Method 1

For films used in Chapter 5, a precursor solution was prepared by dissolving 215.0 mg FAI, 633.9 mg PbI_2, 28.0 mg MABr and 91.8 mg $PbBr_2$ powders to a vial and adding a mixture of 800 μL anhydrous DMF and 200 μL anhydrous DMSO (i.e. a solvent mixture of 4:1 DMF:DMSO).

Precursor Preparation: Method 2

For films used in Chapter 6, a precursor solution was prepared via the following method:

1. A 0.5 mL solution of $MAPbBr_3$ (1.3 M) was made by dissolving 72.78 mg of MABr (GreatCell) and 238.56 mg of $PbBr_2$ (TCI UK Ltd.) in a 4:1 mixture of anhydrous

N,N-dimethylformamide (DMF; Sigma Aldrich) to anhydrous dimethyl sulfoxide (DMSO; Sigma Aldrich).

2. A 1 mL solution of $FAPbI_3$ (1.3 M) was made by dissolving 223.56 mg of FAI (GreatCell) and 599.31 mg of PbI_2 (99.99%; TCI UK Ltd.) in a solvent mixture of 4:1 DMF:DMSO, as above.

3. 0.85 mL of the $FAPbI_3$ solution and 0.15 mL of the $MAPbBr_3$ solution were mixed to give the desired composition.

For both Method 1 and Method 2, the precursor solution was then thoroughly vortex-mixed, before being syringe filtered and spread onto a synthetic quartz-coated substrate that had been cleaned and UV-ozone treated for 20 minutes. The solution was then spin-coated according to the following regime: substrate was accelerated from 0 to 2000 rpm at 200 rpms^{-1}, then held at 2000 rpm for 10 s. It was then accelerated from 2000 to 6000 rpm at 2000 rpms^{-1}, and held at 6000 rpm for 20 s. An antisolvent quench of 100 µL of anhydrous chlorobenzene (Sigma Aldrich) was dripped onto the film 10 s before the end of this final step. The film was then heated at 100° C for 30 minutes.

3.1.2 Spin-Coated Triple Cation Perovskites

Thin films of Cs-containing triple cation perovskites were prepared for time-resolved PL mapping measurements in Chapter 5 (films fabricated by Joel Smith and Onkar Game), and for PXRD and optical spectroscopy measurements in Chapter 7 (films fabricated by me).

For PXRD and optical spectroscopy data presented in Chapter 7, I fabricated thin films of triple cation perovskites of the form $Cs_zFA_xMA_yPbI_{2.55}Br_{0.45}$. The ratio $x = 4y$ was preserved for all values of z, which were 0.03, 0.05, 0.08, 0.1, 0.15. For each composition, the correct quantities of each precursor material required for a stoichiometric mixture (no lead or iodide excess) were calculated. Next, a 1 mL precursor solution of $Cs_zFA_xMA_yPbI_{2.55}Br_{0.45}$ was prepared in a 4:1 mixture of anhydrous dimethyl formamide (DMF) to anhydrous dimethyl sulfoxide (DMSO), as follows:

1. Powders of FAI (Ossila Ltd.), MABr (GreatCell), PbI_2 (99.99%; TCI UK Ltd.) and $PbBr_2$ (TCI UK Ltd.) were added to a vial in the required quantities.

2. Meanwhile, a second vial was weighed and taken into the glovebox, where an unknown quantity of caesium iodide (CsI) powder (Alfa Aesar) was added. This step was necessary because the stock of CsI powder could not be removed from the glovebox for weighing, due to its sensitivity to moisture in the air. Next the vial containing the powder was weighed and the weight of vial by itself was subtracted from the total to determine the weight of the powder.

3. The weight of the CsI powder was used to calculate the quantity of DMSO required to mix a 1.5 M solution of CsI. This quantity of DMSO (Sigma Aldrich) was added to the second vial and the solution was vortex mixed to ensure complete dissolution.

4. The amount of CsI solution required to result in the final composition was calculated, and this amount was added to a third vial. A 1 mL solution of the full triple cation precursor requires a solvent mixture of 800 µL of DMF and 200 µL of DMSO, but the CsI solution already accounts for a certain amount of the DMSO required, therefore this amount of DMSO was subtracted from 200 µL, and the remaining DMSO was added to the first vial along with 800 µL of DMF.

5. The solution in the first vial was thoroughly vortex-mixed to ensure complete dissolution, before being added to the CsI solution to create a precursor solution of the desired triple-cation composition.

For time-resolved PL mapping measurements in Chapter 5, thin films of triple cation perovskites of the form $Cs_{0.05}FA_{0.76}MA_{0.19}PbI_{2.55}Br_{0.45}$ were fabricated. The perovskite precursor solution for these films was made by dissolving 215.0 mg FAI, 633.9 mg PbI_2, 28.0 mg MABr and 91.8 mg $PbBr_2$ powders to a vial and adding a mixture of 800 µL anhydrous DMF, 150 µL anhydrous DMSO and 50 µL of 1.5 M solution of CsI, prepared as described above. Therefore it must be noted that this perovskite composition is not stoichiometric as it has a slight iodide excess.

For both types of precursor solution described above, thin films were then prepared by spin coating the precursor solution onto quartz-coated glass substrates which had

been cleaned and then UV-ozone treated for 20 minutes. For each film, 40 μL of the perovskite solution was spread onto the substrate and spun at 1000 rpm for 10 s, followed by 6000 rpm for 20 s. An antisolvent quench of 100 μL of anhydrous chlorobenzene (Sigma Aldrich) was dripped onto the film 5 s before the end of the second step. The films were then annealed at 110° C for 30 minutes. The above film fabrication method was adapted from the work of Saliba *et al.*[1]

3.1.3 Spray-Coated Triple Cation Perovskites

For fluorescence lifetime imaging studies in Section 5.2.2, triple cation perovskite thin films were fabricated using a method known as vacuum-assisted solution processing (VASP). The fabrication of the films was carried out by Dr. James Bishop, an EPMM colleague. The perovskite precusor was prepared by the following method: 167 mg FAI (Ossila Ltd.), 19 mg MaBr (Dyesol), 68 mg $PbBr_2$ (TCI UK Ltd.), 467 mg PbI_2 (TCI UK Ltd.), and 16 mg CsI (Sigma-Aldrich) were weighed out into a vial to form the triple cation perovskite $(CsI)_{0.05}((FAPbI_3)_{0.85}(MAPbBr_3)_{0.15})_{0.95}$. These powders were then dissolved in a 1 mL mixture of 4: 1 DMF:DMSO (800 L DMF and 200 L DMSO).

Quartz-coated glass substrates (cleaned and UV-ozone treated for 20 mins) were then transferred to a glovebox, and the spray deposition of the precursor mixture was carried out using a Sonotek Exactacoat system mounted with an Impact spray-head. The perovskite precursor was delivered at a rate of 1 $mLmin^{-1}$ through a tip driven at 2 W with a shaping gas at a pressure of 3 Psi. The head was held 10 cm above the substrate, which was mounted on a hotplate held at 40°C. During deposition, the head moved in a line scan over the substrate at 50 mms^{-1} to coat it in the precursor. After deposition, the substrate was left for 30 s to allow an even wet film to form. Subsequently, the substrate was exposed to a partial vacuum ($\sim$ 0.8 mbar) for 5 minutes to draw the DMF out of the film, creating a partially crystallised layer. The film was then annealed at 100°C for 30 minutes to evaporate any remaining DMSO.

3.2 Triple Cation Perovskite Device Fabrication and Testing

PV devices were fabricated from spray-coated $CsI_{0.05}((FAPbI_3)_{0.85}(MAPbBr_3)_{0.15})_{0.95}$ perovskite with the following device architecture: indium tin oxide (ITO)/nanoparticle tin oxide (np-SnO2)/perovskite/spiro-OMeTAD/Au. The np-SnO_2 film was deposited by spin-coating a commercially available np-SnO_2 solution onto the ITO layer, which was then annealed at 150 °C for 30 minutes. Once the perovskite layer had been spray-coated, a layer of doped spiro-OMeTAD was spin-coated onto the perovskite layer. Lastly, a series of 2 mm × 2 mm gold contact electrodes were thermally evaporated on top.

Devices were tested by illuminating the device with an AM 1.5-calibrated solar simulator (simulating 1 Sun illumination) and collecting current-voltage (JV) measurements. The sample was exposed through a 2.6 mm^2 aperture mask to light from an AM 1.5 calibrated solar simulator. PV devices were fabricated and tested in this way as part of a work carried out by Bishop and coworkers to determine the effect of VASP treatment of spray-cast triple cation perovskite films on PSC performance.[2]

3.3 Absorbance and Steady State Photoluminescence Spectroscopy

For absorbance measurements, samples were illuminated with a deuterium-halogen lamp (Ocean Optics) and transmitted light was collected in an optical fibre and passed to a spectrometer (Ocean Optics HR2000+ES) to obtain spectral data.

For steady state PL measurements, samples were illuminated with a 405 nm CW laser at 800 μW in reflection mode and PL emissions were collected in the spectrometer.

A schematic of the combined absorbance/PL system is shown in Figure 3.4, with components for each type of measurement clearly labelled.

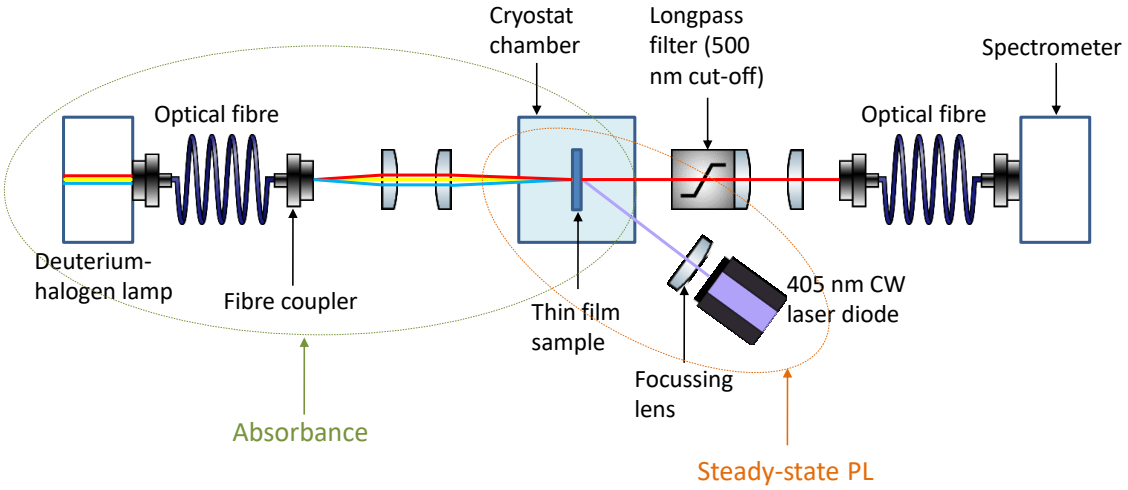

Figure 3.1: Schematic diagram of the experimental setup for optical absorbance and steady state photoluminescence measurements.

3.3.1 Variable Temperature Measurements

For variable temperature absorbance and PL measurements, samples were cooled to 4 K using an Oxford Instruments OptistatDry cryogen-free cryostat. Measurements were taken at regular temperature intervals as the sample was heated back to room temperature.

3.4 Time-Resolved Photoluminescence

3.4.1 Time-Correlated Single-Photon Counting

The fluorescence lifetime is commonly determined for hybrid perovskites through time-resolved photoluminescence (TRPL) measurements. In this thesis, I have used time-correlated single-photon counting (TCSPC)[3,4] to collect TRPL data. The basic operating principle of TCSPC is that the time dependence of the fluorescence in a material can be determined by periodic light excitation of a material and collection of informa-

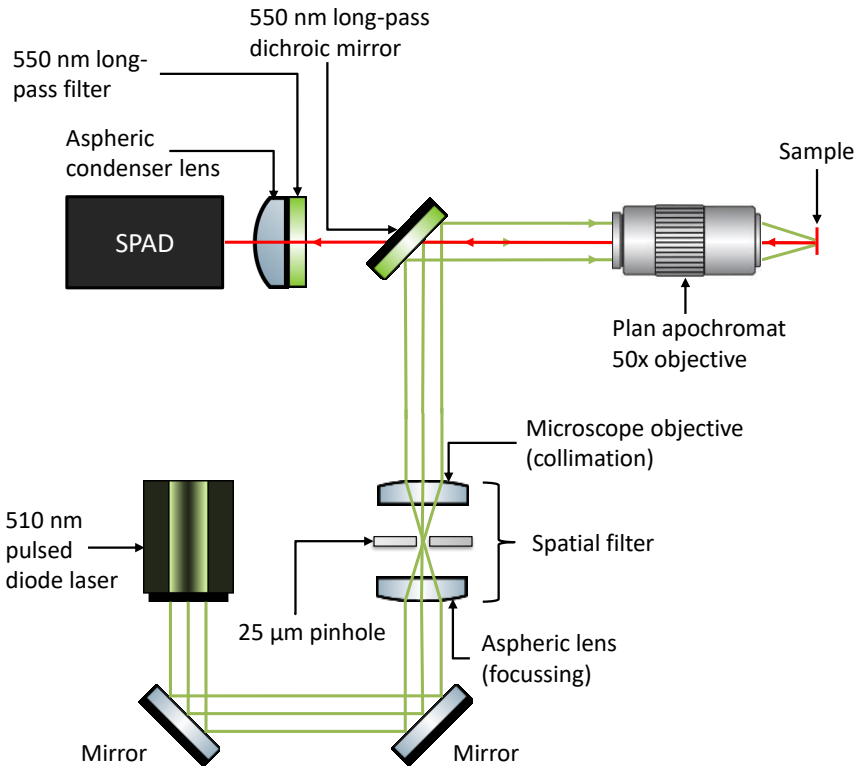

Figure 3.2: Diagram of the optical setup for TCSPC measurements.

tion about photon re-emission events over a large number of cycles. Fluorescence is excited periodically using a pulsed laser and collected at a single-photon photomultiplier or avalanche diode. At each pulse of the laser, a trigger signal is sent to the timing electronics board in a computer, which starts a timer. The first instance of a fluorescence photon on the detector triggers the timer to be turned off. This delay time is recorded, and any subsequent photon events before the next laser pulse are ignored. This process is repeated at each laser pulse, continuing for the desired period of time (integration time). When the measurement is complete, all the delay times are sorted into time bins and plotted as a histogram. This histogram typically takes the form of an exponential decay curve, which represents the decay of the excited charge carrier population.[5] This can be explained by thinking about it thus: the intensity of detected light is determined by the number of photons emitted in any period of time, therefore it is directly proportional to the population of charge carriers remaining in the material.

A schematic of the TCSPC setup used in this thesis is shown in Figure 3.2. The laser diode providing pulsed excitation is the LDH-P-C-510B (PicoQuant GmbH), with a

wavelength range 500-520 nm, centred on 510 nm. The laser diode is driven by the PDL-800B laser driver (Picoquant GmbH), which allows for control of the laser intensity and the repetition rate (2.5 - 40 MHz). The timing electronics for this sytem are facilitated by a TimeHarp 260 PCIe (Peripheral Component Interconnect Express) board (PicoQuant GmbH), which is installed in the motherboard of the PC used for TCSPC experiments. The associated software, TimeHarp 260 Pico, allows the user to collect time-resolved PL data.

The TCSPC method works best when there is only one photon event per excitation cycle, in order to generate histograms which most accurately reflect the time decay of the fluorescence. The reason for this is the so-called 'dead time' of the detector and electronics, which is a time period after each photon event at the detector during which another photon cannot be processed. If the number of photons arriving at the detector in each cycle averages > 1, the time delays collected will be biased towards earlier times, therefore misrepresenting the fluorescence decay in an effect known as 'pile up'. Hence the probability of multiple photon events in each pulse cycle should be kept to a minimum; ideally, only 1 in 20 excitation cycles results in a count at the detector. For TCSPC data presented in this thesis, the laser intensity was selected such that the count rate at the detector never exceeded 5% of the excitation frequency.

The overall timing accuracy of a TCSPC system is determined by the instrument response function (IRF), which is a convolution of the timing errors from all timed processes in the experiment. There are 3 main sources of such timing errors, the first and most important being the timing uncertainty introduced when an incident photon event is converted to an electrical signal in the detector. The second major source of timing error is the excitation source, in this case a pulsed diode laser, which of course has a finite pulse width. However, the laser diode also needs to produce an electrical timing reference signal (know as a sync signal) with which to compare the fluorescence photon signal, which adds a further source timing error. The third notable source of timing error is the timing jitter on the other electronic components of the TCSPC system, caused by the finite rise-fall time of the electronic signals used for timing measurements.

Technically, the total IRF for the system is a convolution of the timing error distri-

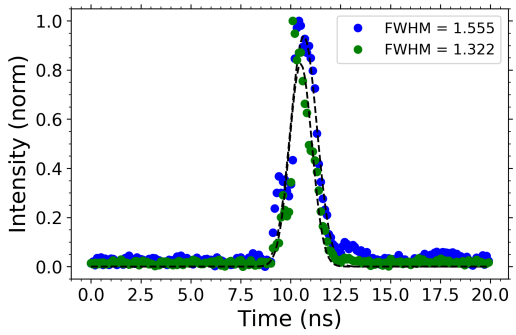

Figure 3.3: Plot of two attempts at measuring the instrument response function, both taken with an integration time of 5 minutes, a 5 MHz laser repetition rate and a histogram bin width of 100 ps. Dashed lines are Gaussian fits to the data.

butions of all the above components, but the FWHM of the total IRF can be estimated using error propogation laws as follows:

$$IRF_{total} \propto \sqrt{\sum IRF^2_{component}} \tag{3.1}$$

The detector used in this TCSPC system is a single photon avalanche diode (SPAD) in the PDM series manufactured by Micro Photon devices. This is listed to have a maximum timing resolution (FWHM) of 250 ps. Other sources of timing uncertainty in this system are:

- the pulsed diode laser has a pulse width of $<$ 110 ps and a pulse-to-pulse jitter of $\approx$2.6 ps;
- the laser driver has an electrical jitter of 40 ps for the laser trigger signal and 20 ps for the sync signal;
- the timing electronics board used has a minimal temporal resolution of 25 ps, and a 20 ps timing precision including contributions from both input channels (laser trigger signal and photon signal from detector).

Using Eq. (3.1), the total IRF can be estimated as:

$$IRF_{total} \approx \sqrt{0.25^2 + 0.11^2 + 0.0026^2 + 0.04^2 + 0.02^2 + 0.025^2 + 0.02^2} \approx 0.28ns \tag{3.2}$$

Having estimated the IRF, it was also measured experimentally. A scattering medium was placed in the sample holder (see diagram in Figure 3.2), and time-resolved measurements were taken with an integration time of 5 minutes, at a 5 MHz laser repetition rate and a histogram bin width of 100 ps. Collected data from two of these runs is shown in Figure 3.3 To estimate the IRF, a Gaussian profile was fitted to these datasets and the FWHM was extracted for each, as shown in Figure 3.3. This shows that the instrument response is $\sim$1.4 ns, which is $\sim$5 times larger than the theoretical IRF. This suggests that there is an additional IRF broadening mechanism that has not been accounted for in the known timing uncertainties of the system. The instrument response function also affects the selection of the time bin width for the histograms, which should not be any larger than 10% of the width of the IRF, therefore in these TCSPC experiments the bin width was set to a maximum of 0.1 ns.

When studying short transients ($\lesssim$ 10 ns), it was necessary to deconvolve the IRF ($\sim$1.5 ns) from the collected data in order to obtain accurate lifetime values. However, the mixed cation hybrid perovskite materials studied in this thesis are expected to have much longer average lifetimes than the IRF (on the order of 100s of ns), therefore as a general rule it was not necessary to perform this deconvolution on the TRPL data presented in Chapter 4 and Chapter 5.

For this thesis, the TCSPC system shown in Figure 3.2 was modified to include mapping functionality—full experimental details for this process can be found in Chapter 4.

Temperature-dependent TCSPC data in Appendix C was collected by mounting the sample into a closed cycle cryostat (Oxford Instruments MicroStatHe) and cooling the sample with liquid helium. Temperature was controlled using an Oxford Instruments ITC4 Temperature Controller.

3.4.2 Streak Camera Measurements

A streak camera is a device used to study ultra-fast light phenomena by collecting intensity, spatial and time-resolved information about incident light. If a spectrometer is placed before the the entrance slit of the streak camera, spatial information becomes information about the wavelength of the incident light. In this way, time-resolved spec-

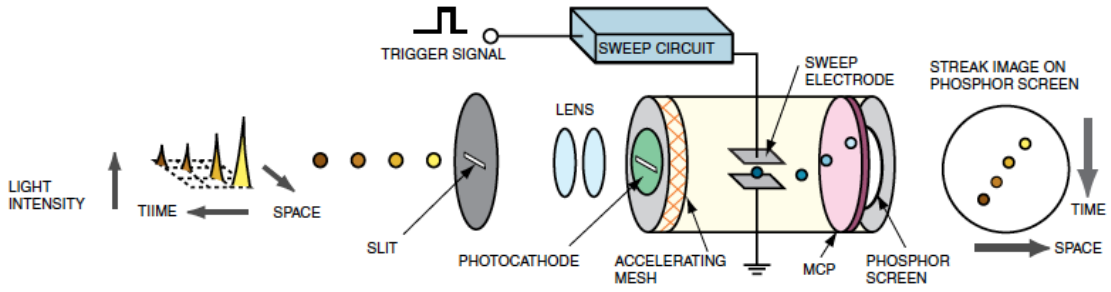

Figure 3.4: Schematic showing how the streak tube operates.[6] The streak tube is placed after a spectrometer which collects light emitted from the sample surface subsequent to pulsed laser excitation.

troscopy can be carried out with an ultra-fast time resolution.[6]

The experimental method used for the streak camera images presented in this thesis was as follows: samples were excited with 515 nm wavelength pulses of 200 fs duration generated from the second harmonic of a regeneratively amplified femtosecond laser system (Pharos from Light Conversion) with a repetition rate of 100 kHz. The excitation spot diameter was 175 μm. The emitted light was resolved spectrally using a Princeton Instruments Acton SpectraPro SP-2300 spectrograph, and temporally using a Hamamatsu Streak camera (C10600 Orca-R2 coupled to a M10911 synchroscan unit). Samples were cooled by liquid nitrogen in a bath cryostat. Streak camera measurements presented in Chapter 6 were collected in collaboration with Dr. Sai Rajendran from the School of Physics and Astronomy at the University of St Andrews.

3.5 X-Ray Diffraction Measurements

In this thesis, both thin film and powder X-ray diffraction (PXRD) measurements were used to characterise mixed cation perovskites. For PXRD measurements presented in Chapter 6, thin films of the double cation perovskite $(FAPbI_3)_{0.85}$ $(MAPbBr_3)_{0.15}$ were fabricated via the method shown in Section 3.1.1. Full details of the data collection and analysis methodology for these samples can be found in Section 6.4.

For all X-ray diffracion measurements presented in Chapter 7, thin films of triple cation perovskites of the form $Cs_zFA_xMA_yPbI_{2.55}Br_{0.45}$, with $z = (0.05, 0.08, 0.1)$, were fabricated as shown in Section 3.1.2.

3.5.1 Thin Film X-Ray Diffraction Measurements

For thin film diffraction data in Chapter 6, X-ray diffraction measurements were taken by Tarek Alanazi, a group colleague from EPMM. X-ray diffraction data was collected using a PANalytical X'Pert Pro, powered by a Philips PW3050/60 (θ/θ) X-ray generator diffractometer (240 mm diameter) with a PW3064 sample spinner. The setup included a 1D-detector in Bragg-Brentano geometry, employing a copper line focus X-ray tube with Ni Kβ absorber (0.02 mm; Kβ = 1.392250 *Å*) Kα radiation (Kα_1 = 1.540598 *Å*, Kα_2 = 1.544426 *Å*, Kα ratio 0.5, Kα_{avg} = 1.541874 *Å*). X-rays were generated from a Cu anode material supplied with a voltage of 45 kV and a current of 40 mA. An incident beam Soller slit of 0.04 rad, a 1° fixed anti-scatter slit, an incident beam mask of 12 mm and a programmable automated divergence slit, giving a constant illuminated length of 140 mm, were used. Data was collected in the range 2θ = 5-80° with a step size of 0.0131°. All scans were carried out under continuous mode.

3.5.2 Powder X-Ray Diffraction Measurements

For PXRD measurements presented in Chapters 6 and 7, thin film samples were prepared as described in Section 3.1.1 and Section 3.1.2, respectively. The material was scraped from the substrate using a razor blade, and the resultant fine powder was loaded into a 0.7 mm borosilicate capillary. Powder diffraction data were obtained using a Bruker D8 Advance powder diffractometer using CuKα radiation and equipped with focusing Göbel mirrors and a high resolution energy-dispersive Lynxeye XE detector. Data were collected in a Debye-Scherrer geometry with rotating capillary stage. Sample temperature for in situ cooling and heating studies was controlled by a co-axial stream of dry nitrogen gas from an Oxford Cryosystems Cryostream 700 Plus, with a flow rate of 5 L/min. These measurements were carried out by Dr. Craig Robertson from the Department of Chemistry at the University of Sheffield.

3.5.3 Powder X-Ray Diffraction Modelling

For this thesis I collaborated with Adam Shnier from the University of the Witwatersrand, who carried out modelling of powder X-ray diffraction data taken for double and triple

cation perovskites. The structural parameters and analysis resulting from this modelling are presented in Chapters 6 and 7.

Instrument Profile

A silicon standard was scanned at room temperature across the 2θ range 10-100°, against which a convolution based fundamental parameter instrument profile was refined. This included convolutions specific to capillary type samples. This profile was then fixed with the exception of the parameter associated with absorption by the sample and used for all refinements in this work.

Refinements of Powder XRD Data

For each composition, the full data set was refined simultaneously using TOPAS-academic V6.1. The background of the diffraction patterns was modelled using a Chebychev polynomial and an exponential decay function for low angle air scattering. A peak constrained to be broad was included to explain the feature, consistent with the glass capillary, which was clear in some of the patterns. Crystallite size broadening was refined as a global parameter. A simple P4/mbm-based model was found to be suitable for these refinements. The unit cell was constrained to be tetragonal, and the rotation of the octahedra about the c-axis was also refined (Glazer notation $a^0a^0c^+$ [7]).

Parametric refinements

For the XRD data in Chapter 7, a more detailed model was applied which included all the features of the above method but with additional parameterisation of the refinements. Where the high temperature phase is evident, the lattice parameter ratio $a/c\sqrt{2}$ and octahedra rotation are defined by single global variables. To further reduce noise and improve reliability of the refined parameters, a 4th order polynomial was fitted for a selected temperature range of the parameter associated with octahedra rotation. Starting parameters for this polynomial were determined by fitting against the locally free parameter such as in the above method. To prevent over-constraining the data, this region was chosen to exclude any sudden shifts in the parameter. This region was chosen for

each composition separately.

3.6 Summary

In this thesis, the solution-processed double cation perovskite $(FAPbI_3)_{0.85}(MAPbBr_3)_{0.15}$ was used for TRPL mapping measurements in Chapter 5, and for absorbance, PL, TRPL and XRD measurements presented in Chapter 6. Solution-processed, spin-coated triple cation perovskites of the form $Cs_zFA_xMA_yPb(I_{0.85}Br_{0.15})_3$ were used for TRPL mapping measurements in Chapter 5, and for absorbance, PL, TRPL and XRD measurements presented in Chapter 7.

Absorbance and PL spectroscopy were used in Chapters 6 and 7 to characterise mixed cation perovskite thin films. TCSPC was used in Chapter 5 to carry out TRPL mapping, and in Chapter 6 for temperature-dependent TRPL measurements. Streak camera measurements were used in Chapter 6 to determine temperature-dependent charge carrier dynamics in $(FAPbI_3)_{0.85}(MAPbBr_3)_{0.15}$. Powder X-ray diffraction measurements were used in Chapters 6 and 7 to determine the temperature dependence of structural properties of mixed cation perovskites. Thin film X-ray diffraction was used in Chapter 7 to determine crystallinity of thin film perovskites in the compositional space $Cs_zFA_xMA_yPb(I_{0.85}Br_{0.15})_3$.

References

[1] M. Saliba, T. Matsui, J.-Y. Seo, K. Domanski, J.-P. Correa-Baena, M. K. Nazeeruddin, S. M. Zakeeruddin, W. Tress, A. Abate, A. Hagfeldt, M. Grätzel, *Energy & Environmental Science* **2016**, *9*, 1989.

[2] J. E. Bishop, J. A. Smith, C. Greenland, V. Kumar, N. Vaenas, O. S. Game, T. J. Routledge, M. Wong-Stringer, C. Rodenburg, D. G. Lidzey, *ACS Applied Materials & Interfaces* **2018**, *10*, 39428.

[3] D. V. O'Conner, D. Phillips, *Time Correlated Single Photon Counting*, Academic Press, **1984**.

[4] W. Becker, *Advanced Time-Correlated Single Photon Counting Techniques*, Springer, **2005**.

[5] M. Wahl, Time-Correlated Single Photon Counting (Technical Note), https://www.picoquant.com/images/uploads/page/files/7253/technote_tcspc.pd, accessed on 2020-09-28, **2020**.

[6] Guide to Streak Cameras — Hamamatsu, https://www.hamamatsu.com/resources/pdf/sys/SHSS0006E_STREAK.pdf, accessed on 2020-09-28.

[7] F. Shojaei, W. J. Yin, *Journal of Physical Chemistry C* **2018**, *122*, 15214.

Chapter 4

Development of a Time-Resolved Photoluminescence Mapping System for Hybrid Perovskites

Note on contributions to this chapter

All work presented in this chapter was carried out by me, with the following exceptions:

- *Dr. Samuele Lilliu* wrote the MATLAB code for integrated control of the time-resolved PL mapping system.
- *Dr. Onkar Game and Joel Smith* fabricated the perovskite samples tested throughout the chapter.

4.1 Introduction

The first major project I undertook during my PhD was to build a time-resolved photoluminescence (TRPL) mapping system for hybrid perovskite thin films.

Photoluminescence (PL) imaging refers to a family of techniques where the PL emission intensity and/or wavelength of a given material is spatially resolved in two dimensions. These techniques are widely used in materials physics to investigate how surface morphology affects PL properties, or as an alternative method of investigating surface

morphology to techniques such as scanning electron microscopy (SEM) and transmission electron microscopy (TEM), which require special sample preparation and can cause damage to sensitive samples due to high energy incident electron beams. PL imaging studies have a limited spatial resolution compared to electron microscopy, due to the diffraction limit of a focussed laser beam, but they have nevertheless been used to great effect to further understand the fundamental properties of hybrid perovskites and aid the optimisation process.[1–4]

One such example is the work of Wen and colleagues,[5] who carried out fluorescence imaging studies on thin films of $CH_3NH_3PbI_xCl_{3-x}$. By mapping PL intensity across their samples, they were able to obtain information about the quality of their films by identifying places where excessive recombination takes place, such as grain boundaries. In order to further investigate the effect of morphology on carrier transport, local carrier lifetime data was also taken. In this way they were able to characterise the film uniformity, and in doing so they showed that a non-uniform film can affect the formation of the electron transporting medium (ETM) or lead to a poor perovskite/ETM interface, causing poor interfacial transport from the perovskite to the ETM (in this case it was PCBM), which limits device efficiency.

More recently, de Quilettes and coworkers[6] extensively investigated the effect of perovskite microstructure on PL emission and lifetimes in $CH_3NH_3PbI_3(Cl)$, in order to compare film fabrication methods and the effect of chlorine content on morphology in iodine-chlorine mixed halide perovskites. They carried out PL imaging of the surface of their films via confocal PL microscopy, which they then combined with time-resolved PL measurements from particular regions of interest, to probe local carrier lifetimes these in regions. As shown in Figure 4.1, it was found that regions of high PL intensity exhibited longer fluorescence lifetimes than those of low intensity. The darkest areas (those with low PL intensity) tended to correspond to grain boundaries, suggesting that grain boundaries are a source of non-radiative recombination. However, this study also showed that certain passivation techniques such as pyridine vapour exposure could brighten the whole image, including the grain boundaries. It was also found that non-radiative recombination at grain boundaries was reduced at higher laser fluences.

De Quilettes *et al.* used PL imaging to differentiate between surface and bulk recombination effects, in order to gain a fuller picture of charge transport in the material,

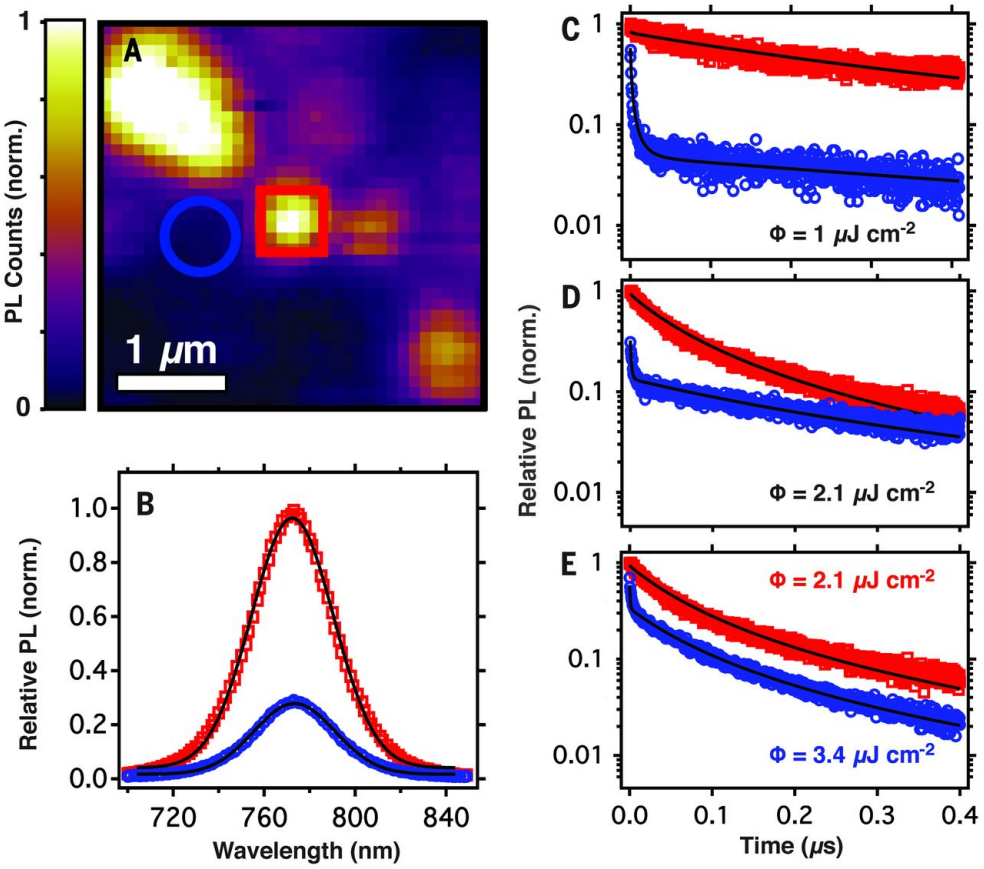

Figure 4.1: **A** A 3 μm–by–3 μm fluorescence image of the perovskite film with bulk lifetime $< \tau > = 1010$ ns ($\tau_c = 433$ ns, $\beta = 0.57$). **B** Relative steady state PL spectra of bright (red square) and dark (blue circle) regions. **C** Time-resolved PL decay curves of bright (red square) and dark (blue circle) regions after excitation at 470 nm, 125 kHz, $\phi = 1$ μJ/cm^2 ($n_0 \sim 5 \times 10^{16}$ cm^{-3}), **D** $\phi = 2.1$ μJ/cm^2 ($n_0 \sim 1 \times 10^{17}$ cm^{-3}), and **E** bright region measured at $\phi = 2.1$ μJ/cm^2 versus dark region measured at $\phi = 3.4$ μJ/cm^2 ($n_0 \sim 1.6 \times 10^{17}$ cm^{-3}), showing that dark regions require higher initial carrier densities to exhibit kinetics dominated by bimolecular recombination. Black traces are simulations to the data. Figure reproduced from de Quilettes *et al.* *Science* **2015** *348*, pp 683.[6]

and TRPL studies supplemented this by shedding light on recominbation times and mechanisms in localised regions. This suggests that an integrated system where the PL intensity and lifetime can be examined concurrently would allow for a more concise picture of the effect of morphology on the PL properties in hybrid perovskites.

Examples of such investigations in the literature include that of Sheng *et. al*,[7] who used fluorescence lifetime imaging to compare the effects of different storage conditions on the ageing of $CH_3NH_3Pb\ Br_3$ samples. They found that samples stored in N_2 retained small, uniformly-sized grains after 2 weeks of storage, with long PL lifetimes consistently throughout the fluorescence lifetime maps. In contrast, when the samples stored in air (relative humidity 50-60%), after 2 weeks the grains had become larger and much less

uniform in size and PL intensity, with shorter PL lifetimes and lower PL intensities on average.

Namkoong and colleagues[8] also carried out PL lifetime mapping, at a spatial resolution of $\sim$ 0.38 μm, facilitated by combining confocal microscopy with a TCSPC system. They also used confocal PL microscopy to map the PL intensity and peak position, also on a $\sim$ 0.38-μm scale, which revealed significant differences in optical properties between grain boundaries and grain interiors. The PL maps and PL lifetime maps revealed the non-radiative recombination mechanisms occurring at grain boundaries of $CH_3NH_3PbI_{3-x}Cl_x$, such as strong PL quenching and shortened PL lifetimes. Overall, it was found that larger grain sizes tended to correspond to better optical properties.

More recently, Adhyaksa *et al.*[9] mapped both PL intensity and lifetime of $CH_3NH_3PbBr_3$ ($MAPbBr_3$) perovskite thin films. Their key conclusion was that crystalline grain boundaries in halide perovskites are detrimental to photovoltaic performance, but that amorphous regions between grains actually provide passivation of the grain boundaries by extending the PL lifetimes at the grain boundaries. Amorphous grain boundaries appeared to be more prevalent in perovskites with larger grains ($\sim$54 μm). As mentioned previously, Namkoong *et al.*[8] suggested that larger perovskite grain sizes yield better optical performance, and perhaps the resultant amorphous grain boundaries are the origin of this effect.

The studies discussed show that time-resolved PL mapping studies have the potential to aid optimisation of perovskite thin films, and showcase the usefulness of this technique within an extremely complex optimisation process. Therefore I set out to develop a TRPL imaging system which creates 2D images of both PL intensity and PL lifetime on a thin film perovskite sample, in order to further understand the correlation betwen surface morphology, PL intensity and carrier lifetimes in hybrid perovskite thin films. The remainder of this chapter describes the development and proof of concept for this experimental system.

4.2 Construction of the TRPL Mapping Setup

The TRPL mapping system was built by incorporating 2D raster scanning capability into a time-correlated single photon counting (TCSPC) setup. The TCSPC setup consists of a 510 nm pulsed diode laser (LDH-P-C-510B, PicoQuant GmbH), a picosecond pulsed laser driver (PDL 800-B, PicoQuant GmbH) and a single-photon avalanche diode (Micro Photon Devices). This equipment is used to obtain time-resolved photoluminescence (TRPL) data as detailed in Section 3.4.1, with the timing electronics controlled by the TimeHarp 260 PCIe board and its associated data collection software (PicoQuant GmbH).

To obtain spatially-resolved maps of fluorescence lifetimes, a raster scan must be carried out over the surface of the material in a 2D lattice, and TRPL data must be collected at each scan point. Here, a few key challenges present themselves: firstly, the sample must be mounted such that it can be moved in two dimensions; secondly, in order to achieve as high a spatial resolution as possible, the laser beam must be clean, Gaussian and focussed to a small area on the sample surface. In addition, it is important to be able to take photomicrographs of the area to be studied, for direct comparison with the lifetime maps. This requires the incorporation of a white light microscope into the system, without interfering with the TCSPC functionality. The following sections detail how these challenges were overcome, leading to the final system, which is shown in the schematic diagram in Figure 4.2.

4.2.1 Sample Mounting

As shown in Figure 4.2, the sample is mounted inside a small vacuum chamber due to the need to keep the perovskites from degrading over the length of the scans. The TRPL measurement at each point took at least 30 seconds, and to get a map which covers a large enough area to be of interest, the scan had to be at least 30×30 points in size, resulting in scans of > 7.5 hours. Therefore the perovskites must be held under vacuum as this length of time in ambient conditions may cause degradation to occur,[10–12] therefore potentially leading to unreliable results. The vacuum chamber is constructed from aluminium in order to minimise weight, which is to allow it to be mounted vertically

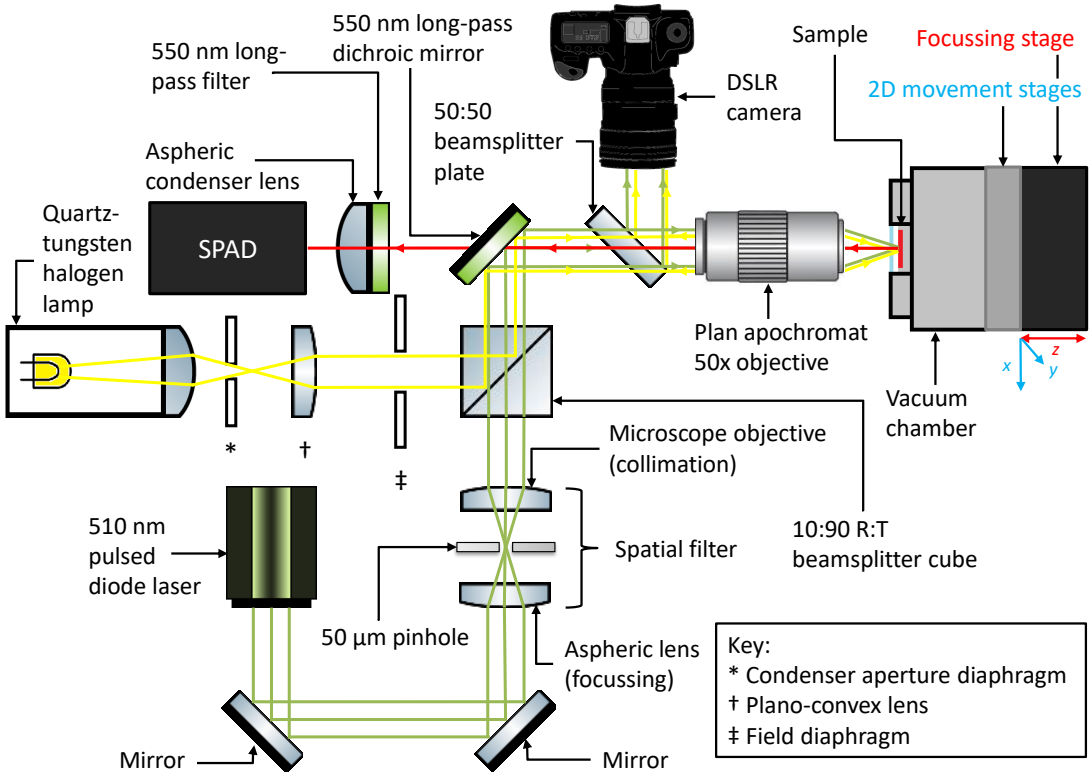

Figure 4.2: Schematic diagram of the TRPL mapping setup, showing the beam paths of the laser (green) and the white light (yellow), and the path of the PL emissions (red).

onto two highly precise linear movement stages with micrometer step size capabilities. These stages, which are both LRM025A-E03 motorized linear stages (Zaber Technologies Inc.), have been bolted together perpendicular to one another to facilitate travel in both *x*- and *y*-directions for raster scanning. These stages are mounted vertically to an L-bracket, such that they are perpendicular to a single-axis stage (the focussing stage), which can be moved towards and away from the microscope objective to achieve fine focus of both the laser beam and the white light microscope images. It was decided that the vibrations in the vacuum hose would be very likely to give rise to significant noise in the measurements. Therefore a valve is attached to the vacuum chamber so that the chamber can be pumped down to vacuum and subsequently isolated. This will slightly reduce the efficacy of the vacuum within the chamber, but this will be a much less significant disadvantage than the potential disruption caused by the vibrations of the vacuum pump.

4.2.2 Laser Beam Optics

The laser beam was aligned parallel to the optics bench with the help of two mirrors arranged as shown in Figure 4.2. The laser beam is elliptical and was therefore circularised using a spatial filter, placed in the beam path after the alignment mirrors. A spatial filter is a device which uses a lens to focus a laser beam down onto a circular pinhole, hence circularising the emerging beam. To prevent loss of power, the pinhole diameter must be slightly larger than the diffraction-limited spot size of the focussed beam. The diffraction-limited spot size D for a focussed laser beam is $D = \lambda f/r$,[13] where λ is the wavelength of the laser, f is the focal length of the focussing lens and r is the radius of the input laser beam. The horizontal radius of the elliptical input beam is 2 mm, which we take as r. For the focussing lens of this system, an aspheric lens with focal length $f = 20$ mm was selected, and the laser wavelength λ is 510 nm. This results in a diffraction-limited spot diameter of 5 μm, however the pinhole selected for the spatial filter had a diameter of 25 μm, as pinholes smaller than this incurred significant power loss in circularising the beam. Beyond the pinhole, the circular beam will be divergent, and therefore it is re-collimated using a second lens, which is achieved in this system with a 10× microscope objective, with a numerical aperture (NA) of 0.25.

Once a circular, Gaussian beam had been achieved, the next step was to focus it down onto the sample surface, which was achieved by placing an objective in the beam path such that the beam emerges from the objective at a distance approximately equal to its working distance from the surface of the sample. The mounting of the sample in the vacuum chamber, as discussed in Section 4.2.1, necessitated the use of a super-long working distance microscope objective: the Mitutoyo Plan Apo SL 50×, which is a plan apochromat super-long working distance microscope objective, was selected for this purpose. This lens has NA = 0.42 and a working distance of 20.5 mm.

It goes without saying that back-scattered laser light must not be allowed to reach the SPAD detector, and therefore a longpass dichroic mirror with a cut-off frequency of 550 nm was inserted into the beam path before the objective lens, as shown in Figure 4.2. This allows laser light to be directed towards the sample, but only allows the fluorescence emissions (which are expected to occur at $\lambda \sim 800$ nm for mixed cation (FA/MA)

perovskites[14,15]) to reach the detector. To further ensure that no scattered laser photons reach the detector, another 550 nm long-pass filter was inserted into the system, closer to the detector, with an aspheric condenser lens (f = 16 mm) placed in front of it to focus all emissions onto the active area of the SPAD. For additional optimisation of fluorescence signal collection, the SPAD itself was mounted on 3 movement stages allowing it to be moved in all 3 dimensions. This allows the fluorescence signal to be optimised by inspecting the data output of a calibration sample while adjusting the SPAD stages.

4.2.3 White Light Microscope

The main logistical challenge for incorporating a white light microscope into the system was the insertion of the required optics to direct the white light onto the sample, whilst not impeding the functionality of the TCSPC system. It was decided that the most efficient way to introduce white light into the system was to reflect it into the path directly after the spatial filter, through a 10:90 reflection:transmission beamsplitter cube. To direct light reflected from the sample into a camera lens to form an image of the surface, a further beamsplitter, this time an ordinary 50:50 plate, was inserted into the system. It was placed between the longpass dichroic mirror and the microscope objective, so that the laser beam itself could also be seen in the microscope image, allowing for visual calibration of the laser focus.

The white light source for the microscope is a quartz-tungsten halogen lamp, and the optics in its light path are arranged in a Köhler illumination configuration[16] to provide adequate illumination of the sample surface. As shown in the schematic in Figure 4.2, this involves passing the white light through a condenser aperture (lever-actuated iris, 15 mm max. aperature), after which it is collimated with a N-BK7 plano-convex lens (f = 100 mm) and then passed through a field aperture—I used a ring-actuated iris diaphragm (Thorlabs GmbH). The DSLR camera used to collect the microscope images is the Canon EOS 700D. Attached to this camera is a telephoto zoom lens (Canon EF 75-300mm f/4-5.6 III) which provides an eyepiece magnification M_e of 0.25×, when extended to its maximum tube length of 300 mm. The total magnification of a microscope system is

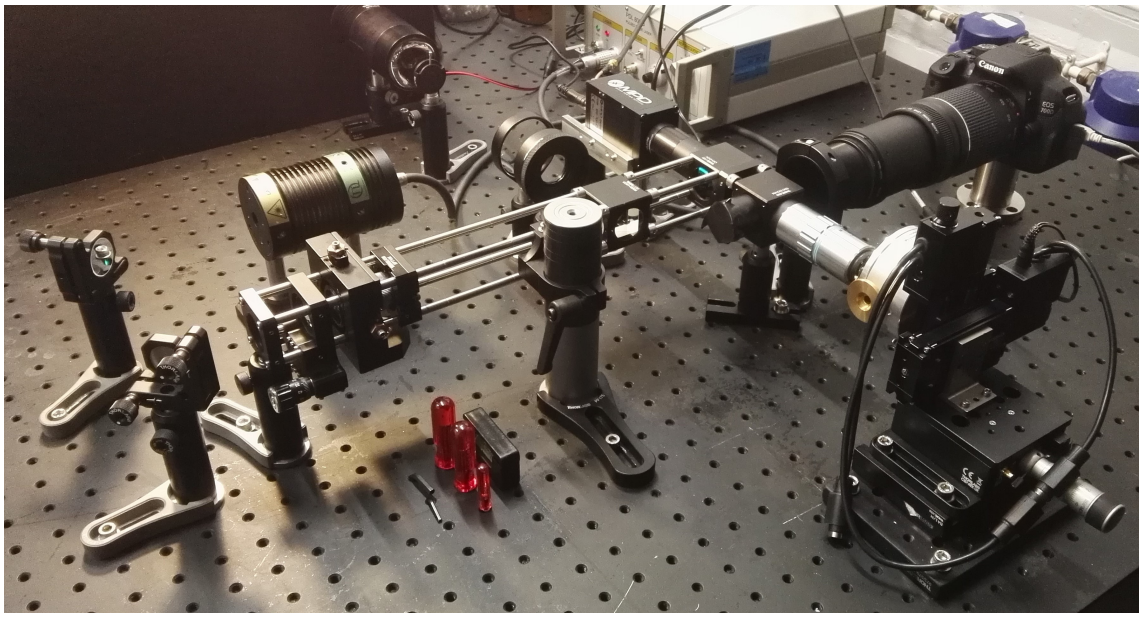

Figure 4.3: Photograph of the completed TRPL mapping setup in the laboratory.

defined as $M = m_o M_e$ where m_o is the magnification of the microscope objective and M_e is the magnification of the eyepiece, which in this case is the DSLR camera. For this microscope, $M_e = 0.25$ and $m_o = 50$ (the objective lens is a $50\times$ plan apochromat), therefore $M = 12.5$.

4.2.4 Software

A piece of purpose-built software was written for this TRPL mapping system, which automates the mapping process by initiating the raster scan and collecting TRPL data at each point. The software was written in MATLAB, along with an associated graphical user interface (GUI) for user-friendly control of all aspects of the TRPL mapping system. This GUI allows control of the motorised stages for setting up raster scans and configuration of measurement settings for TCPSC.

In order to undertake 2D raster scans, the software communicates with the movement stages upon which the sample chamber is mounted. The user can set the x- and y-dimensions of the desired map scan and select a starting point for the map, measured in μm coordinates where (0,0) μm corresponds to both movement stages being at their home position. To locate an appropriate starting point for a map scan, the software allows the user to move the stages around and take photomicrographs of the sample surface at different points. It does this by communicating with digiCamControl, an

open-source application which allows control of a DSLR camera from a PC. However, the TRPL mapping software does not currently allow for a live view of the sample surface, making the selection of a starting point through the GUI cumbersome and inconvenient. Therefore when setting up a map, I used Zaber Console (the software provided by Zaber Technologies Inc. for control of their motorised linear stages) combined with the Live View facility in digiCamControl to select a map starting point, and entered these coordinates into the GUI. Naturally, incorporating the digiCamControl Live View option into the TRPL mapping GUI is an improvement I would have made if I had had more time to develop the system.

The TimeHarp 260 PCIe board, which controls the timing electronics for the SPAD, laser diode and laser driver, comes with a set of C libraries which can be used to control the board and the associated TimeHarp 260 Pico software from within user-built control software. The TRPL mapping software calls these libraries to carry out data acquisition at each scan point, as well as enabling the user to specify measurement settings such as integration time and histogram bin width prior to starting a scan.

At each raster scan point, the TRPL mapping software fits the collected TRPL data to an appropriate model. This fitting model has been selected based on test TRPL data taken on mixed cation perovskites. A selection of this TRPL data is plotted in Figure 4.4, where TRPL measurements were repeated 3 times at each of 2 different locations on the surface of a $(FAPbI_3)_{0.85}(MAPbBr_3)_{0.15}$ thin film. The integration time used here was 30 s, the histogram bin width was 100 ps, and the laser repetition rate was 2.5 MHz. Data from two additional locations on the same film are also shown in Figure A.2 in Appendix A. A thin film sample of $Cs_{0.05}FA_{0.76}MA_{0.19}PbI_{2.55}Br_{0.45}$ was also fabricated and tested in the same way, with 3 repeats at each of 4 locations on the film, with the results shown in Figs. A.3–4.

The plots in Figure 4.4 and Figure A.3 show that the PL decay curves for double and triple cation perovskites, respectively, generally take the form of a double exponential curve, with a fast decay component over the first $\lesssim$ 10 ns and a second component which decays slowly across the rest of the 350 ns time window. I attempted to fit this data to a single exponential decay curve of the form $Ae^{-t/\tau} + C$, where A and τ are

the intensity and time constant of the exponential decay and C is a constant which accounts for the background noise level in the data. I also attempted to fit the data to a double exponential function of the form $A_1e^{-t/\tau_1} + A_2e^{-t/\tau_2} + C$, where the curve consists of a fast decay component with intensity A_1 and time constant τ_1 and a slow decay component with intensity A_2 and time constant τ_2. These plots show that a single exponential curve is a reasonable fit to the data: although the R^2 value is fairly low, it is likely that this cannot be much improved due to the noisy nature of the data and therefore large residuals. The double exponential fit provides a slightly higher value of R^2, most likely due to the fact that it can also account for the small deviation from single-exponential behaviour occurring in the first few nanoseconds of the decay. This slight difference also appears to have an effect on the decay time constant value: the time constant τ of the single exponential is consistently lower than the τ_2 value (slow decay constant) for the double exponential, perhaps again because the single exponential fit decay constant has a contribution from the fast decay in the early part of the time window. Based on this data it is clear that this system will be best for understanding the dynamics of the slow decay component, as the fast component is poorly resolved. Nevertheless, I decided to use the double exponential fit, as it describes the data better and has a marginally higher R^2 value, compared to a single exponential fit.

Figure 4.4 also shows that there is some variation between datasets collected at different times at the same point on the sample surface. The PL intensity is consistent across the tests in Figure 4.4**A**-**C**, whereas the time constant increases with each data acquistion. This suggests that there may be some light-induced effects occurring upon laser excitation of the film, however this should not affect results taken from this system as data at each scan point is collected in the first 30 s of laser illumination. The data in Figure 4.4**F** shows that the double exponential fitting model is not infallible and can sometimes result in values that are nonsensical. Despite having a reasonable value of R^2, the double exponential fit in Figure 4.4**F** has yielded a τ_2 value of 5.6×10^3 ns, which is extremely unlikely to be the fluorescence lifetime in this material. In Section 4.3.1, I discuss methods of detecting and dealing with such values.

A large selection of test data obtained on double and triple cation perovskites (such

as those in Figure 4.4 and Figs. A.2–4) were analysed with the MATLAB Curve Fitting Toolbox, to optimise fitting parameters for the double exponential fit which could then be incorporated into the software. However, when I attempted to deploy the software, it became clear that the parameter C, which accounts for background noise in the signal, was difficult to optimise globally as the background noise level can vary between scans

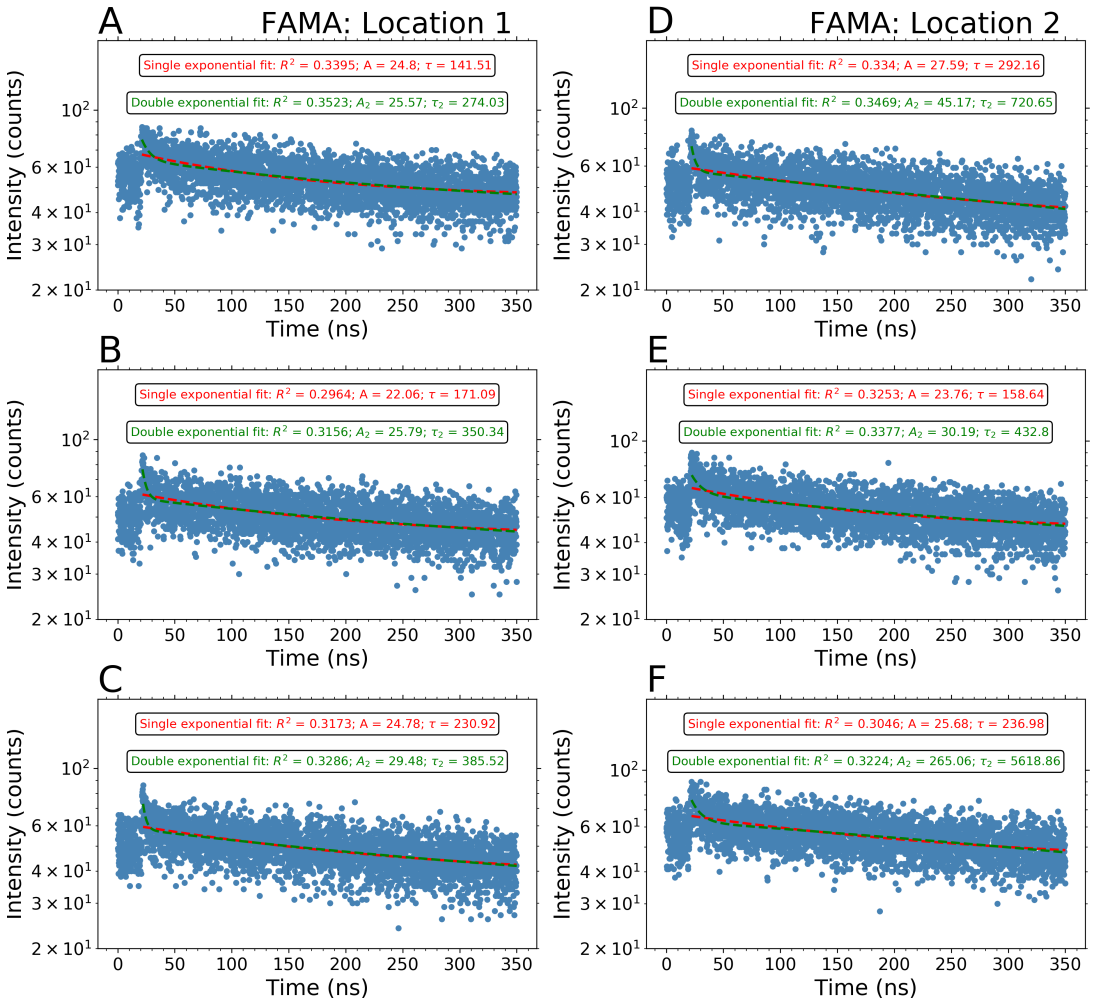

Figure 4.4: **A**-**C** TRPL data traces, all collected at the same arbitrary location on a thin film of $(FAPbI_3)_{0.85}(MAPbBr_3)_{0.15}$, fitted with both a single exponential (red dotted lines) and a double exponential (green dotted lines) fit. **D**-**F** TRPL data traces, all collected at a second arbitrary location on the same thin film of $(FAPbI_3)_{0.85}(MAPbBr_3)_{0.15}$.

or even between points in the same scan, and the C parameter appears to be difficult for the software to optimize without a good starting point. For simplicity, the TRPL mapping software was therefore programmed to fit the decay traces to the function:

$$y(t) = A_1 e^{B_1 t} + A_2 e^{B_2 t} \tag{4.1}$$

where A_1 and A_2 are the intensity of the fast and slow components of the exponential decay respectively. $B_1 = -1/\tau_1$ and $B_2 = -1/\tau_2$, where τ_1 and τ_2 are the characteristic lifetimes of the fast and slow decay components respectively.

From the double exponential fits, the software generates colour maps of A_1, τ_1, A_2 and τ_2 which can be viewed in real time as the scan progresses, enabling the experimenter to terminate the scan if problems occur—keeping in mind that the maps are not background-corrected at this stage. Once the map is complete, the raw data obtained at each scan point is re-fitted during post-processing to the equation:

$$y(t) = A_1 e^{B_1 t} + A_2 e^{B_2 t} + C \tag{4.2}$$

where C is a constant which accounts for the noise background in the data. From here, a number of routes of data analysis can be carried out, as detailed in full in Section 4.3.1.

4.2.5 Calibration and Testing

The laser spot size is the key limiting factor for the spatial resolution of the system. The step size used for the 2D maps will be determined by this, as progressing in smaller steps than the laser itself can resolve will result in inaccurate data. In order to measure the spot size, I used a calibration slide with a 1 mm ruler separated into 10 μm divisions. I took a series of photomicrographs of these surfaces with the laser focussed onto them. Figure 4.5**A** shows the calibration ruler as imaged by the white light microscope, where the smaller sub-divisions are 10 μm wide. This image was used to obtain a value for pixels/μm (applicable to all images with the same pixel dimensions as the image of the ruler, which encompasses all microscope images presented in this thesis). Figure 4.5**B**-**C** show two microscope images of the focussed laser spot, which were measured using the pixels/μm value to estimate the size of the focussed laser spot. Figure 4.5**D** shows a zoomed in version of the laser spot from Figure 4.5**C**. Figure 4.5**D** shows that the focussed laser spot creates an Airy pattern,[17] consisting of a central disk of width $\sim$ 1.5 μm, surrounded by a secondary disk of total width $\sim$ 3 μm. The laser spot in Figure 4.5**B** has similar dimensions, with an inner disk of 1.67 μm and a secondary

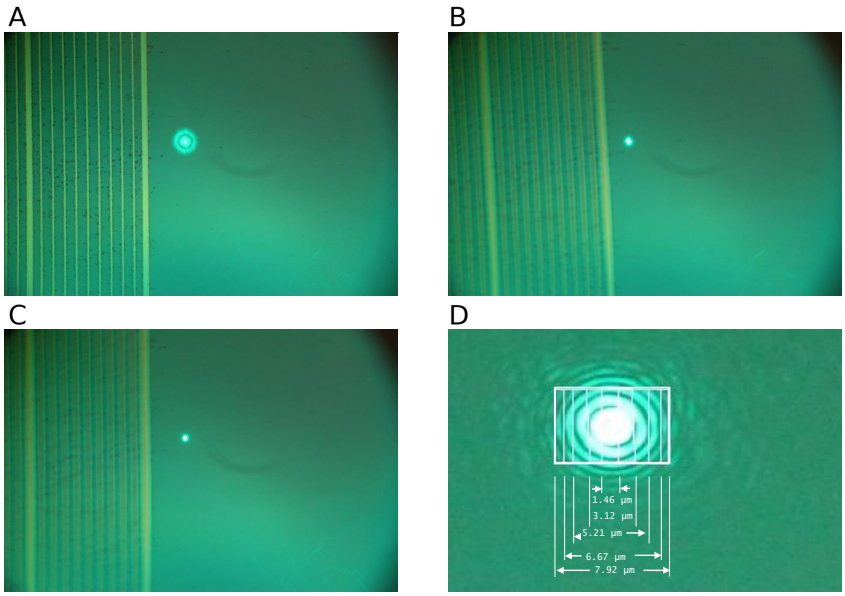

Figure 4.5: **A** A microscope image of the calibration ruler, with each sub-division representing 10 µm. **B**-**C** Microscope images of two different attempts at focussing the laser on the surface of the calibration slide. **D** A zoomed-in microscope image of the focussed laser spot in **C**, showing the approximate diameters of the rings in the Airy pattern, as calculated by finding the pixels/µm value for the image.

disk of 3.43 µm diameter. The Airy pattern in Figure 4.5**D** contains several rings, with a maximum outer radius of $\sim$ 8 µm. If we take the diameter of the Airy disk to be 1.46 µm, then the maps will require step sizes of $\geqslant 2\mu$m. Additional fluorescence from the Airy pattern must be kept in mind when analysing the maps, however if the single-photon statistics condition for TCSPC is being met anyway, it is likely that fluorescence emissions will come from the central disk where most of the laser power is focussed.

For TCSPC measurements, it is important to use the lowest power possible to ensure single-photon statistics, while maintaining an adequate signal-to-noise ratio (SNR). As described in Section 3.4.1, single-photon statistics can generally be ensured by keeping the count rate at the correct level, therefore this was done individually on each sample before mapping, to determine the power setting needed.

The width of the histogram time bins is a key measurement parameter that needs to be carefully chosen. The smallest bin width available for this system is 25 ps, and it has already been established that it is not sensible to choose a bin width $>$ 100 ps (see Section 3.4.1). If the 25 ps bin width was chosen, fits to the data may be more accurate, due to the higher density of points that can be used to inform the fit. However, there is a trade off involved in the selection of this measurement parameter, as a smaller time bin

will mean that there will statistically fewer photon events logged in each bin, therefore leading to a lower SNR.

The integration time is another key factor in determining the SNR of the TCSPC data. It needs to be long enough to ensure sufficient fluorescence signal, but in these experiments it is limited by the overall scan time. Maps will need to be at least 50×30 steps, which is 1500 scan points in total. At an integration time of 30 s, a scan of 50×30 steps will take 12.5 hours. The data in Figure A.1 shows the dependence of the PL intensity parameters A_1 and A_2 on the integration time, and highlights that a 60 s integration time almost doubles the PL intensity compared to a 30 s integration. However, if the integration time were to be doubled, this would push the total scan time up to 25 hours (and in reality it will be longer than this due to the short downtime the software waits between each scan point), a time period over which the sample may face degradation issues even when held under vacuum. Figure 4.6 also shows that it would not be sensible to use any integration time under 30 s, as this significantly reduces the PL intensity and the R^2 value for the double exponential fit. Therefore all maps presented in this thesis (Chapter 5) have been carried out with a 30 s integration time. The repetition rate for the pulsed laser was kept at 2.5 MHz throughout all experiments presented in Chapter 5. Although a higher repetition rate would have potentially increased the fluorescence signal without compromising single-photon statistics, this low repetition rate provides us with a time delay of $<$ 400 ns over which to track the fluorescence decay, which is favourable as we expect fluorescence lifetimes to reach hundreds of ns for hybrid lead halide perovskites.[18,19]

The laser driver (PDL 800-B) allows the output power of the laser diode to be manually varied by means of a potentiometer, controlled by a dial on the front panel, which changes the driving current to vary power output. The actual power output will depend on the laser diode used. Therefore the output power corresponding to different power settings must be measured. I measured the average laser power transmitted to the sample (via all optics) for a number of different settings on the dial, as shown in Figure 4.6**A**, where the number on the x-axis simply refers to the number on the dial, which is an arbitrary decimal number. I measured the power reaching the back aperture

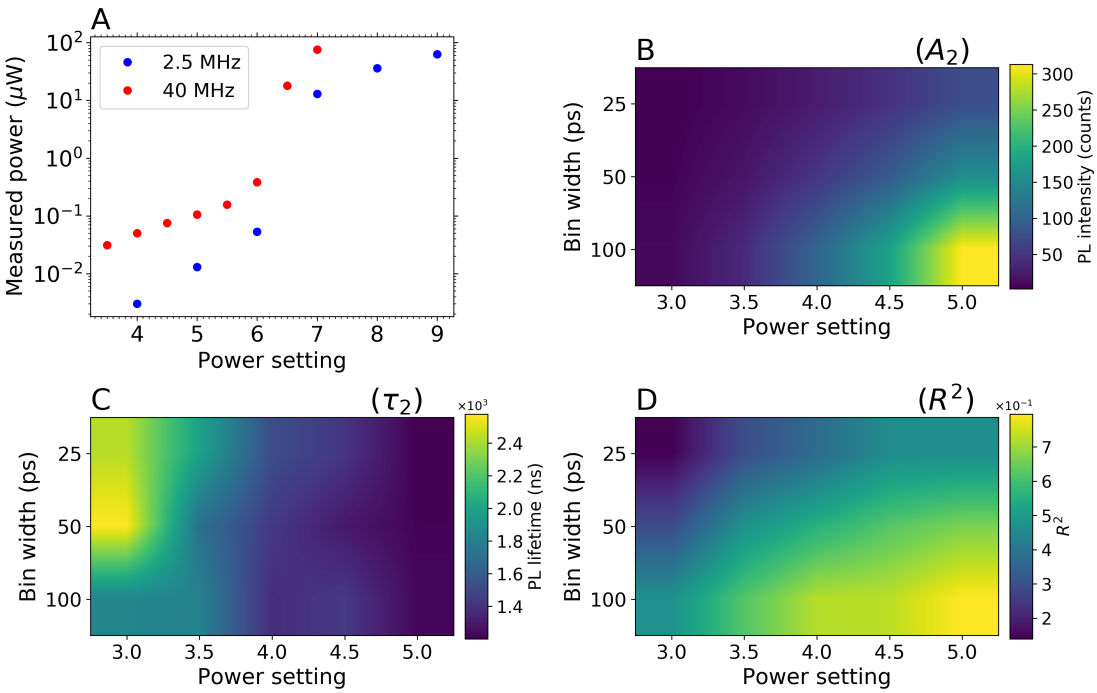

Figure 4.6: **A** Measured laser power as a function of the potentiometer setting on the PDL-800B laser driver, measured at laser repetition rates of 2.5 MHz and 40 MHz. Colour maps of the fitting parameters **B** A_2 (PL intensity), **C** τ_2 (PL lifetime) and **D** R^2 (coefficient of determination) for a double exponential fit to TRPL data taken at varying power setting and histogram bin width.

of the microscope objective, by removing the objective and measuring the average power at the position where the objective would be. It had proven too difficult and unreliable to measure the power of the focussed spot at the sample position, therefore this measurement does not take into account any losses in microscope objective. Figure 4.6**A** shows that the power increases exponentially as the power setting increases, and this trend is seen for both the 40 MHz and 2.5 MHz repetition rates. Generally speaking, measurements taken at 40 MHz are approximately one order of magnitude larger than those taken at 2.5 MHz, which is not far from what is expected given that there has been a 1/16 reduction in repetition rate.

There is a large ramp-up in power when the potentiometer is set to 7.0, which is presumably to do with the dependence of the laser power on driving current in this particular laser diode. However, this is not of too much concern as the power should never need to be set much higher than $\sim$ 5.0, based on several test measurements, such as those in Figure 4.4, which were taken at a power setting of 4.0—here it can be seen that this power setting provides adequate signal-to-noise ratio. This is confirmed

by Figure 4.6**B**-**D**, where the power setting and histogram bin width have been varied and the intensity and time constant of the slow decay component ($A_2 e^{-\frac{t}{\tau_2}}$), along with the R^2 value for the fit, have been calculated. The shows that any power setting of $\sim$ 4.0 gives a slow component PL intensity A_2 on the order of 100s of counts, which suggests an acceptable SNR for this application. This is further evidenced by the R^2 values (Figure 4.6**D**), which increase with both the increase in power and increase in bin width.

The incident laser fluence (ϕ) for the focussed spot can be calculated using the relation:

$$\phi = \frac{P_{AVE}}{f_{pulse} A} \tag{4.3}$$

where P_{AVE} is the measured average laser power (which can be found from Figure 4.6**A**), f_{pulse} is the pulse frequency of the laser, and $A = \pi r^2$ is the area of the focussed laser spot, with r being the radius of the spot (central Gaussian peak). r is determined for each individual map by analysing photomicrographs of the laser spot on the surface of the sample.

Therefore all maps in this thesis are carried out with the following measurement parameters: 30 s integration time, 100 ps bin width and power setting 4.0, which corresponds to $\sim$ 3-30 nW, depending on the alignment of the laser.

4.3 Experimental Proof of Concept

In order to obtain basic proof of concept for the functionality of the TRPL mapping system, a number of initial scans were taken. First I took a spin-coated sample of the fluorescent polymer BODIPY, and used a razor blade to scratch off a line of material of approximately 30 μm in width. I used this scratch to calibrate the coarse focus of the white light microscope, before carrying out a test scan on an area spanning the scratch. This was in order to check the ability of the system to differentiate between areas of high and low signal, and get an idea of the spatial resolution it can achieve when doing

this. A TRPL map scan was carried out spanning this scratch, at a scan size of 80 × 60 steps, with a step size of 2 µm, resulting in maps representing an area of 160 × 120 µm on the sample surface. This area is shown in Figure 4.7.

The results of this scan are shown Figure 4.8. As discussed in Section 4.2.5, the

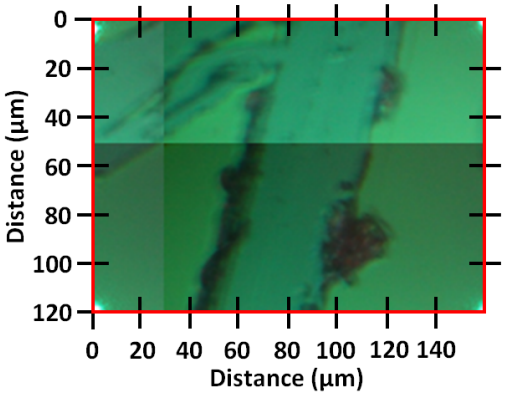

Figure 4.7: A microscope image of the surface of a BODIPY thin film - the red square shows the 160 × 120 µm area on the surface which was mapped using the TRPL imaging system.

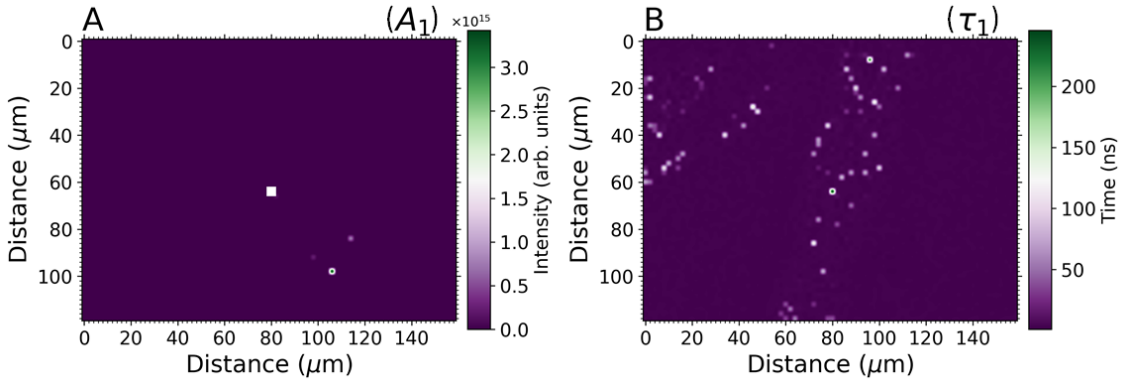

Figure 4.8: Colourmaps of the double exponential fitting parameters **A** A_1 and **B** τ_1, as extracted from fits to the TRPL data for a map of size 160 × 120 µm on the surface of a BODIPY sample (area marked in red Figure 4.7).

TRPL mapping system generates maps of four quantities: A_1, τ_1, A_2 and τ_2, as obtained from a fit to the TRPL data at each scan point of the functional form $y = A_1 e^{-t/\tau_1} + A_2 e^{-t/\tau_2}$. Here only the parameters A_1 and τ_1 have been plotted, as the BODIPY films are unlikely to have any long-time TRPL decay components on the order of 100s of ns. The double exponential fitting protocol is not optimal for this data, and therefore the values of A_1 and τ_1 may not be totally accurate. However this data is only intended as a proof of concept that the mapping system can differentiate between the scratched and unscratched areas in the scan, therefore the extracted parameters A_1 and τ_1 should be sufficient to make this differentiation. The only post-processing that has been applied to Figure 4.8 is that negative values have been removed from the maps (represented by

white squares in the colourmaps).

However, it is clear from Figure 4.8 that some post-processing is required, as the maps are predominantly dark. This suggests that there are some values in each map

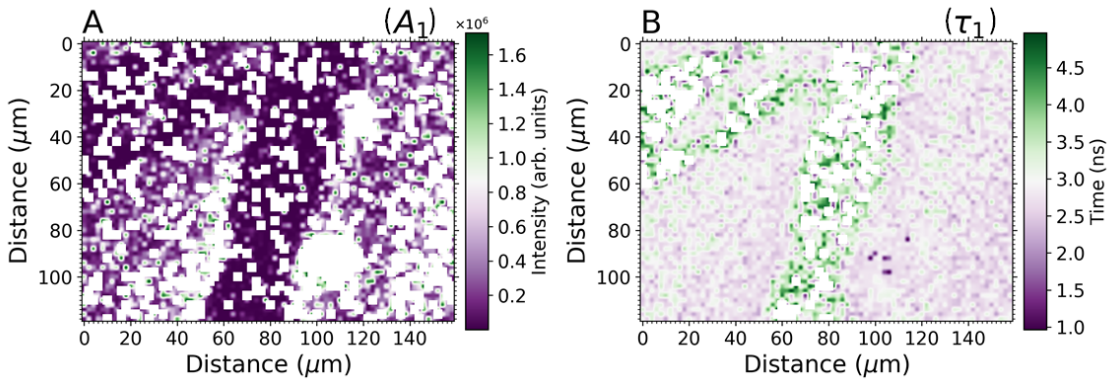

Figure 4.9: Colourmaps of the double exponential fitting parameters **A** A_1 and **B** τ_1 for a 160 × 120 μm TRPL map on the surface of a BODIPY sample (area marked in red Figure 4.7), after post-processing has been applied to remove outliers.

which are so much larger (or smaller) than the majority of the values that they skew the colour scale. Such values will need to be removed in order to evaluate the maps. Here, this was done by removing statistical outliers from the matrix of each of the parameters A_1 and τ_1. The simplest way to determine statistical outliers in a dataset is to find the Z-score for each value in the dataset. The Z-score is defined as the number of standard deviations from the mean at which a given value lies. However, some of the distributions in Figure 4.8 are skewed by a small subset of values which are much larger than the majority of the dataset, which will reduce the effectiveness of using the Z-score to determine whether values are outliers. Therefore a modified Z-score can be calculated, which instead represents the number of median absolute deviations (MADs) from the median of the dataset at which a given point lies. The MAD is defined as the median of the absolute deviations from the median of the data. For a given value X_i in a univariate dataset X, the modified Z-score M_i is calculated thus:

$$M_i = \frac{0.6745(X - \tilde{X})}{\text{MAD}} \tag{4.4}$$

where MAD is the the median absolute deviation of X and is defined as:

$$\text{MAD} = \text{median}(|X_i - \tilde{X}|) \tag{4.5}$$

where $\tilde{X}$ is the median of X.

In order to remove outliers from the maps in Figure 4.8, the Z-score was calculated for all data points in the two parameter matrices, and all points with $|M_i|>$ 5 MADs were removed (or more precisely, set to NaN such that they appear white in the maps). In Figure 4.9, modified maps with outliers outside 5 MADs removed are plotted, which has allowed more map features to be identified. Here it is clear that the system can differentiate between the polymer material and the scratched area, as it generates much lower values for the intensity component A_1 (Figure 4.9**A**) within the scratched area than outside of it, where the material is intact. In Figure 4.9**B**, much longer lifetimes are observed in the scratched area than in the unscratched area. Although it is unclear why the extracted lifetimes would be longer where the material has been removed, this nevertheless shows that the system is able to differentiate between areas of the material with different properties.

The TRPL maps appear to be able to resolve the edge of the scratch to within a few microns, which is consistent with the observation that the majority of the laser power is focussed into the Airy disk (diameter $\sim$ 1.5 μm) and the first Airy ring (outer diameter $\sim$ 3 μm). As the spot size varies slightly between maps due to variations in laser alignment, laser power and scattering effects due to surface morphology, the spot size was measured individually for each map taken, to determine the minimum spatial resolution for each map.

4.3.1 Preliminary Data from Perovskite Thin Films

Once a preliminary proof of concept had been obtained for the system, it was important to confirm that the system was suitable for mapping the perovskite materials for which it was designed, and that the results produced were useful and physically meaningful. A thin film sample of $(FAPbI_3)_{0.85}(MAPbBr_3)_{0.15}$ was fabricated via the method shown in Section 3.1.1, and a TRPL mapping scan was carried out of the surface of this sample.

The scan area was 120 µm by 128 µm, carried out in steps of 4 µm. The scanned area on the surface of the sample is shown in Figure 4.10.

The raw TRPL data collected from every point on the raster scan was analysed by fitting the data to Equation (4.2), to produce the maps shown in Figure 4.11, which

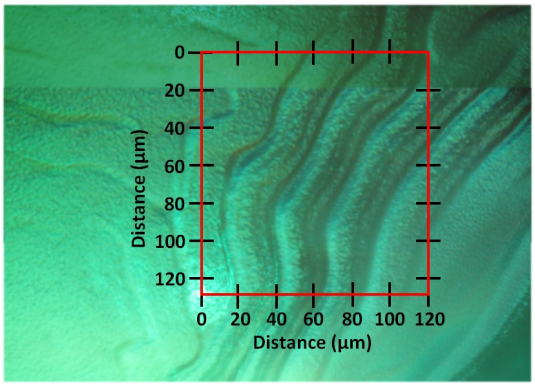

Figure 4.10: A microscope image of the surface of a $(FAPbI_3)_{0.85}(MAPbBr_3)_{0.15}$ film - the red square shows the 120 × 128 µm area on the surface which was mapped using the TRPL imaging system.

are maps of the following 4 parameters: A_1, the intensity of the fast component of the double exponential decay curve; τ_1, the characteristic lifetime of the fast component; A_2, the intensity of the slow component of the double exponential decay curve; and τ_2, the characteristic lifetime of the slow component. In Figure 4.11**A**, it can be seen that the colourmap of the A_1 parameter is predominantly dark, which appears to be a result of the presence of a small number of extremely large values on the order of 10^7. The system is very unlikely to have collected data with such a large intensity component, as the integration time for collection of the TRPL data at each point on the map was only 30 seconds, and a typical signal level for this type of perovskite film over a 30 s integration time is on the order of $10^1 - 10^2$ counts (see Figure 4.4 in Section 4.2.4). Similarly, the map of τ_1 in Figure 4.11**B** is saturated as a result of the comparatively large value $\tau_1 = 809$ ns, which is very unlikely to reflect the characteristic lifetime of the fast decay component, which we expect to span 10s of ns based on the data in Figure 4.4. This leads to the suggestion that such values of A_1 and τ_1 are erroneous i.e. they do not describe the intensity and time constant of the fast decay component of the double exponential fit.

Such erroneous values may be the result of errors encountered in the optimisation of the fit parameter. However they may also simply originate from anomalous data, e.g. data which is too noisy or where no TRPL trace has been collected. Regardless of origin,

it is clear that there will be some values in the maps which are anomalous and do not represent the properties of the PL decay. To investigate the presence and origin of such values, several routes of analysis have been explored:

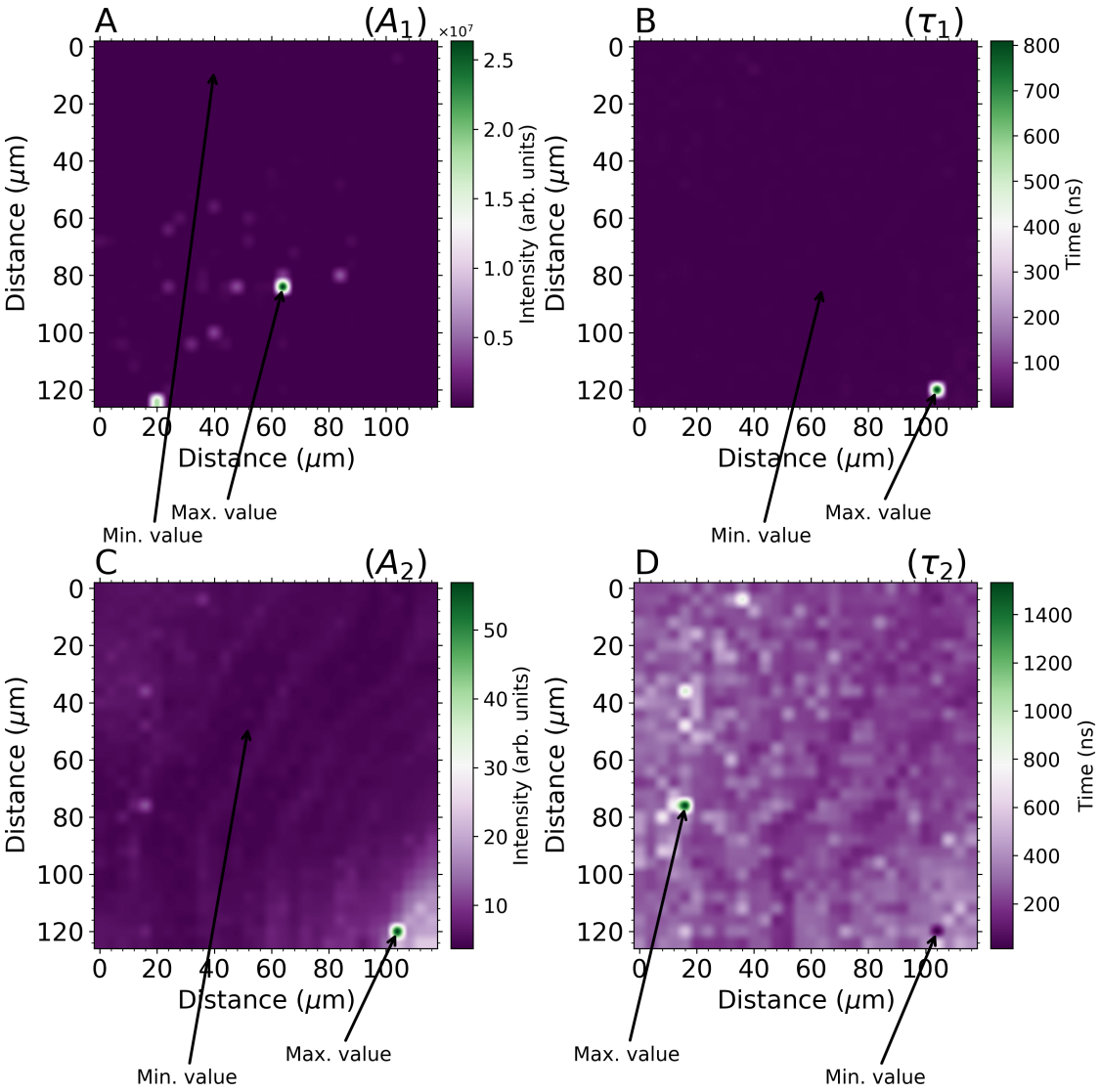

Figure 4.11: Raw colourmaps of the double exponential fitting parameters **A** A_1, **B** τ_1, **C** A_2 and **D** τ_2, as extracted from fits to the TRPL data for a map of size 120 $\times$ 128 µm on the surface of a $(FAPbI_3)_{0.85}(MAPbBr_3)_{0.15}$ sample (area marked in red Figure 4.10), after background correction but prior to any post-processing (for example outlier removal) being applied to the data.

- **Outlier analysis:** It may be possible to identify artifacts based on whether a given value is an outlier in the distribution of parameter values. Therefore outlier detection has been carried out for each set of parameter values. For all parameter values, a median Z-score, M_i, has been calculated using Equation (4.4). For the purpose of this analysis, values with $M_i > 3$ are classified as outliers.

- **Inspection of raw data:** The raw data resulting in the 'extreme' (maximum and minimum) values of all four parameters have been plotted to determine if the form of the raw data leads to anomalous values. In addition, the raw data resulting in parameter values which have been detected as outliers ($M_i > 3$) has also been plotted, to verify the efficacy of outlier detection at identifying invalid parameter values.

- **Investigating relationships between parameters:** Correlations between particular parameters may suggest sets of erroneous values, therefore the relationships between parameter distributions have been examined.

- **Investigating uncertainty on extracted parameters:** To gain added insight into the validity of extracted parameter values, a fractional uncertainty $\Delta x/x$ has also been calculated for each parameter, where x is the parameter value and Δx is the standard deviation error on the fitted parameter. The standard deviation error on each parameter has been determined by taking the square root of the diagonalised covariance matrix of the fit, and gives a measure of the uncertainty in each parameter value.

Parameters $\mathbf{A_1}$ and $\boldsymbol{\tau_1}$

To investigate the origin of the 'extreme' values of the A_1 and τ_1 parameters (e.g. $A_1 \sim 10^7$, $\tau_1 = 809$ ns), the TRPL data corresponding to the minimum and maximum extracted values of A_1 and τ_1 is plotted in Figure 4.12. The TRPL data in these plots has an intensity peak at $t \approx 30$ ns, which then decays over the next 10-20 ns. This should have been fitted to the fast decay component $A_1 e^{-t/\tau_1}$, with intensity parameter A_1 and lifetime parameter τ_1. The PL then undergoes a slow decay which occurs on much longer timescales than the initial fast decay, covering the entire 400 ns time window, which we suspect may correspond to first order trap-assisted recombination.[20] This decay component should have been fitted with the slow component of the double exponential model ($A_2 e^{-\frac{t}{\tau_2}}$), therefore the parameter A_2 represents the maximum PL intensity of the slow decay component and τ_2 represents its charcteristic lifetime.

For all curves in Figure 4.12, the portion of the data representing the fast component

is quite poorly resolved, in other words there are too few data points within the time window over which the fast decay occurs and the signal-to-noise ratio (SNR) is low—hence, the program may not be able to extract A_1 and τ_1 accurately. This is demonstrated in

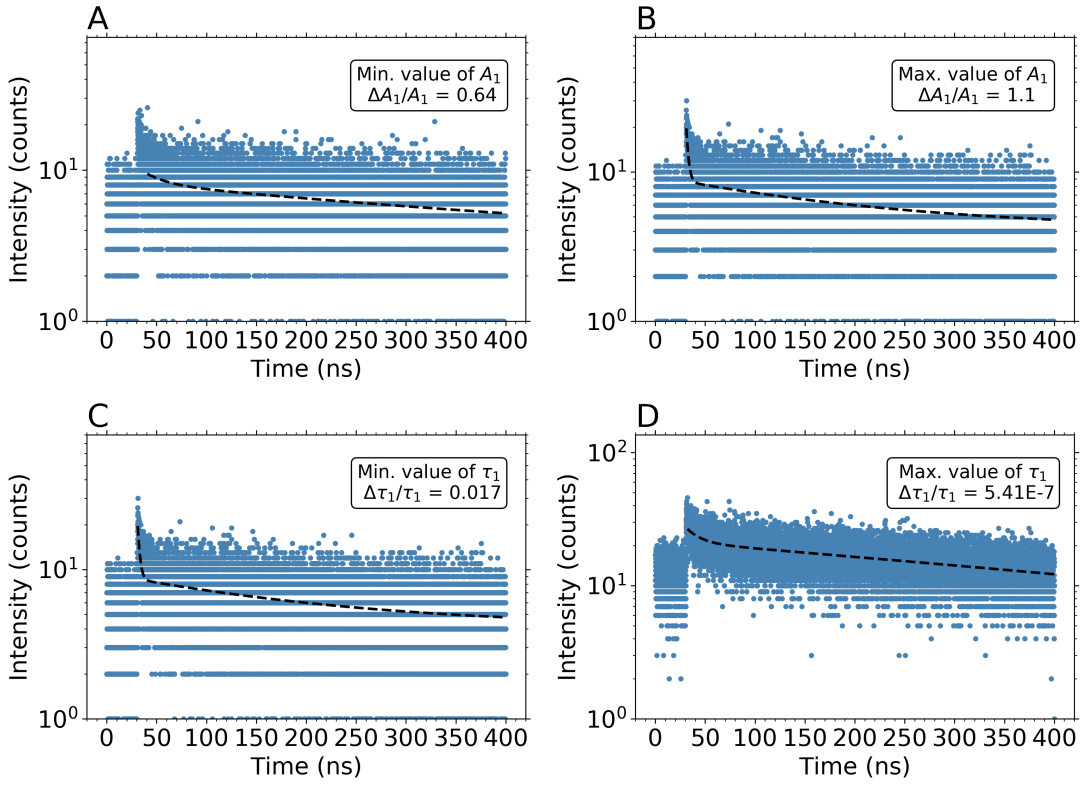

Figure 4.12: TRPL traces resulting in the maximum and minimum values of the fitting parameters A_1 (**A**-**B**) and τ_1 (**C**-**D**), for the TRPL maps displayed in Figure 4.11.

Figure 4.12**A**, where it is shown that the minimum value of A_1 has a large fractional uncertainty ($\Delta A_1/A_1$). The R^2 value of this fit is very low ($R^2 \approx 0.13$), although it is important to note here that R^2 does not exceed 0.5 anywhere in these maps (as shown in Figure A.5 in Appendix A). Hence any R^2 value quoted in this chapter is only used as a comparative measure, in order to compare the goodness of fit between different datasets. These low R^2 values are no doubt due to the low SNR in the data collected for these maps, as seen in Figure 4.12, which will lead to large residuals and therefore a small R^2 in all cases. In Figure 4.12**D**, it can be seen that the maximum value of τ_1 ($\tau_{1_{MAX}} = 809$ ns) appears to be the result of a relatively good fit to the data ($R^2 \approx 0.35$), and indeed the fractional uncertainty on $\tau_{1_{MAX}}$ is very low. Upon inspection of Figure 4.14**B** and Figure 4.14**C**, which plot the TRPL traces yielding the maximum value of A_2 and the minimum value of τ_2, respectively, it is clear that the data plotted in these two plots is the identical to the data displayed in Figure 4.12**D**. This TRPL trace yields the following

parameter values: $A_1 = 25.0$; $\tau_1 = 809$ ns; $A_2 = 56.9$; and $\tau_2 = 14.0$ ns. It appears that this particular trace has been fitted in the opposite way to what is expected: the paramaters A_1 and τ_1 appear to describe the behaviour of the slow decay component, and the parameters A_2 and τ_2 describe the fast component. This peculiarity is most likely due to the fact that the fit parameters were not well optimised for this particular dataset. This anomaly was corrected by swapping the A_1 value for the A_2 value at this matrix position, and the same was done for the τ_1 and τ_2. Such anomalous values must be identified when analysing the maps, and this highlights the importance of inspecting the raw data to check validity of parameter values.

As shown in Figure 4.12**B**, the maximum value of A_1 ($A_{1_{MAX}} = 2.64 \times 10^7$) has an even larger fractional uncertainty, $\Delta A_1/A_1 = 1.12$. Interestingly, it can be seen that Figure 4.12**B** and Figure 4.12**C** plot the same set of TRPL data, revealing that the scan point at which the maximum value of A_1 was obtained also yielded the minimum value of τ_1. This evidence suggests that unusually large values of A_1 ($A_1 \gtrsim 10^5$) are a result of the fact that the faster component of the double exponential has not been fitted accurately, resulting in an arbitrarily large A_1 and an arbitrarily small τ_1.

To investigate this effect, the relationship between A_1 and τ_1 is examined. In Figure 4.13, all parameters have been plotted against all other parameters, with A_1 being plotted against τ_1 in Figure 4.13**A**. If a there is large subset of arbitrarily large A_1 values correpondng to arbitrarily small τ_2 values, we would expect to see a negative correlation between A_1 and τ_1 for large A_1. Figure 4.13**A** indeed shows this expected effect, and therefore it follows that such values of A_1 and τ_1 are invalid and can be removed from the datasets. The plots in Figure 4.13**B**-**E** show no overall correlation between A_1/τ_1 and the other parameters, therefore no further problematic areas of the parameter distributions can be identified from these plots.

The validity of A_1 and τ_1 values is further discussed in Appendix A, where the raw data leading to outlying values of A_1 and τ_1 is inspected and the uncertainties are examined. The analysis in Appendix A showed that A_1 values with $M_i > 3$ and their corresponding τ_1 values are artifacts. As discussed in Appendix A, once these values have been removed the maps are very sparse and the remaining data points bear no

correlation to the sample surface (Figure A.8). In addition, there are some A_1 values with $M_i < 3$ which appear to be artifacts. Therefore it is not trivial to ascertain the

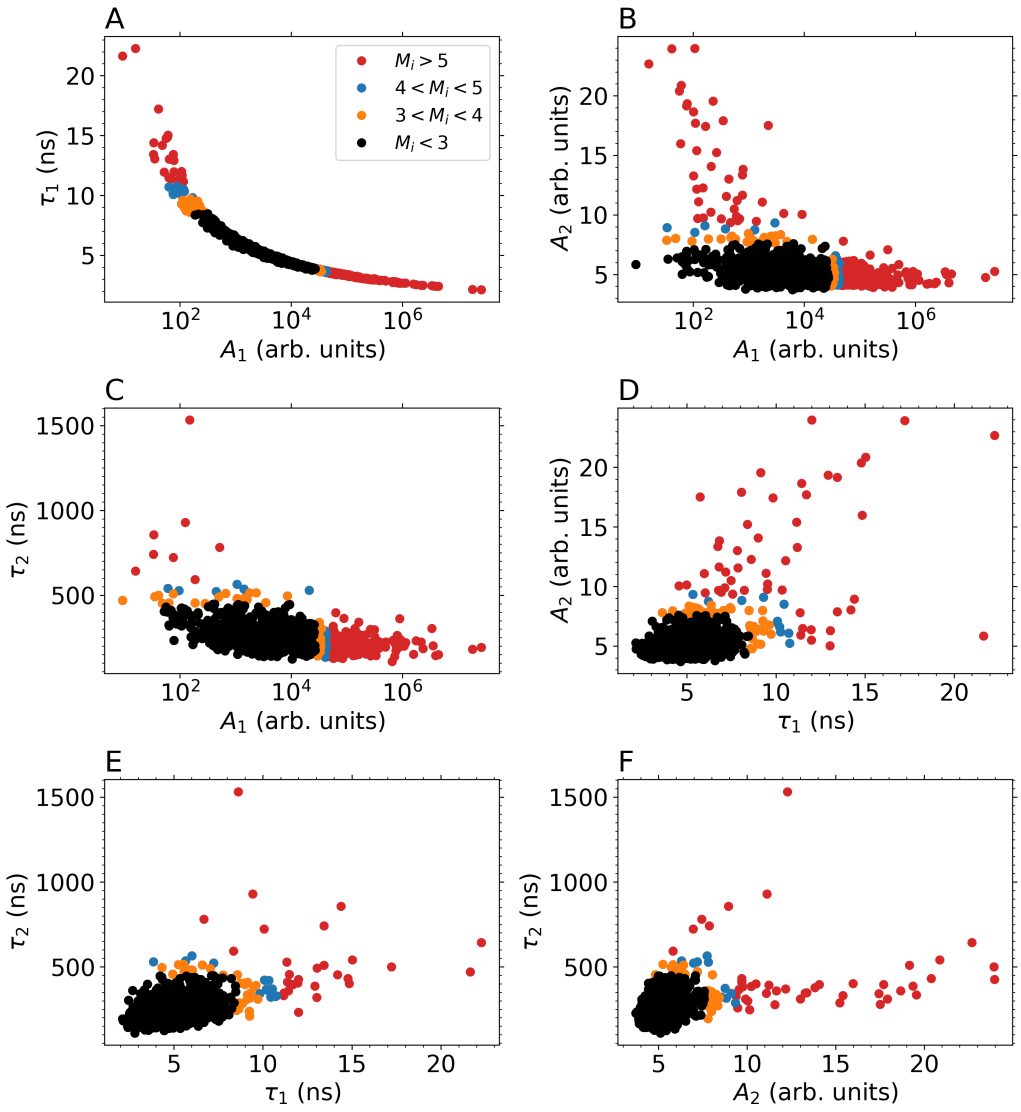

Figure 4.13: Relationships between the fit parameters **A** A_1 and τ_1, **B** A_1 and A_2, **C** A_1 and τ_2, **D** τ_1 and A_2, **E** τ_1 and τ_2 and **F** A_2 and τ_2, for the TRPL maps displayed in Figure 4.11.

validity of A_1/τ_1 values, which is not surprising considering that the fast decay component of the data is generally poorly resolved (see Figure 4.12). For the above reasons, A_1 and τ_1 values will not be presented in this thesis.

Parameters A_2 and τ_2

Returning briefly to Figure 4.11, it can be seen that the maps of the fit parameters A_2 and τ_2 (the intensity and time constant of the slow decay component) appear to correlate to some extent with the morphology seen in Figure 4.10. Based on my findings

in Section 4.2.5, this slow component appears to be the dominant PL decay process,

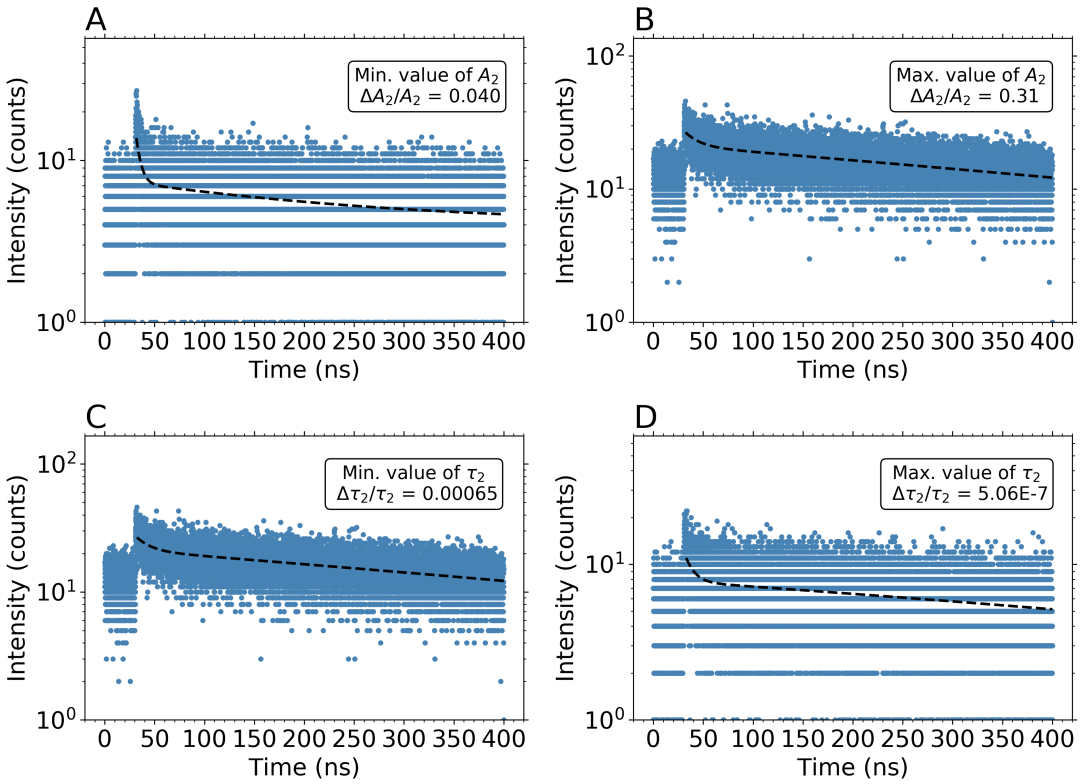

Figure 4.14: TRPL traces resulting in the maximum and minimum values of the fitting parameters A_2 (**A**-**B**) and τ_2 (**C**-**D**), for the TRPL maps displayed in Figure 4.11.

therefore these parameters are of utmost interest. Here I discuss the origin of extreme and outlying values of these parameters and the detection of artifacts.

The raw data in Figure 4.14**A** yielded the minimum value of $A_{2_{MIN}} = 3.71$, $\Delta A_{2_{MIN}}/A_{2_{MIN}} = 0.04$, which is very small, suggesting that this minimum value of A_2 is not likely to be an artifact. The raw data in Figure 4.14**B** yielded the maximum value of A_2 ($A_{2_{MAX}} = 56.9$), which has already been identified as an incorrectly assigned value and this error has been corrected.

The plot of A_2 vs τ_2 in Figure 4.13**F** shows a weak positive correlation between the two parameters at values of A_2 larger than ~ 10, where values of A_2 are statistical outliers ($M_i > 5$). This may suggest a fitting artifact of some kind or it may simply be related to a particular physical process in the film. To investigate this, TRPL traces resulting in values of A_2 classified as statistical outliers are plotted in Figure 4.15**A**-**C**. The fractional uncertainty on the resultant A_2 values is $\Delta A_2/A_2 = 0.0666$, 0.0679, and 0.0279 for the Z-score ranges $M_i > 5$, $4 < M_i < 5$ and $3 < M_i < 4$, respectively. This suggests that most outlying parameters of A_2 are in fact fairly well optimised and are

therefore not likely to be fitting artifacts. Therefore the weak correlation in Figure 4.13**F**

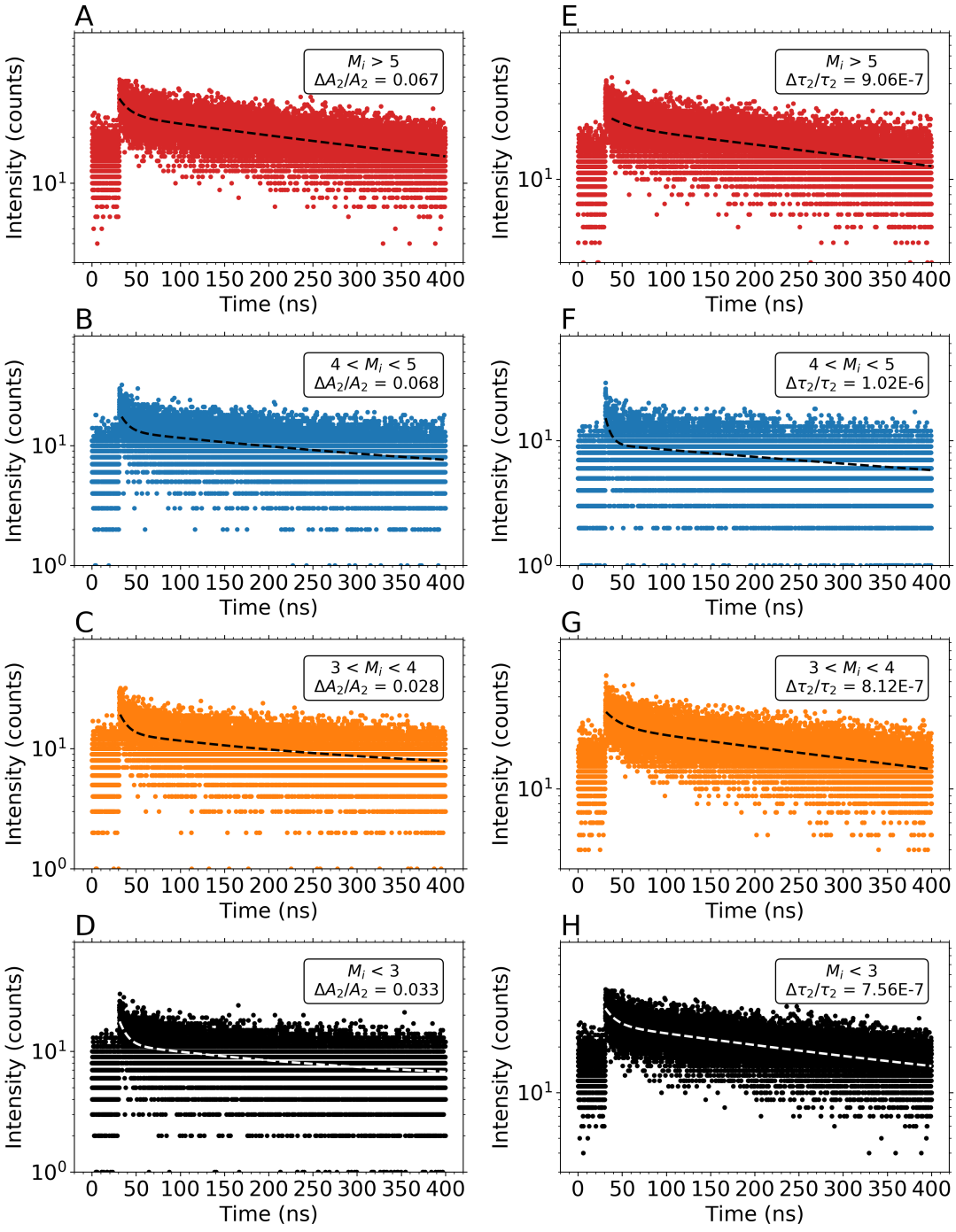

Figure 4.15: TRPL traces resulting in statistically outlying values of the fitting parameters A_2 (**A**-**D**) and τ_2 (**E**-**H**), for the TRPL maps displayed in Figure 4.11.

is likely to be the result of a physical process. Figure 4.15**D** also confirms that non-outlying values of A_2 are generated by a good fit to the data, and these pieces of evidence suggests that none of the A_2 values generated by the system are artifacts.

The minimum extracted value of τ_2, whose corresponding data is plotted in Figure 4.14**C**, has already been identified as an incorrectly assigned value and this error has been corrected. Figure 4.14**D** shows the trace resulting in the maximum value of τ_2. This trace yields the value $\tau_{2_{MAX}} = 1532$ ns, with $\Delta\tau_2/\tau_2 = 5.06 \times 10^{-7}$. Figure A.7**D** shows that this value of $\Delta\tau_2/\tau_2$ is in fact quite low compared to errors for other values of this parameter, which are mostly on the order of 10^{-6}. This suggests that $\tau_{2_{MAX}}$ is not an artifact, despite being much larger than expected.

In Figure 4.15**E**-**G**, the data resulting in outlying values of τ_2 is plotted, and this shows that these so-called outlier values are in fact associated with a relatively small fractional uncertainty, suggesting that outlying values of τ_2, generally speaking, are not artifacts and should remain in the maps. An example curve yielding a value of τ_2 with $M_i < 3$ is plotted in Figure 4.15**B**, and this data appears to have been fitted with reasonable success, exhibiting a similarly small fractional uncertainty to those observed in the 'outlier' values, and confirming that the majority of the values in the τ_2 distribution are likely to be valid.

Therefore the maps for A_2 and τ_2 will be displayed with no values removed, however this analysis has highlighted the need to carefully assess the validity of parameter values for each map that is collected. To achieve this, it is necessary to combine outlier detection with the inspection of raw data and the examination of parameter uncertainties.

4.4 Conclusions

This section shows that I have successfully developed a time-resolved PL mapping system, which is capable of creating PL lifetime and intensity maps, at a minimum spatial resolution of 2 μm. In the case of most hybrid perovskite thin films, a resolution of a few hundred nanometres would be desirable to resolve individual grains and to therefore distinguish between grain boundaries and grain interiors. Therefore, in this thesis I will focus on film morphology on a larger scale, investigating features on the order of tens of microns in size. The aim of such studies will be to investigate how such features are affected by processing conditions and in turn how this affects the optical properties of the material.

My preliminary data analysis shows that the most useful information about fluorescence intensity and lifetime is in the slow decay component (A_2e^{-t/τ_2}), where the extracted PL intensities and lifetimes clearly correlate with the surface morphology of the sample. Therefore the analysis presented in this thesis will focus on the parameters A_2 and τ_2.

References

[1] G. E. Eperon, S. N. Habisreutinger, T. Leijtens, B. J. Bruijnaers, J. J. van Franeker, D. W. DeQuilettes, S. Pathak, R. J. Sutton, G. Grancini, D. S. Ginger, R. A. J. Janssen, A. Petrozza, H. J. Snaith, *ACS Nano* **2015**, *9*, 9380.

[2] A. Osherov, E. M. Hutter, K. Galkowski, R. Brenes, D. K. Maude, R. J. Nicholas, P. Plochocka, V. Bulović, T. J. Savenije, S. D. Stranks, *Advanced Materials* **2016**, *28*, 10757.

[3] D. W. DeQuilettes, W. Zhang, V. M. Burlakov, D. J. Graham, T. Leijtens, A. Osherov, V. Bulović, H. J. Snaith, D. S. Ginger, S. D. Stranks, *Nature Communications* **2016**, *7*, 11683.

[4] S. Wieghold, J. P. Correa-Baena, L. Nienhaus, S. Sun, K. E. Shulenberger, Z. Liu, J. S. Tresback, S. S. Shin, M. G. Bawendi, T. Buonassisi, *ACS Applied Energy Materials* **2018**, *1*, 6801.

[5] X. Wen, R. Sheng, A. W. Y. Ho-Baillie, A. Benda, S. Woo, Q. Ma, S. Huang, M. A. Green, *The journal of physical chemistry letters* **2014**, *5*, 3849.

[6] D. W. de Quilettes, S. M. Vorpahl, S. D. Stranks, H. Nagaoka, G. E. Eperon, M. E. Ziffer, H. J. Snaith, D. S. Ginger, *Science* **2015**, *348*, 683.

[7] R. Sheng, X. Wen, S. Huang, X. Hao, S. Chen, Y. Jiang, X. Deng, M. A. Green, A. W. Ho-Baillie, *Nanoscale* **2016**, *8*, 1926.

[8] G. Namkoong, H. J. Jeong, A. Mamun, H. Byun, D. Demuth, M. S. Jeong, *Solar Energy Materials and Solar Cells* **2016**, *155*, 134.

[9] G. W. P. Adhyaksa, S. Brittman, H. Āboliņš, A. Lof, X. Li, J. D. Keelor, Y. Luo, T. Duevski, R. M. A. Heeren, S. R. Ellis, D. P. Fenning, E. C. Garnett, *Advanced Materials* **2018**, *30*, 1804792.

[10] G. Niu, W. Li, F. Meng, L. Wang, H. Dong, Y. Qiu, *Journal of Materials Chemistry A* **2014**, *2*, 705.

[11] G. Niu, X. Guo, L. Wang, *Journal of Materials Chemistry A* **2015**, *3*, 8970.

[12] Q. Wang, B. Chen, Y. Liu, Y. Deng, Y. Bai, Q. Dong, J. Huang, *Energy and Environmental Science* **2017**, *10*, 516.

[13] A. Lipson, S. Lipson, H. Lipson, *Optical Physics*, Cambridge University Press, Cambridge, United Kingdom, 4th editio edn., **2010**.

[14] N. Pellet, P. Gao, G. Gregori, T.-Y. Yang, M. K. Nazeeruddin, J. Maier, M. Grätzel, *Angewandte Chemie* **2014**, *126*, 3215.

[15] C. C. Chen, S. H. Chang, L. C. Chen, F. S. Kao, H. M. Cheng, S. C. Yeh, C. T. Chen, W. T. Wu, Z. L. Tseng, C. L. Chuang, C. G. Wu, *Solar Energy* **2016**, *134*, 445.

[16] A. Koehler, *Journal of the Royal Microscopical Society* **1894**, *14*, 261.

[17] G. B. Airy, *Transactions of the Cambridge Philosophical Society* **1835**, *5*, 287.

[18] S. Brittman, G. W. P. Adhyaksa, E. C. Garnett, *MRS Communications* **2015**, *5*, 7.

[19] L. K. Ono, E. J. Juarez-Perez, Y. Qi, *ACS Applied Materials & Interfaces* **2017**, *9*, 30197.

[20] M. B. Johnston, L. M. Herz, *Accounts of Chemical Research* **2016**, *49*, 146.

Chapter 5

Time-Resolved Photoluminescence Mapping Studies on Mixed Cation Mixed Halide Perovskite Thin Films

Note on contributions to this chapter

All work presented in this chapter was carried out by me, with the following exceptions:

- *Dr. James Bishop* fabricated the spray-cast triple cation perovskites and the PV devices based on the same, and carried out the device testing.
- *Dr. Onkar Game* and *Joel Smith* fabricated the spin-coated double and triple cation perovskites tested in this chapter.

5.1 Introduction

The mixed-cation, mixed-halide hybrid perovskite $(FAPbI_3)_{0.85}(MAPbBr_3)_{0.15}$ has garnered much research interest over the past few years due to its excellent PV performance. This particular blend has yielded the best efficiency in the $(FAPbI_3)_x(MAPbBr_3)_{1-x}$ parameter space.[1] It was later found that incorporating a small amount of caesium (Cs) into the A-cation site increased not only the power conversion efficiency but also the stability of the perovskite. Devices made by Saliba and coworkers based on

$Cs_{0.05}FA_{0.79}MA_{0.16}Pb(I_{0.83}Br_{0.17})_3$ reached a stabilised power conversion efficiency (PCE) of 21.1%, and the devices retained 90% of their initial PCE for over 250 hours.[2]

Mixed cation perovskites have been shown to exhibit a great deal of sensitivity to processing conditions in terms of the resulting morphology,[3] and film morphology leads to long-range heterogeneity of PL emission properties on the order of 10s - 100s of μm in hybrid perovskites.[4] It has been postulated that one reason for such heterogeneity may be spatial differences in lattice strain resulting from processing conditions.[5] These strain effects directly influence the macroscopic optical properties and stability of hybrid perovskite films.[3] For example, Jones *et al.*[6] showed that areas of higher lattice strain were associated with shorter fluorescence lifetimes in hybrid perovskites, therefore spatial mapping of the fluorescence lifetimes across a large area ($\sim 10^3$ μm^2) on a solution-processed thin film may shed further light on the nature of these effects.

Long-range heterogeneity has also been shown to be a result of so-called 'super-grain' structures, which are structurally uniform regions which have been shown to have a lateral area of ~ 25 μm^2, revealed by nano-focus XRD measurements made on $MAPbI_3$ thin films.[7] For mixed cation perovskites, these 'super-grains' have been shown to be up to 250 μm^2, and it is possible that this contributes to improved performance in mixed-cation perovskite PV devices as compared to $MAPbI_3$.[4] It should be noted that changes in material thickness between different areas of the film may also lead to variations in carrier lifetime, as it has been shown that the thickness of the film influences the carrier lifetime in perovskite thin films, with thicker films exhibiting longer lifetimes.[8]

Local variations in carrier lifetime may give important insight into the superior stability and photovoltaic performance of mixed cation perovskites. As shown in the previous chapter, the time-resolved PL mapping system has a minimum resolution of ~ 1.5 μm, therefore it cannot easily be used to image individual perovskite grains, which are known to be on the order of hundreds of nanometres for mixed cation perovskite blends.[9] In this chapter, the TRPL imaging system is used to investigate long-range heterogeneity in carrier lifetimes in the double cation perovskite $(FAPbI_3)_{0.85}(MAPbBr_3)_{0.15}$ and the triple cation perovskite $Cs_{0.05}FA_{0.76}MA_{0.19}Pb(I_{0.85}Br_{0.15})_3$, and correlate it with surface morphological features.

In recent years, mixed cation perovskites have been successfully deposited by spray-coating,[10–12] a method which would make these materials much more scalable for photovoltaic applications.[13,14] However, spray-coating often leads to a non-uniform morphology which is problematic for device performance, and one way of mitigating this effect is through vacuum-assisted solution processing (VASP).[15,16] As part of this work, I study the effect of vacuum-assisted solution processing (VASP) treatment on the film morphology and resultant spatial variations in carrier lifetime of spray-coated triple-cation perovskites.

5.2 Results and Discussion

5.2.1 Correlating Surface Morphology with PL Intensity and Lifetimes in Mixed Cation Perovskite Thin Films

Double Cation Perovskites

To carry out TRPL imaging, thin film samples of the double cation, mixed halide perovskite $(FAPbI_3)_{0.85}(MAPbBr_3)_{0.15}$ were fabricated by spin-coating, with a chlorobenzene anti-solvent quench applied 5 s before the end of the spin cycle. For full details of the sample fabrication process, see Section 3.1.1. The first TRPL mapping image to be discussed is the same scan as that which was discussed in Section 4.3.1. This scan was carried out over a 120 $\times$ 128 μm area on the surface of a thin film sample, and a microscope image of the mapped area on the sample surface is shown in Figure 5.1**A**. The TRPL data at each scan point was fitted to the double exponential function $y = A_1e^{-t/\tau_1} + A_2e^{-t/\tau_2}$ and maps of A_1, τ_1, A_2 and τ_2 were generated. In Section 4.3.1, some statistical analysis was carried out on the maps, to determine the validity of fitted parameter values and remove any anomalous values. As discussed in Section 4.3.1, the slow component of the double exponential (A_2e^{-t/τ_2}) is likely to give the most accurate representation of the PL intensity and lifetime in the material. Hence only maps of the parameters A_2 and τ_2 are presented, as shown in Figure 5.1**C**,**E**. When discussing the microscope images or PL maps, locations on the sample will be referred to using the notation (x,y) μm where x and y are the locations on the x- and y-axis,

respectively, as displayed on the image or map.

The sample surface in Figure 5.1**A** shows a distinct wrinkle pattern, with three large wrinkles whose peaks appear at the approximate locations (30, 128) μm, (50, 128) μm and (70, 128) μm. These wrinkles are $\sim$ 20 μm in width. It can be seen in Figure 5.1**C** that the PL intensity map contains striations, the shapes of which appear similar to the shapes of the wrinkles observed in the microscope image. The white striations in the PL image, such as at those starting at approximately (40, 128) μm and (60, 128) μm, represent higher PL intensities than the darker striations either side of them. Interestingly, these regions of higher PL intensity correspond to the recesses between the wrinkles seen in Figure 5.1**A**, whereas the darker regions (lower PL intensity) correspond to the wrinkles themselves. This is contrary to expectation, as one might assume that the wrinkles will have a higher emission intensity as they appear thicker than the rest of the film as seen in the microscope image. The absence of this effect suggests instead that the wrinkle features are centres of non-radiative recombination.

In order to give further insight into the recombination mechanisms taking place in the material under these experimental conditions, I have calculated an estimated initial charge carrier density n_0 based on the laser fluence used. Using Equation (4.3), and taking the laser spot radius r as 1.83 μm, which has been determined from the image of the laser spot shown in Figure B.1**A** in Appendix B, the laser pulse fluence ϕ has been determined to be 90.2 nJcm^{-2}. This corresponds to $n_0 \approx 2.5 \times 10^{15}$ cm^{-3}, which has been calculated using Equation (C.3) in Appendix C. At this relatively low value of initial charge carrier density, recombination is expected to be largely monomolecular, dominated by trap-assisted processes.[17] This can be visualised thus: at low carrier concentrations, the concentration of photo-excited electrons is the same or lower than the concentration of traps, meaning that trapping is equally as likely as recombination via spontaneous emission. Therefore the rate of spontaneous emission (measured TRPL signal) reflects the trap-assisted (Shockley-Read-Hall) recombination rate.

The map of the PL lifetimes in Figure 5.1**E** shows that the wrinkles are much less well-resolved in this map than in the PL intensity map. Nevertheless, there is some dependence of the PL lifetimes on the film morphology observed in Figure 5.1**E**. There

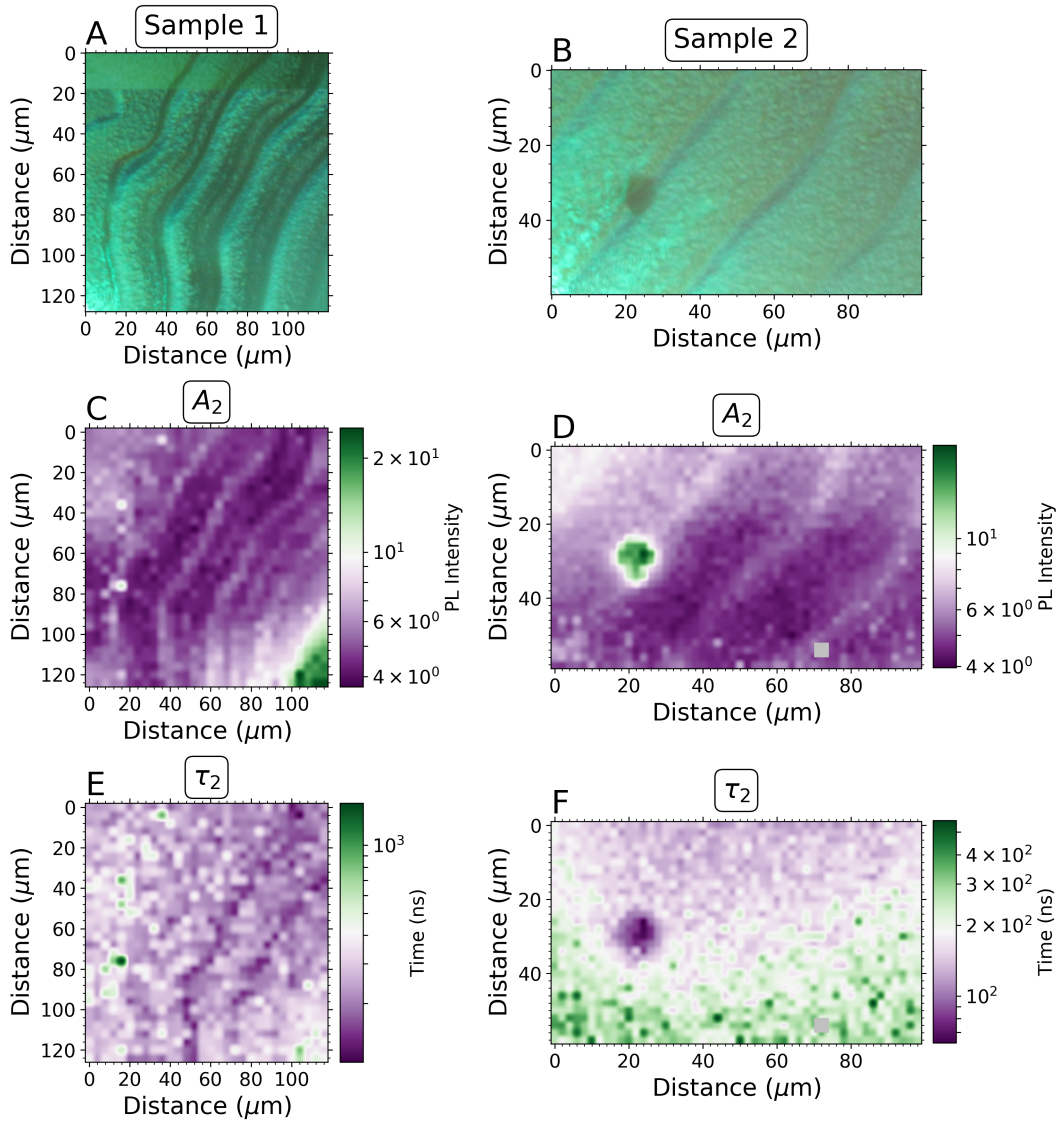

Figure 5.1: **A** Microscope image of the surface of a $(FAPbI_3)_{0.85}(MAPbBr_3)_{0.15}$ film (Sample 1), fabricated by spin-coating with an anti-solvent quench applied 5 s before the end of the spin cycle. The red square shows the 120 × 128 µm area on the surface which was mapped using the TRPL imaging system. **B** PL intensity and **C** PL lifetime images of the area shown in **A** on the surface of Sample 1. **D** Microscope image of the surface of a $(FAPbI_3)_{0.85}(MAPbBr_3)_{0.15}$ film (Sample 2), also fabricated by spin-coating with an anti-solvent quench applied 5 s before the end of the spin cycle. The red square shows the 100 × 60 µm area on the surface which was mapped using the TRPL imaging system. **E** PL intensity and **F** PL lifetime images of the area shown in **D** on the surface of Sample 2. The parameters have been extracted from fits to the slow component of a double exponential model applied to the TRPL data collected at each scan point. Grey squares denote data points where the parameter value A_2/τ_2 was calculated to be statistically outlying, or in some cases where the software was not able to optimise the parameter.

are some dark striations in the lifetime map, starting at (50, 128) μm and (70, 128) μm, locations which correspond to the peaks of the wrinkle features. The peaks of these wrinkles are also local minima in PL intensity, as observed in Figure 5.1**C**, which suggests that they are centres of non-radiative recombination. If the parameter τ_2 is associated with defect-assisted recombination, as is possible based on the initial charge carrier density $n_0 \approx 2.5 \times 10^{15}$ cm^{-3}, then the shorter lifetimes combined with lower PL intensities on the wrinkles points towards the presence of a higher density of defects in the wrinkles. These observations show that the PL intensity in the film is much more sensitive to the presence of the wrinkles than the PL lifetimes in the film.

The PL intensity map in Figure 5.1**C** becomes much brighter towards the bottom right corner. Upon examination of Figure 5.1**A**, there appears to be a fourth, shallower wrinkle in this corner of the map, which peaks at (100, 128) μm. However this wrinkle is bright unlike the other three wrinkles, suggesting that it has a lower defect density than the other wrinkles. The top left corner of the scan area also appears relatively flat, however it does not have an elevated PL intensity. These observations show that it is not trivial to elucidate the effect of the wrinkling pattern on the emission properties.

For comparison, a second sample of $(FAPbI_3)_{0.85}(MAPbBr_3)_{0.15}$, fabricated in the same way as the previous sample, was mapped using the TRPL mapping system, with an estimated laser fluence of $\phi \approx 102$ nJcm^{-2}, which corresponds to an approxmate initial charge carrier density of $n_0 \approx 3.56 \times 10^{15}$ cm^{-3}. The mapped area on this sample is pictured in Figure 5.1**B**, and here it can be seen that the surface morphology includes wrinkles similar to those observed on the first sample. These wrinkles are however on a slightly different length scale, which may suggest that they have a different origin. The PL intensity image for this scan, displayed in Figure 5.1**D**, shows several diagonal regions of elevated PL intensity spanning the surface. Upon closer inspection, it appears that these diagonal regions do not correlate spatially with the wrinkles observed in Figure 5.1**B**, but are in fact offset by ~ 10 μm to the left-hand side of each wrinkle. This is somewhat consistent with the effects observed in Figure 5.1**C**, where areas of elevated PL intensity occur in the recesses between the wrinkles. However it is interesting that these striations of elevated PL only span a limited width of the space between the

wrinkles. This suggests that there are effects within the film leading to inhomogeneity in carrier lifetimes that cannot be observed as morphological features, such as strain variations as proposed by Jones *et al.*[6]

The lifetime image in Figure 5.1**F** is fairly uniform and does not show any discernible correlation with the wrinkle features. This suggests that for this particular sample the wrinkles have not had much of an effect on the local carrier lifetime. This suggests that, as for the previous sample, the PL lifetimes are more insensitive to processing conditions than the PL intensity. There is however some long-range heterogeneity in lifetimes observed in Figure 5.1**F**, which suggests that the quality of the film varies spatially even over 100s of μm, which could be due to long-range strain variations in the film, or it may simply be due to thickness variations.[8]

The sample shown in Figure 5.1**B** also contains a small dark spot, which corresponds to the highest PL intensities of the whole PL image in Figure 5.1**C**, and the corresponding lifetimes at this spot are the shortest in the image ($<$ 100 ns). This suggests that this spot has a large radiative recombination rate. One possible explanation for this is that this spot is a very large structurally uniform area, or a 'super-grain', as its area is $\sim$ 75 μm^2 which is consistent with observations of super-grains in mixed cation perovskites.[4] It is also possible that this spot is a displaced clump of material from elsewhere in the film, which may have been caused by scratching incurred in the film from tweezers.

Wrinkled morphology has been previously reported for various mixed-cation perovskite thin film compositions.[18,19] Sveinbjörnsson and coworkers found that the wrinkles occurred when preparing the mixed cation, mixed halide perovskite $(FAPbI_3)_{0.85}$ $(MAPbBr_3)_{0.15}$, but not when preparing $MAPbI_3$, suggesting that the wrinkle formation is related specifically to the presence of the mixed cations and/or halides in the composition.[18] Bush and coworkers[20] fabricated thin films of the mixed cation, mixed halide $Cs_{0.17}$ $FA_{0.83}Pb(Br_{0.17}I_{0.83})_3$, using a chlorobenzene anti-solvent quench administered 5 s before the end of the spin cycle, similarly to our method shown in Section 3.1.1. They found that this method resulted in a film with 10-20 μm-wide ridges, which is consistent with the effects we have seen in our films.

Solution processing of polymer films can provide some insight on the origin of wrinkled

morphology in thin films. When mixed phase polymer solutions, such as polymer:fullerene blends, are spin-coated, a so-called 'transient wetting layer' is formed, composed of one of the material phases. This layer breaks down on thermal annealing, leading to a wrinkled film where wrinkles correspond to phase-segregated domains.[21,22] The partially crystallised film traps some solvent in it, which only evaporates once the film is heated above its glass transition temperature (i.e. during thermal annealing). This solvent loss during annealing leads to a fluctuation in film thickness which is observed as a wrinkled film morphology.[23] The solvent evaporation rate affects the spatial distribution of the volume fraction of the solute[24] (in our case the perovskite), therefore changes in this rate alter the surface morphology of the final film, i.e. the dimensions of the wrinkles.[25]

It is possible that the wrinkles observed in the $(FAPbI_3)_{0.85}(MAPbBr_3)_{0.15}$ films in Figure 5.1 are thickness variations due to solvent evaporation in the film. The removal of solvent from these films is facilitated in part by an anti-solvent quench, and therefore the solvent evaporation rate during spin-coating annealing will be strongly influenced by the exact parameters of the quench, such as the time during the spin cycle at which it is applied and the speed at which the anti-solvent is dripped. The microscope images in Figure 5.1**A** and **B** show that the size and shape of the wrinkles varies dramatically between samples, which suggests that sample-to-sample variations in processing conditions lead to variations in surface morphology. This evidence suggests that the wrinkles result from solvent evaporation effects, as such effects would be highly sensitive to the parameters of the anti-solvent quenching process, which can vary somewhat between samples.

However, it is not clear whether the wrinkles in the $(FAPbI_3)_{0.85}(MAPbBr_3)_{0.15}$ films are phase-separated domains as indicated for polymer blend films. Although this effect has been previously suggested for perovskite thin films,[26] no evidence for this has previously been uncovered in mixed halide perovskites.[27] In the case of mixed cation, mixed halide perovskites, these phases would be the iodine-rich $FAPbI_3$ phase and the bromine-rich $MAPbBr_3$ phase. However, if the wrinkles in Figure 5.1**A**&**B** were due to phase separation in the film, it would likely result in distinct domains of different fluorescence lifetimes correlating with the wrinkles. Such an effect is only weakly present in

Figure 5.1**E**, and is not present at all in Figure 5.1**F**. Therefore it is not trivial to ascertain whether the wrinkles in these films represent phase-segregated domains, however the wrinkles may nevertheless still be the result of solvent evaporation effects during spin-coating and thermal annealing.

In hybrid perovskites, a wrinkled surface morphology has been previously attributed to the evolution of various film stresses during processing. Film stress occurs during spin coating, as crystallites begin to nucleate and constrain the movement of the film.[28] Compressive strain during spin-coating may also come from the large change in lattice constant occurring as the film passes through the intermediate phase to the black phase, as noted by Chen *et al.* when depositing the triple cation perovskite $Cs_{0.15}(FA_{0.83}MA_{0.17})_{0.85}Pb(I_{0.7}Br_{0.3})_3$ via an anti-solvent-assisted method.[29] Then when the film is cooling post-annealing, compressive strain occurs due to differences in the thermal expansion coefficient of the perovskite and the substrate.[5] Therefore it is also possible that the strain variations described above are responsible for the wrinkle formation in the $(FAPbI_3)_{0.85}(MAPbBr_3)_{0.15}$ studied here. It has been shown in hybrid perovskites that local strain variations are correlated with enhanced defect concentrations,[30] which is consistent with our observations on both $(FAPbI_3)_{0.85}(MAPbBr_3)_{0.15}$ films that the wrinkles appear to be centres of non-radiative recombination and therefore have an elevated defect density. This evidence suggests that the wrinkles may therefore be more likely to be associated with areas of varying strain in the film.

Regardless of their origin, the wrinkles may not be hugely detrimental to photovoltaic performance, as the lifetime maps are fairly uniform despite the non-uniform surface morphology. In the first sample (Figure 5.1**E**), the majority of fluorescence lifetimes take a value between 100 and 400 ns, while in the second sample (Figure 5.1**F**), the majority of lifetime values are in the range 150-300 ns. The most obvious explanation for the higher variability in lifetimes in the first sample is that there is a higher density of wrinkles in this sample, which would suggest that the wrinkles do have a small but noticeable effect on fluorescence lifetime behaviour in the thin films. For both samples, the fluorescence lifetime is fairly uniform across the sample despite the wrinkles, suggesting the insensitivity of the carrier lifetimes to morphological features, which may go part of the way

to explaining the excellent photovoltaic performance of $(FAPbI_3)_{0.85}(MAPbBr_3)_{0.15}$. In fact it is even possible that the wrinkle patterning may be advantageous for solar cell performance as it may act as a light-trapping structure.[31–33]

Triple Cation Perovskites

TRPL mapping experiments were also carried out on the triple cation perovskite $Cs_{0.05}FA_{0.76}MA_{0.19}PbI_{2.55}Br_{0.45}$, to determine whether the effect of surface morphology on the heterogeneity of the PL emission properties may play a part in the enhanced photovoltaic performance and stability of these perovskites as compared to the FA/MA double cation perovskite. Two samples of $Cs_{0.05}$ $FA_{0.76}MA_{0.19}PbI_{2.55}Br_{0.45}$, fabricated as described in Section 3.1.2, were mapped over an area of 100 μm by 60 μm on the surface of the thin film in steps of 2 μm. For this scan, the laser fluence was $\phi \approx 94.3$ nJcm^{-2}, corresponding to $n_0 \approx 5.12 \times 10^{15}$ cm^{-3}. The scanned area on the first sample is shown in Figure 5.2**A**, as imaged by the white light microscope. As can be seen here, the surface of this thin film is covered with a wrinkle pattern, similar to the one seen on the $(FAPbI_3)_{0.85}(MAPbBr_3)_{0.15}$ films. Wrinkled morphology has been documented in Cs-containing double and triple cation perovskite thin films previously.[27,34]. The PL intensity and lifetime images for this sample are shown in Figure 5.2**C** and **E**, respectively.

The PL intensity image in Figure 5.2**C** shows a large central region which exhibits lower PL intensities than those on the edges of the scan. This central region appears to correspond loosely to the morphology, as its outer edge (white band) correlates with the presence of a large wrinkle feature. The PL lifetime image in Figure 5.2**E** shows that this central region also exhibits slightly shorter lifetimes than the rest of the film. These observations suggest that this central area of the scan is the most defect-dense area, which may be due to local strain variations as was suggested for the $(FAPbI_3)_{0.85}(MAPbBr_3)_{0.15}$ films. There is a very dark region in the top left corner of the intensity image, which corresponds to a surface feature which appears to be a cluster of very closely spaced wrinkles. This may be due to the presence of a higher density of defects associated with the wrinkle features, as was postulated for the $(FAPbI_3)_{0.85}(MAPbBr_3)_{0.15}$ films.

The outer edges of the PL image have much higher intensities than those in the

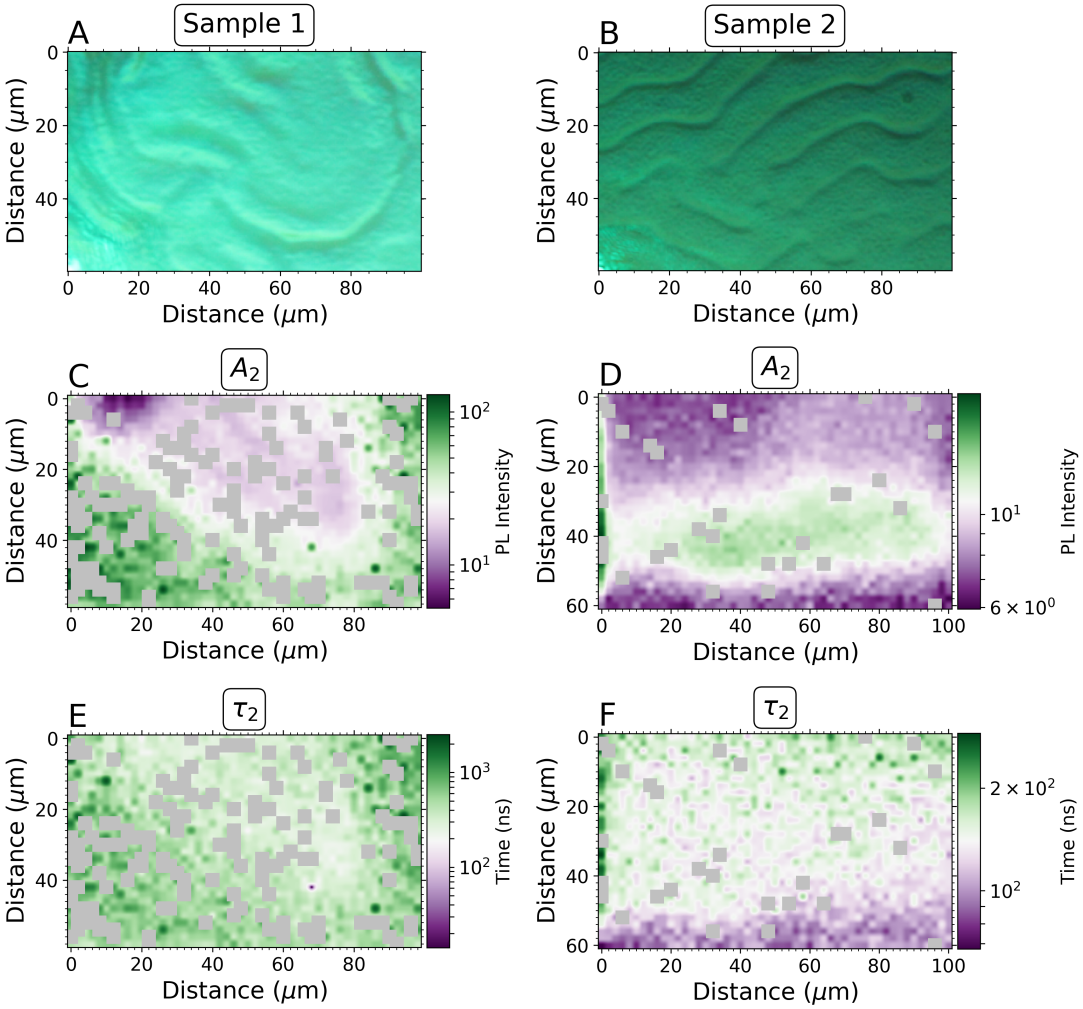

Figure 5.2: **A** Microscope image of the surface of a $Cs_{0.05}FA_{0.81}MA_{0.14}PbI_{2.55}Br_{0.45}$ film (Sample 1), fabricated by spin-coating with an anti-solvent quench applied 5 s before the end of the spin cycle. The red square shows the 120 × 128 µm area on the surface which was mapped using the TRPL imaging system. **B** PL intensity and **C** PL lifetime images of the area shown in **A** on the surface of Sample 1. **D** Microscope image of the surface of a $Cs_{0.05}FA_{0.81}MA_{0.14}PbI_{2.55}Br_{0.45}$ film (Sample 2), also fabricated by spin-coating with an anti-solvent quench applied 5 s before the end of the spin cycle. The red square shows the 100 × 60 µm area on the surface which was mapped using the TRPL imaging system. **E** PL intensity and **F** PL lifetime images of the area shown in **D** on the surface of Sample 2. The parameters have been extracted from fits to the slow component of a double exponential model applied to the TRPL data collected at each scan point. Grey squares denote data points where the parameter value A_2/τ_2 was calculated to be statistically outlying, or in some cases where the software was not able to optimise the parameter.

centre. In conjunction with this, these outer areas also have longer lifetimes than those in the centre. This suggests that the overall film quality in these areas is better. There is no discernible correlation between the wrinkles in the bottom left corner and the PL intensity image—this whole area appears to be fairly homogeneous in terms of PL intensity. Within

the central area there are some small wrinkles as seen in Figure 5.2**A**, but in general these do not appear to correlate with the PL intensity map, with the exception of the wrinkle located around (0, 40) μm, where the PL intensity is slightly lower than in the surrounding area, again potentially due to a higher defect density due to the local strain in the wrinkle. Overall, observations of the PL intensity and lifetime images for this sample suggest that the emission properties of $Cs_{0.05}FA_{0.76}MA_{0.19}PbI_{2.55}Br_{0.45}$ are less sensitive to surface morphology than those of $(FAPbI_3)_{0.85}(MAPbBr_3)_{0.15}$, which exhibited a much stronger correlation between wrinkles features and PL intensity variations (Figure 5.1).

The second sample of $Cs_{0.05}FA_{0.76}MA_{0.19}PbI_{2.55}Br_{0.45}$ also exhibits a wrinkled pattern, as shown in the microscope image in Figure 5.2**B**. The laser fluence used for this scan was $\phi \approx 94.3$ nJcm^{-2}, corresponding to $n_0 \approx 5.12 \times 10^{15}$ cm^{-3}. The PL intensity image taken from this film is shown in Figure 5.2**D**, and it can be seen that the PL image does not show any distinct correlation with the wrinkle features. This is not consistent with previous observations, as Bercegol and coworkers[34] observed a strong variation in PL intensity correlating with the wrinkle features in Cs-containing triple cation perovskites. The wrinkles in Figure 5.2**B** appear narrower and shallower than those in the first triple cation sample, therefore it may be the case that they are too small to be resolved when mapping with a step size of 2 μm.

Despite this, there is some long-range heterogeneity in the PL intensity image on the order of 10s of μm. Interestingly, the area of the PL image with the highest intensities corresponds to an area of the film with a slightly lower density of wrinkles and where the wrinkles appear shallower. This suggests that the wrinkle features may be the cause of some heterogeneity in the film. This is in alignment with the observations made on the $(FAPbI_3)_{0.85}(MAPbBr_3)_{0.15}$ films, where the wrinkles had an adverse effect on PL intensity. The PL lifetimes do not appear to be affected in the same way however, as the PL lifetime map for this sample, shown in Figure 5.2**F**, does not reveal any changes in lifetime corresponding to this same area of the film. There are however some long-range variations in the PL lifetime, which becomes longer towards the upper part of the scan. This suggests that the film is not completely homogeneous and that the film quality varies between different areas of the film; this may be due to long-range strain variations

in the film which do not manifest as morphological features but are nevertheless present.

5.2.2 Effect of VASP Treatment on Surface Morphology in Spray-Coated Triple Cation Perovskite Thin Films

The TRPL mapping system was also used to determine the effect of vacuum-assisted solution processing (VASP) treatment on time-resovled PL properties in spray-coated films of the triple cation perovskite $Cs_{0.05}FA_{0.81}$ $MA_{0.14}PbI_{2.55}Br_{0.45}$. The data presented in this section, including TRPL mapping and device data, was included in a paper published by Bishop and coworkers.[11] Samples were fabricated as described in Section 3.1.3 and some were subjected to the VASP treatment while others were only spray-coated. A selected sample of each type was then mapped with the TRPL imaging system—a 200 $\times$ 200 μm area on the surface of each sample was imaged. The laser fluences used for these scans were $\phi \approx 45.4$ nJcm^{-2} ($n_0 \approx 2.46 \times 10^{15}$ cm^{-3}) and $\phi \approx 71.6$ nJcm^{-2} ($n_0 \approx 3.89 \times 10^{15}$ cm^{-3}) for the non-VASP-treated film and the VASP-treated film, respectively. Optical microscope images of the mapped area on the non-VASP-treated and VASP-treated thin films are shown in Figure 5.3**A** and **B**, respectively. The PL intensity maps of the samples without and with VASP treatment applied are shown in Figure 5.3**C** and **D**, respectively.

The microscope image in Figure 5.3**A** shows that without the VASP treatment, the film morphology consists of large 'flower-like' features on the order of $\sim$ 60 - 120 μm in size, separated by cracks of $\sim$ 5 - 10 μm in width. Some of these structures have raised central bumps of varying width. These 'flower-like' structures have been observed previously in the morphology of spray-coated hybrid perovskites, and have been identified as large perovskite crystallites.[10,35] The effect of these crystallites on the PL emissions is clear from Figure 5.3**C**, where it can be seen that the 'flower-like' crystallite features are clearly resolved by differences in PL intensity. The PL intensity map shows that the cracks between the flower-crystallites appear to exhibit elevated PL intensity as compared to the bulk of the flower-crystallites, although these cracks are generally on the order of the step size used for the map (5 μm), therefore we cannot be certain that these elevated emissions definitely originate from the cracks and it may in fact originate from the edges

of the crystallite features. The central bump of one of the largest flower-crystallites,

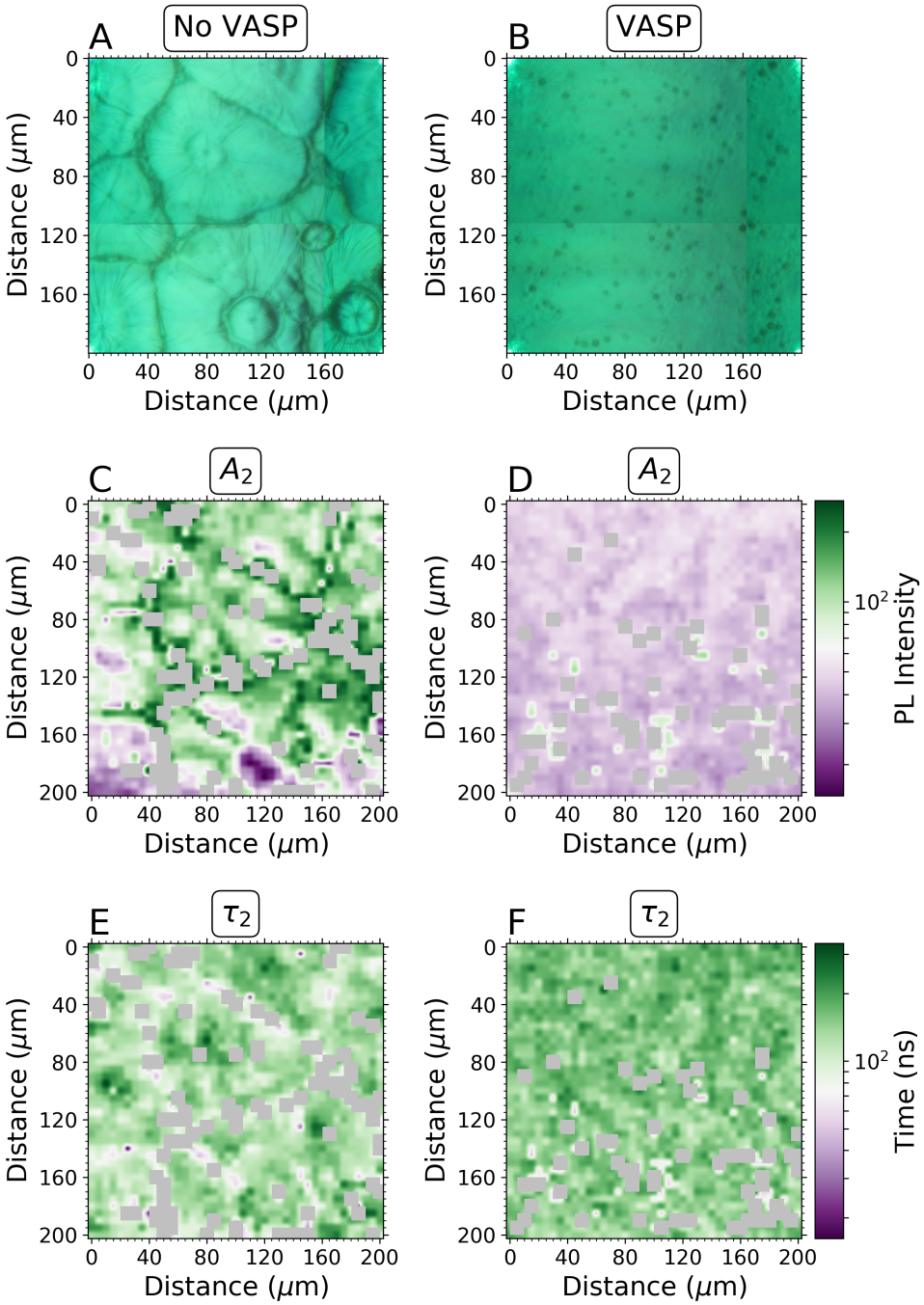

Figure 5.3: Microscope image of the 200 × 200 µm area on the surface of a spray-coated $Cs_{0.05}FA_{0.81}MA_{0.14}PbI_{2.55}Br_{0.45}$ thin film, **A** where the VASP treatment was not used and **B** where the sample was VASP-treated for 5 mins after spray coating. **C** PL intensity and **E** PL lifetime images of the spray-coated $Cs_{0.05}FA_{0.76}MA_{0.19}PbI_{2.55}Br_{0.45}$ thin film which was not VASP treated. **D** PL intensity and **F** PL lifetime images of the spray-coated $Cs_{0.05}FA_{0.76}MA_{0.19}PbI_{2.55}Br_{0.45}$ thin film which was VASP treated for 5 mins. PL intensity and lifetime parameters have been extracted from fits to the slow component of a double exponential model applied to the TRPL data collected at each scan point. Grey squares denote data points where the parameter value A_2/τ_2 was calculated to be statistically outlying, or in some cases where the software was not able to optimise the parameter at all.

located at ∼(120,180) μm, exhibits the lowest PL emissions of the whole image, which suggests that this feature is a non-radiative recombination centre. This behaviour is also seen in the central bump of the crystallite in the bottom right corner of the image, where the emission intensity is lower than in most of the surrounding material. In other flower-crystallites in the image, where these central bumps appear less raised, the PL intensity does not vary so much in the bumps as opposed to the surrounding crystallite, suggesting that the more raised these bumps are, the more detrimental the effect on the PL emissions. It is clear that these flower-crystallites lead to non-uniformity in the PL emissions of the film, which may be hugely detrimental to photovoltaic performance.

In contrast, the spray-coated film which was treated with vacuum exposure has a much more uniform morphology, as seen in Figure 5.3**B**. The thin film surface is largely homogeneous, with a number of small dark spots on the surface of $\sim 5 - 10\mu$m in width. The PL intensity image in Figure 5.3**D** shows that this homogeneity extends to the PL emissions also. Although the PL emissions appear on average lower than in the film which was not VASP treated, the intensity is significantly more uniform, which suggests that there are no significant areas of non-radiative recombination. Although the step size is slightly too large to capture the effects of the small black features seen in Figure 5.3**B**, which are generally around the same order of magnitude as the 5 μm step size, there are some spots on the PL image with elevated PL intensity which correlate spatially to these black spots in the microscope image. This suggests that the black spot features may be large, highly ordered crystal domains, perhaps nucleation sites caused by the spray-coating process.

The maps of PL lifetime for the samples without and with VASP treatment applied are shown in Figure 5.3**E** and **F**, respectively. For the thin film which was not exposed to vacuum, Figure 5.3**E** shows that the crystallite features cause heterogeneity in the fluorescence lifetime values. Similarly to the observations made on the double- and triple-cation spin-coated samples presented in Section 5.2.1, the surface morphology has a much less significant effect on the lifetimes than it does on the PL intensity. This suggests that the fluorescence lifetimes of such perovskites are somewhat insensitive to surface features. This suggests that such surface features, which in the case of all

samples presented in this thesis are results of the processing method, do not denote underlying inhomogeneity in distribution of elements, such as areas of iodide excess, nor do they correlate with the presence of degradation products such as PbI_2.

The PL lifetime map in Figure 5.3**E** shows that the cracks between the 'flower'-crystallites generally correspond to the shortest lifetimes, although as before it cannot be said for certain whether this correlation can be drawn, as the crack widths are on the order of the step size of the map. If the cracks do correlate with higher PL intensities and shorter lifetimes, this suggests that there is an increased rate of radiative recombination in these areas. The lifetimes on the 'flower'-crystallites are generally longer than those in the cracks between them. The longest lifetimes in the map correspond to the central bumps of the 'flower'-crystallites, and these central bumps also exhibit the lowest PL intensities in the maps in Figure 5.3**C**. A longer lifetime on these central bumps suggests that they contain fewer defects, as the lifetime τ_2 reflects the trap-assisted recombination rate.

The PL lifetime map of the thin film that was VASP-treated is shown in Figure 5.3**F**, and here it can be seen that there is little heterogeneity in the PL lifetime across the film surface,and that the lifetimes are on average longer than those observed in the film which was not vacuum-treated. This shows that the VASP treatment has not only been successful in homogenising the surface morphology, but also that this has had the positive effect of lengthening the fluorescence lifetimes across the film. There are small spots of shortened lifetime in this map, which correspond to the small black spots in the microscope image in Figure 5.3**B**, which in turn correlate with areas of heightened PL intensity. These black features may be nucleation sites of highly ordered crystal grains, as this would lead to higher radiative recombination rates in these areas.

To elucidate the effect of the VASP treatment on device performance, solar cell devices were fabricated with the spray-cast triple cation perovskite as an absorber layer. The device architecture was as follows: indium tin oxide as the transparent conducting oxide, nanoparticle tin oxide (np-SnO_2) as the electron-transporting medium, spray-coated $Cs_{0.05}FA_{0.81}MA_{0.14}PbI_{2.55}Br_{0.45}$ as the absorber layer, spiro-OMeTAD as the hole-

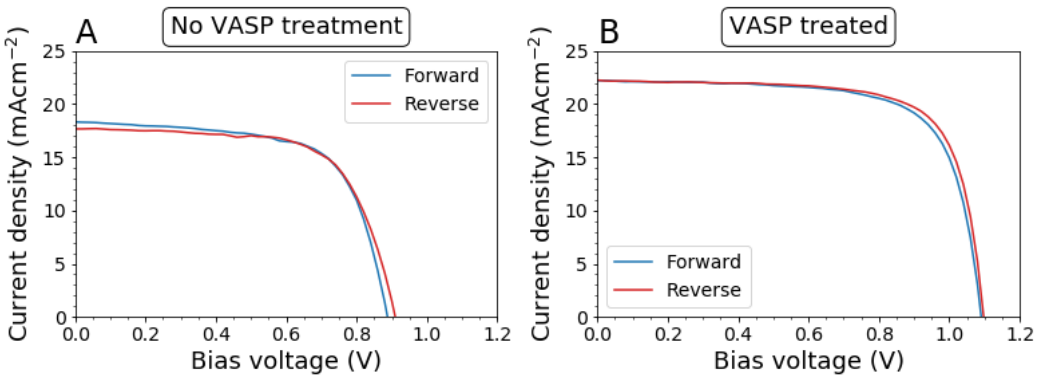

Figure 5.4: $J-V$ curves for PV devices where the spray-cast perovskite layer has **A** not been VASP treated, and **B** for those where it has been VASP treated. Curves shown are for the champion pixel of each type of device.

transporting medium, and a gold electrode. Two types of device were fabricated: devices with a perovskite layer that was not VASP treated, and devices with a VASP-treated perovskite layer. These devices were tested by performing current-voltage ($J-V$) measurements while illuminating the device with a solar simulator (1 Sun at AM 1.5G). More details on the fabrication and testing of devices can be found in Section 3.2.

The $J-V$ curves for both the non-VASP-treated and VASP-treated devices are shown in Figure 5.4. Table 5.1 shows some of the key device metrics, calculated from the JV curves, for the champion pixels of the VASP treated and non-VASP treated devices.

The devices which were not VASP treated achieved a champion power conversion efficiency (PCE) of 10.8%, whereas the VASP treated devices achieved a champion PCE of 17.8%. This significant increase in PCE is consistent with the TRPL maps, where it was observed that the PL lifetimes were on average longer in the VASP-treated films and there was much less long-range heterogeneity in the PL lifetimes in these films.

The V_{OC} in a PV device is limited by recombination: the V_{OC} will be at its maximum if all recombination is radiative. The VASP treatment increases the overall lifetimes of the film, which is consistent with the observation of an increased V_{OC} for the VASP-treated device. The J_{SC} also increases for the VASP-treated device, and this may be due to the increased uniformity and longer lifetimes on the VASP-treated form as this will improve the charge transport and charge carrier extraction from the absorber layer.

In contrast, the devices which were not VASP treated exhibited lower fill factors and lower J_{SC} than those that were, which may be due to the non-uniform surface

Table 5.1: Summary of key device metrics for PV devices where the spray-cast perovskite layer has not been VASP treated, and for those where it has been VASP treated. Metrics shown are for the champion pixel of each type of device.

	No VASP treatment		VASP treated	
	Forward scan	Reverse scan	Forward scan	Reverse scan
V_{OC} (V)	0.887746	0.909786	1.09069	1.0977
J_{SC} ($mAcm^{-2}$)	-18.3269	-17.6746	-22.218	-22.2602
Fill factor (%)	66.1387	66.4765	71.2295	72.8021
PCE (%)	10.7606	10.6895	17.2609	17.7893

morphology—as Figure 5.3**E** shows, there are shorter τ_2 lifetimes at the boundaries of the flower-crystallites, which suggests excessive trap-assisted recombination at these boundaries, which will lead to lower fill factors and possibly lower J_{SC} as well due to inhibited charge carrier transport at the grain boundaries.

The VASP treatment has therefore been shown to improve device efficiency in solar cell devices based on spray-coated triple cation perovskites, due to improvements in open-circuit voltage and short-circuit current caused by lengthening of carrier lifetimes and increased homogeneity of carrier lifetimes in the perovskite layer.

5.3 Conclusions

Time-resolved PL mapping studies on double and triple cation perovskites have shown that surface morphology correlates with PL emission properties. Thin films of the double cation perovskite $(FAPbI_3)_{0.85}(MAPbBr_3)_{0.15}$ and the triple cation perovskite $Cs_{0.05}FA_{0.76}MA_{0.19}PbI_{2.55}Br_{0.45}$ have both been shown to exhibit wrinkled surface morphology, which may result either from compressive strain variations in the film during annealing or from inhomogeneity in solvent evaporation during thermal annealing. These wrinkle features appear to strongly affect the resulting PL intensity, whereas PL lifetimes appear less sensitive to these surface features. The correlation between morphological features and PL emission properties is a lot more pronounced in the double cation perovskite than in the triple cation perovskite. This suggests that the incorporation of Cs into the mixed cation perovskite composition leads to thin films whose emission properties are less sensitive to processing-driven changes in surface morphology, which may be a

contributing factor to the superior stability of the triple cation perovskite as compared to the double cation perovskite.

In this chapter I have also demonstrated the success of the TRPL imaging system in characterising the effect of the VASP treatment on the morphology and carrier lifetimes of spray-coated triple cation perovskite thin films. The PL lifetime images have revealed that the VASP treatment increases the overall lifetimes across the film as well as leading to a much smaller degree of inhomogeneity in carrier lifetimes in the spray-cast thin film. This increased lifetime homogeneity demonstrably leads to better device performance in PV devices based on the VASP-treated films. These studies highlight the key role that time-resolved PL mapping techniques play in the optimisation process of hybrid perovskites for photovoltaic applications.

References

[1] N. J. Jeon, J. H. Noh, W. S. Yang, Y. C. Kim, S. Ryu, J. Seo, S. I. Seok, *Nature* **2015**, *517*, 476.

[2] M. Saliba, T. Matsui, J.-Y. Seo, K. Domanski, J.-P. Correa-Baena, M. K. Nazeeruddin, S. M. Zakeeruddin, W. Tress, A. Abate, A. Hagfeldt, M. Grätzel, *Energy & Environmental Science* **2016**, *9*, 1989.

[3] D. P. McMeekin, Z. Wang, W. Rehman, F. Pulvirenti, J. B. Patel, N. K. Noel, M. B. Johnston, S. R. Marder, L. M. Herz, H. J. Snaith, *Advanced Materials* **2017**, *29*.

[4] E. M. Tennyson, T. A. Doherty, S. D. Stranks, *Nature Reviews Materials* **2019**, *4*, 573.

[5] J. Zhao, Y. Deng, H. Wei, X. Zheng, Z. Yu, Y. Shao, J. E. Shield, J. Huang, *Science Advances* **2017**, *3*, eaao5616.

[6] T. W. Jones, A. Osherov, M. Alsari, M. Sponseller, B. C. Duck, Y. K. Jung, C. Settens, F. Niroui, R. Brenes, C. V. Stan, Y. Li, M. Abdi-Jalebi, N. Tamura, J. E. MacDonald, M. Burghammer, R. H. Friend, V. Bulović, A. Walsh, G. J. Wilson, S. Lilliu, S. D. Stranks, *Energy and Environmental Science* **2019**, *12*, 596.

[7] S. Lilliu, T. G. Dane, M. Alsari, J. Griffin, A. T. Barrows, M. S. Dahlem, R. H. Friend, D. G. Lidzey, J. E. Macdonald, *Advanced Functional Materials* **2016**, *26*, 8221.

[8] S. Wieghold, J. Tresback, J. P. Correa-Baena, N. T. P. Hartono, S. Sun, Z. Liu, M. Layurova, Z. A. Vanorman, A. S. Bieber, J. Thapa, B. Lai, Z. Cai, L. Nienhaus, T. Buonassisi, *Chemistry of Materials* **2019**, *31*, 3712.

[9] S. Wieghold, J. P. Correa-Baena, L. Nienhaus, S. Sun, K. E. Shulenberger, Z. Liu, J. S. Tresback, S. S. Shin, M. G. Bawendi, T. Buonassisi, *ACS Applied Energy Materials* **2018**, *1*, 6801.

[10] Y. S. Chou, L. H. Chou, A. Z. Guo, X. F. Wang, I. Osaka, C. G. Wu, C. L. Liu, *ACS Sustainable Chemistry and Engineering* **2019**, *7*, 14217.

[11] J. E. Bishop, J. A. Smith, C. Greenland, V. Kumar, N. Vaenas, O. S. Game, T. J. Routledge, M. Wong-Stringer, C. Rodenburg, D. G. Lidzey, *ACS Applied Materials & Interfaces* **2018**, *10*, 39428.

[12] J. E. Bishop, C. D. Read, J. A. Smith, T. J. Routledge, D. G. Lidzey, *Scientific Reports* **2020**, *10*, 1.

[13] A. T. Barrows, A. J. Pearson, C. K. Kwak, A. D. F. Dunbar, A. R. Buckley, D. G. Lidzey, *Energy & Environmental Science* **2014**, *7*, 2944.

[14] S. Ulična, B. Dou, D. H. Kim, K. Zhu, J. M. Walls, J. W. Bowers, M. F. Van Hest, *ACS Applied Energy Materials* **2018**, *1*, 1853.

[15] Q. Chen, H. Zhou, Z. Hong, S. Luo, H. S. Duan, H. H. Wang, Y. Liu, G. Li, Y. Yang, *Journal of the American Chemical Society* **2014**, *136*, 622.

[16] X. Li, D. Bi, C. Yi, J. D. Décoppet, J. Luo, S. M. Zakeeruddin, A. Hagfeldt, M. Grätzel, *Science* **2016**, *353*, 58.

[17] S. D. Stranks, V. M. Burlakov, T. Leijtens, J. M. Ball, A. Goriely, H. J. Snaith, *Physical Review Applied* **2014**, *2*, 034007.

[18] K. Sveinbjörnsson, K. Aitola, J. Zhang, M. B. Johansson, X. Zhang, J. P. Correa-Baena, A. Hagfeldt, G. Boschloo, E. M. Johansson, *Journal of Materials Chemistry A* **2016**, *4*, 16536.

[19] A. Tejada, S. Braunger, L. Korte, S. Albrecht, B. Rech, J. A. Guerra, *Journal of Applied Physics* **2018**, *123*, 175302.

[20] K. A. Bush, N. Rolston, A. Gold-Parker, S. Manzoor, J. Hausele, Z. J. Yu, J. A. Raiford, R. Cheacharoen, Z. C. Holman, M. F. Toney, R. H. Dauskardt, M. D. McGehee, *ACS Energy Letters* **2018**, *3*, 1225.

[21] S. Y. Heriot, R. A. Jones, *Nature Materials* **2005**, *4*, 782.

[22] S. Coveney, N. Clarke, *Physical Review Letters* **2013**, *111*, 125702.

[23] T. Wang, A. J. Pearson, D. G. Lidzey, R. A. Jones, *Advanced Functional Materials* **2011**, *21*, 1383.

[24] Y. Mouhamad, P. Mokarian-Tabari, N. Clarke, R. A. Jones, M. Geoghegan, *Journal of Applied Physics* **2014**, *116*, 123513.

[25] P. Mokarian-Tabari, M. Geoghegan, J. R. Howse, S. Y. Heriot, R. L. Thompson, R. A. Jones, *European Physical Journal E* **2010**, *33*, 283.

[26] F. Léonard, R. C. Desai, *Physical Review B - Condensed Matter and Materials Physics* **1998**, *58*, 8277.

[27] S. Braunger, L. E. Mundt, C. M. Wolff, M. Mews, C. Rehermann, M. Jošt, A. Tejada, D. Eisenhauer, C. Becker, J. A. Guerra, E. Unger, L. Korte, D. Neher, M. C. Schubert, B. Rech, S. Albrecht, *Journal of Physical Chemistry C* **2018**, *122*, 17123.

[28] V. Brand, K. Levi, M. D. McGehee, R. H. Dauskardt, *Solar Energy Materials and Solar Cells* **2012**, *103*, 80.

[29] B. Chen, Z. Yu, K. Liu, X. Zheng, Y. Liu, J. Shi, D. Spronk, P. N. Rudd, Z. Holman, J. Huang, *Joule* **2019**, *3*, 177.

[30] T. W. Jones, A. Osherov, M. Alsari, M. Sponseller, B. C. Duck, Y.-K. Jung, C. Settens, F. Niroui, R. Brenes, C. V. Stan, Y. Li, M. Abdi-Jalebi, N. Tamura, J. E. Macdonald, M. Burghammer, R. H. Friend, V. Bulović, A. Walsh, G. J. Wilson, S. Lilliu, S. D. Stranks **2018**.

[31] J. B. Kim, P. Kim, N. C. gard, S. J. Oh, C. R. Kagan, J. W. Fleischer, H. A. Stone, Y. L. Loo, *Nature Photonics* **2012**, *6*, 327.

[32] M. Kaltenbrunner, G. Adam, E. D. Głowacki, M. Drack, R. Schwödiauer, L. Leonat, D. H. Apaydin, H. Groiss, M. C. Scharber, M. S. White, N. S. Sariciftci, S. Bauer, *Nature Materials* **2015**, *14*, 1032.

[33] G. Nasti, S. Sanchez, I. Gunkel, S. Balog, B. Roose, B. D. Wilts, J. Teuscher, G. Gentile, P. Cerruti, V. Ambrogi, C. Carfagna, U. Steiner, A. Abate, *Soft Matter* **2017**, *13*, 1654.

[34] A. Bercegol, F. J. Ramos, A. Rebai, T. Guillemot, J. B. Puel, J. F. Guillemoles, D. Ory, J. Rousset, L. Lombez, *Journal of Physical Chemistry C* **2018**, *122*, 23345.

[35] W.-C. Chang, D.-H. Lan, K.-M. Lee, X.-F. Wang, C.-L. Liu, *ChemSusChem* **2017**, *10*, 1405.

Chapter 6

Correlating Phase Behaviour with Photophysical Properties in Mixed-Cation Mixed-Halide Perovskite Thin Films

Correlating Phase Behaviour with Photophysical Properties in Mixed-Cation Mixed-Halide Perovskite Thin Films

Claire Greenland,[1] *Adam Shnier,*[2] *Sai K. Rajendran,*[3] *Joel A. Smith,*[1] *Onkar S. Game,*[1] *Daniel Wamwangi,*[4] *Graham A. Turnbull,*[3] *Ifor D. W. Samuel,*[3] *David G. Billing*[2] *and David G. Lidzey*[1*]

[1] Department of Physics and Astronomy, University of Sheffield, Hicks Building, Hounsfield Road, Sheffield S3 7RH, United Kingdom

[2] School of Chemistry, University of the Witwatersrand, Johannesburg 2050, South Africa

[3] Organic Semiconductor Centre, SUPA, School of Physics and Astronomy, University of St Andrews, North Haugh, St Andrews KY16 9SS, United Kingdom

[4] School of Physics, University of the Witwatersrand, Johannesburg 2050, South Africa

[*]E-mail: d.g.lidzey@sheffield.ac.uk

Advanced Energy Materials

Volume 10, Issue 4, January 2020

DOI: 10.1002/aenm.201901350

Foreword

Mixed cation, mixed halide perovskites of the form $(FAPbI_3)_x(MAPbBr_3)_{1-x}$ have demonstrated great promise as PV absorber layers. PV devices based on perovskites in this compositional range have been extensively tested, and the optimum composition in terms of the power conversion efficiency (PCE) of the devices is $(FAPbI_3)_{0.85}(MAPbBr_3)_{0.15}$. Therefore it is of paramount importance to study the optoelectronic properties of this material, to understand how these fundamental properties contribute to the excellent device metrics displayed by this material, a topic which is also the focus of much of Chapter 5. Furthermore, the temperature dependence of optoelectronic properties can reveal the underlying mechanisms behind the thermal stability of this material, which is also key to the performance and long-term operational stability of the material. In this chapter we have investigated the phase behaviour of $(FAPbI_3)_{0.85}(MAPbBr_3)_{0.15}$ along with its temperature-dependent optical properties such as band gap and Stokes shift, to elucidate the links between phase behaviour and optoelectronic properties in this material.

Collaborating Author Declaration

All authors of this publication make the following declaration:

"I, a collaborating author on this publication, agree that the experimental work and/or the analysis and interpretation of work and/or the text within this publication is primarily completed by Claire Greenland and suitable for use in this thesis."

Manuscript

Abstract

Mixed cation perovskites currently achieve very promising efficiency and operational stability when used as the active semiconductor in thin-film photovoltaic devices. However an in-depth understanding of the structural and

photophysical properties that drive this enhanced performance is still lacking. Here we explore the prototypical mixed-cation mixed-halide perovskite $(FAPbI_3)_{0.85}(MAPbBr_3)_{0.15}$, and present temperature-dependent X-ray diffraction measurements that we correlate with steady state and time-resolved photoluminescence data. Our measurements indicate that this material adopts a pseudo-cubic perovskite α phase at room temperature, with a transition to a pseudo-tetragonal β phase occurring at $\sim$260 K. We find that the temperature dependence of the radiative recombination rates correlates with temperature-dependent changes in the structural configuration, and observed phase transitions also mark changes in the gradient of the optical band gap. Our work illustrates that temperature-dependent changes in the perovskite crystal structure alter the charge carrier recombination processes and photoluminescence properties within such hybrid organic-inorganic materials. Our findings have significant implications for photovoltaic performance at different operating temperatures, as well as providing new insight on the effect of alloying cations and halides on the phase behaviour of hybrid perovskite materials.

6.1 Introduction

Recent years have seen rapid progress in the development of high efficiency perovskite solar cells, with new material systems, compositional engineering and passivation techniques used to increase power conversion efficiencies beyond 24%.[1] Indeed, perovskite materials have many favourable properties for photovoltaic applications, such as strong optical absorption,[2] long diffusion lengths,[3] long carrier lifetimes[4] and high defect tolerance.[5] They can also be deposited from solution using low cost, low temperature processes, with large area devices being fabricated by methods such as slot-die coating and spray coating.[6,7]

A perovskite material is defined as any material adopting the structure ABX_3, where A is a monovalent cation (typically Cs or alkylammonium ions), B is a divalent metal cation (commonly Pb or Sn) and X is a halide anion (commonly I, Br or Cl). The single-cation hybrid perovskite $MAPbI_3$, where MA is the organic molecule methylammonium

($CH_3NH_3^+$), has been utilised as an absorber layer for perovskite solar cells (PSCs) since their advent in 2009.[8] Whilst $MAPbI_3$ has dominated the PSC research field for a number of years, its poor thermal stability and sub-optimal band gap limit its usefulness for photovoltaic applications.[9,10]

The replacement of MA with the larger cation $HC(NH_2)_2^+$ (formamidinium or FA) to form $FAPbI_3$ has been shown to reduce the band gap, bringing it closer to the Shockley-Queisser optimum band gap for solar cell absorber layers ($\sim$1.4 eV).[11] Although at room temperature $FAPbI_3$ does not form a stable cubic perovskite phase, it is possible to stabilise the cubic perovskite phase by incorporating 20% MA back into the A-site.[12] Additionally the inclusion of a mixed halide into the perovskite allows the band gap to be further tuned and its stability and optoelectronic properties to be optimised.[13] As such, highly efficient perovskite solar cell (PSC) devices have been demonstrated based on the mixed cation lead mixed halide perovskite system $(FAPbI_3)_{1-x}(MAPbBr_3)_x$ ($0 < x < 1$), in which $x = 0.15$ has been shown to yield optimum device performance.[14–16] Despite advances in device performance arising on the basis of empirical studies, the fundamental properties of these multi-cation materials are not yet fully understood.

A number of research groups have used temperature-dependent techniques to gain a deeper understanding of hybrid perovskite materials and their optoelectronic properties. Such studies provide insight into the intrinsic properties of the material and have relevance to the practical operation of PSC devices, which can typically be exposed to a wide range of temperatures during operation.[17] The phase behaviour of mixed cation, mixed halide perovskites has been investigated by a number of authors. Measurements made by Xie *et al.* revealed that materials in the $(FAPbI_3)_{1-x}(MAPbBr_3)_x$ compositional range generally adopt a cubic perovskite structure at room temperature, contributing to their superior thermal stability.[18] Weber *et al.* have also reported a tetragonal-to-cubic phase transition at $\sim$280 K for the single halide perovskite $(FAPbI_3)_{0.8}(MAPbI_3)_{0.2}$.[19] However the addition of the mixed halide in $(FAPbI_3)_{1-x}(MAPbBr_3)_x$ will have an as yet undocumented and potentially significant effect on the phase behaviour.[20] Various studies have documented the temperature-dependent charge carrier dynamics and photoluminescence properties of hybrid perovskite materials, and the relationship between

phase behaviour and these properties has been studied extensively in $MAPbI_3$, most notably by the Herz group.[21,22] However, this relationship has not yet been explored in mixed-cation mixed-halide systems, despite their superior photovoltaic performance.

In this work, we explore both the optical and structural properties of thin films of the mixed cation, mixed halide perovskite $(FAPbI_3)_{0.85}(MAPbBr_3)_{0.15}$ as a function of temperature between 4 K and 350 K. We perform variable temperature powder X-ray diffraction studies over the temperature range 80-350 K in order to identify structural phase transitions. We then compare our findings with results obtained from steady-state photoluminescence and absorption spectroscopy, at a range of temperatures from 4 K to 300 K. We also draw a comparison with time-resolved photoluminescence measurements taken with a streak camera at temperatures from 77 K to 300 K, which allows us to characterise charge carrier recombination dynamics. This combinatorial study of crystal structure with PL and absorption measurements highlights the complex phase behaviour and photophysics at play in alloyed perovskite materials and the implications this has for device performance.

6.2 Results and Discussion

6.2.1 Powder X-ray Diffraction

First we discuss variable temperature powder X-ray diffraction (PXRD) data recorded from $(FAPbI_3)_{0.85}(MAPbBr_3)_{0.15}$. The perovskite was synthesised and prepared as described in the 'Experimental Methods' section, and all spectroscopic measurements in Section 2.2 and 2.3 were made on such polycrystalline films. An SEM image of a typical thin film is shown in Figure C.1 in Appendix C. To collect PXRD data, a powder was created by scraping thin films from substrates using a razor blade. PXRD data was then recorded at regular temperature intervals while cooling the powder from 315 K to 80 K, and subsequently while re-heating it from 80 K to 350 K.

We plot XRD patterns recorded on cooling and heating cycles in Figure 6.1**A** and Figure 6.1**B**, respectively. We can immediately identify strong scattering peaks at $Q = 0.997$ and 1.996 $Å^{-1}$, which we associate with the (100) and (200) crystal planes of the

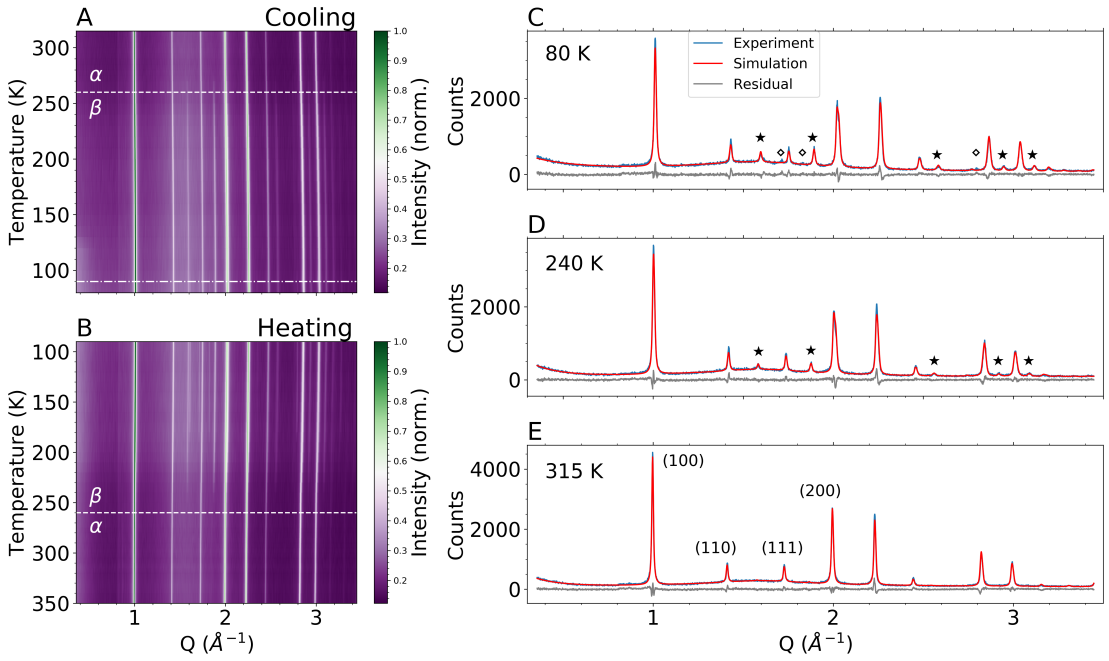

Figure 6.1: Variable temperature PXRD characterisation of powder samples of $(FAPbI_3)_{0.85}(MAPbBr_3)_{0.15}$. Temperature-dependent powder X-ray scattering measurements across a wide Q-range whilst **A** cooling from 315 K to 80 K and **B** heating from 90 K to 350 K. PXRD line profiles for the sample at **C** 80 K (in the proposed γ phase), **D** 240 K (representative of the intermediate β phase) and **E** 315 K (the high temperature pseudo-cubic α phase). Peaks marked ★ denote peaks which are characteristic of the β phase; ◇ denotes further additional peaks which are characteristic of the γ phase, which have not been fitted with the structural model.

cubic phase, respectively. We also observe weaker scattering features at 1.412 and 1.728 Å^{-1}, which correspond to the (110) and (111) crystal planes of the cubic phase, respectively. Careful inspection of Figure 6.1**A** and Figure 6.1**B** also reveals that there is a gradual shift of all peaks to larger Q at low temperature; this result is consistent with a thermally-induced contraction of the lattice, as we discuss below. It is apparent that as the temperature is reduced to ∼260 K a series of additional peaks appear at 1.583, 1.879 and 2.560 Å^{-1}. The emergence of these peaks can be seen more clearly in Figs. C.2–3 (Appendix C), which display the full PXRD patterns at all temperatures on both cooling and heating.

For completeness we show the normalised peak positions and peak widths (full width at half-maximum) as a function of temperature in Figure C.4 (Appendix C), which were fitted using a Pearson VII empirical profile. The peaks shift to smaller Q-values as the temperature is increased, with a broadening in the distribution of peak positions observed above 270 K. We also find that as the temperature is reduced between 270 K and 210

K many of the peaks broaden. We attribute much of this broadening to different crystallographic planes no longer being equivalent as the symmetry of the unit cell changes on cooling. For example, the (100) plane becomes inequivalent to (001), resulting in a splitting of peaks. Interestingly, we observe upon heating that the temperature range over which this behaviour is observed shifts to 230-270 K.

To obtain structural information from our scattering data, we have used Rietveld refinements, with details of the modelling given in the 'Experimental Methods' section. Figure 6.1**C**-**E** plots the measured and simulated XRD patterns for 80 K, 240 K and 315 K together with the residuals. The refined models fit well to the experimental data, and this analysis has allowed us to identify a series of different structural changes that occur across the studied temperature range. Specifically, above 260 K we propose that the material assumes a pseudo-cubic α phase approximating the space group $Pm\text{-}3m$, as previously reported for single-cation perovskites.[23,24] This phase is denoted by α in accordance with previous studies referring to a photoactive cubic phase for hybrid perovskites.[19,25] Over the temperature range 250-90 K, the material appears to adopt a pseudo-tetragonal phase resembling space group $P4/mbm$. This intermediate tetragonal phase has been observed in a study on $FAPbI_3$ by Weber *et al.*; here we refer to it as the β phase, using the notation convention of Weber and colleagues.[26] As the temperature is reduced below 90 K, the material assumes a structure which we suggest is a variation on the β phase. This phase (as seen in $FAPbI_3$ where it appears below $\sim$140 K) has also been identified as $P4/mbm$ and is denoted as the γ phase.[27,28] For each proposed phase, we have included a schematic of the modelled unit cell in Figure 6.2**C**-**E**.

Our identification of these phase transitions is largely based on the temperature dependence of two key parameters: the tilt angle of the lead-halide-lead bond and the lattice parameter ratio $c\sqrt{2}/a$.

In Figure 6.2**A**, we explore the tilt angle formed by the Pb-X-Pb bonds as a function of temperature, where X denotes the halide. The Pb-X-Pb bond angle in the pseudo-cubic α phase has a value of $\sim$176°. As the temperature is reduced between 275 K and 250 K we clearly observe a gradual tilting of the Pb-X-Pb bond, with the angle reducing to between $161° < x < 170°$ as the structure adopts a pseudo-tetragonal β phase. We

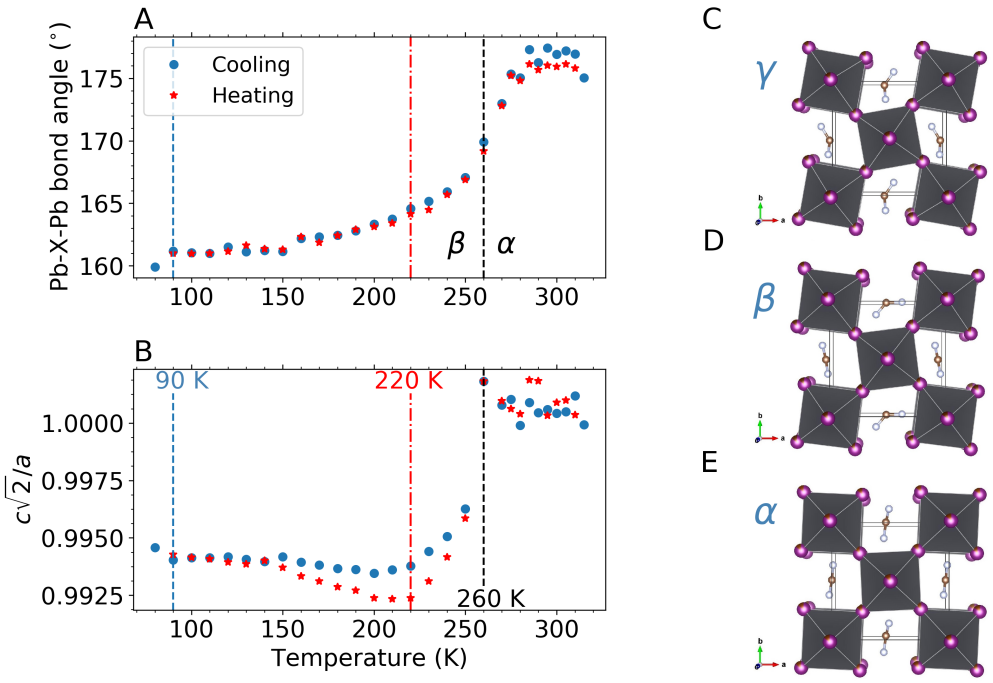

Figure 6.2: Temperature dependence of **A** the Pb-X-Pb bond angle and **B** the reduced lattice parameter ratio $c\sqrt{2}/a$. These parameters have been extracted from the Rietveld refinement model applied to the PXRD data, upon both heating and cooling of the sample. Proposed unit cells for the **C** γ phase (below 90 K), **D** β phase (pseudo-tetragonal, 90-250 K) and **E** α phase (pseudo-cubic, above 260 K), generated from the Rietveld models.

note that Fabini and coworkers studied the structure of the perovskite $FAPbI_3$ as a function of temperature, observing a similar gradual change in Pb-I-Pb bond angle for the α to β phase transition. Fabini *et al.* also found that as the rate of change of this angle decreased, the $FAPbI_3$ perovskite subsequently underwent a β to γ phase transformation.[29] This is in contrast to the results shown in Figure 6.2**B**, where the bond angle gently plateaus after the phase transformation; this result is suggestive of a stabilisation of the β phase over a larger temperature range.

Using our structural model, we have also determined the unit cell parameters along the *a*, *b* and *c* axes as a function of temperature from the experimental data, as shown in Figure C.5 in Appendix C. This figure also shows the volume of a single lead-halide octahedron, plotted as a functio of temperature. We can use the linear change in the octahedral volume to determine the volumetric thermal expansion coefficient (α_V) of the different perovskite phases. Here, we find that α_V in the α phase is around 154×10^{-6} K^{-1}. However in the β phase, α_V could best be described by a second order polynomial, suggesting a dramatic change in the thermal expansion coefficient;

this result is consistent with the presence of additional processes driving the expansion which accompany changes in bond length – for example changes in the Pb-X-Pb bond angles. When we separate the volumetric thermal expansion into linear thermal expansion along the different crystal axes, we find that changes in the *a*-axis appear linear with temperature, whereas changes in the *c*-axis define the non-linear shape observed in the volumetric expansion shown in Figure S4.

Figure 6.2**B** plots the ratio $c\sqrt{2}/a$ as a function of temperature, where a and c are lattice parameters along the a and c axes. In comparing the cubic and tetragonal unit cells the c/a ratio is fundamental to differentiating these systems. In this case we use the reduced lattice parameter ratio $c\sqrt{2}/a$, where the scaling factor of $\sqrt{2}$ is included to make the lattice parameters of the cubic unit cell comparable to those of the tetragonal unit, which is based on the modelled two-octahedra unit cell. It can be seen that $c\sqrt{2}/a$ has a complex dependence on temperature, but apparently reaches a minimum around 200-220 K on both cooling and re-heating. As the rotation of the PbX_6 octahedra occurs about the *c*-axis, it is expected that the $c\sqrt{2}/a$ ratio in the β phase will exceed unity in accordance with previous findings.[29] In Figure 6.2**B** however we observe exactly the opposite, and this peculiarity requires further investigation—for example through neutron diffraction experiments, which should provide sensitivity to the contributions of the organic cations.

At 90 K upon heating the sample, there is a discontinuity observed in the Pb-X-Pb bond angle (Figure 6.2**A**), a process that is also accompanied by a sudden drop in the $c\sqrt{2}/a$ ratio as shown in Figure 6.2**B**. Interestingly, we also observe weak scattering features at Q = 1.72, 1.83 and 2.80 Å^{-1} at this same temperature. This observation suggests a possible phase change between 80 and 90 K. We note that Weber and coworkers observed a low temperature γ phase during cooling of the β phase in a neutron diffraction study of $FAPbI_3$, and this γ phase included additional weak peaks which were attributed to the FA being rotationally locked in a variety of positions.[26] However the contribution of FA cations to the total scattering is insignificant compared to that of the PbX framework (see Figure C.6 in Appendix C), therefore the orientation of the FA cation remains unresolvable here.

The origin of the weak additional peaks observed at 90 K is unclear, as we were unable to fit them with the Rietveld model. We find that these peaks persist on heating past the suggested γ to β phase change and up to $\sim$220 K. During heating from 150 K to 220 K, the values of the $c\sqrt{2}/a$ ratio (Figure 6.2**B**) are lower than those observed on cooling. This temperature range apparently coincides with the region in which these unidentified peaks persist on re-heating. Furthermore, these additional peaks disappear around the temperature at which $c\sqrt{2}/a$ reaches its minimum value. It is possible that such hysteresis effects may be related to a restriction of movement in the structure, or may be caused by the presence of an additional phase in the material associated with the unidentified peaks. The structural features associated with these peaks may have an energy barrier to their formation and/or to their assimilation into the tetragonal phase; such a phenomenon would explain the temperature difference between the appearance and disappearance of the unassigned peaks. It may also explain the thermal hysteresis in the peak broadening behaviour as discussed above.

6.2.2 Absorption and Photoluminescence

In this section, we report on the optical properties of a $(FAPbI_3)_{0.85}(MAPbBr_3)_{0.15}$ thin film, measured while the film was heated from 4 K to 300 K, with full experimental details given in Section 6.4.

We first discuss temperature-dependent absorbance and photoluminescence (PL) spectra as shown in Figure 6.3**A** and Figure 6.3**B**, respectively. Here it can be seen that the absorption edge undergoes a blueshift as temperature is increased from 4 K to 300 K, a process which is accompanied by a similar blueshift of the PL emission maximum. We have extracted the optical band gap from the photoluminescence spectra by applying a Jacobian transformation to the intensity data at each temperature and fitting a Gaussian function to the resultant emission peaks. Using this, the band gap is then determined by the mean of the Gaussian. We have additionally determined the band gap from the absorbance spectra for each temperature using Tauc plots.[30] We note here that there is likely to be a systematic error in the energy-value of the band edge determined here, due to the contribution of excitonic absorption to the absorbance spectrum as described

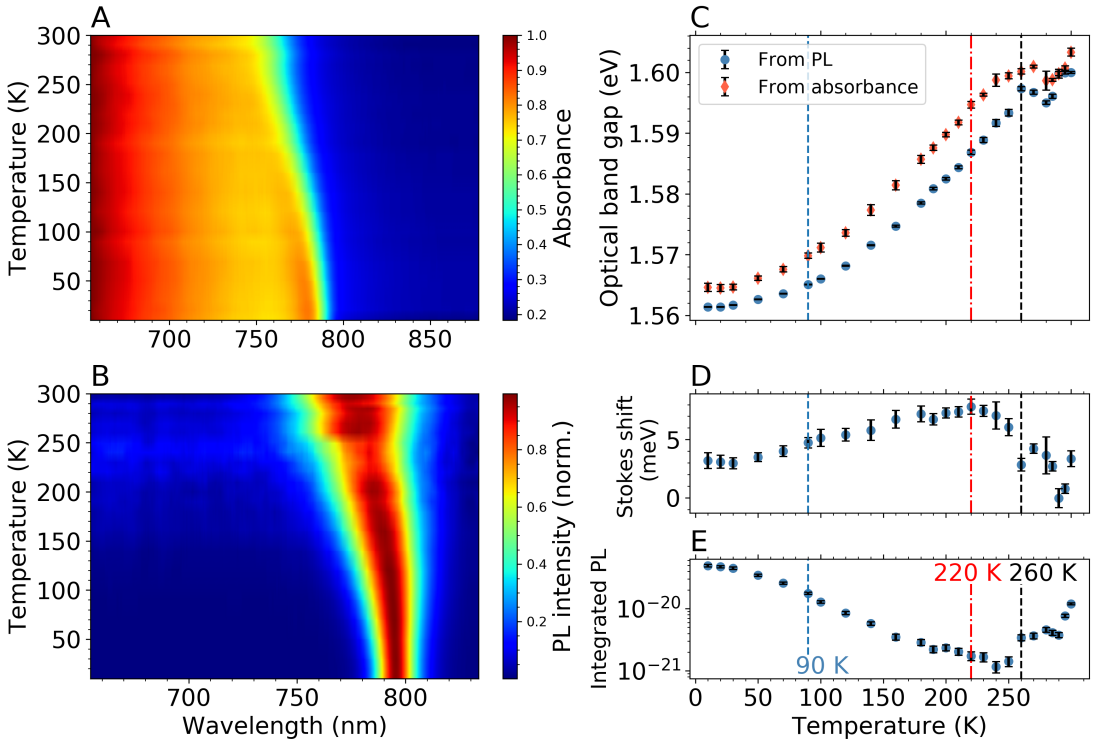

Figure 6.3: Temperature dependence of **A** the absorption spectra and **B** the PL spectra for $(FAPbI_3)_{0.85}(MAPbBr_3)_{0.15}$ perovskite thin films on heating from 4 K to 300 K. **C** Variation of the band edge with temperature, as extracted from PL (blue circles) and absorbance (orange diamonds) spectra in **A** and **B** respectively. Variation of the **D** Stokes shift and **E** integrated photoluminescence with temperature from 4 K to 300 K. Vertical dashed lines correspond to key temperatures where we see changes in structural configuration upon heating of the material - 90 K (blue), 220 K (red) and 260 K (black).

by Elliott's theory of excitons.[31]

We plot the temperature-dependent optical band gap determined using both experimental methods in Figure 6.3**C**. Here it can be seen that the optical band gap as determined from the PL emission spectra undergoes an increase of ∼34 meV over the entire temperature range. Interestingly, the band gap increase is not monotonic across the whole temperature range, but rather it reaches a local maximum at ∼260 K and then reduces slightly up to ∼280K, where it begins to increase again. This behaviour is also apparent in the temperature-dependent band edge values extracted from the optical absorbance, where a discontinuity in the trend is observed at ∼270 K. Another notable feature of the band gap variation is a small change in gradient at ∼90-100 K.

The empirical Varshni relation is generally used to describe the evolution of the band gap (E_g) of a semiconductor with temperature (T), with many semiconductors exhibiting a reduction in band gap with increasing temperature as a result of electron-

phonon interactions and lattice expansion. The Varshni relation is as follows:

$$E_g(T) = E_g(T=0) - \frac{\alpha T^2}{T+\beta} \tag{6.1}$$

where α and β are material constants.[32] Clearly the positive value of dE_g/dT that we observe in this perovskite is inconsistent with the Varshni relation, with similar behaviour being reported previously in $MAPbI_3$.[33,34] Recent calculations show that this is a result of the reduction in the overlap of Pb-6s and I-5s orbitals, which causes a decrease in the valence band maximum as the lattice expands.[35,36]

Our measurements show that the band gap energy undergoes a slight redshift above 260 K, and the blueshift resumes at ∼280 K. This discontinuity is indicative of a temperature range in which a structural phase transition occurs, with this effect observed in previous studies on a range of different perovskite compositions.[27,37] For example, Zheng and coworkers reported a redshift in E_g of $(FAPbI_3)_{0.8}(MAPbI_3)_{0.2}$ between 100 K and 160 K which they attributed to a phase transition occurring gradually between the low temperature orthorhombic and the intermediate tetragonal phases.[38]

As detailed in Section 2.1, our PXRD measurements have revealed that, when cooling the sample, there is a high temperature phase transition from the pseudo-cubic phase to a tetragonal β phase at 260 K, and a low temperature phase transition that occurs between 80 K and 90 K. Upon reheating of the sample past 90 K, an intermediate structural configuration forms and is present up to 210-220 K, resulting in a deviation from the trend in lattice parameters observed upon cooling (see Figure 6.2**B**). Between 220 K and 260 K we observe the same tetragonal β phase as observed upon cooling. To compare trends in spectroscopic parameters with these temperature ranges, we mark these key temperatures on the plots in Figure 6.3; the blue vertical lines indicate 90 K, the red lines indicate 220 K and the black lines indicate 260 K. We deduce that the redshift observed in the band gap above 260 K is likely to be a result of this high temperature transition into the cubic phase. We also postulate that the non-linearity of the blueshift at lower temperatures may be correlated with the low temperature phase transition, as the change in gradient occurs at ∼90-100 K.

We plot the temperature-dependent absorbance spectra at selected temperatures in

Figure C.1 in Appendix C. Here it is apparent that there is an excitonic-like absorption peak located just below the band edge at low temperatures, which is a well-documented phenomenon in the hybrid perovskite material family.[2,39] This begins to flatten at ∼90 K, which is the temperature at which we observe the low temperature γ to β structural phase transition in the PXRD data. We postulate that this excitonic feature appears as a result of this low temperature phase transition, as the exciton binding energy in the low temperature phase is larger than $k_B T$ over this temperature range (4-90 K). A similar effect has previously been observed in $MAPbI_3$ as it transforms to a low temperature orthorhombic phase.[40]

Figure 6.3**D** shows the temperature dependence of the Stokes shift, which has been plotted as the difference between the band edge as determined from Tauc plots and the band gap as extracted from steady state PL emission spectra. It can be seen that the Stokes shift increases in an approximately linear fashion with increasing temperature, starting from 3.19 meV at 10 K. The Stokes shift reaches a maximum of 7.83 meV at 220 K, where the trend reverses, and continues to drop up to 300 K. We note that the Stokes shift can provide a measure of the proportion of the PL emission that originates from sub-bandgap states,[41] therefore a large Stokes shift would suggest a very disordered or defect-ridden material. In general, the distribution of sub-bandgap states decreases exponentially below the band edge, therefore if the participation of these states in the emission is temperature-dependent, then the Stokes shift is likely to follow an exponential distribution (with some associated activation energy). The observed Stokes shift is non-exponential, therefore we speculate that it is more likely to be influenced by polaronic effects,[42] as detailed below.

It has been found in hybrid perovskites that photoexcitation causes significant lattice deformation,[43] and therefore photoexcited electrons or holes may be localised by their own distortion field,[44] giving rise to self-trapped electrons (STEs) or holes, which then may form small polarons through interactions with LO phonons.[45,46] These interactions have been shown to lead to an elevated Stokes shift in lead halide and perovskite structures.[47,48] Here we find that the Stokes shift-temperature gradient reverses at 220 K, a temperature which coincides with a change in the temperature gradient of the ratio

$c\sqrt{2}/a$ on heating of the material (see Figure 6.2**B**). This correlation suggests that the Stokes shift is influenced by the shape and size of the unit cell. This observation supports our hypothesis that polaronic effects are the origin of the temperature dependence of the Stokes shift, because the shape of the unit cell will affect its polarisation and therefore influence the interaction between STEs and phonons.

We note that the broadening of the emission linewidth with increasing temperature that is observed in Figure 6.3**B** is consistent with other observations in hybrid lead halide perovskites.[33,35,49] It has been proposed that the dominant mechanism for these broadening effects is Fröhlich coupling of photoexcited charge carriers with LO phonon modes.[50,51] We believe that these polaronic effects, originating from Fröhlich interactions between self-trapped electrons and phonon modes, are consistent with our observation of a Stokes shift which increases with temperature.

Figure 6.3**E** plots the CW integrated PL emission intensity derived from Figure 3B. It can be seen that there is a near logarithmic decrease in the PL intensity with increasing temperature. This decrease in intensity indicates the activation of a series of thermally-induced non-radiative recombination centres as the film is heated.[52,53] Interestingly, there is a departure from this trend at ~260 K, with the PL intensity increasing with increasing temperature. This temperature apparently coincides with the transition from the tetragonal β phase to the pseudo-cubic α phase observed in the PXRD data. This observation suggests a reduction in non-radiative recombination rates in the pseudo-cubic phase.

6.2.3 Recombination Dynamics

Recombination dynamics in photovoltaic cells are governed by three different recombination pathways, each of which depends to a different degree on the charge carrier density in the conduction band, n. The rate of change of n is given by:[54]

$$\frac{dn}{dt} = -k_3 n^3 - k_2 n^2 - k_1 n \tag{6.2}$$

The constant k_1 describes the rate of monomolecular recombination. In the perovskite $MAPbI_3$ it has been shown that the predominant monomolecular process is trap-assisted

recombination, because the exciton binding energy of hybrid perovskites at room temperature is significantly lower than the thermal energy.[55] The rate constant k_2 corresponds to bimolecular processes such as electron-hole recombination, which are more heavily dependent on the charge carrier density. In the hybrid perovskites investigated here, we expect this to be largely radiative recombination of free electrons and holes, as the dominant species in $MAPbI_3$ at room temperature has been shown to be free carriers.[56] The third order constant k_3 is the Auger rate constant, which describes the rate of any three-body recombination process mediated either by a third charge carrier or a phonon.

In this study we used a streak camera to obtain time-resolved photoluminescence (TRPL) data, at a series of temperatures from 77 K to 315 K, using a pulsed laser focussed onto the sample with a resultant excitation fluence of 3.1 μJcm^{-2}. Full streak camera data shown in the Supporting Information (Figs. C.8–9) indicates a broadening in the emission peak with increasing temperature, a finding that is in agreement with the steady state PL data obtained from continuous wave measurements (see Figure 6.3**B**). Another key observation from this data is an increase in the apparent PL lifetime as we raise the temperature from 77 K to 200 K, followed by a decrease which continues up to $\sim$ 290 K. This suggests that there is a decrease in the radiative recombination efficiency as the temperature is raised up to 200 K, with a subsequent increase in this quantity at higher temperatures.

We also analysed the temperature dependence of the PLQY to supplement our findings. The PLQY of the thin films was measured using an integrating sphere at room temperature, with PL excited with a pulsed laser at $\sim$3 μJcm^{-2}, i.e. the same fluence we used for the TRPL measurements. The sample was then transferred to a cryostat and time-integrated PL emission was collected with a streak camera, at the same set of temperatures used for the TRPL measurements, again at a fluence of $\sim$3 μJcm^{-2}. By scaling the room temperature PLQY value to temperature-dependent values of the integral PL, we obtained the PLQY as a function of temperature (see Supplementary Note 2 in Appendix C for details). Figure 6.4**A** plots the PLQY of the film determined as a function of temperature. It can be seen that the PLQY is effectively constant at temperatures up to 100 K, but then decreases up to $\sim$270 K, after which it

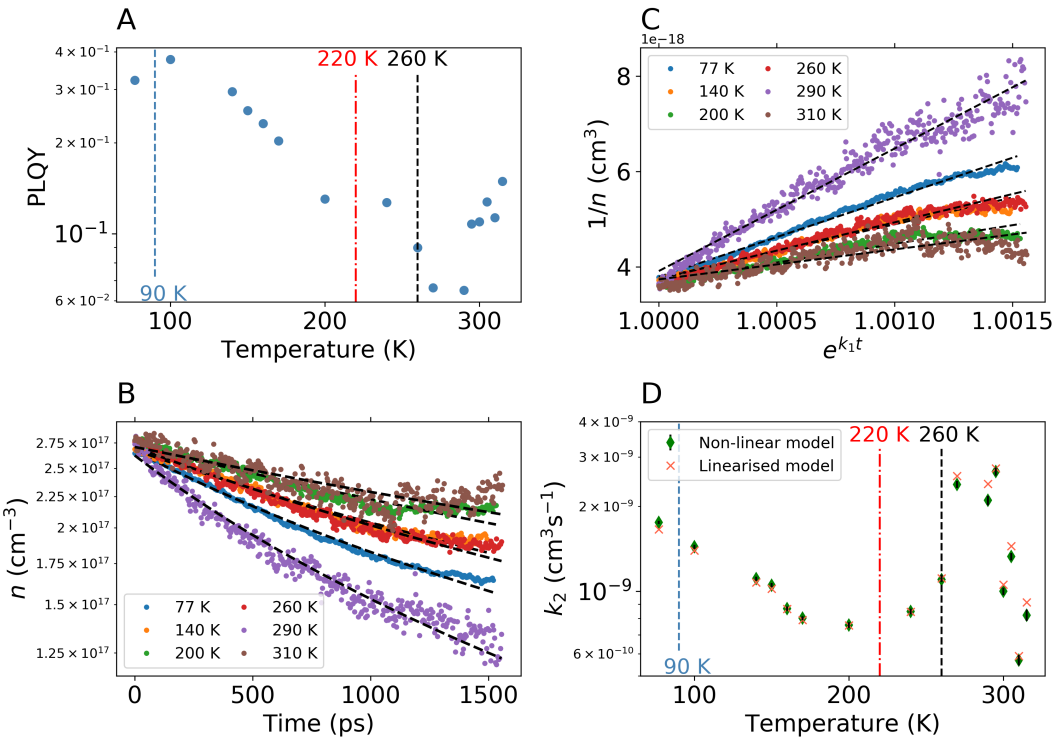

Figure 6.4: **A** Temperature dependent values of the PLQY for $(FAPbI_3)_{0.85}(MAPbBr_3)_{0.15}$, as scaled from the room temperature value using the method shown in the Appendix C. **B** Charge carrier density n as a function of time as calculated from PL decay traces extracted from streak camera images, taken at a laser fluence of 3.1 μJcm^{-2}. Dashed black lines denote fits to the data using the analytical solution to the rate equation, from which temperature-dependent values of k_2 were extracted. **C** Plot of $1/n(t)$ vs $e^{k_1 t}$, which allowed us to linearise the model from Equation (6.4) and extract values of k_2 by fitting a linear regression to the data. Dashed black lines denote linear fits. **D** Temperature dependence of the bimolecular recombination rate k_2 as determined from fits shown in **B** and **C**. Vertical dashed lines in **A** and **D** correspond to the key temperatures where we see changes in structural configuration upon heating of the material - 90 K (blue), 220 K (red) and 260 K (black).

undergoes an increase up to 315 K. These results are consistent with changes in bimolecular radiative recombination rates as we demonstrate below, although there may also be contributions to such effects from changes in non-radiative processes.

Bimolecular Recombination Rates

To analyse the TRPL streak camera images, we have selected data at a time delay of < 1600 ps by averaging time-resolved PL intensity data across the central two-thirds of the peak emission spectrum. We utilised rate equation (6.2) to attempt to quantify the bimolecular recombination rate k_2 as a function of temperature. Here we consider a simplified version of Equation (6.2) given by:

$$\frac{dn}{dt} = -k_2 n^2 - k_1 n \tag{6.3}$$

Buizza *et al.*[57] recently presented an analytical solution to this modified form of the rate equation, which is as follows:

$$n(t) = \frac{k_1 \alpha}{e^{k_1 t} - \alpha k_2} \quad for \quad \frac{1}{\alpha} = \frac{k_1}{n_0} + k_2 \tag{6.4}$$

where n_0 is the initial charge carrier density. This model assumes that the charge carrier density is low enough such that Auger recombination has a negligible effect on the PL emissions. The TRPL data presented here was collected at a laser excitation fluence of $\sim$3 μJcm^{-2}, which corresponds to an initial charge carrier density of n_0 $\sim 10^{17}$ cm^{-3} in the $(FAPbI_3)_{0.85}(MAPbBr_3)_{0.15}$ film. It has been shown in lead halide perovskites that PL signal is proportional to n^2 at excitation densities in the region $10^{17} < n_0 < 10^{18}$, demonstrating that bimolecular recombination dominates the PL dynamics at these fluences and that Auger processes make a negligible contribution.[58]

Using the approximation that the PL signal is proportional to n^2,[59] we scaled the PL decay traces using the relation $n(t) = \sqrt{\frac{I(t)}{I_0}} n_0$ where $I(t)$ is the time dependence of the PL intensity. A selection of data processed in this way is shown in Figure 6.4**B**, where we plot the charge carrier density as a function of time at a selection of different temperatures. In order to obtain estimates of k_2, we fitted the $n(t)$ curves to Equation (6.4). To obtain an estimate for the temperature-dependent monomolecular rate k_1, we collected TRPL traces at low fluence ($\sim$ 30 nJcm^{-2}) via TCSPC measurements, at a series of temperatures from 77 K to 300 K (see Figure C.2 in Appendix C). At such a low excitation fluence (equivalent to a photoexcited carrier density of $n_0 \sim 10^{15}$ cm^{-3}), the density of electron traps will be much larger than the concentration of photoexcited electrons. A consequence of this is that electron-hole recombination is almost monomolecular and is solely determined by the rate of trapping, and thus the PL decay rate reflects the monomolecular recombination rate k_1.[60] We therefore fitted these traces to an exponential model (see Supplementary Note 3 in Appendix C for full details) to obtain approximate values for k_1, which were in the range $\sim$ 1-3 $\times 10^6$ s^{-1} at all temperatures, which is in good agreement with previous studies on similar hybrid perovskites.[61,62] These values of k_1, which correspond to lifetimes on the order of 100s of ns, will have a negligible effect on the TRPL dynamics, because the streak camera

only probes time dynamics up to a maximum delay of 1.6 ns. As a result, we fix k_1 at 10^6 s^{-1} for all temperatures.

Fits to the data from the analytical solution expressed in Equation (6.4) are shown as dashed black lines in Figure 6.4**B**. We have also extracted k_2 values using a linearised version of Equation (6.4), using a similar method to that of Shaw *et al.*, who analysed the bimolecular process of exciton-exciton annihilation.[63] Linearised data and fits are shown in Figure 6.4**C**. Our extracted value of k_2 at room temperature is 9.98 $\times 10^{-10}$ cm^3s^{-1}, which is in reasonable agreement with reported values of k_2 in hybrid perovskites: 1.1 $\times 10^{-10}$ cm^3s^{-1} ($FAPbI_3$); 11 $\times 10^{-10}$ cm^3s^{-1} ($FAPbBr_3$);[62] and 9.2 $\times 10^{-10}$ cm^3s^{-1} ($MAPbI_3$).[64] The temperature dependence of the quantity k_2, as extracted from fits to the analytical solution, is shown in Figure 6.4**D**. Starting from 77 K, we find that k_2 decreases with increasing temperature, and reaches a minimum value at around 200 K. This trend in k_2 is consistent with previous experimental and theoretical results presented for $MAPbI_3$ over this temperature range.[21,64] Above 200 K, k_2 increases and reaches a maximum value at 290 K, from which point it again undergoes a decrease as temperature is increased to 315 K. Values of k_2 from the linearised model show very good agreement with those extracted from the analytical solution, but there is increased scatter in the data above 260 K, suggesting that the model employed here does not fully describe the PL dynamics in this temperature range—most likely resulting from higher order recombination processes for which the model cannot account.

Interestingly, we find that the decrease in PLQY observed as the temperature is increased to 200 K (Figure 6.4**A**) correlates with decreasing bimolecular rates, however above this temperature, the PLQY continues to decrease up to $\sim$280 K while we see an apparent increase in k_2. This suggests it is not just bimolecular recombination rates that affect the quantum yield over this temperature range, but that higher order non-radiative processes also become important.

We suspect that the observed reduction in k_2 with increasing temperature between 100 K and 200 K, and again between 290 K and 315 K, may result from a decrease in charge carrier mobility within the framework of the Langevin model. Indeed, it is known that a decrease in electron mobility occurs on increasing temperature in hybrid

lead halide perovskites.[65,66] Such reduced carrier mobility will reduce the likelihood that electrons and holes will move within each other's joint Coulomb capture radii, thereby reducing the bimolecular recombination rate.

The Langevin model has however been shown to overestimate k_2 in hybrid lead halide perovskites,[33,67] and thus this theory is not sufficient to predict temperature-dependent recombination rates. Recent theoretical work has used the Shockley-van Rooesbroeck relation,[68] which describes the radiative recombination rate as a function of temperature using the following:

$$R_{RAD} = \int_0^\infty \rho(E, T)P(E, T)dE \tag{6.5}$$

where $\rho(E, T)dE$ is the density of photons in the material in the interval dE, and $P(E, T)dE$ is the probability per unit time that a photon of energy E is absorbed.[64] The quantity R_{RAD} can then be used to find the bimolecular recombination rate k_2, which is predicted to decrease with increasing temperature due to the thermal broadening of the Fermi-Dirac and Bose-Einstein distribution functions. In Figure 6.4**D** we observe a decrease of k_2 on heating the sample from 100 K to 200 K, and thus we conclude that over this temperature range, changes in the recombination rate are indeed dominated by changes in bimolecular recombination. However, this trend does not hold across the entire temperature range, as we observe an increase in k_2 at temperatures between $\sim$200 K and $\sim$290 K. This suggests that, in this temperature region, there is a second effect that competes with the thermal broadening effects and determines the overall recombination rates.

To explore the origin of this competing effect, we revisit our temperature-dependent structural parameters shown in Figure 6.2, which we determined from Rietveld fits to PXRD data. It can be seen in Figure 6.2**B** that the lattice parameter ratio $c\sqrt{2}/a$ reaches a minimum at $\sim$200-220 K on heating, and subsequently increases up to 260 K, where it stabilises again. If we compare this to temperature-dependent trends in k_2, we observe that this rate also reaches a minimum at $\sim$200 K. As was shown earlier, the magnitude of the Stokes shift is also influenced by such changes in structural configuration, with this effect most likely to result from polaronic effects rather than from changes in the

distribution of sub-bandgap states. Therefore we suggest that polaronic effects arising from structural changes on heating of the sample are responsible for the deviation of k_2 from the trend predicted by the Shockley-van Rooesbroeck model between 200 K and 290 K. One possible mechanism for this is defect tolerance induced by the formation of large polarons.[69]

6.3 Conclusions

In summary, we have presented experimental evidence for two structural phase transitions occurring in $(FAPbI_3)_{0.85}(MAPbBr_3)_{0.15}$ upon cooling and heating between 350 K and 80 K. The material exists in a pseudo-cubic α phase at room temperature, and transforms to a pseudo-tetragonal β phase at around 260 K. We also present evidence for the occurrence of a low temperature phase transition at approximately 80-90 K, where the material assumes a structure which can be most accurately described as a variation on the tetragonal phase with reduced symmetry. Our identification of such transitions is based on an analysis of temperature-dependent changes in structural parameters such as the Pb-X-Pb tilt angle and unit cell volume, which have been determined from Rietveld refinements applied to the XRD data. The β phase appears to stabilise over a large temperature range. The reduced lattice parameter ratio $c\sqrt{2}/a$ exhibits a complex temperature dependence which may suggest an intermediate structural configuration or the presence of an additional phase in the 100-220 K region.

We have observed that the optoelectronic properties of this material depend strongly on temperature, exhibiting trends that correlate with identified phase transitions and other changes in structural configuration. We have shown that the integrated PL intensity is correlated with the phase behaviour, with this quantity increasing by $\sim$60% when the material undergoes a phase transition to the pseudo-cubic perovskite phase. Our measurements also reveal a complex dependence of the Stokes shift on temperature, and this trend correlates with changes in the reduced lattice parameter ratio $c\sqrt{2}/a$.

Furthermore, we have demonstrated that bimolecular recombination rates in this material have a negative temperature gradient in the pseudo-tetragonal phase up to $\sim$200 K, which is consistent with the predictions of the Shockley-van Rooesbroeck model

for radiative recombination. At a temperature of ∼200 K, this trend reverses, coinciding with changes in the lattice parameter ratio $c\sqrt{2}/a$ as determined from temperature-dependent PXRD data. We have suggested that these changes in crystal structure lead to polaronic effects which compete with the thermal broadening as described by Shockley-van Rooesbroeck in determining recombination rates. We therefore propose, with evidence from steady state and time-resolved PL data, that changes in the size and shape of the unit cell alter the emission properties, and suggest that this may be due, at least in part, to polaron formation in the material.

Finally, we note that the observed high temperature phase transition to the pseudo-cubic perovskite phase is within the expected operating temperature range of a photovoltaic cell, when used under outdoor conditions. This will clearly affect the photovoltaic performance of cells based on $(FAPbI_3)_{0.85}(MAPbBr_3)_{0.15}$, through its effect on the band gap (and therefore the available V_{OC}). Encouragingly however, the low temperature of the tetragonal-cubic phase transition relative to $MAPbI_3$ makes this material more thermally stable—a property that will be advantageous to long-term stable photovoltaic cell operation.

6.4 Experimental Methods

Materials Fabrication: $MAPbBr_3$ solution (1.3 M) was made by dissolving MABr (Greatcell) and $PbBr_2$ (TCI UK Ltd.) in a 4:1 mixture of anhydrous N,N-dimethylformamide (DMF) to anhydrous dimethyl sulfoxide (DMSO) (Sigma Aldrich). $FAPbI_3$ solution (1.3 M) was also made by dissolving FAI (Greatcell) and PbI_2 (99.99%, TCI UK Ltd.) in a 4:1 DMF:DMSO mixture. Next the $FAPbI_3$ solution (0.85 mL) and the $MAPbBr_3$ solution (0.15 mL) were mixed to give the desired composition.

The solution was then thoroughly vortex-mixed, before being syringe filtered and spread onto a synthetic quartz-coated substrate that had been cleaned and UV-ozone treated. The solution was then spin-coated according to the following regime: substrate was accelerated from 0 to 2000 rpm at 200 rpms^{-1}, then held at 2000 rpm for 10 s. It was then accelerated from 2000 to 6000 rpm at 2000 rpms^{-1}, and held at 6000 rpm for 20 s. An antisolvent quench of 100 μL of anhydrous chlorobenzene (Sigma Aldrich) was

dripped onto the film 10 s before the end of this final step. The film was then heated at 100° C for 30 minutes.

Powder X-Ray Diffraction Measurements: Thin film samples were prepared via the protocol above and scraped from the substrate using a razor blade; the resultant fine powder was loaded into a 0.7 mm borosilicate capillary. Powder diffraction data were obtained using a Bruker D8 Advance powder diffractometer using CuKα radiation and equipped with focusing Göbel mirrors and a high resolution energy-dispersive Lynxeye XE detector. Data were collected in a Debye-Scherrer geometry with rotating capillary stage. Sample temperature for in situ heating studies was controlled by a co-axial stream of dry nitrogen gas from an Oxford Cryosystems Cryostream 700 Plus, with a flow rate of 5 L/min.

Powder X-Ray Diffraction Modelling: Structural information modelling of the variable temperature powder X-ray diffraction (PXRD) data was performed primarily using structure model based Rietveld refinements with a fundamental parameters (FP) approach. FP involves refining an instrument profile to describe the intensity and broadening characteristics of the diffractometer used. This allows greater accuracy of the peak positions and uses fewer free parameters, improving the stability of the refinements. The instrument profile was refined against a silicon standard. The space group assignments made are based on the symmetry of the PbX_6^{4-} octahedra.

The model used in the Rietveld refinements employed a model based on the $P4/mbm$ space group in which the halide mixture (substitution) has been accounted for using site occupancy factors; this assumes that the different halides are uniformly distributed across the halide sites. The contribution of the organic cations to the PXRD pattern is minimal as seen in Figure C.6 (Appendix C), thus the effect of the 15% MA on the diffraction pattern was considered negligible. FA was excluded from the symmetry constraints of the phases. Pb was allowed movement in the $ab-$plane by adjusting site occupancies and replicating Pb as per the $P4$ symmetry. The refinements were performed using TOPAS v5 (Bruker) The data was fitted using Monte-Carlo assisted sequential Rietveld refinements with TOPAS v5 (Bruker). Along with the symmetry constraints of the model this method was essential in stabilising the refinements.

Analytical Pearson VII functions[70] were applied in separate refinements which can be found in Appendix C (Figure C.4). The Pearson VII fits provide a more direct observation of the changes in apparent peak position and width.

Absorption and Steady State Photoluminescence: For absorption measurements, samples were illuminated with a deuterium-halogen lamp (Ocean Optics) and transmitted light was collected in an optical fibre and passed to an Ocean Optics HR2000+ES spectrometer to obtain spectral data. For PL measurements, samples were illuminated with a 405 nm CW laser at 800 μW in reflection mode and PL emissions were collected in the aforementioned spectrometer. Samples were cooled to 4 K using an Oxford Instruments OptistatDry cryostat, and absorption and PL measurements were taken at regular intervals as the system was heated back to room temperature.

Streak Camera Measurements: The samples were excited with 515 nm wavelength pulses of 200 fs duration generated from the second harmonic of a regeneratively amplified femtosecond laser system (Pharos from Light Conversion) with a repetition rate of 100 kHz. The excitation spot diameter was 175 μm. The emitted light was resolved spectrally using a Princeton Instruments Acton SpectraPro SP-2300 spectrograph, and temporally using a Hamamatsu Streak camera (C10600 Orca-R2 coupled to a M10911 synchroscan unit). Samples were cooled by liquid nitrogen in a bath cryostat.

Photoluminescence Quantum Yield: The photoluminescence quantum yield (PLQY) was measured by using 200 fs duration 515 nm laser pulses at 100 kHz (Pharos from Light Conversion) focused to a 175 μm spot diameter on the sample in an integrating sphere. The emitted light was collected using an optical fiber and spectrally resolved using an Oriel Instruments 77400 spectrometer coupled to an Andor iDUS420-BV CCD camera. The spectral sensitivity of the system was scaled using a calibrated quartz tungsten halogen lamp Bentham CL6-H. The room temperature PLQY was obtained using the method described by de Mello *et al.*[71] Temperature-dependent time-integrated PL emission was recorded using a Hamamatsu streak camera with the same excitation density as that used for the PLQY measurement, with the sample cooled using a bath cryostat.

Low Fluence TCSPC Measurements: The samples were illuminated with a 507 nm

pulsed laser (PicoQuant-LDH-510-C) operating at 2.5 MHz with a maximum time delay of 350 ns. Timing electronics were controlled through a TimeHarp 260 (PICO) PCIe board with a time resolution of 100 ps. Photoluminscence was detected with a silicon SPAD (single-photon avalanche diode) detector, without wavelength selection. For temperature-dependent measurements, samples were cooled in an Oxford Instruments MicroStat with continuous flow liquid helium and the sample temperature was monitored by an Oxford Instruments temperature controller.

Crystallographic data

Crystallographic data (excluding structure factors) for the structure(s) reported in this paper have been deposited with the Cambridge Crystallographic Data Centre as supplementary publication no. CCDC 1898355-1898366. Copies of the data can be obtained free of charge from www.ccdc.cam.ac.uk/conts/retrieving.html or on application to The Director at the following address: Cambridge Crystallographic Data Centre (CCDC), 12 Union Road, Cambridge CB2 1EZ, UK.

Supporting Information

Supporting Information is available from the Wiley Online Library or from the author. Within this thesis, it can be found in Appendix C.

Acknowledgements

C.G. and J.A.S. would like to thank the UK EPSRC for funding their PhD studentships via the Centre for Doctoral Training in "New and Sustainable Photovoltaics" (EP/L01551X/1). We also thank the UK STFC and EPSRC for part-funding this work via grants ST/R002754/1 "Synchrotron Techniques for African Research and Technology" and "Hybrid Polaritonics" (EP/M025330/1). A.S. hereby acknowledges the financial assistance of the South Africa National Research Foundation (NRF), University of the Witwatersrand - Material and Energy Research Group (MERG) and DST-NRF Centre of Excellence in Strong Ma-

terials (CoE-SM) towards this research. Opinions expressed and conclusions arrived at are those of the author and are not necessarily to be attributed to the funding organisations.

The authors gratefully acknowledge Dr. Craig C. Robertson from the Department of Chemistry at the University of Sheffield for collecting the PXRD data. C. G. would also like to thank Dr. David Coles and Dr. Kyriacos Georgiou for help with photoluminescence quantum yield measurements.

Conflict of Interest

D.G.L. is a director of the company Ossila Ltd that retails materials and equipment used in perovskite photovoltaic research.

6.5 Additional Material: Fitting Model Based on PLQY

The following material was not included in the final published manuscript, however it still provides an interesting perspective on and discussion of the data, therefore I have included it here.

In addition the the kinetic model described in Section 6.2.3 of the published paper, we also used a simplified model to attempt to quantify the recombination dynamics, using the concept of the photoluminescence quantum yield (PLQY) to attempt to separate contributions to the PL decay dynamics from radiative and non-radiative pathways. The PLQY can be expressed in terms of the radiative (k_r) and non-radiative (k_{nr}) decay rates as follows:

$$PLQY = \frac{k_r}{k_r + k_{nr}} \tag{6.6}$$

where $k_r + k_{nr} = R_{TOT}$, the total recombination rate. If we neglect Auger recombination as justified above, then we can express R_{TOT} in terms of equation (6.2) in the following way:

$$R_{TOT} = -\frac{1}{n}\frac{dn}{dt} = k_1 + nk_2 \tag{6.7}$$

We can then express the PLQY defined by (6.6) as $PLQY = \tau_f/\tau_r$, where τ_r is the radiative lifetime of the material and $\tau_f = 1/R_{TOT}$ is the measured fluorescence decay lifetime.[72] If we take τ_f to be the overall PL lifetime as determined from time-resolved PL emission, we can in principle find the radiative and non-radiative decay rates from the PLQY and τ_f.

As described in Section 6.2.3, we used a streak camera to obtain time-resolved photoluminescence (TRPL) data, at a series of temperatures from 77 K to 300 K, using a pulsed laser focussed onto the sample with a resultant excitation fluence of 3.1 μJcm^{-2}. Sample streak camera data shown in the Supporting Information (see Figs. C.8–9 in Appendix C) indicates a broadening in the emission peak with increasing temperature, a finding that is in agreement with the steady state PL data obtained from continuous wave measurements (see Figure 6.3**B**). To analyse the TRPL streak camera images, we

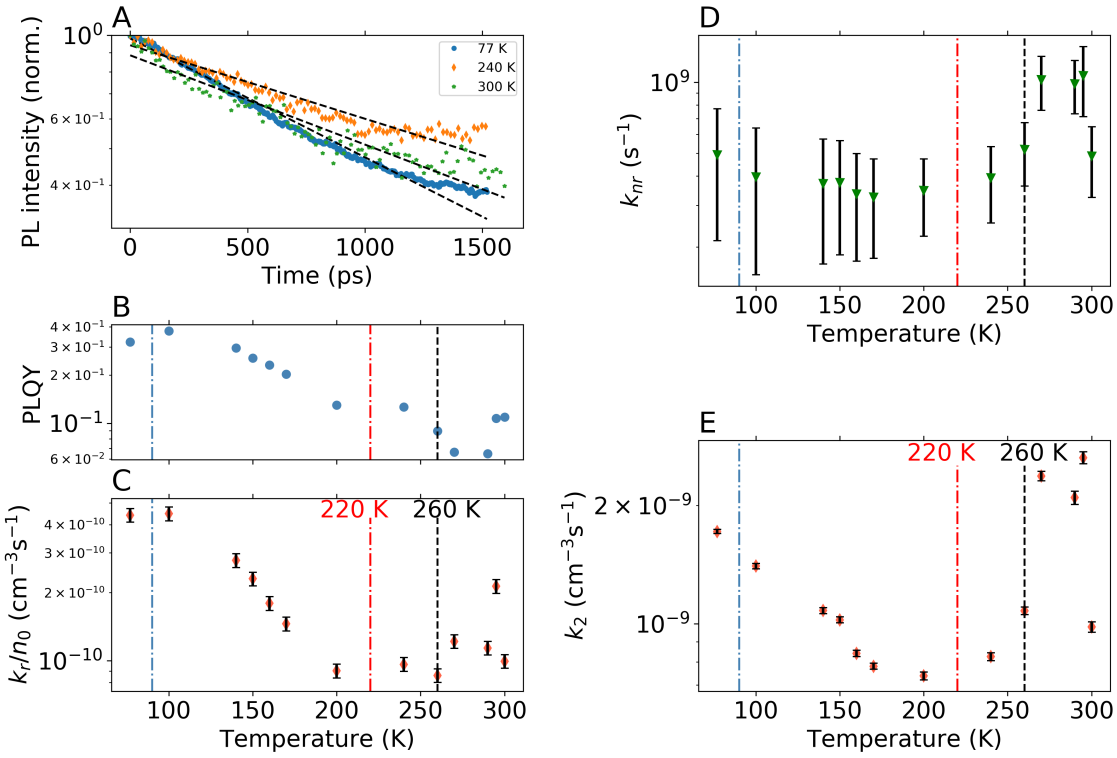

Figure 6.5: **A** PL decay traces extracted from streak camera images taken at a laser fluence of 11.2 μJcm^{-2}. For the full set of streak camera images, see Figs. C.8–9 in the Supporting Information (Appendix C). **B** Temperature dependence of the PLQY. **C** Temperature dependence of the quantity k_r/n_0 where k_r is the radiative decay rate as extracted from the PLQY-based model and n_0 is the estimated initial charge carrier density in the film upon laser excitation. **D** Temperature dependence of the non-radiative recombination rate k_{nr} as determined from the PLQY-based method. **E** Temperature dependence of the bimolecular recombination rate k_2 as determined from fits to the data using the analytical solution to the rate equation. Vertical dashed lines in **B**-**E** correspond to the key temperatures where we see phase transitions upon heating of the material - 90 K (blue) and 260 K (black).

selected data at a time delay of $<$ 1600 ps by averaging time-resolved PL intensity data across the central two-thirds of the emission peak. A selection of data processed in this way is shown in Figure 6.5**A**, where we plot the PL emission intensity as a function of time recorded at a selection of different temperatures at a laser fluence of 3.1 μJcm^{-2}. We find that there is an increase in the overall PL lifetime as we raise the temperature from 77 K to 240 K, with a subsequent decrease in lifetime at 300 K. We have fitted these TRPL decay traces using a single exponential function of the form:

$$I = I_0 e^{-\left(\frac{t}{\tau}\right)} \tag{6.8}$$

where I_0 is the initial PL intensity and τ is the characteristic lifetime of the decay. The R^2 values for the fits shown in Figure 6.5**A** are 0.985 (77 K), 0.939 (240 K) and 0.925

(300 K)—this suggests that there is an increasing divergence from mono-exponential behaviour as the temperature is increased, therefore the PLQY-based model may become less accurate at higher temperatures. From the single exponential fit, we can take τ to be τ_f, the total fluorescence decay lifetime. We use τ_f along with the PLQY value for each temperature to determine k_r and k_{nr} as detailed above.

In order to apply our PLQY-based model to the TRPL data, we first measured the PLQY of the thin films using an integrating sphere at room temperature, with PL excited with a pulsed laser at $\sim$3 μJcm^{-2}, i.e. the same fluence we used for the TRPL measurements. The sample was then transferred to a cryostat and time-integrated PL emissions were collected at the same temperatures as those used for the temperature-dependent streak measurements, again exciting the sample at $\sim$3 μJcm^{-2}—see Section 6.4 for full details. The relative change in integrated PL emission intensity as function of temperature was used to calculate the temperature dependence of the PLQY from the room temperature value, via the method outlined in Supplementary Note 2 in Appendix C. The PLQY as a function of temperature is shown in Figure 6.5**B**. It can be seen that the PLQY increases as a function of temperature up to 100 K, then decreases up to $\sim$270 K, after which it undergoes a slight increase.

Substituting these PLQY values into Equation (6.6), we obtained k_r and k_{nr} as a function of temperature. In this simplified model we assume that the radiative rate is dominated by the bimolecular recombination rate k_2, as expressed by Equation (6.7) with $k_r \approx nk_2$. We have therefore scaled each value of k_r by $n_0(T)$ to obtain a quantity comparable to k_2. Values of k_r/n_0 at a series of temperatures from 77 K to 300 K are shown in Figure 6.5**C**. It can be seen that this quantity decreases as temperature is increased up to $\sim$200 K, but subsequently begins to increase as the film is heated further. For comparison, the temperature dependence of the bimolecular rate k_2, as determined by the analytical method in Section 6.2.3, is shown in Figure 6.5**E**.

As discussed in Section 6.2.3, a reduction in the bimolecular recombination rate k_2 is observed across the temperature range 80-200 K, and this trend is also present in the quantity k_r/n_0. This agreement suggests that this simplified PLQY-based model can be used to predict temperature-dependent trends in the radiative recombination

rate. However the value of k_r/n_0 is almost an order of magnitude lower than k_2 at all temperatures, which suggests that the accuracy of predicted values is limited. This could be to do with errors propagating from inaccurate determination of the PLQY as applied in Equation (6.6) and from errors in τ_f owing to the inaccuracy of fitting the data to a single exponential model. It could also be a result of errors in determining n_0 for scaling of k_r.

It was proposed in Section 6.2.3 that the reduction in the bimolecular recombination rate k_2 that the decrease in k_2 with increasing temperature is consistent with the Shockley-van Rooesbrook model, which predicts a decreasing radiative recombination rate with increasing temperature due to the broadening of the Fermi-Dirac distribution. This same interpretation can be given for the temperature-dependent trend in k_r/n_0 in the range 80-200 K.

Similarly to k_2, the reduction in k_r/n_0 with increasing temperature does not continue across the whole temperature range. The trend in k_r/n_0 reverses above $\sim$200 K. As discussed in Section 6.2.3, we suggest that changes in lattice parameters on heating of the sample give rise to polaronic effects which result in the deviation of radiative rates from the trend predicted by the Shockley-van Rooesbroeck model above 200 K. We suggest that this may be due to enhanced defect tolerance induced by the formation of large polarons.[69] There is however a difference between the temperature dependence of k_r/n_0 and k_2 above 200 K, where the relative increase in k_2 is much larger than that of k_r/n_0. I suspect that this originates from the fact that the single exponential fit used to determine k_r/n_0 from the measured lifetime τ_f becomes less reliable as the temperature is increased, as evidenced by the increasing R_2 value of the fits shown in Figure 6.5**A** with increasing temperature. It is also possible however that the radiative recombination rate becomes less dominated by bimolecular recombination at temperatures above 200 K, perhaps due to the polaronic effects proposed to affect the recombination dynamics in this temperature range.

Figure 6.5**E** plots the non-radiative recombination rate k_{nr} as determined using our PLQY model. The interpretation of this rate is not straightforward, as it may contain contributions from Shockley-Read-Hall (SRH) trap-mediated recombination, usually via

iodine interstitials,[73] and third order Auger processes. However, we have previously provided justification that Auger processes should have a negligible effect on the PL emissions at this excitation fluence, therefore we expect the majority of non-radative processes to be trap-mediated.

It can be seen that k_{nr} reduces gradually between 77 K and ∼170 K, although there is a large uncertainty in such values across this range. Above 200 K, this rate increases as the film is returned to ∼270 K. Our steady state PL results (Figure 6.3) hint that there may a thermally induced activation of trap states as the temperature is increased up to ∼ 260 K, and therefore we might expect an increase in the non-radiative rate with increasing temperature. However we only observe a weak increase in k_nr that apparently occurs over the temperature range 170-270 K. We suggest that this is due to the fact that the PL emission does not decay in a simple monoexponential fashion, which leads to inaccurate determine of k_{nr} and suggests the presence of higher order recombination processes which are difficult to quantify using this simplified model.

References

[1] NREL: Best Research-Cell Efficiencies Chart, accessed at https://pvdpc.nrel.gov/, **2019**.

[2] V. D'Innocenzo, G. Grancini, M. J. P. Alcocer, A. R. S. Kandada, S. D. Stranks, M. M. Lee, G. Lanzani, H. J. Snaith, A. Petrozza, *Nat. Commun.* **2014**, *5*, 3586.

[3] S. D. Stranks, G. E. Eperon, G. Grancini, C. Menelaou, M. J. P. Alcocer, T. Leijtens, L. M. Herz, A. Petrozza, H. J. Snaith, *Science (New York, N.Y.)* **2013**, *342*, 341.

[4] C. Wehrenfennig, G. E. Eperon, M. B. Johnston, H. J. Snaith, L. M. Herz, *Adv, Mater.* **2014**, *26*, 1584.

[5] K. X. Steirer, P. Schulz, G. Teeter, V. Stevanovic, M. Yang, K. Zhu, J. J. Berry, *ACS Energy Lett.* **2016**, *1*, 360.

[6] K. Hwang, Y.-S. Jung, Y.-J. Heo, F. H. Scholes, S. E. Watkins, J. Subbiah, D. J. Jones, D.-Y. Kim, D. Vak, *Adv, Mater.* **2015**, *27*, 1241.

[7] J. E. Bishop, D. K. Mohamad, M. Wong-Stringer, A. Smith, D. G. Lidzey, *Sci. Rep.* **2017**, *7*, 7962.

[8] A. Kojima, K. Teshima, Y. Shirai, T. Miyasaka, *J. Am. Chem. Soc.* **2009**, *131*, 6050.

[9] W. Tress, N. Marinova, O. Inganäs, M. K. Nazeeruddin, S. M. Zakeeruddin, M. Grätzel, *Adv. Energy Mater.* **2015**, *5*, 1400812.

[10] B. Conings, J. Drijkoningen, N. Gauquelin, A. Babayigit, J. D'Haen, L. D'Olieslaeger, A. Ethirajan, J. Verbeeck, J. Manca, E. Mosconi, F. D. Angelis, H.-G. Boyen, *Adv. Energy Mater.* **2015**, *5*, 1500477.

[11] G. E. Eperon, S. D. Stranks, C. Menelaou, M. B. Johnston, L. M. Herz, H. J. Snaith, *Energy Environ. Sci.* **2014**, *7*, 982.

[12] N. Pellet, P. Gao, G. Gregori, T.-Y. Yang, M. K. Nazeeruddin, J. Maier, M. Grätzel, *Angew. Chem.* **2014**, *126*, 3215.

[13] T. Jesper Jacobsson, J.-P. Correa-Baena, M. Pazoki, M. Saliba, K. Schenk, M. Grätzel, A. Hagfeldt, *Energy Environ. Sci.* **2016**, *9*, 1706.

[14] W. S. Yang, J. H. Noh, N. J. Jeon, Y. C. Kim, S. Ryu, J. Seo, S. I. Seok, *Science* **2015**, *348*, 1234.

[15] N. J. Jeon, J. H. Noh, W. S. Yang, Y. C. Kim, S. Ryu, J. Seo, S. I. Seok, *Nature* **2015**, *517*, 476.

[16] D. Bi, W. Tress, M. I. Dar, P. Gao, J. Luo, C. Renevier, K. Schenk, A. Abate, F. Giordano, J.-P. Correa Baena, J.-D. Decoppet, S. M. Zakeeruddin, M. K. Nazeeruddin, M. Grätzel, A. Hagfeldt, *Sci. Adv.* **2016**, *2*, e1501170.

[17] E. Skoplaki, A. Boudouvis, J. Palyvos, *Sol. Energy Mater. Sol. Cells* **2008**, *92*, 1393.

[18] L.-Q. Xie, L. Chen, Z.-A. Nan, H.-X. Lin, T. Wang, D.-P. Zhan, J.-W. Yan, B.-W. Mao, Z.-Q. Tian, *J. Am. Chem. Soc.* **2017**, *139*, 3320.

[19] O. J. Weber, B. Charles, M. T. Weller, *J. Mater. Chem. A* **2016**, *4*, 15375.

[20] G. Kieslich, J. M. Skelton, J. Armstrong, Y. Wu, F. Wei, K. L. Svane, A. Walsh, K. T. Butler, *Chem. Mater.* **2018**, *30*, 8782.

[21] R. L. Milot, G. E. Eperon, H. J. Snaith, M. B. Johnston, L. M. Herz, *Adv. Funct. Mater.* **2015**, *25*, 6218.

[22] M. C. Gélvez-Rueda, N. Renaud, F. C. Grozema, *J. Phys. Chem. C* **2017**, *121*, 23392.

[23] M. T. Weller, O. J. Weber, P. F. Henry, A. M. Di Pumpo, T. C. Hansen, *Chem. Commun.* **2015**, *51*, 4180.

[24] T. Chen, B. J. Foley, C. Park, C. M. Brown, L. W. Harriger, J. Lee, J. Ruff, M. Yoon, J. J. Choi, S.-H. Lee, *Sci. Adv.* **2016**, *2*, e1601650.

[25] M. T. Weller, O. J. Weber, J. M. Frost, A. Walsh, *J. Phys. Chem. Lett.* **2015**, *6*, 3209.

[26] O. J. Weber, D. Ghosh, S. Gaines, P. F. Henry, A. B. Walker, M. S. Islam, M. T. Weller, *Chem. Mater.* **2018**, *30*, 3768.

[27] H.-H. Fang, F. Wang, S. Adjokatse, N. Zhao, J. Even, M. Antonietta Loi, *Light: Sci. Appl.* **2016**, *5*, e16056.

[28] D. H. Fabini, T. A. Siaw, C. C. Stoumpos, G. Laurita, D. Olds, K. Page, J. G. Hu, M. G. Kanatzidis, S. Han, R. Seshadri, *J. Am. Chem. Soc.* **2017**, *139*, 16875.

[29] D. H. Fabini, C. C. Stoumpos, G. Laurita, A. Kaltzoglou, A. G. Kontos, P. Falaras, M. G. Kanatzidis, R. Seshadri, *Angew. Chem., Int. Ed.* **2016**, *55*, 15392.

[30] J. Tauc, *Mater. Res. Bull.* **1968**, *3*, 37.

[31] R. J. Elliott, *Phys. Rev.* **1957**, *108*, 1384.

[32] Y. Varshni, *Physica* **1967**, *34*, 149.

[33] K. Wu, A. Bera, C. Ma, Y. Du, Y. Yang, L. Li, T. Wu, *Phys. Chem. Chem. Phys.* **2014**, *16*, 22476.

[34] H.-H. Fang, R. Raissa, M. Abdu-Aguye, S. Adjokatse, G. R. Blake, J. Even, M. A. Loi, *Adv. Funct. Mater.* **2015**, *25*, 2378.

[35] M. I. Dar, G. Jacopin, S. Meloni, A. Mattoni, N. Arora, A. Boziki, S. M. Zakeeruddin, U. Rothlisberger, M. Grätzel, *Sci. Adv.* **2016**, *2*, e1601156.

[36] S. Meloni, G. Palermo, N. Ashari-Astani, M. Grätzel, U. Rothlisberger, *J. Mater. Chem. A* **2016**, *4*, 15997.

[37] E. S. Parrott, T. Green, R. L. Milot, M. B. Johnston, H. J. Snaith, L. M. Herz, *Adv. Funct. Mater.* **2018**, *28*, 1802803.

[38] H. Zheng, J. Dai, J. Duan, F. Chen, G. Zhu, F. Wang, C. Xu, *J. Mater. Chem. C* **2017**, *5*, 12057.

[39] M. Hirasawa, T. Ishihara, T. Goto, *J. Phys. Soc. Jpn.* **1994**, *63*, 3870.

[40] E. M. Hutter, M. C. Gélvez-Rueda, A. Osherov, V. Bulović, F. C. Grozema, S. D. Stranks, T. J. Savenije, *Nature Materials* **2017**, *16*, 115.

[41] A. D. Wright, R. L. Milot, G. E. Eperon, H. J. Snaith, M. B. Johnston, L. M. Herz, *Adv. Funct. Mater.* **2017**, *27*, 1700860.

[42] R. Williams, K. Song, *J. Phys. Chem. Solids* **1990**, *51*, 679.

[43] R. Gottesman, E. Haltzi, L. Gouda, S. Tirosh, Y. Bouhadana, A. Zaban, E. Mosconi, F. De Angelis, *J. Phys. Chem. Lett.* **2014**, *5*, 2662.

[44] E. T. Hoke, D. J. Slotcavage, E. R. Dohner, A. R. Bowring, H. I. Karunadasa, M. D. McGehee, *Chem. Sci.* **2015**, *6*, 613.

[45] A. J. Neukirch, W. Nie, J. C. Blancon, K. Appavoo, H. Tsai, M. Y. Sfeir, C. Katan, L. Pedesseau, J. Even, J. J. Crochet, G. Gupta, A. D. Mohite, S. Tretiak, *Nano Lett.* **2016**, *16*, 3809.

[46] D. Cortecchia, J. Yin, A. Bruno, S.-Z. A. Lo, G. G. Gurzadyan, S. Mhaisalkar, J.-L. Brédas, C. Soci, *J. Mater. Chem. C* **2017**, *5*, 2771.

[47] V. Plekhanov, *Prog. Mater. Sci.* **2004**, *49*, 787.

[48] K. Gauthron, J.-S. Lauret, L. Doyennette, G. Lanty, A. Al Choueiry, S. J. Zhang, A. Brehier, L. Largeau, O. Mauguin, J. Bloch, E. Deleporte, *Opt. Express* **2010**, *18*, 5912.

[49] C. Wehrenfennig, M. Liu, H. J. Snaith, M. B. Johnston, L. M. Herz, *J. Phys. Chem. Lett.* **2014**, *5*, 1300.

[50] A. D. Wright, C. Verdi, R. L. Milot, G. E. Eperon, M. A. Pérez-Osorio, H. J. Snaith, F. Giustino, M. B. Johnston, L. M. Herz, *Nat. Commun.* **2016**, *7*, 11755.

[51] S. Ghosh, Q. Shi, B. Pradhan, P. Kumar, Z. Wang, S. Acharya, S. K. Pal, T. Pullerits, K. J. Karki, *J. Phys. Chem. Lett.* **2018**, *9*, 4245.

[52] J. Kim, S.-H. Lee, J. H. Lee, K.-H. Hong, *J. Phys. Chem. Lett.* **2014**, *5*, 1312.

[53] W.-J. Yin, T. Shi, Y. Yan, *Appl. Phys. Lett.* **2014**, *104*, 063903.

[54] M. B. Johnston, L. M. Herz, *Acc. Chem. Res.* **2016**, *49*, 146.

[55] J. Even, L. Pedesseau, C. Katan, *J. Phys. Chem. C* **2014**, *118*, 11566.

[56] Y. Yamada, T. Nakamura, M. Endo, A. Wakamiya, Y. Kanemitsu, *J. Am. Chem. Soc.* **2014**, *136*, 11610.

[57] L. R. V. Buizza, T. W. Crothers, Z. Wang, J. B. Patel, R. L. Milot, H. J. Snaith, M. B. Johnston, L. M. Herz, *Adv. Funct. Mater.* **2019**, 1902656.

[58] M. Saba, M. Cadelano, D. Marongiu, F. Chen, V. Sarritzu, N. Sestu, C. Figus, M. Aresti, R. Piras, A. Geddo Lehmann, C. Cannas, A. Musinu, F. Quochi, A. Mura, G. Bongiovanni, *Nat. Commun.* **2014**, *5*.

[59] F. Deschler, M. Price, S. Pathak, L. E. Klintberg, D.-D. Jarausch, R. Higler, S. Hu, T. Leijtens, S. D. Stranks, H. J. Snaith, M. Atatu, R. T. Phillips, R. H. Friend, *J. Phys. Chem. Lett* **2014**, *5*, 1421.

[60] S. D. Stranks, V. M. Burlakov, T. Leijtens, J. M. Ball, A. Goriely, H. J. Snaith, *Phys. Rev. Appl.* **2014**, *2*, 034007.

[61] D. P. McMeekin, G. Sadoughi, W. Rehman, G. E. Eperon, M. Saliba, M. T. Hörantner, A. Haghighirad, N. Sakai, L. Korte, B. Rech, M. B. Johnston, L. M. Herz, H. J. Snaith, *Science* **2016**, *351*, 151.

[62] W. Rehman, R. L. Milot, G. E. Eperon, C. Wehrenfennig, J. L. Boland, H. J. Snaith, M. B. Johnston, L. M. Herz, *Adv, Mater.* **2015**, *27*, 7938.

[63] P. E. Shaw, A. Ruseckas, I. D. Samuel, *Adv. Mater.* **2008**, *20*, 3516.

[64] C. L. Davies, M. R. Filip, J. B. Patel, T. W. Crothers, C. Verdi, A. D. Wright, R. L. Milot, F. Giustino, M. B. Johnston, L. M. Herz, *Nat. Commun.* **2018**, *9*, 293.

[65] H. Oga, A. Saeki, Y. Ogomi, S. Hayase, S. Seki, *J. Am. Chem. Soc.* **2014**, *136*, 13818.

[66] T. J. Savenije, C. S. Ponseca, L. Kunneman, M. Abdellah, K. Zheng, Y. Tian, Q. Zhu, S. E. Canton, I. G. Scheblykin, T. Pullerits, A. Yartsev, V. Sundstro, V. Sundström, *J. Phys. Chem. Lett* **2014**, *5*, 4.

[67] K. Tanaka, T. Takahashi, T. Ban, T. Kondo, K. Uchida, N. Miura, *Solid State Communications* **2003**, *127*, 619.

[68] A. Filippetti, P. Delugas, A. Mattoni, *J. Phys. Chem. C* **2014**, *118*, 24843.

[69] K. Miyata, D. Meggiolaro, M. T. Trinh, P. P. Joshi, E. Mosconi, S. C. Jones, F. De Angelis, X.-Y. Zhu, *Sci. Adv.* **2017**, *3*, e1701217.

[70] R. Young (Ed.), *The Rietveld Method*, Oxford University Press, Oxford, UK, **1995**.

[71] J. C. De Mello, H. F. Wittmann, R. H. Friend, *Adv. Mater.* **1997**, *9*, 230.

[72] J. R. Lakowicz (Ed.), *Principles of Fluorescence Spectroscopy*, Springer US, Boston, MA, 3rd edn., **2006**.

[73] D. Meggiolaro, S. G. Motti, E. Mosconi, A. J. Barker, J. Ball, C. Andrea, R. Perini, F. Deschler, A. Petrozza, F. De Angelis, *Energy Environ. Sci* **2018**, *11*, 22.

Chapter 7

Effect of Caesium Incorporation on the Phase Behaviour and Emission Properties of Triple Cation Perovskites

Note on contributions to this chapter

All work presented in this chapter was carried out by me, with the following exceptions:

- *Adam Shnier* carried out the structural refinements on the X-ray diffraction data, supervised by Prof. Daniel Wamwangi and Prof. David. G. Billing at the University of the Witwatersrand.
- *Dr. Craig C. Robertson* carried out the powder X-ray diffraction measurements in the Department of Chemistry at the University of Sheffield.

Abstract

Triple cation perovskite thin films including a mixed organic-inorganic A-site cation have been implemented in high efficiency photovoltaic devices and are a promising candidate for solar applications due to their increased long-term sta-

bility as compared to other hybrid perovskites. However the phase behaviour and temperature-dependent optical properties of such materials has not been explored previously, despite the fact that this avenue of investigation may reveal much about the fundamental properties of the material which drive this elevated stability. Here it is demonstrated that the triple cation mixed halide perovskite $Cs_zFA_xMA_yPbI_{2.55}Br_{0.45}$, where $x = 4y$, exhibits complex phase behaviour which varies depending on the value of z. It is found that all materials in this compositional range adopt a pseudo-cubic α phase at room temperature, and that triple cation perovskites with $z = 0.05, 0.08, 0.1$ undergo two structural phase transitions in the temperature range 80-310 K. At high temperatures, the materials undergo a transition to a pseudo-tetragonal β phase at $\sim$260-270 K, with the transition temperature appearing to be around 10 K higher when increasing z from 0.05 to 0.08/0.1. This work illustrates that the addition of Cs into a mixed cation, mixed halide perovskite alters the phase behaviour of the material in a way that has significant implications for the temperature-dependent optical properties and therefore the real-world implementation of these Cs-containing triple cation blends.

7.1 Introduction

Hybrid lead halide perovskites of the form ABX_3, where A is a monovalent cation, B is lead and X is a halide anion, have been rapidly gaining traction as potential photovoltaic cell absorbers since their first experimental demonstration in 2009.[1] Perovskite solar cells (PSCs) have recently achieved a record efficiency of 25.2%,[2] owing their success in part to the beneficial photophysical properties of hybrid perovskites such as long carrier lifetimes and diffusion lengths, strong optical absorption, and high defect tolerance.[3–6] In addition, these compounds are relatively simple to fabricate by low temperature, solution-based processes, therefore large area devices can be processed by methods such as spray coating and slot-die coating.[7,8]

Mixed-cation perovskites, where the A-site comprises a combination of organic and/or inorganic cations, have been demonstrated to produce high efficiency PSCs of vari-

ous compositions, with the first mixed cation PSCs being demonstrated based on FA^+ (the organic molecule $HC(NH_2)_2^+$ or formamidinium) and MA^+ (the organic molecule $CH_3NH_3^+$ or methylammonium).[9] Mixed cation systems can be manipulated through compositional engineering to tune properties such as optical band gap and optimise the efficiency of PSCs.[10,11] The inclusion of Cs^+ ions into the A-site in addition to FA^+ and MA^+ has been demonstrated to improve not only device performance[12–14] but also the moisture and thermal stability of the perovskite.[15,16] These improvements can partially be attributed to the longer diffusion lengths and carrier lifetimes[15] and better crystalline quality[17] of Cs-containing triple cation perovskites, as compared to $MAPbI_3$. Saliba and coworkers[18] were the first to demonstrate PSCs based on triple cation perovskites, and their devices based on $Cs_{0.05}FA_{0.79}MA_{0.16}Pb(I_{0.83}Br_{0.17})_3$ reached a stabilised power conversion efficiency (PCE) of 21.1%. They found that the addition of the Cs cation enhanced device stability, with the devices retaining 90% of their initial PCE for over 250 hours. To further highlight the advantages of such perovskites, Matsui *et al.* showed that a room temperature process with no annealing stage could be used to fabricate triple cation blends of the form $Cs_{0.1}FA_{0.8}MA_{0.1}Pb(I_{0.83}Br_{0.17})_3$ which demonstrated a stabilised PCE of 17.7%.[17]

Temperature-dependent investigations can allow researchers not only to gain a deeper understanding of the fundamental properties of hybrid perovskite materials, but also to determine how device behaviour may be affected by varying temperature in real-world operating conditions. Double cation perovskites of the form $(FAPbI_3)_{1-x}(MAPbBr_3)_x$ have been shown to adopt a cubic perovskite structure at room temperature, an effect which contributes to their enhanced thermal stability compared to single cation perovskites.[19] Weber *et al.* showed that varying the FA/MA ratio in $(FAPbI_3)_{1-x}(MAPbI_3)_x$ perovskites affects the tetragonal-to-cubic phase transition,[20] which in turn affects the thermal stability of the material, therefore a similar effect may be expected when varying the amount of Cs incporated into the A-site.

Despite elevated interested in Cs-containing triple cation perovskite systems due to their excellent photovoltaic performance, the relationship between phase behaviour and optical properties has not yet been widely explored in these systems. It has been

proposed that phase behaviour in triple cation perovskites is driven by a change from static to dynamic disorder in the lattice as the temperature is increased, in the same way as $MAPbI_3$ (see Section 2.1.2).[21] The static disorder at low temperatures forms a sub-bandgap density of states, otherwise known as a band tail,[22] which evolves with increasing temperature due to the changing nature of disorder (static to dynamic) in the lattice.[21]

In this chapter, the effects of Cs inclusion on the structural and optical properties of perovskites across the $Cs_zFA_xMA_yPb(I_{0.85}Br_{0.15})_3$ parameter space are explored. 5 different stoichiometric blends are fabricated, with $z = (0.03, 0.05, 0.08, 0.1, 0.15)$, while maintaining a ratio of $x = 4y$, resulting in: $Cs_{0.03}FA_{0.776}MA_{0.194}X$; $Cs_{0.05}FA_{0.76}MA_{0.19}X$; $Cs_{0.08}FA_{0.736}MA_{0.184}X$; $Cs_{0.1}FA_{0.72}MA_{0.18}X$; and $Cs_{0.15}FA_{0.68}MA_{0.17}X$, respectively, where $X = Pb(I_{0.85}Br_{0.15})_3$. These blends will hereafter be referred to as 3% Cs, 5% Cs, 8% Cs, 10% Cs and 15% Cs. Variable temperature steady-state photoluminescence and absorbance measurements are performed at a range of temperatures from 4 K to 300 K on all 5 triple cation blends, in order to determine the temperature dependence of a variety of photophysical properties. Powder X-ray diffraction studies are also carried out on 3 selected blends over the temperature range 80-350 K, in order to identify structural phase transitions and determine the temperature dependence of various structural parameters. Findings from these two methods are then compared, in order to investigate the effect of increasing caesium incorporation on the phase behaviour of triple cation perovskites and how this influences key optical properties.

7.2 Results and Discussion

First, the effect of Cs incorporation on the structure and optical properties of thin films at room temperature was investigated. To achieve this, thin film X-ray diffraction, absorbance and photoluminscence measurements were carried out on a series of Cs-containing blends. For these preliminary measurements, triple cation perovskite thin films with Cs concentrations of 3%, 5%, 8%, 10% and 15% were fabricated, as described in Section 3.1.2. For the purpose of comparison, thin films of $FA_{0.85}MA_{0.15}Pb(I_{0.85}Br_{0.15})_3$ were fabricated as described in Section 3.1.1, corresponding to the equivalent perovskite

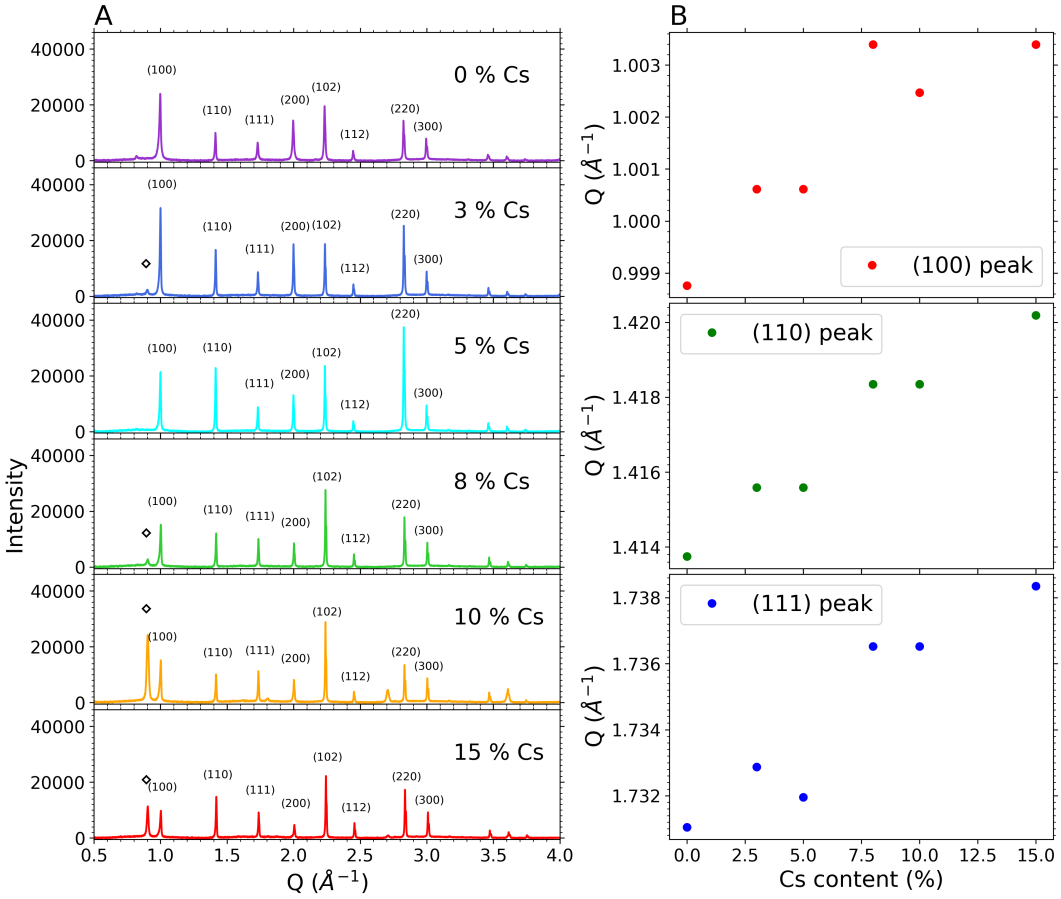

Figure 7.1: **A** Room temperature X-ray diffraction patterns collected from $Cs_zFA_xMA_yPbI_{2.55}Br_{0.45}$ thin films at different concentrations of Cs, including 0%, which corresponds to $FA_{0.85}MA_{0.15}PbI_{2.55}Br_{0.45}$. Peaks marked with ⋄ denote PbI_2 reflection. **B** Peak position of the (100), (110) and (111) reflections as a function of Cs content in the perovskite thin film.

with 0% Cs. To determine the effect of Cs incorporation on the crystal structure of triple cation perovskites, room temperature X-ray diffraction was carried out on the 0-15% Cs perovskite thin films, with the results displayed in Figure 7.1. These plots show that the characteristic peaks for the (100), (110), (111) and (200) crystal planes in the perovskite structure are present for all blends. In Figure 7.1, the position in Q (the scattering vector) of the (100), (110) and (111) peaks is plotted as a function of Cs incorporation. Here it can be seen that Q for each of these peaks increases linearly with increasing Cs content. For a cubic crystal, the interplanar spacing for the plane with the Miller index (hkl), referred to as d_{hkl}, is related to Q in the following way:

$$d_{hkl} = \frac{4\pi n}{2Q} \tag{7.1}$$

where n is the order of the Bragg reflection. d_{hkl} is related to the lattice parameter a by

$$d_{hkl} = \frac{a}{\sqrt{h^2 + k^2 + l^2}} \tag{7.2}$$

for a cubic lattice, which is the structural configuration we expect these Cs-containing triple cation perovskites to assume at room temperature.[23]

The ionic radius of Cs is much smaller than that of FA or MA, therefore increasing Cs content will cause the effective A-cation size to decrease and hence lead to a smaller unit cell (smaller value of a), which is consistent with our observations of a decreasing value of d_{hkl} (increasing Q-value of perovskite peak reflections) with increasing Cs content.

In the 3% Cs blend, a peak is observed at $\sim$0.9 Å^{-1}, which can be attributed to scattering from the (001) plane of lead iodide (PbI_2). PbI_2 is a common degradation product of lead iodide perovskites, with this degradation caused by a variety of intrinsic and extrinsic mechanisms.[24–26] This peak is present in all other Cs-containing compositions, with the notable exception of 5% Cs. This suggests that the stoichiometry of the 5% Cs blend is less prone to PbI_2 formation during fabrication than any other blend in the compositional range. This particular composition was also found to be highly stable in the work of Saliba *et al.*,[18] who reported a stabilised PCE of $\sim$18% for over 250 hours. The dependence of the PbI_2 peak intensity on Cs content is shown in Figure 7.2**A**, which shows that there is a small increase in the intensity of the PbI_2 reflection when increasing the Cs content from 0% to 8%, followed by a significant increase ($\sim$2 orders of magnitude) between 8% and 10% Cs inclusion. These results suggest that a significantly greater proportion of the 10% and 15% Cs films are composed of PbI_2 compared to the films with lower Cs content, especially in the 10% film, where the scattering intensity is apparently greater than the intensity of the perovskite (100) feature at Q $\sim$1.0 Å^{-1}. Whilst it is clear that the PbI_2 content is highest in the 10% Cs film, the most likely explanation for the significant increase in scattering intensity compared to the perovskite (100) crystal plane is the degree of orientation in the films with higher Cs content. When PbI_2 forms in perovskite films, it is common for it to form with 'out-of-plane' (OOP)

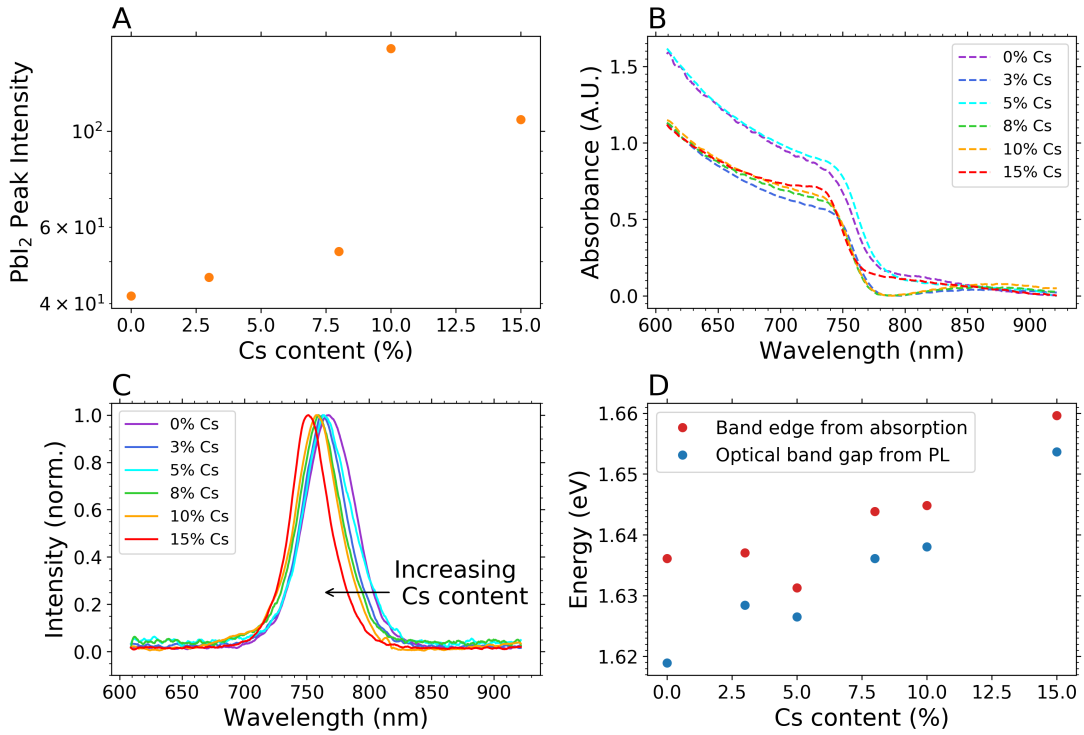

Figure 7.2: **A** Variation of the intensity of the XRD peak characteristic of PbI_2 (lead iodide) with increasing Cs content in the perovskite. **B** Absorbance spectra for Cs-containing triple cation perovskites with 3-15% Cs inclusion in the A-site. Absorbance spectrum for equivalent perovskite with 0% Cs inclusion is shown for comparison. **C** PL spectra for Cs-containing triple cation perovskites with 3-15% Cs inclusion in the A-site. PL spectrum for equivalent perovskite with 0% Cs inclusion is shown for comparison. **D** Variation of the band edge (red markers) and the optical band gap as determined from the peak position of the PL spectrum (blue markers) with increasing Cs inclusion in the A-site of the perovskite.

orientation, such that the coherent scattering domain of the PbI_2 phase is normal to the substrate surface.[27,28] Due to the nature of the Bragg-Brentano geometry that these XRD measurements employed, the scattering intensity of these OOP reflections is greatly exaggerated. These results also suggest that higher Cs content modifies the orientation of the perovskite phase during crystallisation.

To examine the effect of Cs inclusion on optical properties, photoluminescence (PL) and absorbance data were also collected for the 0-15% Cs perovskite thin films. The absorbance spectra are plotted in Figure 7.2**B**: this plot shows an apparent increase in the absorbance near the band edge with increasing Cs content in the range 3-15% Cs. The exception to this trend is the 5% Cs blend, which exhibits a near-band edge absorbance which is higher than that of any of the other blends, including the 0% Cs perovskite. This strengthened absorbance cannot be explained by film thickness, as

there is no correlation between Cs content and film thickness, as shown in Table D.1 in Appendix D. This may suggest that increasing Cs inclusion enhances the absorption coefficient in these triple cation perovskite blends. This increase in absorption strength for the 5% Cs blend may be a contributing factor to its superior performance. However it may be possible that there is simply a larger sample-to-sample variation in Cs thin films than in the other blends, a variation which may be partially due to a larger uncertainty in resultant Cs concentration when processing the 5% Cs blend, as the Cs concentration is relatively small.

In Figure 7.2**C** it can be seen that the PL emission peak shifts to shorter wavelengths as the Cs concentration is increased, indicating a widening of the band gap as more Cs is incorporated into the A-site. Figure 7.2**D** plots the variation with Cs content of the optical band gap, E_g, as extracted from the PL emission curves in Figure 7.2**C** by extracting the energy value at the peak of the PL emission. This data shows an increase in band gap energy with increasing Cs content, which is is consistent with our observation of a decrease in the interplanar spacing d_{hkl} with increasing Cs content, because a decrease in interplanar spacing suggests a decrease in the size of the unit cell, which is expected to lead to a wider optical band gap. Figure 7.2**D** also shows the absorption edge as a function of Cs content, determined by taking the mid-point of the absorbance drop-off for the spectra in Figure 7.2**B**. The absorption edge shifts towards higher energies as the Cs content is increased, with the notable exception of the 5% Cs blend, which slightly defies the trend. This may be due to a peculiarity in the electronic structure of the 5% Cs blend, however it is much more likely to be the result of a larger sample-to-sample variation when fabricating this blend, as discussed earlier.

7.2.1 Variable Temperature Absorption and Photoluminescence

Next, a new set of thin films of all 5 Cs-containing blends (3%, 5%, 8%, 10%, and 15% Cs) were fabricated, and these were used to carry out variable temperature UV-visible absorbance and PL spectroscopy measurements. Absorbance and PL spectra were collected at a selection of temperatures while heating the film from 4 K to 300 K. Full datasets for these measurements are shown in Figure 7.3 and Figure 7.4. The absorbance

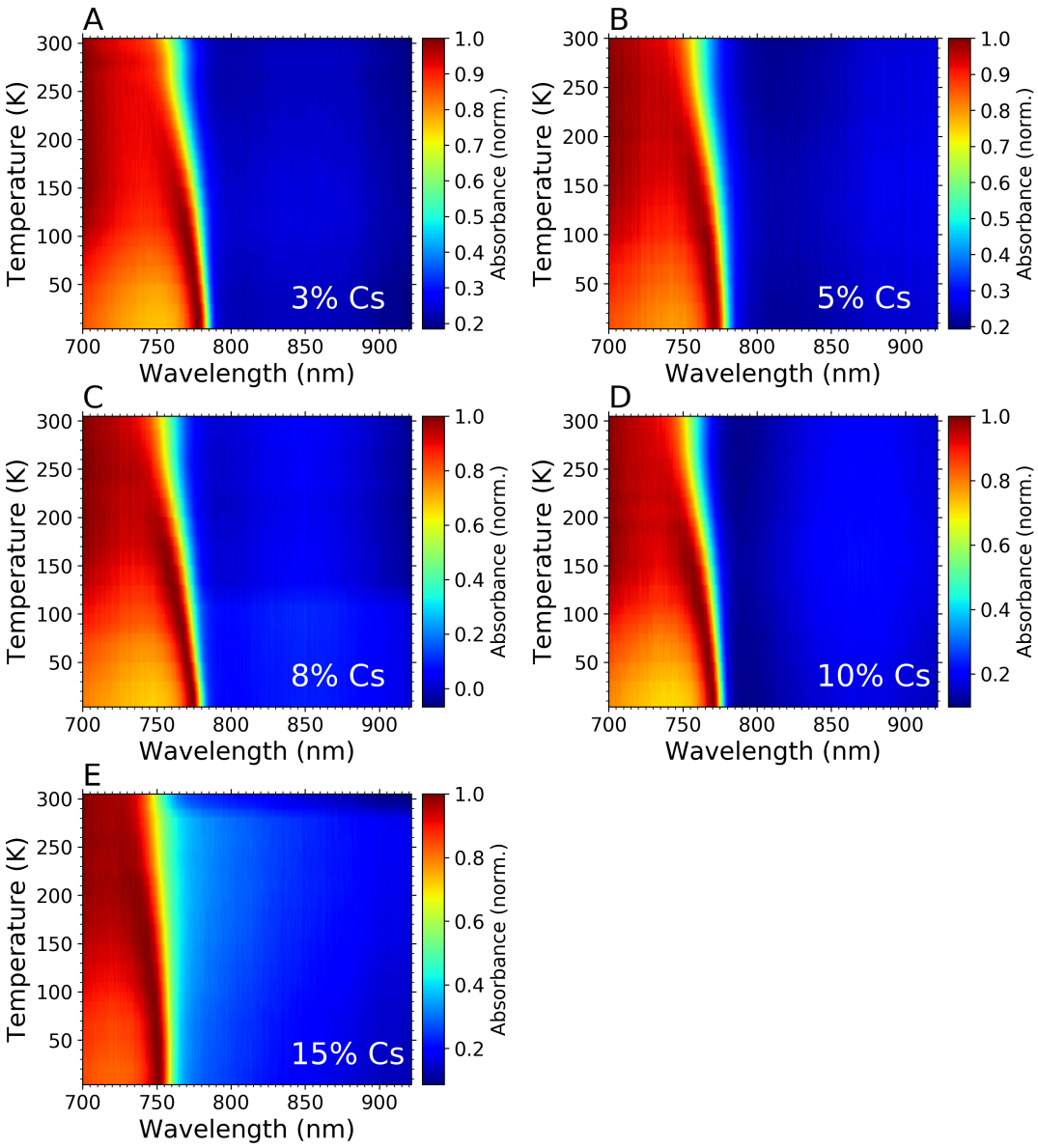

Figure 7.3: Temperature dependence of the absorbance spectra on heating of a $Cs_zFA_xMA_yPb(I_{0.85}Br_{0.15})_3$ thin film, with concentrations of **A** 3%, **B** 5%, **C** 8%, **D** 10%, and **E** 15% Cs.

data in Figure 7.3 show that, for all compositions, a blueshift in the band edge occurs with increasing temperature. Similarly, the temperature-dependent PL spectra (Figure 7.4) show a blueshift in the PL emission peak wavelength as temperature is increased. These data also show a broadening of the emisson peak with increasing temperature, an effect which has been widely reported in lead halide perovskites.[29,30] The dominant mechanism governing these effects has been described as Fröhlich interactions of photoexcited electrons with longitudinal optical (LO) phonons.[31,32]

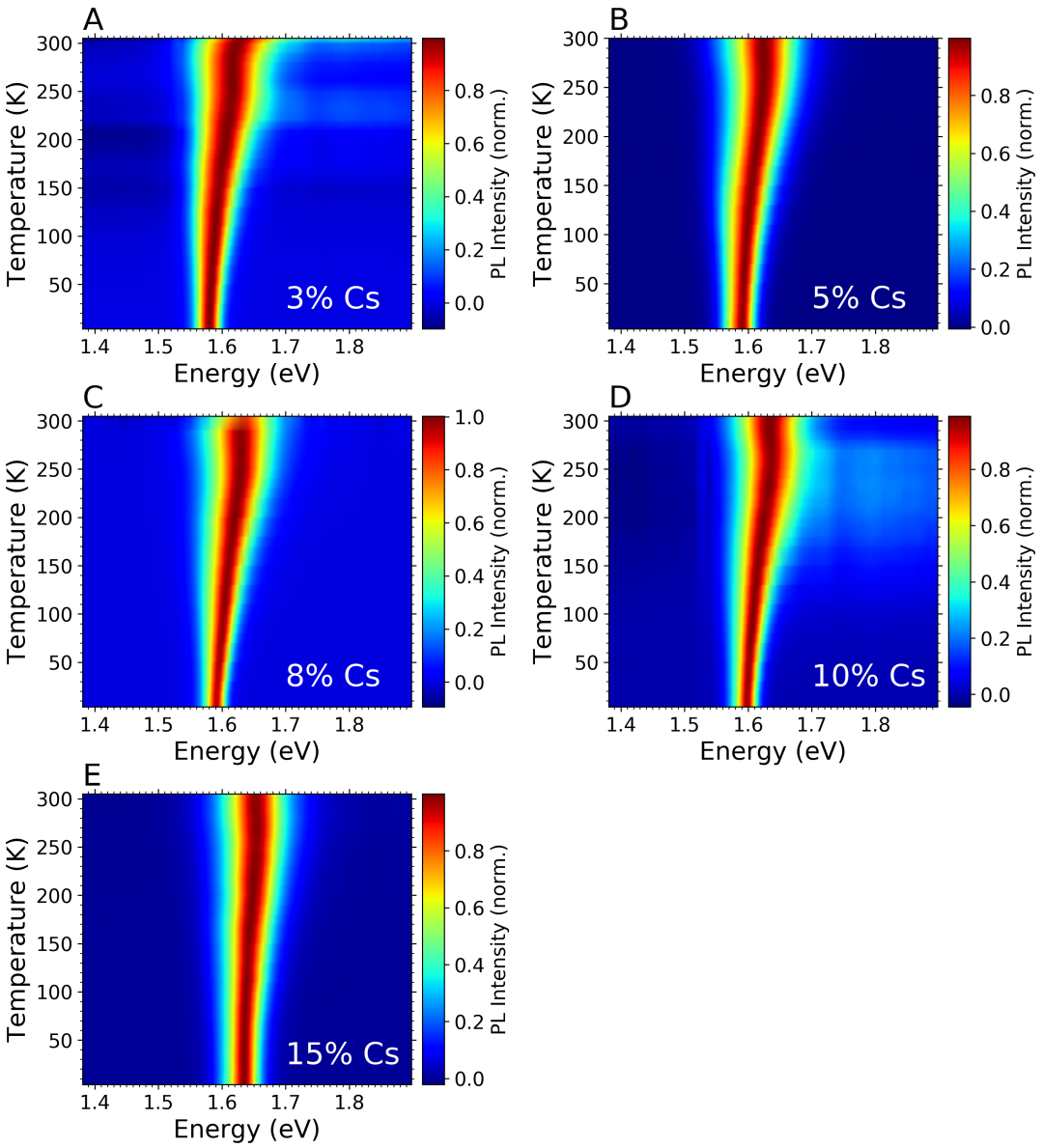

Figure 7.4: Temperature dependence of the PL spectra on heating of $Cs_zFA_xMA_yPb(I_{0.85}Br_{0.15})_3$ thin films with concentrations of **A** 3%, **B** 5%, **C** 8%, **D** 10%, and **E** 15% Cs.

In order to further explore the temperature-dependent optical properties of the Cs blends, 3 of the Cs-containing compositions (5%, 8%, and 10%) were selected, and the variable temperature absorbance and PL spectroscopy measurements were repeated, this time collecting data on both cooling and heating of the films. Absorbance and PL spectra were collected at regular temperature intervals during a cooling cycle from 300 K to 4 K, then during a subsequent heating cycle where the films were brought back up to 300 K. From the spectra obtained, various analysis techniques have been applied to determine the optical properties of the films during cooling and heating.

First, a Jacobian transformation was used to transform the PL emission spectra into energy space. The resultant photoluminescence spectra were fitted to a number of different models. It was found that, due to the asymmetry in the data, it was necessary to use an asymmetric pseudo-Voigt function to fit the spectra, which is a linear combination of Gaussian and Lorentzian distributions with the addition of an asymmetry parameter which introduces variability in the full-width at half-maximum (FWHM).[33] The asymmetric pseudo-Voigt distribution to which the data was modelled has the following functional form:

$$y(E) = f\frac{2A_L/\pi\gamma_L}{1+4[(E-\mu)/\gamma_L]^2} + (1-f)\left(\frac{A_G}{\gamma_G}\sqrt{\frac{4\ln 2}{\pi}}\exp\left(-4\ln 2\frac{E-\mu}{\gamma_G}\right)\right) \quad (7.3)$$

where μ is the mean of the Voigt function, a is the asymmetry parameter, A is the area under the distribution and γ is the FWHM. In this model, the Gaussian and Lorentzian components share a common μ value but each component has its own value of a, A and γ—the subscripts L and G denote parameters characteristic of the Lorentzian and Gaussian components respectively. For full details of the pseudo-Voigt model, see Appendix D. Plots of the temperature dependence of Voigt fitting parameters not presented in the following paragraphs can be found in Figure D.3.

In Figure 7.5**A**, PL emission curves for the 5% Cs perovskite at 4 K, 200 K and 300 K are plotted, fitted with the asymmetric pseudo-Voigt function shown in Equation (7.3). The red dashed lines show the PL peak energy, which is the energy value at the peak of the PL emission curve. The dashed black lines mark the value of μ, the mean of the Voigt function, which characterises the mean energy of the PL emission. Figure 7.5**A** shows that the PL emission curves are asymmetrical, with a slight skew towards lower energies, and the mean emission energy μ is shifted to a lower energy as a result. This asymmetry in the PL spectra was observed at all temperatures and for all Cs-containing compositions studied. One possible origin of this asymmetry is self-absorption effects within the film, where emitted PL is re-absorbed and re-emitted.[34] Self-absorption can occur in thin films when the absorption edge is within the linewidth of the PL emission, which is the case for all of these films as can be seen in Figure 7.2.

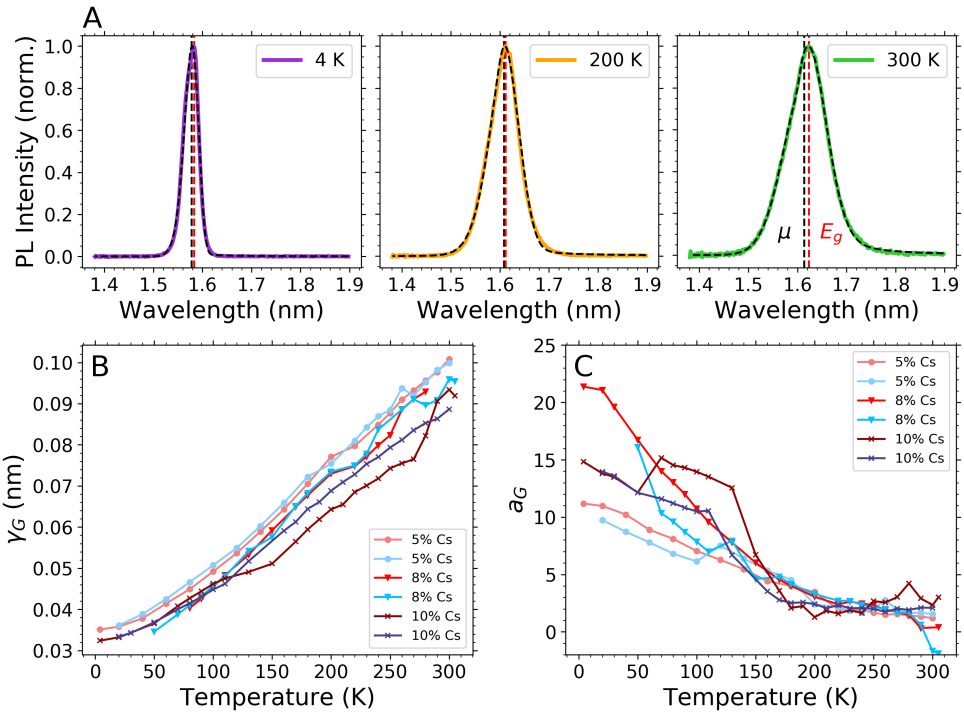

Figure 7.5: **A** PL specta recorded at temperatures of 4 K, 200 K and 300 K for a triple cation perovskite thin film with 5% Cs content. Temperature dependence of **B** the Gaussian FWHM γ_G and **C** the Gaussian asymmetry parameter a_G, from a pseudo-Voigt fitting model applied to the PL spectra at all temperatures on heating and cooling, for triple cation perovskite thin films with 5%, 8% and 10% Cs content.

It is also possible that this asymmetry is due to disorder-induced band tail recombination, as observed in hybrid perovskites previously.[21,22]

Figure 7.5**B** shows the temperature dependence of γ_G, the FWHM of the Gaussian component of the pseudo-Voigt fit, upon both heating and cooling of each film. In Figure 7.4, it was observed for all compositions that the PL emission peak broadens with increasing temperature, and this is reflected in the increase in γ_G with increasing temperature. It is interesting that it should be the Gaussian FWHM that reflects this broadening, considering that the Lorentzian character f is in the range $0.8 < f < 1$ for the majority of the datasets (see Figure D.3**A** in Chapter D) and therefore the PL emission curves have a predominantly Lorentzian character.

Figure 7.5**A** shows that the PL emission curves for all temperatures are skewed towards lower energies, suggesting that the asymmetry parameter a is positive. Again, it is the Gaussian component of the curve that reflects this, because a positive value of a_G for all temperatures and compositions was obtained, as shown in Figure 7.5**C**. a_G

decreases with increasing temperature, which may point towards an explanation for the origin of the asymmetry in the PL emission. It was proposed earlier that the asymmetry in the PL emission is due to band tail recombination. Indeed, Baranowski and coworkers[21] demonstrated the presence of an exponential tail in the density of states at very low temperatures in Cs-containing triple cation perovskites through low-temperature PL measurements. They proposed that this band tail is induced by static disorder in the perovskite lattice in the low temperature orthorhombic phase, and that the trapping behaviour associated with the band tail changes with increasing temperature, as the nature of the disorder in the lattice evolves from static to dynamic. This results in reduced emission from the band tail as temperature is increased, due to an increase in non-radiative recombination via deep traps. If the asymmetry observed in our PL emission curves is indeed related to disorder-induced band tail recombination, we would expect to observe reduced asymmetry in the PL with increasing temperature. This is consistent with observations of a_G in Figure 7.5**C**, therefore it is proposed that the asymmetry in the PL emission originates from disorder-induced band-tail recombination.

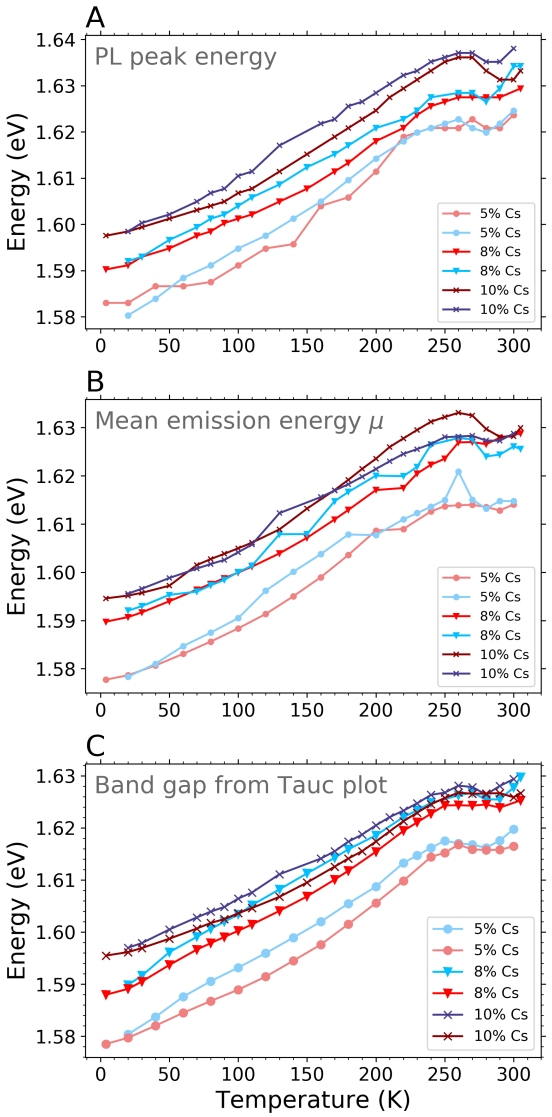

Figure 7.6: Temperature dependence of **A** the optical band gap as extracted from the PL emission peak, and **B** the mean energy of emitted photons μ and **C** the band gap as extracted from Tauc plots generated from the absorbance spectra, for 5%, 8% and 10% Cs perovskite compositions at a series of temperatures from 4 K to 300 K, on both heating and cooling of the film.

Figure 7.6**A** shows the temperature dependence of the PL peak energy, which is the energy value at the maximum value of PL intensity. Figure 7.6**B** shows the temperature

Table 7.1: Optical band gap (E_G) at room temperature (300 K), and the overall change in optical band gap (ΔE_G) on cooling the film to 4 K, and on subsequently re-heating the film to 300 K, for triple cation perovskite compositions of varying Cs content.

Cs content (%)	$E_{G_{300K}}$ (eV)	ΔE_G (meV) - cooling	ΔE_G (meV) - heating
5	1.624	- 44.3	+ 40.7
8	1.634	- 42.1	+ 39.1
10	1.638	- 39.6	+ 35.7

dependence of μ as extracted from fits to the data using (7.3), where μ characterises the mean energy of emitted photons, taking into account the skew of the asymmetrical emission curve. This plot shows that μ varies with temperature in a similar way to the PL peak energy, with slightly lower values as expected due to the skew of the PL data. This is discussed further in Section D.3 in Appendix D. However, it is the PL peak energy which is likely to represent the band gap, E_g, as the peak energy represents the wavelength at which optical transitions are most likely to occur, therefore the analysis in this thesis will found on this quantity. In Table 7.1, the value of E_g as determined by the peak PL energy is listed for all 3 compositions at room temperature as well as the overall change in optical band gap ΔE_G on both cooling and heating of the film in the temperature range 4-300 K.

The data in Table 7.1 show that there is a widening of the optical band gap with increasing Cs content, which mirrors findings from Figure 7.2**C** and is consistent with the behaviour we expect when there is increased incorporation of the smaller Cs atom into the structure. A widening in the optical band gap with increasing temperature is observed for all 3 perovskite compositions, which is consistent with trends observed for other hybrid lead halide perovskites.[35,36] Here it should be noted that this trend is the opposite to that expected in semiconductors as described by the empirical Varshni relation.[37] This behaviour has been attributed to lattice expansion-induced reduction in the overlap of Pb-6s and I-5s orbitals, which causes a decrease in the valence band maximum on heating of the material.[38] As Meloni and coworkers determined through density functional theory (DFT) calculations, the reduction or increase in orbital overlap is proportional to the ratio of the lattice constant to the size of the *s*- and *p*-orbitals of the B (Pb) and X (I/Br) atoms, and it is only changes in the lattice constant that

will alter this ratio when both temperature and Cs content are varied, because the size of the Pb/I/Br orbitals will not change. Table 7.1 shows that the overall blueshift in E_G, across the temperature range 4-300 K, decreases as Cs content is increased. This trend suggests that the more Cs is included in the A-cation site the smaller the overall change in the lattice constant i.e. there is less overall thermal expansion of the lattice. To investigate this effect in more detail, temperature-dependent X-ray diffraction has been carried out, which is discussed in Section 7.2.2.

In Figure 7.6**A**, the temperature-dependent trends in the PL peak energy for all 3 compositions are plotted, on both cooling (blue markers) and heating (red markers) of the film. The PL peak energy is taken here as a measure of the optical band gap E_g. Here it can be seen for all compositions that the band gap increases monotonically, up to a local maximum where a slight redshift occurs, or in some cases the band gap reaches a plateau. This discontinuity in the apparent blueshift occurs at varying temperatures depending on Cs content. The temperature point at which the redshift or plateau occurs will henceforth be referred to as the 'discontinuity temperature'. It is speculated here that the discontinuity temperature should give an indication of the temperature at which the phase transition to the high temperature cubic phase happens in these triple cation perovskites. This discontinuity phenomenon has been previously demonstrated to correlate with a structural phase transition in a variety of hybrid perovskite materials,[29,39–41] and it was shown in Chapter 6 that this phenomenon holds for a double-cation mixed-halide perovskite.

For comparison, the band gap of the thin films was also determined from the absorbance spectra. As described in Section 2.2.3, an accurate value of the band edge can only be obtained through fitting of the absorption coefficient to the full model as laid out by R. J. Elliot[42], which includes contributions from both excitonic and continuum absorption. However, due to time constraints this full treatment, which is not trivial, was unable to be applied, and instead the band gap energy was estimated using Tauc plots.[43] Tauc plots were generated by plotting $(\alpha hf)^2$ against hf where $\alpha = 2.303A/t$ (A is the absorbance as determined from UV-visible absorbance spectroscopy, and t is the film thickness, as shown in Table D.1). From the Tauc plots, the band gap was

Table 7.2: The 'discontinuity temperature', suspected to denote the temperature at which the cubic phase transition occurs, for all perovskite compositions on both heating and cooling cycles, as extracted from PL emission curves and Tauc plots.

Cs content (%)	**Discontinuity temperature (K)**			
	From PL		From Tauc plot	
	Cooling	Heating	Cooling	Heating
5 (from Figure 7.6)	260	270	250	260
5 (average from 3 repeats)		270 ± 5		270 ±10
8 (from Figure 7.6)	265	265	270	265
8 (average from 3 repeats)		265 ± 0		268.3 ± 2.5
10 (from Figure 7.6)	265	265	260	265
10 (average from 3 repeats)		268.3 ± 2.5		263.3 ± 2.5

estimated by fitting a straight line to the linear region representing the absorption edge and extrapolating this to find the x-axis intercept. The extracted values are shown in Figure 7.6**C**, and this data also shows a blueshift in the band edge with increasing temperature. For each composition on both heating and cooling, there is a discontinuity in this blueshift similar to that seen in the peak PL energy (E_g).

For each composition, the 'discontinuity temperature' in the E_G vs T relationship as extracted from both the Tauc plots and the PL emission curves has been determined, on both heating and cooling cycles. The discontinuity temperature has also been determined from the temperature dependence of E_g extracted from two additional sets of variable temperature absorbance and PL data. These datasets were collected on a heating cycle only, and the temperature variation of the optical band gap for these datasets is shown in Figure D.4. In these plots, it is clear that there is a distinct difference between the compositions in terms of temperature variation of the band gap which persists between different samples of the same type. This suggests that the absorbance and PL data is repeatable despite sample-to-sample variation in film fabrication. The mean discontinuity temperature from all 3 heating cycle datasets has been determined, in order to obtain a more statistically significant value.

This protocol has been carried out for all 3 perovskite compositions (with additional variable temperature band gap data also shown in Figure D.4), and Table 7.2 gives a summary of discontinuity temperatures obtained from both PL spectra and Tauc plots. As mentioned earlier, the discontinuity temperature should give an estimate of the tem-

perature at which the high temperature phase transition occurs. Table 7.2 shows that the apparent phase transition temperature, as determined from the temperature-dependent band gap as extracted from the PL spectra, is ∼270 K for the 5% Cs blend on heating from 4-310 K, whereas this temperature is slightly lower for the 8% and 10% blends (∼265-268 K). When the optical band gap is instead extracted from the Tauc plot, the phase transition again appears to occur at 270 K for the 5% Cs blend, but this time with a larger uncertainty (± 10 K). For the 8% and 10% Cs compositions, the apparent phase transition as determined from Tauc plots is again slightly lower than that of the 5% blend, this time in the range ∼263-268 K.

For the 8% and 10% compositions, there is only a small (< 5 K) difference between the apparent phase transition temperatures observed on cooling and heating of the film. The same cannot be said for the 5% Cs blend, where the apparent phase transition temperature is 10-20 K lower on cooling than on heating. This suggests that the 5% Cs blend has some thermal hysteresis in its optical properties, perhaps driven by similar thermal hysteresis effects in its crystal structure, which will be investigated in Section 7.2.2. However, it may also simply be a product of the much larger uncertainty found in the values of discontinuity temperature for the 5% blend, which is 2-4 times larger than the uncertainty observed for the discontinuity temperature in the 8% and 10% Cs compositions. This elevated uncertainty may be partially due to a larger sample-to-sample variation for the 5% composition, as proposed previously.

It can also be seen in Figure 7.6**A** that there is a much larger discrepancy in band gap values between heating and cooling cycles for the 5% Cs blend than the other 2 blends—this may originate, at least in part, from an elevated degree of energetic disorder in this particular composition. Therefore, the effect of Cs inclusion on the extent of electronic and structural disorder in the perovskite was examined. This was done by calculating the Urbach energy, E_U, for all 3 of the compositions as a function of temperature. E_U was calculated from the absorbance spectra, with the results shown in Figure 7.7**A**. The Urbach tail is an exponential tail in the absorption spectrum just below the band edge, from which the quantity E_U can be extracted, which is a measure of electronic disorder in the film. For all compositions, this quantity is in the range 6-11

meV at 4 K, and increases monotonically as temperature is increased. This behaviour is consistent with expectation—electronic disorder in a material is expected to increase as the temperature is increased, due to the increasing availability of electronic states.

Not only does the 5% Cs perovskite have the highest value of E_U of all the compositions, but it also undergoes the largest change in E_U over the temperature range 4-300 K (ΔE_U). This suggests that not only does this blend have the highest degree of electronic disorder, but also that this disorder increases more with increasing temperature than that of the 8% or 10% perovskites. In contrast, the 8% perovskite exhibits the lowest value of both E_U and ΔE_U, suggesting that this composition is the least energetically disordered. Interestingly, analysis of E_U has uncovered what appears to be a higher degree of energetic disorder in the 5% Cs, despite the fact that it has been shown to be the most stable and best performing of the compositional range.

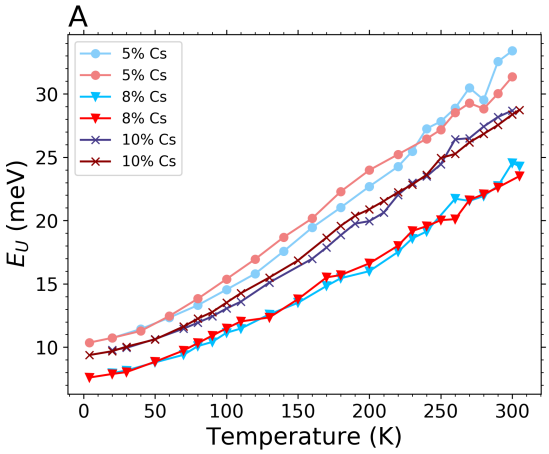

Figure 7.7: Temperature dependence of the Urbach energy, E_U, on both heating and cooling for 5%, 8% and 10% Cs films.

When collecting the temperature-dependent PL data, one key observation made was the instability of the PL signal over time after laser illumination. Interestingly, these PL instability effects only occurred when the thin films were above a certain temperature and held under vacuum. In ambient conditions however, the PL was observed to be largely stable over a timescale of a few minutes at room temperature. It was also observed that the 'activation temperature' of these effects varied by small amounts (~10-20 K) depending on the Cs content of the films. To investigate this phenomenon further, an experiment was conducted to monitor PL instability effects in the 8% Cs blend, which showed the most pronounced PL instability above the 'activation temperature'. This experiment was carried out by continuously illuminating the sample with a CW laser

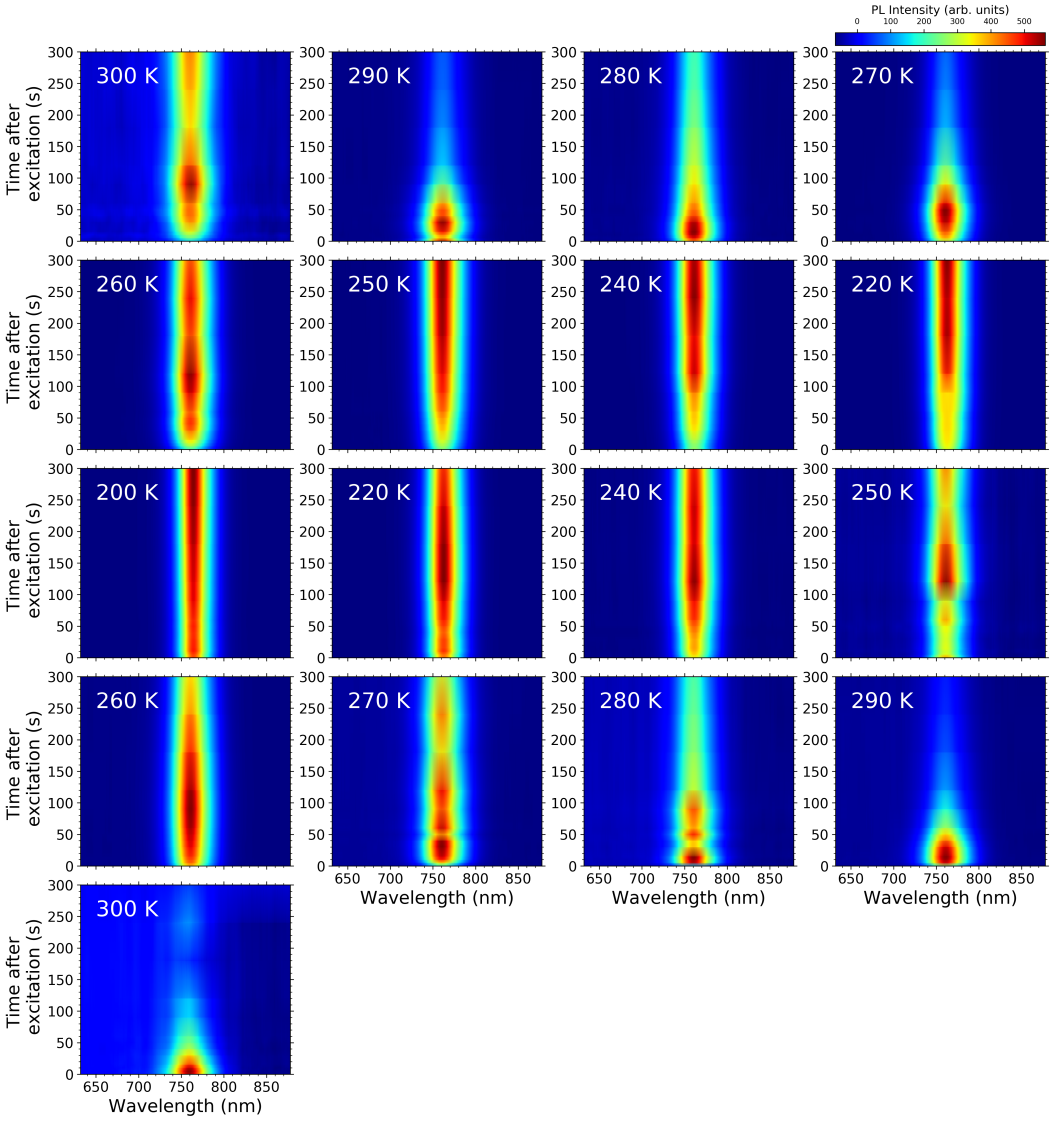

Figure 7.8: Time dependence of the PL spectra for an 8% Cs perovskite thin film, with PL spectra collected at intervals between 0 and 300 s after laser illumination, for a selection of temperatures on cooling the film from 300 K to 200 K and heating back to 300 K.

(estimated power density $\sim$1.77 kWm^{-2}) and collecting PL traces at a series of time intervals after the laser was switched on, up to a total illumination time of 300 s. The data is shown in Figure 7.8 and from these plots it can be seen that, in the temperature range 300-270 K on both cooling and subsequent heating, the PL emissions are highly unstable over the first 200-300 s after laser illumination, undergoing a rapid drop in intensity. Conversely, it can be seen that the PL intensity actually grows slightly under prolonged illumination in the temperature range 220-250 K on both cooling and heating. When the sample has been cooled to 200 K, the PL intensity does not change significantly

over the 300 s light soaking period.

One possible explanation for this PL instability above ∼220-240 K is halide segregation, an effect which has been reported to occur in mixed halide (I/Br) perovskites where the material separates into iodide-rich and bromide-rich regions within the film when subjected to illumination. Knight and coworkers found that when the mixed halide perovskite $MAPb(Br_{0.5}I_{0.5})_3$ was held under vacuum, the PL signal characteristic of the mixed phase ($\lambda \sim 745$ nm) underwent a significant drop in intensity over the first 15 s under illumination, as part of a photo-induced halide segregation process.[44] Our data (Figure 7.8) shows a continual decrease of the PL signal under illumination over a period of 300 s at room temperature, but only when the sample was held under vacuum—under ambient conditions, the PL signal was observed to be largely stable over this time period. However, the effects of halide segregation are widely reported as a drop in PL intensity in the first few seconds, followed by a PL redshift to what has been identified as an iodide-rich phase, accompanied by a gradual increase in PL intensity of this phase.[45,46] This effect is believed to be the result of light-induced lattice distortions which allow mobility of halide anions.[47] This suggests that these Cs-containing mixed halide perovskites are susceptible to such lattice distortions and that this causes some degree of halide segregation, but that this segregation is suppressed by the presence of Cs in the lattice, as has been previously proposed.[48,49] The PL instability effects appear to be the most pronounced in the 8% blend, suggesting that it is the most susceptible to halide segregation. This may indicate a lower level of phase purity or phase stability in this composition compared to the other compositions studied. In other words, the thin film contains the lowest proportion of pure perovskite phase crystal domains and therefore has an elevated propensity to form iodide- or bromide-rich domains.

It can also be speculated that the 'activation temperature' of the observed PL instability effects may be related to the tetragonal-cubic phase transition in these materials, as it is reported in the literature that halide segregation occurs in the cubic perovskite phase, but not in the tetragonal phase.[46] The observed changes in PL behaviour begin to occur in the range 220-240 K in all films, which is lower than the apparent phase transition temperatures inferred from Figure 7.6**A**. However, in Chapter 6 a gradual

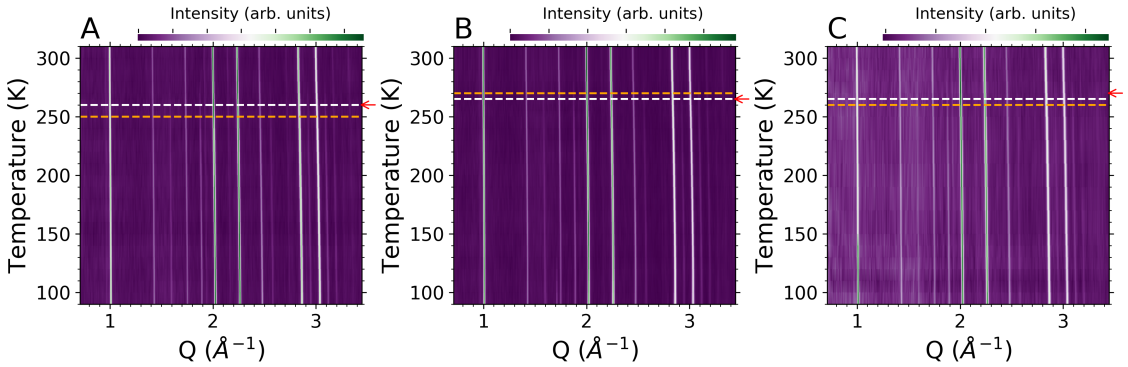

Figure 7.9: Temperature dependent powder X-ray diffraction patterns recorded on cooling from 315 K to 80 K, collected from perovskite powders of compositions **A** 5% Cs, **B** 8% Cs and **C** 10% Cs. Orange dashed lines mark the 'discontinuity temperature', acquired from the temperature variation of the band gap obtained from absorbance data, which is postulated to correspond to the cubic phase transition in these materials. White dashed lines mark the 'discontinuity temperature' as obtained from the temperature variation of the band gap obtained from PL spectra. The red arrows mark the approximate temperature where the diffractions peaks corresponding to the β phase appear in the spectra.

change in lattice parameters leading up to the tetragonal-cubic phase transition was found for $(FAPbI_3)_{0.85}(MAPbBr_3)_{0.15}$, therefore these Cs-containing blends may undergo similar structural changes prior to the cubic phase transition and these may result in the early onset of halide segregation effect.

7.2.2 Variable Temperature Powder X-Ray Diffraction

In order to investigate the effect of Cs incorporation on the phase behaviour of triple cation perovskites, variable temperature powder x-ray diffraction (PXRD) was carried out on powdered samples of 5% Cs, 8% Cs and 10% Cs. The perovskites were prepared as described in Section 3.1.2 in Chapter 3, and a powder was obtained by scraping the thin films from the substrates using a razor blade, in a nitrogen environment to prevent moisture ingress. X-ray diffraction measurements were then carried out at a series of temperatures on cooling and heating of the powder, as described in Section 3.5.

In Figure 7.9, colourmaps showing the evolution of the powder x-ray diffractograms as a function of temperature on cooling of the powder sample are plotted. At a temperature of 310 K before cooling the samples, the diffraction patterns include the peaks we expect for the (100), (110) and (111) crystal planes of cubic perovskites. The positions at which these appear for each composition are listed in Table D.2 in Appendix D. The diffraction patterns at 310 K also contain the characteristic peaks for the (200), (112), (220), (300) and (222) planes, as labelled in Figure 7.10. The (100), (110) and (111) peaks (at ∼1.0,

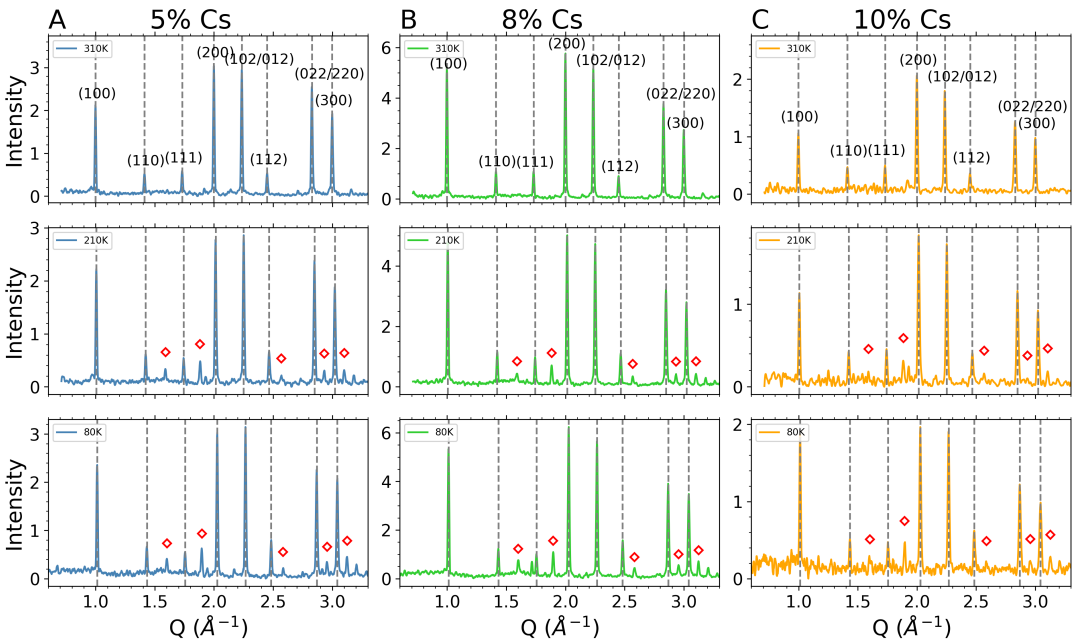

Figure 7.10: Powder x-ray diffraction data recorded at temperatures of 310 K, 210 K and 80 K for 3 different Cs-containing perovskites on cooling of the sample: **A** 5 %, **B** 8 % and **C** 10 % Cs.

1.41 and 1.73 Å^{-1} respectively) shift to higher values of Q for all compositions as the temperature is lowered to 90 K, as expected with thermal contraction of the lattice.

Upon cooling of the sample, a series of new peaks (at $Q \approx 1.59, 1.88, 2.57, 2.93, 3.10$ Å^{-1}) begin to appear within the temperature range ~280-260 K for all compositions. In Figure 7.10, XRD patterns recorded at temperatures of 310, 210 and 80 K are plotted for all compositions. The new peaks appearing in the range ~280-260 K are marked with red diamonds in Figure 7.10, and here it is asserted that these peaks are characteristic of the tetragonal perovskite phase, commonly known as the β phase.[50] Therefore the appearance of these peaks indicates a phase transition from the pseudo-cubic α phase to the tetragonal β phase.

The X-ray diffractograms for all temperatures on cooling of the 5% Cs perovskite powder are plotted in Figure 7.11, where the appearance of the peaks corresponding to the β phase is marked with the orange circle. The discontinuity temperatures obtained from temperature-dependent absorbance and PL data (Table 7.2) are also marked on this plot. The same protocol has been carried out for the other compositions, as shown in Figs. D.5–6, where the x-ray diffraction patterns for the 8% and 10% Cs perovskites on cooling of the powder are plotted. In Figs. D.7–9, the diffraction patterns for all compositions recorded on heating are plotted. From these figures, it can be seen that

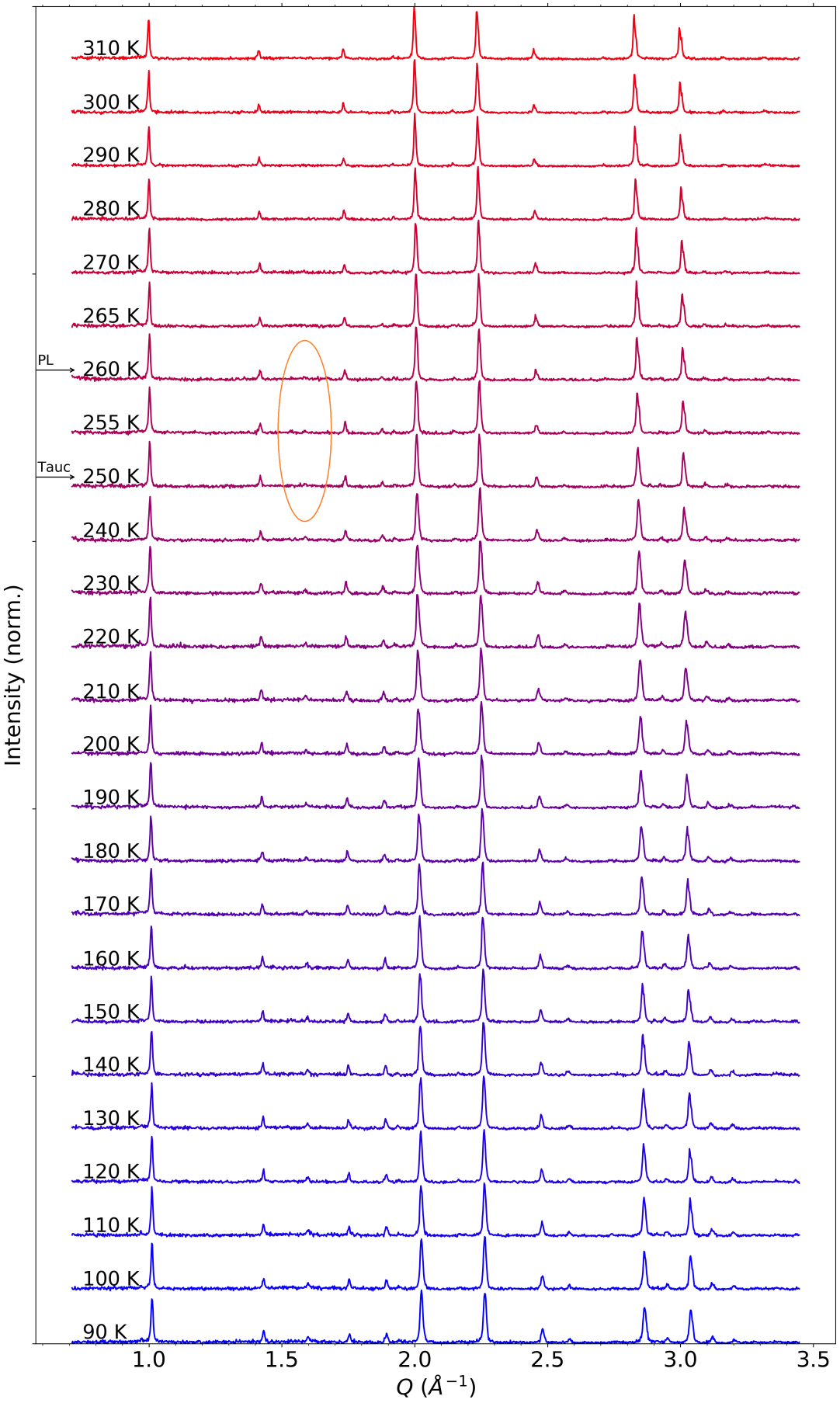

Figure 7.11: XRD patterns as collected at a series of temperatures while cooling the powder sample of 5% Cs triple cation perovskite from 310 K to 90 K. The orange circle highlights the appearance of the peaks associated with the β phase.

the discontinuity temperatures found from optical data generally coincide (within ∼10 K) with the temperatures at which the tetragonal diffraction peaks appear in the XRD data, adding evidence to the assertion that the 'discontinuity temperature' in the band gap blueshift is associated with the tetragonal-cubic phase transition. This correlation can also be seen in Figure 7.9, where the discontinuity temperatures obtained from absorbance and PL data are shown—the white dashed lines denote the discontinuity temperature found from the PL data and the orange dashed lines denote the discontinuity temperature found from the absorbance data—and the red arrows denote the temperatures at which the tetragonal peaks appear.

It is clear from the XRD data that the 5% Cs composition has a lower phase transition temperature than that of the 8% and 10% compositions. Between the 8% and 10% Cs blends it is not trivial to ascertain which has the lowest phase transition temperature, because the diffractograms in Figure D.6 have a poor signal-to-noise ratio and therefore the appearance of the β phase cannot be easily determined. From Figure D.6 and Figure D.9, it can be estimated that in the 10% Cs blend these peaks appear in the temperature range ∼260-270 K. From Figure D.5 and Figure D.8, it can be seen that these peaks appear in the range ∼265-270 K for the 8% composition, which suggests that the addition of the extra 2% Cs into the composition barely shifts the phase transition temperature.

However, it is not only the appearance of additional peaks in the XRD data which can indicate a phase transition. In fact, the phase behaviour can only be fully determined by finding the temperature dependence of certain unit cell parameters, which can be found by applying structural refinements to the XRD data. In order to fully probe the phase behaviour of these materials, structural refinements have been carried out as described in Section 3.5 on diffractograms collected at all temperatures for all compositions. In order to make the modelled unit cells comparable over the full temperature range, where the unit cell may be tetragonal or cubic, the model was set up such that:

$$\frac{a}{\sqrt{2}} = b = c \quad \text{for a cubic unit cell} \tag{7.4}$$

and

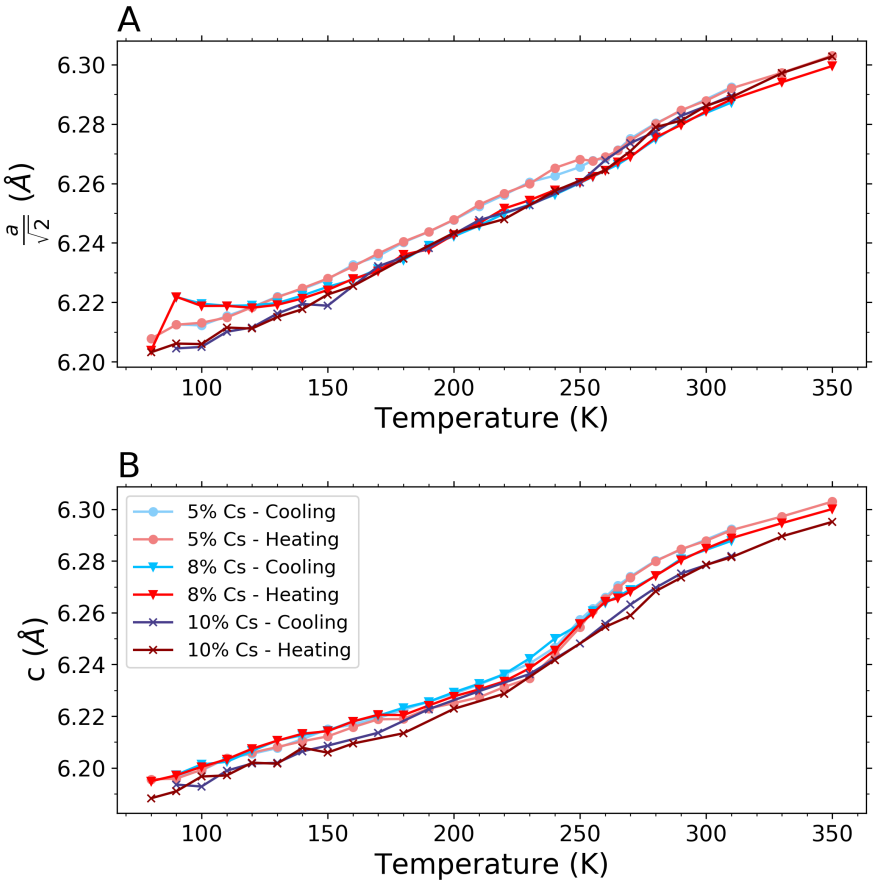

Figure 7.12: Temperature dependence of the unit cell parameterss **A** $a/\sqrt{2}$ and **B** c. Unit cell dimensions a, b and c have been determined from structural refinements applied to the powder XRD data taken on both cooling and heating cycles for the 5%, 8% and 10% Cs perovskite blends. All raw data is shown in Figure 7.11 and Figs. D.5–9.

$$\frac{a}{\sqrt{2}} = b \neq c \quad \text{for a tetragonal unit cell} \tag{7.5}$$

where $\frac{a}{\sqrt{2}}$, b and c are the dimensions of the modelled unit cell.

The parameters $\frac{a}{\sqrt{2}}$, b and c were determined from the Rietveld structural refinements, along with the Pb-X-Pb bond angle (where X is the halide anion) and the Pb-X bond length. The temperature dependence of both $\frac{a}{\sqrt{2}}$ and c is plotted in Figure 7.12. In Figure 7.12**A** it can be seen that the $\frac{a}{\sqrt{2}}$ parameter increases with increasing temperature, as expected through thermal expansion of the lattice. The c parameter (Figure 7.12**B**) follows a similar trend with temperature, however in the temperature range 80-250 K values of $\frac{a}{\sqrt{2}}$ and c differ by a small margin, as expected for the tetragonal phase where $\frac{a}{\sqrt{2}} \neq c$.

The change in the $\frac{a}{\sqrt{2}}$ and c parameters over the full temperature range was also calculated, with the results summarised in Table 7.3 in Appendix D. Table 7.3 shows that

Table 7.3: Overall change in the lattice parameters $\frac{a}{\sqrt{2}}$ and c over the temperature range 80-310 K on both cooling and heating of the powder sample.

Cs content (%)	$\Delta\frac{a}{\sqrt{2}}$ (Å)		Δc (Å)	
	Cooling	Heating	Cooling	Heating
5	0.1130	0.1347	0.09555	0.1074
8	0.09265	0.1354	0.09045	0.1052
10	0.1203	0.1408	0.08837	0.1069

the 10% Cs blend undergoes the largest increase in $\frac{a}{\sqrt{2}}$ on both cooling and heating, but it exhibits the smallest overall change in band gap across the temperature range 4-310 K, as shown earlier (Table 7.1). The 5% blend undergoes the largest change in c-parameter across the 80-310 K temperature range, and also exhibits the largest change in optical band gap over the 4-310 K range. These results broadly suggest that it is the lengthening of the lattice constant c with increasing temperature which drives the widening of the band gap, supporting the DFT calculations of Meloni *et al.* as discussed previously. The c-axis is the dimension of the unit cell which becomes unequal to the other dimensions when the material transforms to the tetragonal unit cell, therefore this may explain why the temperature gradient of E_G (as shown in Figure 7.6**A**,**C**) is not constant across the whole 4-250 K temperature range and the cubic phase transition above this temperature causes a discontinuity in E_G values.

An interesting feature observed in the temperature dependence of the $a/\sqrt{2}$ parameter is a discontinuity in its increase between 80 and 90 K for the 8% Cs perovskite. This suggests that a phase transition occurs in this perovskite in the temperature range 80-90 K, which is postulated to be a variation on the tetragonal β phase with lowered symmetry, similar to the transition observed in the double cation perovskite $(FAPbI_3)_{0.85}(MAPbBr_3)_{0.15}$, as discussed in Chapter 6. This phase has been shown to appear at low temperatures in $FAPbI_3$ perovskite previously and is commonly referred to as the γ phase.[51] For the 5% Cs and 10% Cs perovskite compositions, such a discontinuity is not observed in $\frac{a}{\sqrt{2}}$, which may suggest that such a phase transition does not occur in these materials at this temperature. However, the temperature dependence of other structural parameters indicates the occurrence of a phase transition in this temperature range for the 5% and 10% Cs compositions, which will be discussed later in

this section.

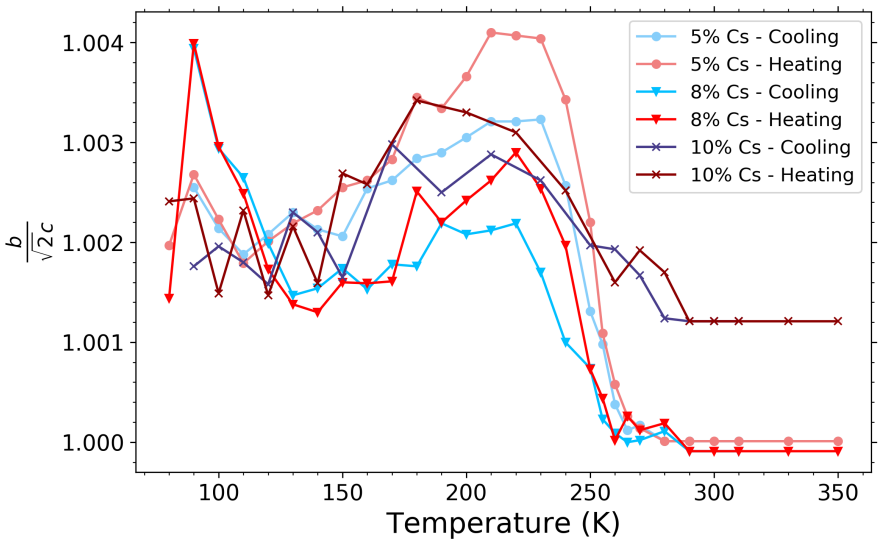

Figure 7.13: Temperature dependence of the lattice parameter ratio $b\sqrt{2}/c$ as calculated from Rietvield structural refinements applied to the XRD data in Figure 7.11 and Figs. D.5–9.**D** Temperature dependence of the Pb-X-Pb bond angle, where X is the halide. **E** Temperature dependence of the Pb-X bond length, where X is the halide.

The temperature dependence of the lattice parameter ratio $\frac{b}{\sqrt{2}c}$ is plotted in Figure 7.13, which is expected to exhibit the following behaviour:

$$\frac{b}{\sqrt{2}c} = \begin{cases} 1, & \text{for cubic unit cell} \\ \neq 1, & \text{otherwise} \end{cases}$$

In Figure 7.13 it can be seen that, for the 5% and 8% Cs blends, $\frac{b}{\sqrt{2}c}$ undergoes a sharp increase at 90 K followed by a sharp decrease, with this effect being largest for the 8% Cs blend. The ratio then reaches a minimum at 110 K (5% Cs)/120 K (8% Cs). In the 8% Cs blend, the appearance of a new peak in the diffractogram was observed when the sample is cooled to 120 K, which increases in intensity as the sample is further cooled to 80 K, as shown in Figure 7.10**B**. This new peak, along with the discontinuity in $\frac{b}{\sqrt{2}c}$ in the range 80-120 K for the 8% composition may be due to the low temperature phase transition from the β phase to the γ phase. For the 5% and 10% blends, the $\frac{b}{\sqrt{2}c}$ discontinuity may also originate from a low temperature γ phase transition, even in the absence of any additional diffraction peaks in the 80-120 K temperature range—the signal from the γ phase may have been too weak for these compositions to show up in the diffractograms.

Above 110/120 K, the ratio $\frac{b}{\sqrt{2}c}$ continues to increase, reaching a maximum in the

range 210-230 K. This local maximum coincides with the disappearance of both of the new diffraction peaks observed in the 8% Cs blend. This increase above 110/120 K suggests a lengthening of the unit cell axis associated with the *b* parameter, as the temperature is increased across this range. From ∼230 K onwards, the ratio decreases monotically before flattening at a value of 1, at approximately 280 K and 290 K for the 5% and 8% Cs compositions, respectively. The rapid drop in $\frac{b}{\sqrt{2}c}$ across the range ∼230-290 K suggests that the phase transition from the β phase to the α phase occurs over this temperature range, with the flattening at $\frac{b}{\sqrt{2}c} = 1$ suggesting that the cubic phase has stabilised. These observations correlate reasonably well with the temperature dependence of the band gap—in Figure 7.6**A**, the blueshift in the band gap does not resume until 280-290 K, which coincides with the temperature at which the cubic phase appears to stabilise. These observations also correlate with our finding that changes in the *c*-axis lattice constant drive the widening and narrowing of the band gap, as the discontinuity in E_G (Figure 7.6) occurs in the temperature range where a rapid change in the lattice parameter $\frac{b}{\sqrt{2}c}$ is taking place during the phase transition to the cubic phase.

In Section 7.2.1, it was suggested that the instability in the PL intensity above ∼220 K observed in Figure 7.7**B** is associated with halide segregation processes, however previous studies show that these processes generally can only occur in the cubic perovskite phase[46] and this PL instability occurs below the apparent cubic phase transition temperature as determined from the PL and absorbance measurements. It was therefore proposed that the occurrence of the PL instability at lower temperatures than the cubic phase transition may be due to a gradual transition to the cubic phase occuring in the 220-260 K temperature range. The drop in $\frac{b}{\sqrt{2}c}$ between ∼220 and ∼280 K does indeed indicate a gradual transformation to the cubic unit cell, therefore this may lead to light-induced segregation effects causing PL instability below the phase transition temperature.

The temperature trends in $\frac{b}{\sqrt{2}c}$ for the 10% Cs blend are much more difficult to determine due to a high degree of noise in the data. This is most likely due to difficulties in refining the structural parameters due to the low signal/noise ratio in the diffraction data (see Figure D.6). Nevertheless, a stabilisation of the ratio at temperatures above

290 K on heating is observed, which can be attributed to a phase transition to the cubic phase. A notable effect here is the stabilisation of the ratio at ∼1.001 rather than 1 as expected for the cubic phase, which is most likely to be due to the difficulty in refining the parameters for the 10% Cs due to the high noise levels in the diffraction data.

Another notable feature observed in the temperature dependence of $\frac{b}{\sqrt{2}c}$ for all compositions is a discrepancy in this ratio between heating and cooling cycles occurring between 110 K and ∼260 K, which is most pronounced around the local maximum at ∼220 K. This thermal hysteresis in unit cell size may be the origin of the thermal hysteresis observed in the band gap values shown in Figure 7.6. In the case of the 8% Cs blend, the appearance of an additional peak in the diffractogram at Q ∼1.71 Å^{-1} is observed at 80 K (see Figure 7.10). The full diffraction patterns recorded on cooling, which are displayed in Figure D.5, show that this peak first appears at ∼120 K. The full patterns recorded on heating, displayed in Figure D.8, show that this peak remains in the diffraction patterns on heating and persists up to ∼210 K. This plot also shows that there is also a splitting of the tetragonal phase peak at ∼1.59 Å^{-1} which begins to occur at 90 K and strengthens on heating the film further, again persisting up to ∼210 K.

In Chapter 6 similar hysteresis behaviour was observed in the lattice parameter ratio for the double cation perovskite $(FAPbI_3)_{0.85}(MAPbBr_3)_{0.15}$—the temperature-dependent lattice parameter ratio of this material exhibits hysteresis between heating and cooling cycles in the 150-250 K range, with this hysteresis peaking at 220 K, which was also a local minimum in the lattice parameter ratio $\frac{c\sqrt{2}}{a}$ (this is equivalent to the inverse of $\frac{b}{\sqrt{2}c}$, hence there is a local minimum in this parameter, which is equivalent to a local maximum in $\frac{b}{\sqrt{2}c}$). This temperature correlated with the disappearance of unidentified peaks in the diffraction patterns, which appeared at 90 K on cooling and persisted up to 220 K on re-heating. These peaks, along with the thermal hysteresis effects, were associated with the possible presence of an additional phase in the material. However, the thermal hysteresis effects observed in Figure 7.13 are also present for the 5% and 10% Cs blends, whose variable temperature X-ray diffractograms did not show any additional peaks in the 80-120 K range, therefore the thermal hysteresis is likely to

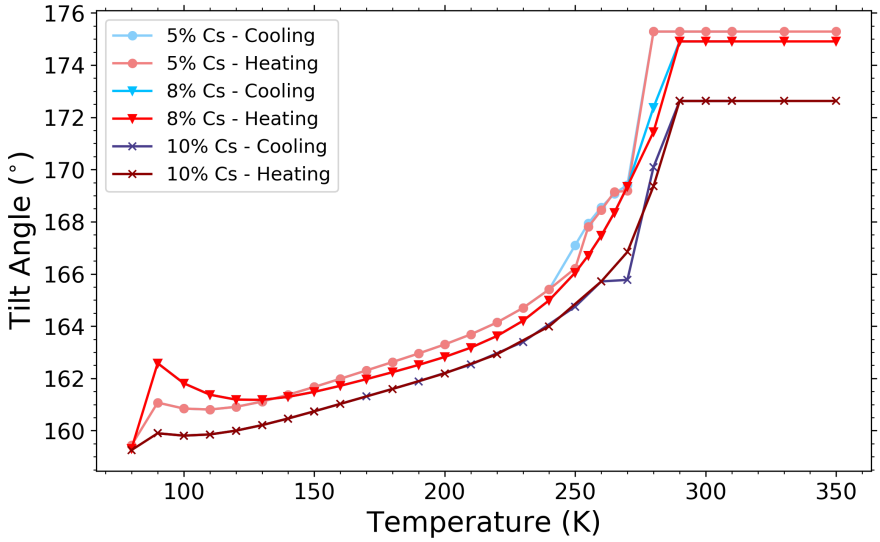

Figure 7.14: Temperature dependence of the Pb-X-Pb bond angle (or tilt angle), where X is the halide, for all compositions on heating and cooling of the powder, as calculated from Rietveld structural refinements applied to the XRD data in Figure 7.11 and Figs. D.5–9.

have a different origin.

If the thermal hysteresis behaviour is not associated with any additional phase, it may instead be related to structural disorder: at high temperatures (before cooling) there may be disorder in the distribution of atoms across the lattice sites, and the process of cooling to 80 K may introduce some sort of order which takes advantage of the different atom sizes to reduce the energy of the lower symmetry phase (i.e. the tetragonal β phase), and therefore this order persists throughout the tetragonal phase on re-heating of the material.

From the structural refinements the tilt angle was also determined, which quantifies the angle formed by Pb-X-Pb bonds in degrees—the temperature dependence of this parameter is shown in Figure 7.14. There is a discontinuity in this parameter occuring at 90 K for all compositions, and in a similar way to $\frac{b}{\sqrt{2}c}$ the discontinuity is largest for the 8% Cs compositon. It is asserted that this discontinuity in bond angle provides further evidence of a phase transition to the lower symmetry γ phase occurring in the materials at this temperature.

Above 90 K, the tilt angle increases with a varying gradient up to 280 K (5% Cs)/290 K (8% Cs, 10% Cs). The steeper part of the temperature gradient (spanning ~240-290 K) coincides with the gradual phase transition to the cubic phase which was proposed based on observations of the temperature dependence of the $\frac{b}{\sqrt{2}c}$ ratio. The tilt angle,

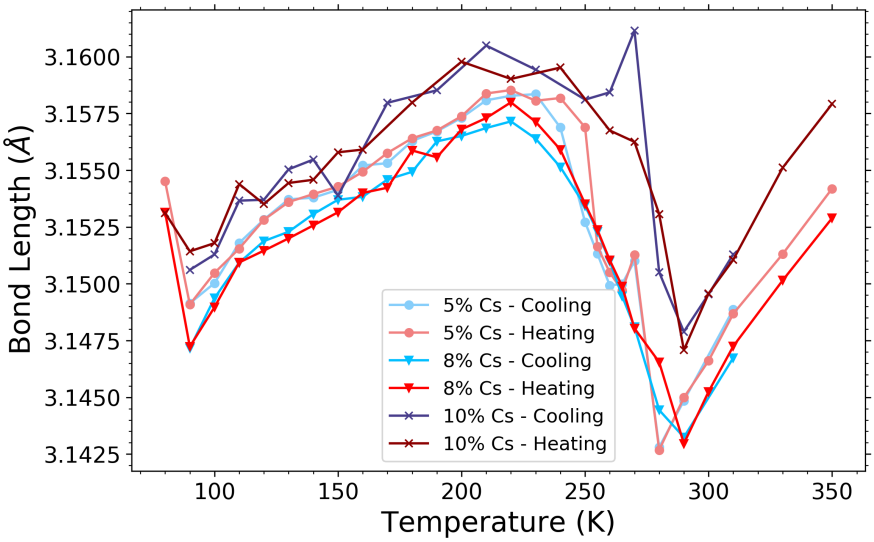

Figure 7.15: Temperature dependence of the Pb-X bond length, where X is the halide, for all compositions on heating and cooling of the powder, as calculated from Rietvield structural refinements applied to the XRD data in Figure 7.11 and Figs. D.5–9.

similarly to $\frac{b}{\sqrt{2}c}$, is stable above 280/290 K, again suggesting that the cubic phase has stabilised above this temperature. In the cubic phase we would expect a tilt angle of 180°, however the angle stabilises at ∼175° for the 5% and 8% compositions and ∼173° for the 10% Cs composition.

This may be a result of the fact that hybrid perovskites are very dynamic systems at near-ambient temperatures.[52] This deviation of the Pb-X-Pb bond angle from the expected value could be an indication of the halide dynamically rotating out of the plane of the Pb atoms of adjacent octahedra. Again the 10% Cs blend exhibits a different trend, with a tilt angle which stabilises 2° lower, which is believed to be a result of the difficulty in refining the 10% Cs diffraction data due to a low signal-to-noise ratio.

The final parameter to be refined was the length of the Pb-X bond angles. The bond length as a function of temperature is plotted in Figure 7.15. A drop in the bond length is observed as the Cs content in the blends is increased from 5% to 8%, which holds not only at room temperature but also across the majority of the temperature range studied. However as the Cs content is further increased to 10%, the bond lengths become slightly higher than those of the 5% or 8% Cs blends. Considering that the Pb-X bond length is correlated with both bond energy and unit cell size, this may indicate that this bond has a higher bond energy for the Pb-X bonds, possibly due to an instability in the structure—earlier a larger inclusion of PbI_2 degradation products was identified in

the 10% Cs blend as compared to the 5%/8% Cs blends, which does indicate instability in the structure. However, the parameters refined for the 10% Cs have been shown to be considerably less accurate due to poor signal-noise ratio in the diffractograms, therefore it is possible that the anomalous bond lengths in the 10% Cs blend are a result of this.

For all compositions, the bond length undergoes a sharp decrease between 80 and 90 K, although for the 10% Cs composition it is not clear whether this effect is simply due to noise in the data. This sharp decrease in the bond length strengthens the assertion that all compositions undergo a structural phase change to the γ phase at around 90 K. As with $\frac{b}{\sqrt{2}c}$ and the tilt angle, this effect is most pronounced in the 8% Cs data. These anomalously large changes in lattice properties at the phase transitions may point towards a lower level of phase purity in the 8% Cs perovskite than in the other perovskites, or a more significant incoporation of the γ phase in this perovskite. This is supported by the observation that the 8% Cs blend exhibits additional diffraction peaks at low temperature which are not associated with the tetragonal phase. These additional peaks are not observed for the 5% and 10% perovskite, which suggests that there is a more significant incorporation of the γ phase in the 8% Cs perovskite. However, it is possible that the various discrepancies observed in the 8% Cs blend fall within the error on the calculation of the structural parameters, due to the relatively low signal-to-noise ratio in the X-ray diffraction data (see Figure 7.10 for examples). Therefore these results may not be statistically significant enough to claim that the 8% Cs perovskite is a less 'phase pure' material.

Above 90 K there is an increase in bond length, up to a maximum at 220 K for the 5% and 8% Cs blends. From this maximum point the bond length decreases, up to 280 K (5% Cs)/290 K (8% Cs, 10% Cs), from which point it begins to increase with increasing temperature again. As determined from the temperature dependent trends in $\frac{b}{\sqrt{2}c}$ and the tilt angle, these temperatures signify the stabilisation of the cubic phase, however the bond length continues to increase with increasing temperature, which is to be expected as the lattice will continue to expand above this temperature. These temperatures at which the cubic phase stabilises according to the bond length also correlate with the resumption of the blueshift in band gap, which was speculated to be

due to the full stabilisation of the cubic phase. These results bring further evidence that the cubic phase transition occurs at slightly higher temperatures as the Cs content in the perovskite is increased.

7.3 Conclusions

In this chapter, experimental evidence has been presented for notable changes to the phase behaviour of $Cs_zFA_xMA_yPbI_{2.55}Br_{0.45}$, where $x = 4y$, on increasing the Cs fraction z across the range $z = 0.05 - 0.1$. From both structural and optical data, the presence of two structural phase transitions occurring in the temperature range 80-310 K, has been demonstrated for triple cation perovskites with 5%, 8% and 10% Cs concentration.

It has been demonstrated that the optical band gap of $Cs_zFA_xMA_yPbI_{2.55}Br_{0.45}$ widens as z is increased, as expected through inclusion of the smaller cation Cs into the A-site cation in the perovskite lattice. It has also been shown that the overall blueshift of the optical band gap in the temperature range 4-300 K decreases as z is increased, and it is speculated that the band gap widening with increasing temperature is driven by the lengthening of the lattice constant c.

Structural refinements of variable temperature x-ray diffraction data demonstrated that all 3 compositions undergo two distinct structural phase transitions within the temperature range 80-310 K. For all 3 materials, the flattening of the lattice parameter ratio $\frac{b}{\sqrt{2}c}$ and Pb-X-Pb tilt angle (above 280 K and 290 K for the 5% and 8/10% Cs compositions respectively) signifies the stabilisation of a cubic phase in the perovskite material. This suggests that the cubic phase transition occurs at slightly higher temperatures when Cs incorporation into the A-cation site is increased. This high temperature structural phase transition is also reflected in the temperature dependence of the optical band gap as determined from PL and absorbance measurements, where a discontinuity in the blueshift of the gap is observed, coinciding with the disappearance of the diffraction peaks in the XRD data which correspond to the tetragonal β phase. The stabilisation of the cubic phase at 280/290 K coincides with the temperature at which the band gap blueshift resumes after the discontinuity associated with the phase transition. The elevated stability of 5% Cs as previously shown in the literature may be attributed to

the lower temperature at which the tetragonal-cubic phase transition occurs, as this will result in the perovskite being more thermally stable at ambient temperature.

Furthermore evidence that the $\beta \rightarrow \alpha$ phase transition in these materials occurs across a wide temperature range (∼60-70 K) has been presented, as shown by the behaviour of the $\frac{b}{\sqrt{2}c}$ ratio, and that this is reflected in the fluorescence behaviour of these materials. It has been speculated that changes in the unit cell size during the transition are linked to the appearance of apparent partially suppressed halide segregation effects, which become more pronounced when the full phase transition has occurred, as the cubic perovskite phase makes halide segregation effects more energetically favourable.

The second phase transition observed in all blends was a low temperature transition to a γ phase, which was identified as a lower symmetry variation on the β phase. This transition occurred at ∼90 K in all 3 compositions, and was characterised by discontinuities in lattice parameter $\frac{a}{\sqrt{2}}$, lattice parameter ratio $\frac{b}{\sqrt{2}c}$, Pb-X-Pb bond angle and bond length. The discontinuity observed in $\frac{b}{\sqrt{2}c}$, $\frac{a}{\sqrt{2}}$ and the bond angle had the largest magnitude for the 8% Cs composition, an effect which may point towards lower phase purity in this composition, however it is also possible that this result is not statistically significant due to the signal-to-noise ratio in the XRD data.

References

[1] A. Kojima, K. Teshima, Y. Shirai, T. Miyasaka, *Journal of the American Chemical Society* **2009**, *131*, 6050.

[2] NREL: Best Research-Cell Efficiencies Chart, https://pvdpc.nrel.gov/, accessed on 2020-08-04.

[3] C. Wehrenfennig, G. E. Eperon, M. B. Johnston, H. J. Snaith, L. M. Herz, *Advanced Materials* **2014**, *26*, 1584.

[4] S. D. Stranks, G. E. Eperon, G. Grancini, C. Menelaou, M. J. P. Alcocer, T. Leijtens, L. M. Herz, A. Petrozza, H. J. Snaith, *Science (New York, N.Y.)* **2013**, *342*, 341.

[5] V. D'Innocenzo, *Nature Commun.* **2014**, *5*.

[6] K. X. Steirer, P. Schulz, G. Teeter, V. Stevanovic, M. Yang, K. Zhu, J. J. Berry, *ACS Energy Letters* **2016**, *1*, 360.

[7] A. T. Barrows, A. J. Pearson, C. K. Kwak, A. D. F. Dunbar, A. R. Buckley, D. G. Lidzey, *Energy & Environmental Science* **2014**, *7*, 2944.

[8] Y. Galagan, F. Di Giacomo, H. Gorter, G. Kirchner, I. de Vries, R. Andriessen, P. Groen, *Advanced Energy Materials* **2018**, *8*, 1801935.

[9] N. Pellet, P. Gao, G. Gregori, T.-Y. Yang, M. K. Nazeeruddin, J. Maier, M. Grätzel, *Angewandte Chemie* **2014**, *126*, 3215.

[10] N. J. Jeon, J. H. Noh, W. S. Yang, Y. C. Kim, S. Ryu, J. Seo, S. I. Seok, *Nature* **2015**, *517*, 476.

[11] D. Bi, W. Tress, M. I. Dar, P. Gao, J. Luo, C. Renevier, K. Schenk, A. Abate, F. Giordano, J.-P. Correa Baena, J.-D. Decoppet, S. M. Zakeeruddin, M. K. Nazeeruddin, M. Gra tzel, A. Hagfeldt, *Science Advances* **2016**, *2*, e1501170.

[12] Y. Sun, J. Peng, Y. Chen, Y. Yao, Z. Liang, *Scientific Reports* **2017**, *7*, 1.

[13] M. Abdi-Jalebi, Z. Andaji-Garmaroudi, S. Cacovich, C. Stavrakas, B. Philippe, J. M. Richter, M. Alsari, E. P. Booker, E. M. Hutter, A. J. Pearson, S. Lilliu, T. J. Savenije, H. Rensmo, G. Divitini, C. Ducati, R. H. Friend, S. D. Stranks, *Nature* **2018**, *555*, 497.

[14] T. Singh, T. Miyasaka, *Advanced Energy Materials* **2018**, *8*.

[15] S. Liu, W. Huang, P. Liao, N. Pootrakulchote, H. Li, J. Lu, J. Li, F. Huang, X. Shai, X. Zhao, Y. Shen, Y. B. Cheng, M. Wang, *Journal of Materials Chemistry A* **2017**, *5*, 22952.

[16] R. Zhang, D. Liu, Y. Wang, T. Zhang, X. Gu, P. Zhang, J. Wu, Z. D. Chen, Y. Zhao, S. Li, *Electrochimica Acta* **2018**, *265*, 98.

[17] T. Matsui, J.-Y. Seo, M. Saliba, S. M. Zakeeruddin, M. Grätzel, *Advanced Materials* **2017**, *29*, 1606258.

[18] M. Saliba, T. Matsui, J.-Y. Seo, K. Domanski, J.-P. Correa-Baena, M. K. Nazeeruddin, S. M. Zakeeruddin, W. Tress, A. Abate, A. Hagfeldt, M. Grätzel, *Energy & Environmental Science* **2016**, *9*, 1989.

[19] L.-Q. Xie, L. Chen, Z.-A. Nan, H.-X. Lin, T. Wang, D.-P. Zhan, J.-W. Yan, B.-W. Mao, Z.-Q. Tian, *Journal of the American Chemical Society* **2017**, *139*, 3320.

[20] O. J. Weber, B. Charles, M. T. Weller, *Journal of Materials Chemistry A* **2016**, *4*, 15375.

[21] M. Baranowski, J. M. Urban, N. Zhang, A. Surrente, D. K. Maude, Z. Andaji-Garmaroudi, S. D. Stranks, P. Plochocka, *Journal of Physical Chemistry C* **2018**, *122*, 17473.

[22] A. D. Wright, R. L. Milot, G. E. Eperon, H. J. Snaith, M. B. Johnston, L. M. Herz, *Advanced Functional Materials* **2017**, *27*, 1700860.

[23] P. Boonmongkolras, D. Kim, E. M. Alhabshi, I. Gereige, B. Shin, *RSC Advances* **2018**, *8*, 21551.

[24] N. Aristidou, I. Sanchez-Molina, T. Chotchuangchutchaval, M. Brown, L. Martinez, T. Rath, S. A. Haque, *Angewandte Chemie International Edition* **2015**, *54*, 8208.

[25] H.-S. Kim, J.-Y. Seo, N.-G. Park, *ChemSusChem* **2016**, *9*, 2528.

[26] A. J. Pearson, G. E. Eperon, P. E. Hopkinson, S. N. Habisreutinger, J. T.-W. Wang, H. J. Snaith, N. C. Greenham, *Advanced Energy Materials* **2016**, *6*, 1600014.

[27] T. Du, C. H. Burgess, J. Kim, J. Zhang, J. R. Durrant, M. A. McLachlan, *Sustainable Energy and Fuels* **2017**, *1*, 119.

[28] B.-w. Park, N. Kedem, M. Kulbak, D. Y. Lee, W. S. Yang, N. J. Jeon, J. Seo, G. Kim, K. J. Kim, T. J. Shin, G. Hodes, D. Cahen, S. I. Seok, *Nature Communications* **2018**, *9*, 3301.

[29] K. Wu, A. Bera, C. Ma, Y. Du, Y. Yang, L. Li, T. Wu, *Phys. Chem. Chem. Phys.* **2014**, *16*, 22476.

[30] C. Wehrenfennig, M. Liu, H. J. Snaith, M. B. Johnston, L. M. Herz, *Journal of Physical Chemistry Letters* **2014**, *5*, 1300.

[31] A. D. Wright, C. Verdi, R. L. Milot, G. E. Eperon, M. A. Pérez-Osorio, H. J. Snaith, F. Giustino, M. B. Johnston, L. M. Herz, *Nature Communications* **2016**, *7*, 11755.

[32] S. Ghosh, Q. Shi, B. Pradhan, P. Kumar, Z. Wang, S. Acharya, S. K. Pal, T. Pullerits, K. J. Karki, *The Journal of Physical Chemistry Letters* **2018**, *9*, 4245.

[33] A. L. Stancik, E. B. Brauns, *Vibrational Spectroscopy* **2008**, *47*, 66.

[34] Y. Fang, H. Wei, Q. Dong, J. Huang, *Nature Communications* **2017**, *8*.

[35] H.-H. Fang, R. Raissa, M. Abdu-Aguye, S. Adjokatse, G. R. Blake, J. Even, M. A. Loi, *Advanced Functional Materials* **2015**, *25*, 2378.

[36] M. I. Dar, G. Jacopin, S. Meloni, A. Mattoni, N. Arora, A. Boziki, S. M. Zakeeruddin, U. Rothlisberger, M. Gra tzel, *Science Advances* **2016**, *2*, e1601156.

[37] Y. Varshni, *Physica* **1967**, *34*, 149.

[38] S. Meloni, G. Palermo, N. Ashari-Astani, M. Grätzel, U. Rothlisberger, *Journal of Materials Chemistry A* **2016**, *4*, 15997.

[39] H. Zheng, J. Dai, J. Duan, F. Chen, G. Zhu, F. Wang, C. Xu, *Journal of Materials Chemistry C* **2017**, *5*, 12057.

[40] R. L. Milot, G. E. Eperon, H. J. Snaith, M. B. Johnston, L. M. Herz, *Advanced Functional Materials* **2015**, *25*, 6218.

[41] E. S. Parrott, T. Green, R. L. Milot, M. B. Johnston, H. J. Snaith, L. M. Herz, *Advanced Functional Materials* **2018**, *28*, 1802803.

[42] R. J. Elliott, *Physical Review* **1957**, *108*, 1384.

[43] J. Tauc, *Mat. Res. Bull.* **1968**, *3*, 37.

[44] A. J. Knight, A. D. Wright, J. B. Patel, D. P. McMeekin, H. J. Snaith, M. B. Johnston, L. M. Herz, *ACS Energy Letters* **2019**, *4*, 75.

[45] E. T. Hoke, D. J. Slotcavage, E. R. Dohner, A. R. Bowring, H. I. Karunadasa, M. D. McGehee, *Chemical Science* **2015**, *6*, 613.

[46] A. J. Barker, A. Sadhanala, F. Deschler, M. Gandini, S. P. Senanayak, P. M. Pearce, E. Mosconi, A. J. Pearson, Y. Wu, A. R. Srimath Kandada, T. Leijtens, F. De Angelis, S. E. Dutton, A. Petrozza, R. H. Friend, *ACS Energy Letters* **2017**, *2*, 1416.

[47] R. E. Beal, N. Z. Hagström, J. Barrier, A. Gold-Parker, R. Prasanna, K. A. Bush, D. Passarello, L. T. Schelhas, K. Brüning, C. J. Tassone, H.-G. Steinrück, M. D. McGehee, M. F. Toney, A. F. Nogueira, *Matter* **2020**, *2*, 207.

[48] M. Deepa, M. Salado, L. Calio, S. Kazim, S. M. Shivaprasad, S. Ahmad, *Physical Chemistry Chemical Physics* **2017**, *19*, 4069.

[49] W. Zhou, S. Chen, Y. Zhao, Q. Li, Y. Zhao, R. Fu, D. Yu, P. Gao, Q. Zhao, *Advanced Functional Materials* **2019**, *29*, 1809180.

[50] O. J. Weber, D. Ghosh, S. Gaines, P. F. Henry, A. B. Walker, M. S. Islam, M. T. Weller, *Chemistry of Materials* **2018**, *30*, 3768.

[51] H.-H. Fang, F. Wang, S. Adjokatse, N. Zhao, J. Even, M. Antonietta Loi, *Light: Science & Applications* **2016**, *5*, e16056.

[52] A. Bernasconi, L. Malavasi, *ACS Energy Letters* **2017**, *2*, 863.

Chapter 8

Conclusions

For this PhD project, I successfully designed and built a time-resolved PL mapping system for hybrid perovskites. In Chapter 4, proof of concept is demonstrated for this system, which works by raster scanning a pulsed laser over the surface of a sample and taking time-resolved photoluminescence (TRPL) data at each map point. Maps of fluorescence lifetime can be generated by fitting the TRPL data collected at each map point to a double exponential fit. In Chapter 5, measurements taken with the TRPL mapping system reveal several interesting links between surface morphology and fluorescence lifetimes in thin films of double and triple cation perovskite. Both of these types of films have wrinkled surface morphology as a result of local strain variations and/or solvent evaporation effects during processing. It was found through TRPL mapping that these wrinkles appear to correlate with areas of higher defect density, highlighting the need to control the fabrication process carefully to avoid such effects.

The TRPL mapping system also revealed the effect of vacuum-assisted solution processing (VASP) on the emission properties of spray-cast triple cation perovskites. The VASP treatment leads to a greater surface uniformity which in turn correlates with greater homogeneity in fluorescence lifetimes across the surface. This effect is demonstrably linked to enhanced performance in PV devices where the spray-coated perovskite layer is VASP-treated, as it is shown in Chapter 5 that such devices display overall better device metrics than those where the perovskite layer was not VASP treated. These findings show that the TRPL mapping system is a powerful tool which can link morphology with emission properties and therefore assist in optimising the spray-coating process.

This is especially important in the move towards the commercialisation of perovskites, as spray-coating is one route towards fabricating large-area perovskite modules at low cost.

The TRPL mapping results presented in this thesis showcase the potential of TRPL imaging as a versatile tool to aid in the optimisation process of hybrid perovskite thin films. In the future, this could easily go beyond thin films: the ability to quantify the homogeneity of PL lifetimes would be extremely useful for assessing the quality of interfaces between the perovskite and electron-/hole-transporting media. An interesting project for a future PhD student would be to adapt the mapping system to include wavelength selection; this may allow for spatial mapping of effects such as halide segregation (discussed in Chapter 7), which is characterised by a shift in emission wavelength.

In Chapter 6, two phase transitions were identified for $(FAPbI_3)_{0.85}(MAPbBr_3)_{0.15}$, a high temperature transition at $\sim$ 260 K (-13°C) and a low temperature transition at $\sim$ 80 K (-193°C). The high temperature transition was identified as a transition from the pseudo-cubic α phase which the material assumes at room temperature to a pseudo-tetragonal unit cell. The low temperature transition was speculated to be a transition from the pseudo-tetragonal phase to a similar tetragonal phase with lowered symmetry, as suggested by a set of additional diffraction peaks observed in the XRD patterns for this phase. The finding that the high temperature phase transition for $(FAPbI_3)_{0.85}(MAPbBr_3)_{0.15}$ is below room temperature is significant, as this effect underlies the superior thermal stability of the material as compared to $MAPbI_3$ (where the transition to the cubic phase occurs at $\sim$ 350 K).

This material undergoes a blueshift in its band gap with increasing temperature, an effect which has been widely documented in hybrid perovskites. It was further revealed that the band gap of this material is phase-dependent, with the high temperature phase transition shown to cause a discontinuity in the band gap blueshift. There is also found to be a dependence of recombination rates in this material on the lattice parameters and shape of the unit cell, which is speculated to be the result of polaron formation in the material. This is a finding that not only adds to our understanding of the fundamental properties of hybrid perovskites, but also hints at the possibility of tuning the

recombination properties by compositional engineering.

In Chapter 7, it was found that the phase behaviour in Cs-containing triple cation perovskites is very similar to that of the double cation perovskite $(FAPbI_3)_{0.85}(MAPbBr_3)_{0.15}$. Cs-containing perovskites of the form $Cs_zFA_xMA_yPbI_{2.55}Br_{0.45}$ blends with z = 0.05, 0.08 and 0.15 were shown to undergo a high temperature phase transition in the temperature range 260-280 K from the pseudo-cubic α phase to the pseudo-tetragonal β phase, and a low temperature phase transition in the range 80-90 K to the lower symmetry γ phase. The high temperature cubic-tetragonal phase transition was shown to shift to higher temperatures with increasing Cs concentration, which may be part of the reason why 5% Cs was found in the literature to be the optimum stable composition. The next step from here would be an extension of these studies on Cs-containing triple cation perovskites to include the determination of temperature-dependent recombination rates, as was done for the double cation perovskite in Chapter 6. This would give additional insight into the origin of the superior performance of the 5% Cs composition as compared to the double cation perovskite, as well as further elucidating the fundamental properties of these fascinating materials.

Appendices

Appendix A

Supporting Information for Chapter 4

Development of a Time-Resolved Photoluminescence Mapping System for Hybrid Perovskites: **Supporting Information**

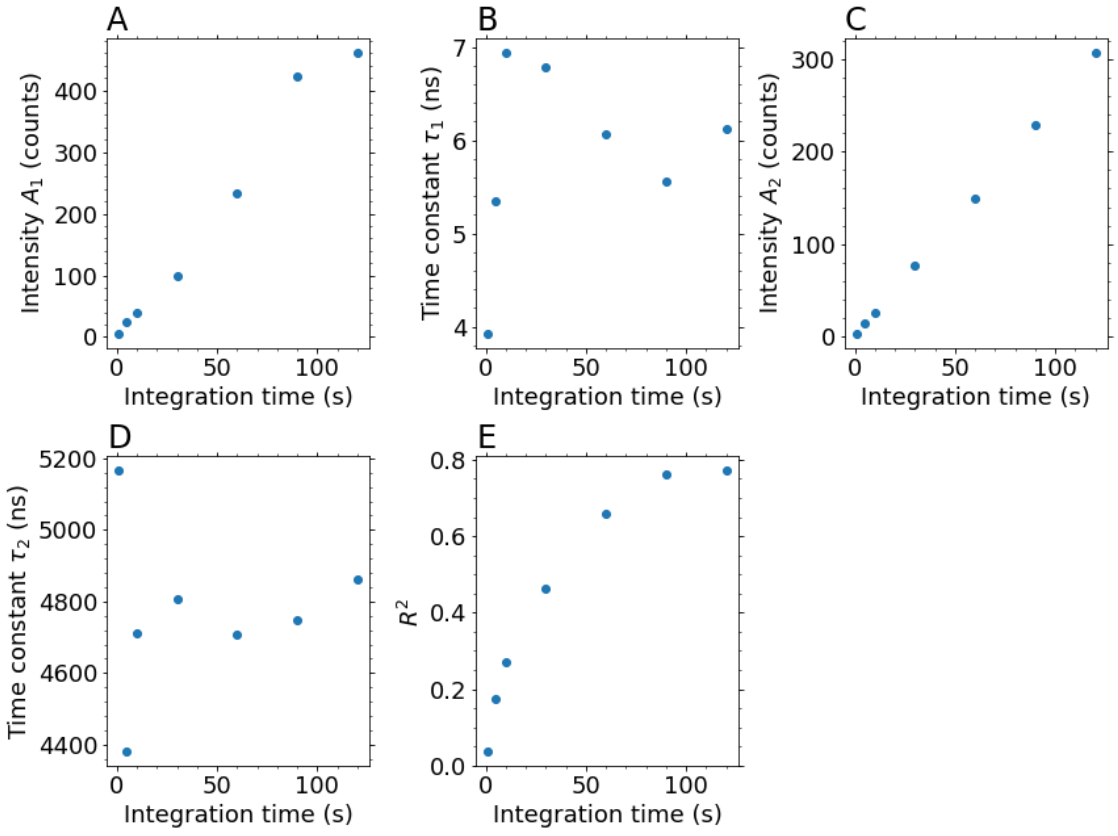

Figure A.1: Fit parameters of a double exponential fit ($A_1e^{-t/\tau_1} + A_2e^{-t/\tau_1}$) applied to time-resolved PL (TRPL) data from hybrid perovskite thin films, where the data was collected at a series of different integration times. **A** A_1, **B** τ_1, **C** A_2, and **D** τ_2 as a function of integration time.

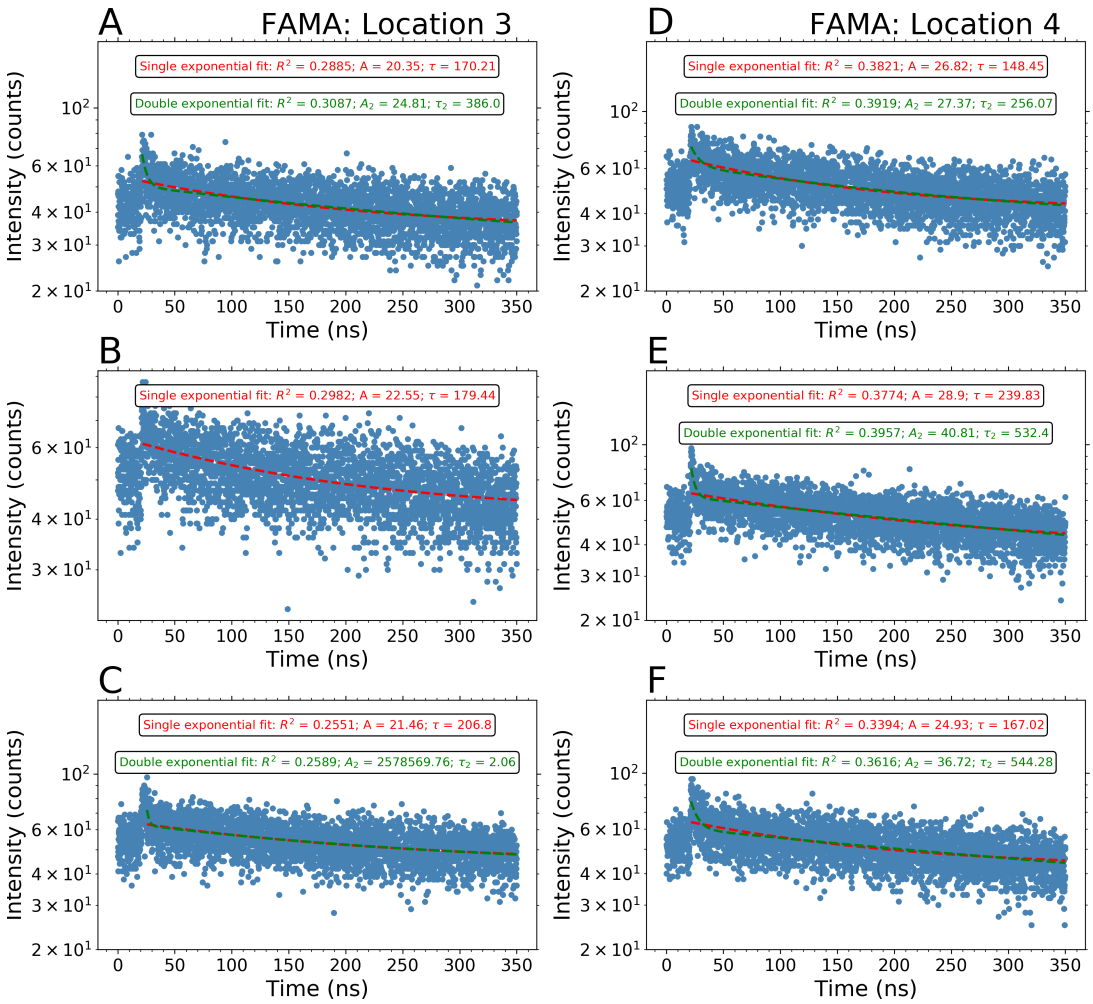

Figure A.2: **A**-**C** TRPL data traces, all collected at a third arbitrary location on a thin film of $(FAPbI_3)_{0.85}(MAPbBr_3)_{0.15}$, fitted with both a single exponential (red dotted lines) and a double exponential (green dotted lines) fit. Data taken at the first and second locations on the film are shown in Figure 4.4 in Chapter 4. **D**-**F** TRPL data traces, all collected at a fourth arbitrary location on the same thin film of $(FAPbI_3)_{0.85}(MAPbBr_3)_{0.15}$.

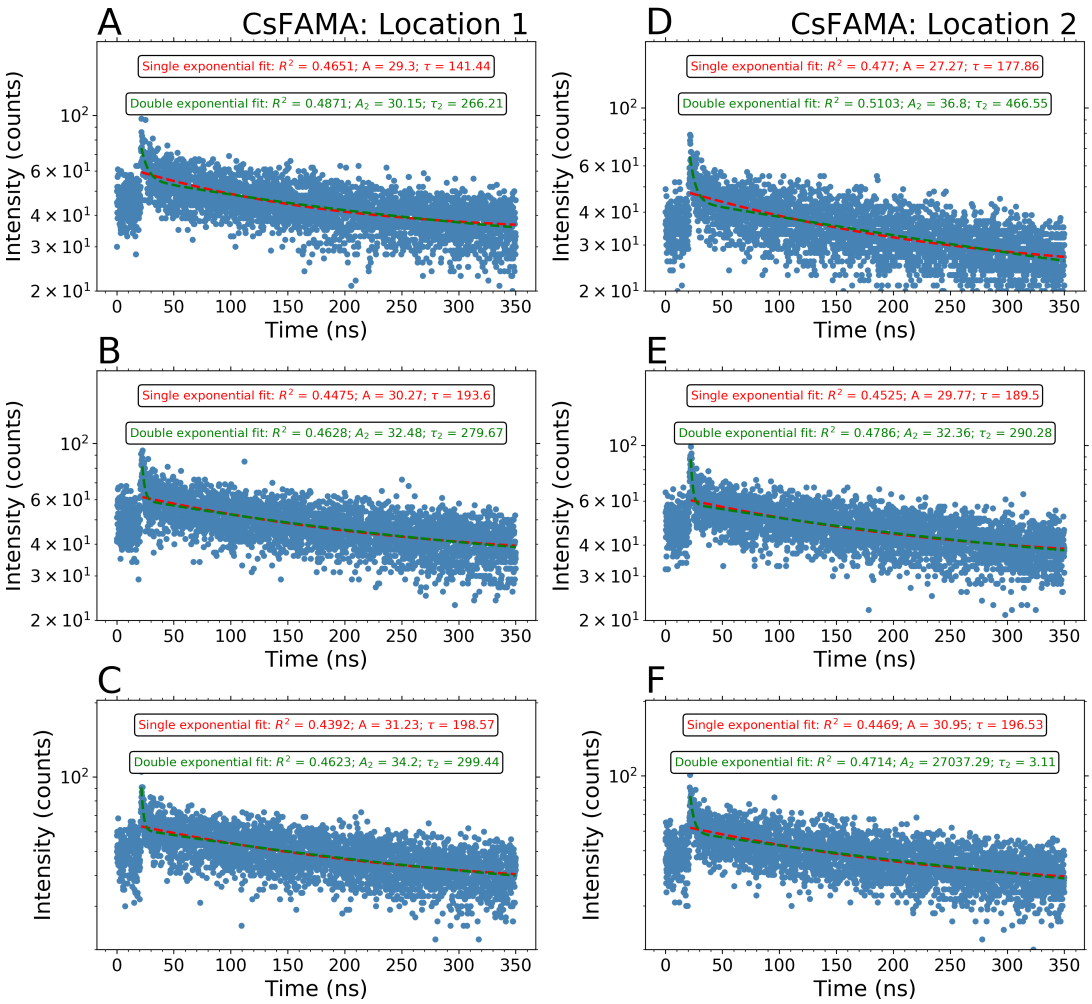

Figure A.3: **A**-**C** TRPL data traces, all collected at an arbitrary location on a thin film of the triple cation perovskite $Cs_{0.05}FA_{0.76}MA_{0.19}PbI_{2.55}Br_{0.45}$, fitted with both a single exponential (red dotted lines) and a double exponential (green dotted lines) fit. Data taken at the first and second locations on the film are shown in Figure 4.4 in Chapter 4. **D**-**F** TRPL data traces, all collected at a second arbitrary location on the same thin film of $Cs_{0.05}FA_{0.76}MA_{0.19}PbI_{2.55}Br_{0.45}$.

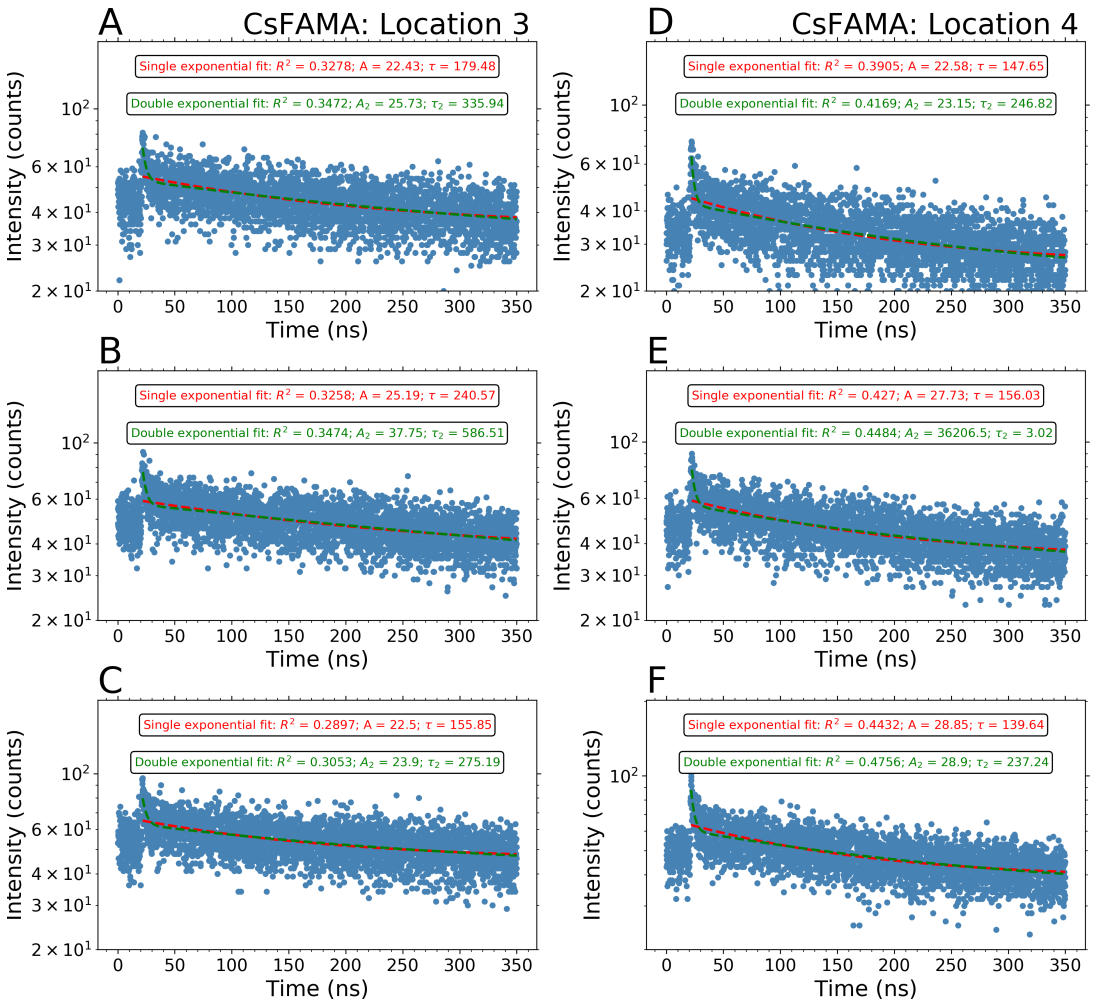

Figure A.4: **A**-**C** TRPL data traces, all collected at a third arbitrary location on a thin film of the triple cation perovskite $Cs_{0.05}FA_{0.76}MA_{0.19}PbI_{2.55}Br_{0.45}$, fitted with both a single exponential (red dotted lines) and a double exponential (green dotted lines) fit. Data taken at the first and second locations on the film are shown in Figure 4.4 in Chapter 4. **D**-**F** TRPL data traces, all collected at a fourth arbitrary location on the same thin film of $Cs_{0.05}FA_{0.76}MA_{0.19}PbI_{2.55}Br_{0.45}$.

Supplementary Note 1: Outlying Values of Parameters A_1 and τ_1

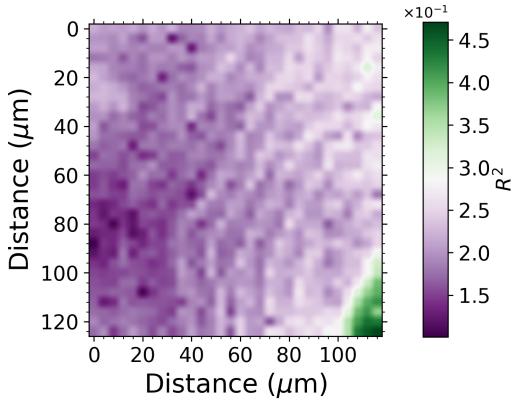

Figure A.5: Colourmaps of the R^2 value for the double exponential fit applied to the TRPL data for a map of size 120 × 128 μm on the surface of a $(FAPbI_3)_{0.85}(MAPbBr_3)_{0.15}$ sample (area marked in red Figure 4.10).

In Section 4.3.1, the process of extracting double exponential fitting parameters from TRPL data collected at each point on a map scan was described. To determine whether there are any invalid values which need to be removed from such maps, outlying values of each set of parameters were discovered using the median average deviation M_i of each value. To determine whether outlying values of the parameters A_1 and τ_1 correspond to fitting artifacts of the double exponential fit, the TRPL traces resulting in outlying values of these parameters are plotted in Figure A.6. The traces in these plots are colour-coded according to the M_i value of the given parameter: red traces denote $M_i > 5$; blue traces denote $4 < M_i < 5$; orange traces denote $3 < M_i < 4$; and black traces denote $M_i < 3$ (i.e. the parameter is not an outlier).

It can be seen from Figure A.6**A** that a typical trace resulting in a value of A_1 larger than 5 MADs above the median has been fitted poorly, as it results in $A_1 = 2.06 \times 10^5$, which is approximately four orders of magnitude larger than the maximum TRPL signal. The fractional uncertainty on this value is $\Delta A_1/A_1 = 1.04$. Figure A.6**B**-**C** shows that outliers in the $4 < M_i < 5$ and $3 < M_i < 4$ ranges again appear to be a result of the data having a poorly resolved fast component, and this is confirmed by their resultant values of $\Delta A_1/A_1$, which are 0.779 and 0.825, respectively. Fits to the data in Figure A.6**A**-**C** also result in very small τ_1 values ($\tau_1 = 3.06$, 3.63 and 3.73 ns, respectively). This gives further evidence to the suggestion made in the main text that extremely large values of A_1 ($A_1 \gtrsim 10^5$) are a result of the fact that the faster component of the double exponential has not been fitted accurately, resulting in an arbitrarily large A_1 and an

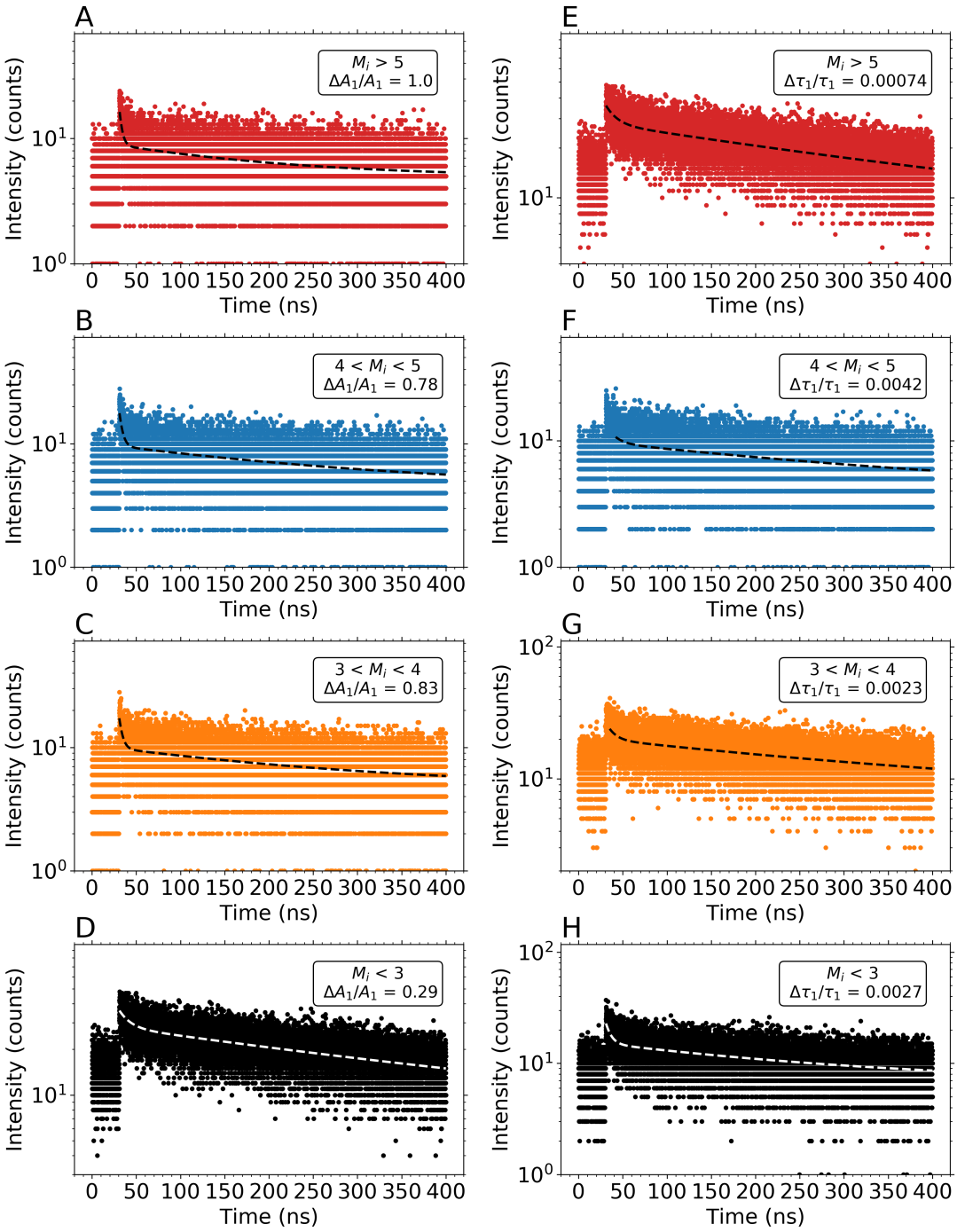

Figure A.6: TRPL traces resulting in statistically outlying values of the fitting parameters A_1 (**A**-**D**) and τ_1 (**E**-**H**), for the TRPL maps displayed in Figure 4.11.

arbitrarily small τ_1.

In Figure A.6**E**-**G**, TRPL traces yielding outlying values of τ_1 are plotted. These τ_1 values appear at first glance to have been generated by a reasonable fit to the data, and this is confirmed by their very small fractional errors ($\sim 10^{-3}$ for all datasets).

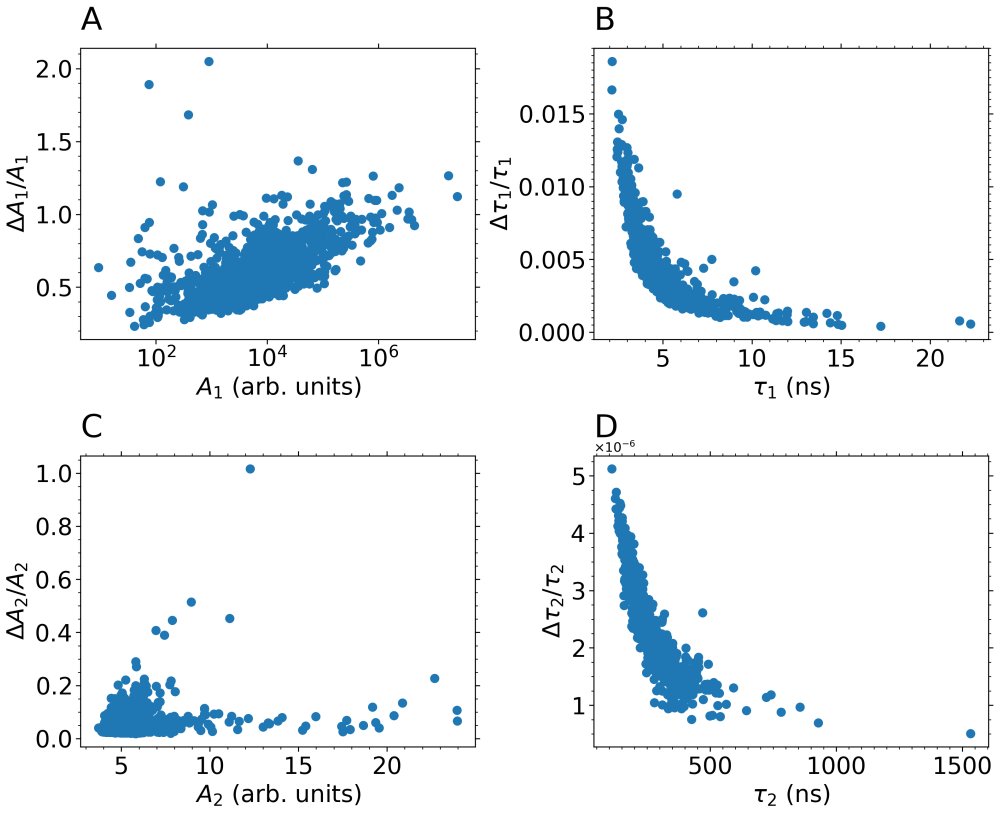

Figure A.7: Relationships between the fit parameters **A** A_1 **B** τ_1 **C** A_2 **D** τ_2 and their respective fractional uncertainty errors, for the TRPL maps displayed in Figure 4.11.

Similarly, the data trace yielding a non-outlying value of τ_1, shown in Figure A.6**H**, yields a very small fractional error on τ_1. This evidence suggests that the only τ_1 values that are artifacts are those associated with unreliably large A_1 values. This analysis highlights the fact that the M_i value is not a always the best metric for discovering artifacts.

In addition to outlier analysis, the fractional uncertainty on individual parameter values can also give insight into the validity of these values. In Figure A.7, extracted values of all parameters have been plotted against their respective fractional uncertainty values. Looking at Figure A.7**A**, it can be seen that A_1 is directly proportional to $\Delta A_1/A_1$, suggesting that the larger the A_1 value the less reliable it is likely to be. Figure A.7**B** shows that the errors on τ_1 are inversely proportional to τ_1 for small values of τ_1, in other words the smaller the τ_1 value the less it can be relied upon. These trends reflect the previously observed effect that there are a subset of A_1 and τ_1 values which are artifacts as they result from a bad fit to a poorly resolved part of the dataset. At higher values of τ_1, the uncertainty value flattens out, reflecting the τ_1 values which have been fitted correctly. This suggests that the approximate value of fractional uncertainty

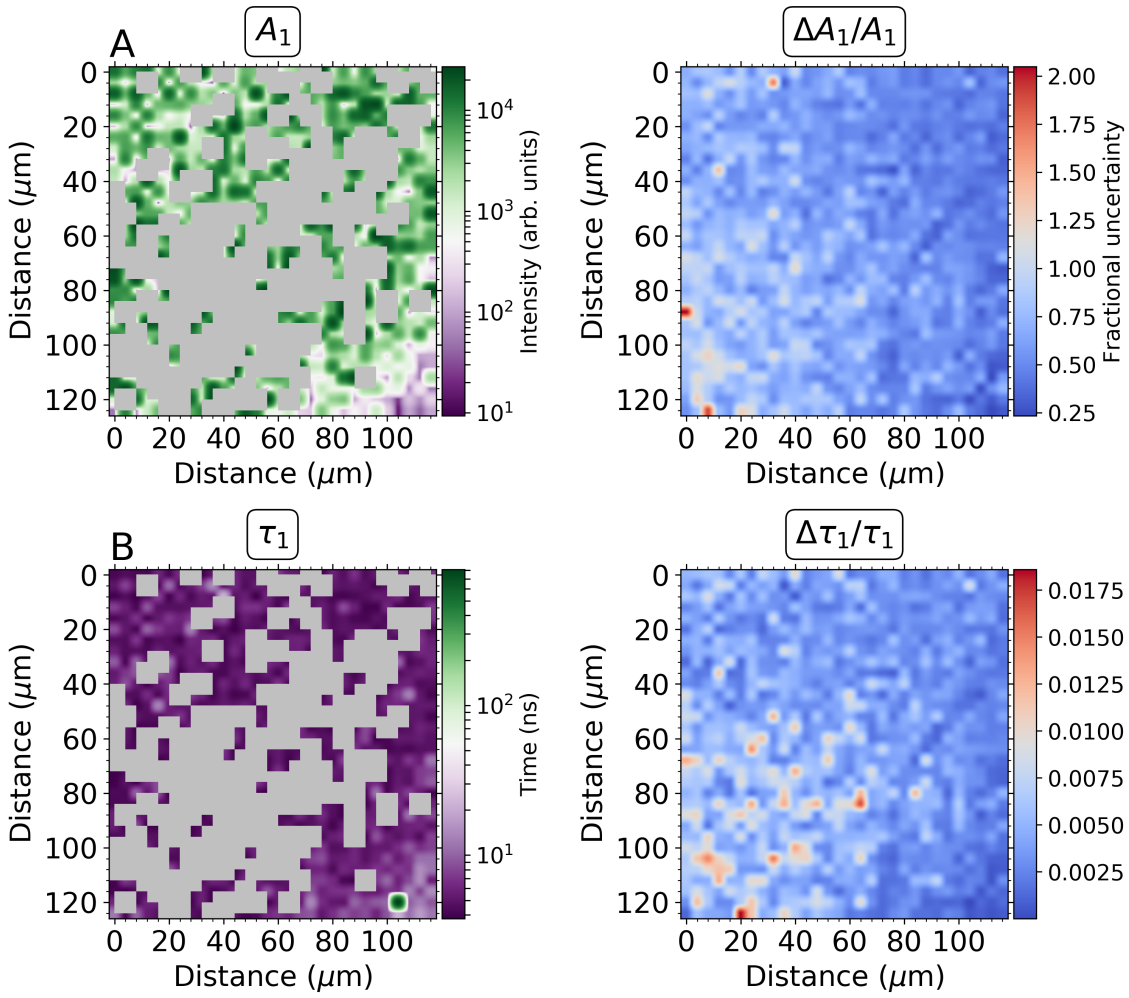

Figure A.8: Maps of **A** the parameter A_1 and **B** the parameter τ_1. In these maps, A_1 values with $M_i > 3$ have been removed, along with the τ_1 values at the corresponding points. To the right of each map, a map of the fractional uncertainty for each parameter set is shown.

at which the errors in τ_1 level out is the cut-off for sensible values of τ_1.

Therefore it appears to be sensible to remove all A_1 values with $M_i > 3$, along with the τ_1 values at the corresponding map points, with the modified maps shown in Figure A.8. This shows that the remaining data is not only a small proportion of the maps, but also that it does not clearly correspond to features on the sample surface (Figure 4.10). To investigate this further, an example of TRPL data which yielded a non-outlying value of A_1 ($M_i < 3$) has been plotted in in Figure A.6**D**. This data appears to have been fitted much more accurately ($\Delta A_1/A_1 = 0.293$), which indicates that there is a small subset of A_1 values which are not artifacts. However, Figure A.8**A** shows that even with outlying values removed, some values of A_1 appear to be uncharacteristically

large ($\sim 10^4$) given the signal level in the data of $\sim 10^1 - 10^2$ counts.

All of the above evidence suggests that it is not trivial to ascertain the validity of A_1 and τ_1 values, which is not unexpected considering the fact that the fast decay component is generally poorly resolved in the data. This leads to the conclusion that maps of A_1 and τ_1 do not give useful information about the film and may be misleading, therefore should not be included when analysing the maps.

Appendix B

Supporting Information for Chapter 5

Time-Resolved Photoluminescence Mapping Studies on Mixed Cation Mixed Halide Perovskite Thin Films:

Supporting Information

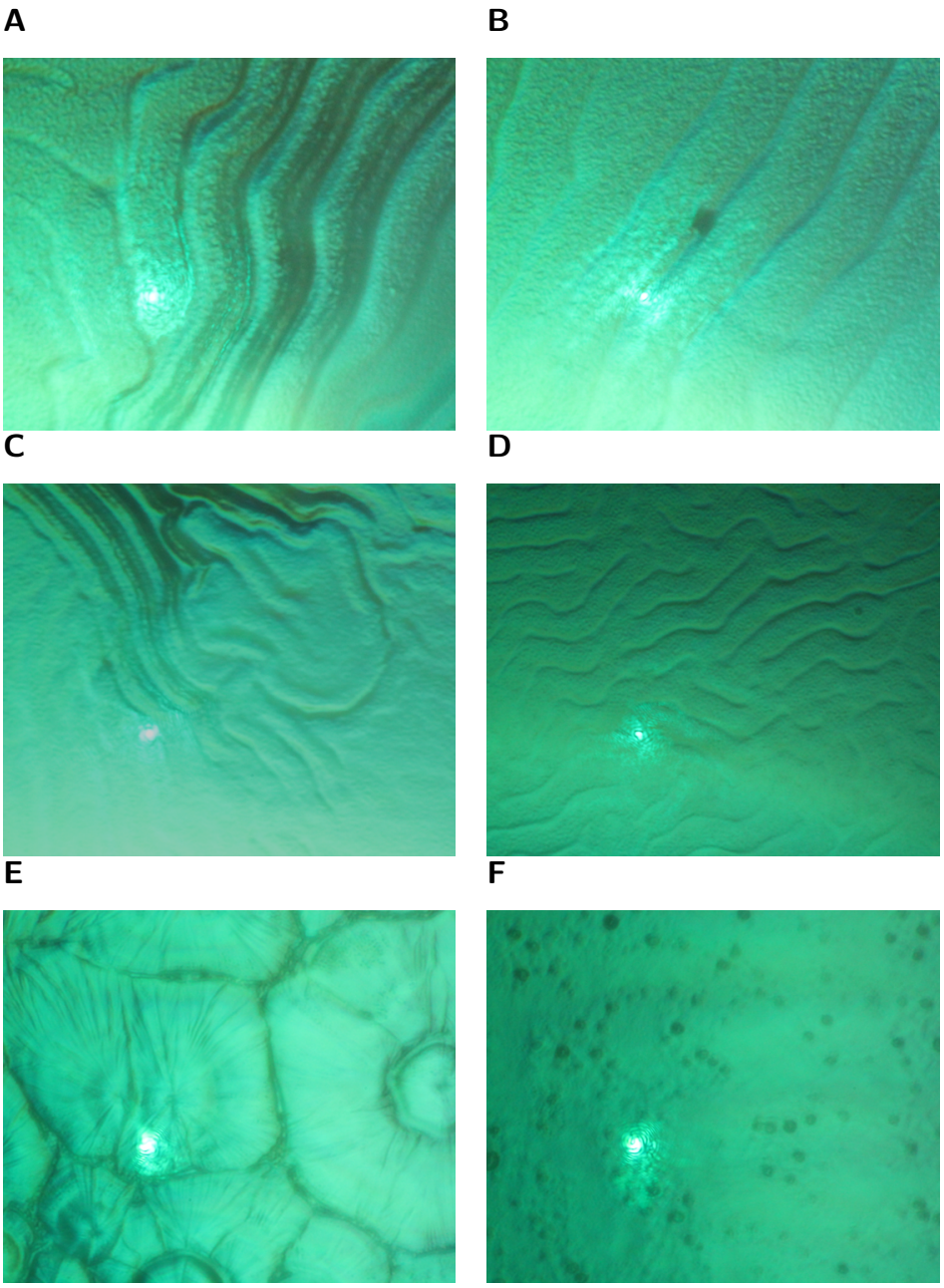

Figure B.1: **A** Microscope image of the focussed laser spot on a $(FAPbI_3)_{0.85}(MAPbBr_3)_{0.15}$ thin film. The laser is illuminating the starting point of the 120 $\times$ 128 µm map scan undertaken on this film, with the full scan area highlighted in Figure 5.1**A**. **B** Microscope image of the focussed laser spot on a $(FAPbI_3)_{0.85}(MAPbBr_3)_{0.15}$ thin film. The laser is illuminating the starting point of the 100 $\times$ 60 µm map scan undertaken on this film, with the full scan area highlighted in Figure 5.1**D**. **C**,**D** Microscope images of the focussed laser spot on two $Cs_{0.05}$ $FA_{0.76}MA_{0.19}PbI_{2.55}Br_{0.45}$ thin films. In each image, the laser is illuminating the starting point of a 100 $\times$ 60 µm map scan undertaken on the given film, with the full scan areas highlighted in Figure 5.2**A** and Figure 5.2**D**. **E**,**D** Microscope images of the focussed laser spot on spray-cast $Cs_{0.05}$ $FA_{0.76}MA_{0.19}PbI_{2.55}Br_{0.45}$ thin films, where **E** vacuum-assisted solution processing (VASP) treatment has not been used and **F** VASP treatment has been used. In each image, the laser is illuminating the starting point of a 160 $\times$ 160 µm map scan undertaken on the given film, with the full scan areas highlighted in Figure 5.3**A** and Figure 5.3**D**, respectively.

Appendix C

Supporting Information for Chapter 6

Correlating Phase Behaviour with Photophysical Properties in Mixed-Cation Mixed-Halide Perovskite Thin Films:

Supporting Information

*Claire Greenland, Adam Shnier, Joel A. Smith, Onkar S. Game, Sai K. Rajendran, Daniel Wamwangi, Graham A. Turnbull, Ifor D. W. Samuel, David G. Billing and David G. Lidzey**

All data has been collected from a solution-processed thin film of $(FAPbI_3)_{0.85}(MAPbBr_3)_{0.15}$ fabricated as described in Section 6.4, unless otherwise stated.

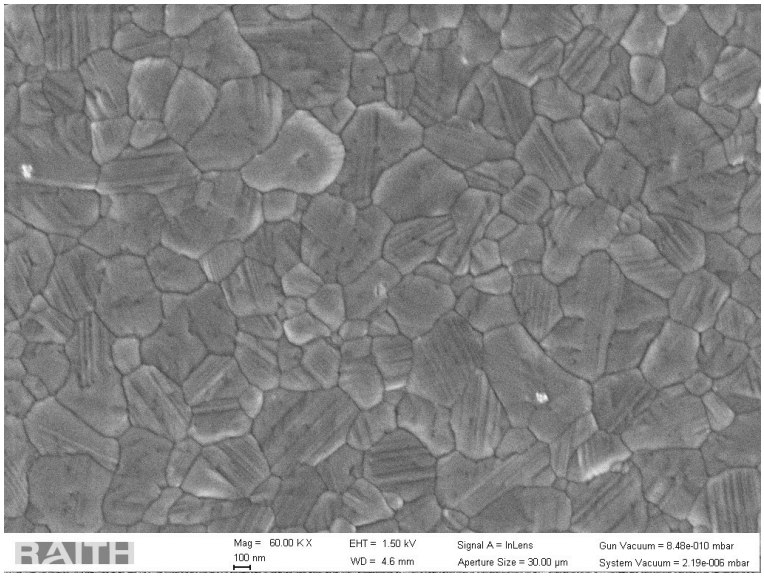

Figure C.1: Scanning electron microscopy (SEM) image of the sample surface.

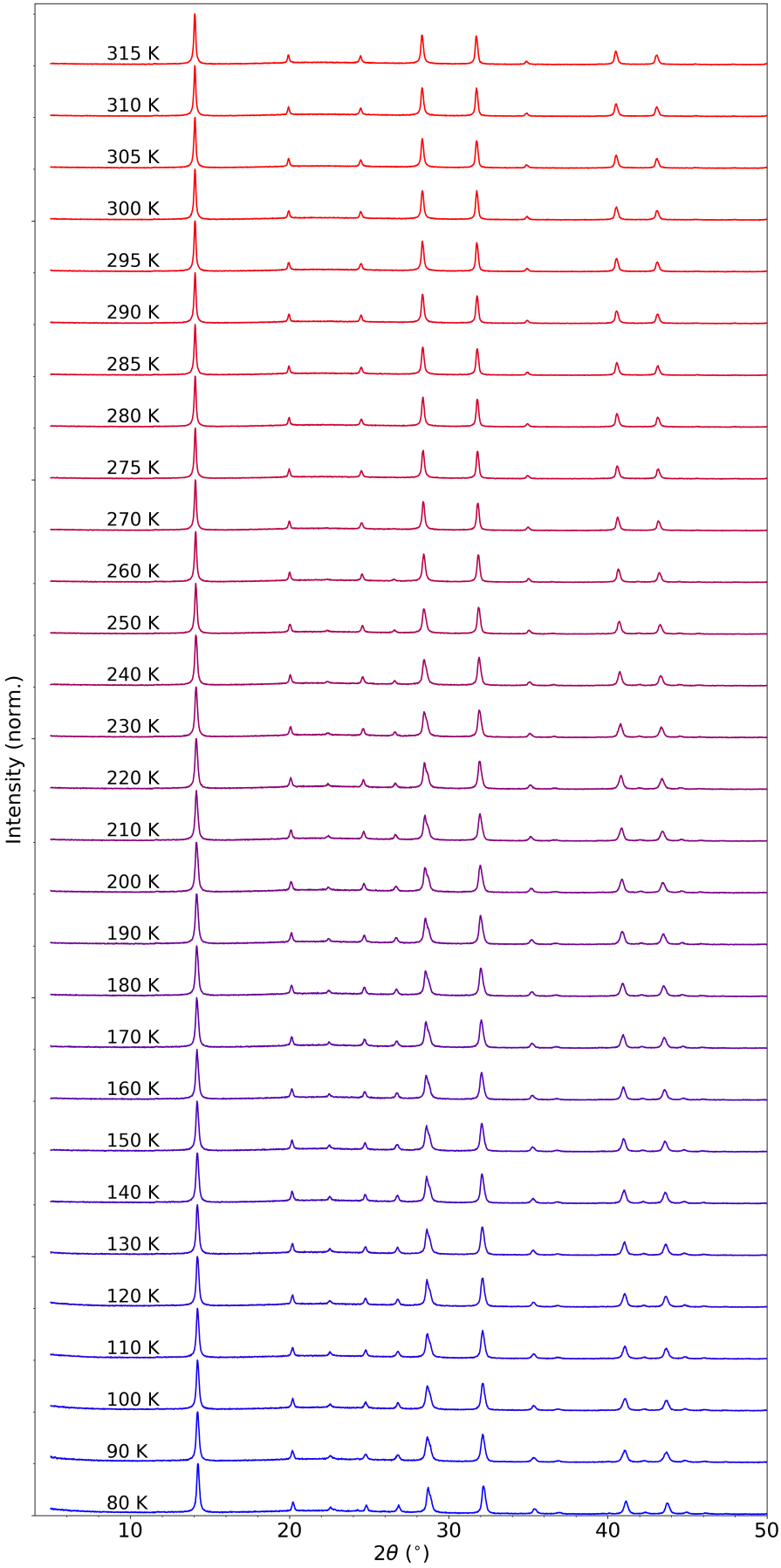

Figure C.2: XRD patterns as collected at a series of temperatures while cooling the sample from 315 K to 80 K.

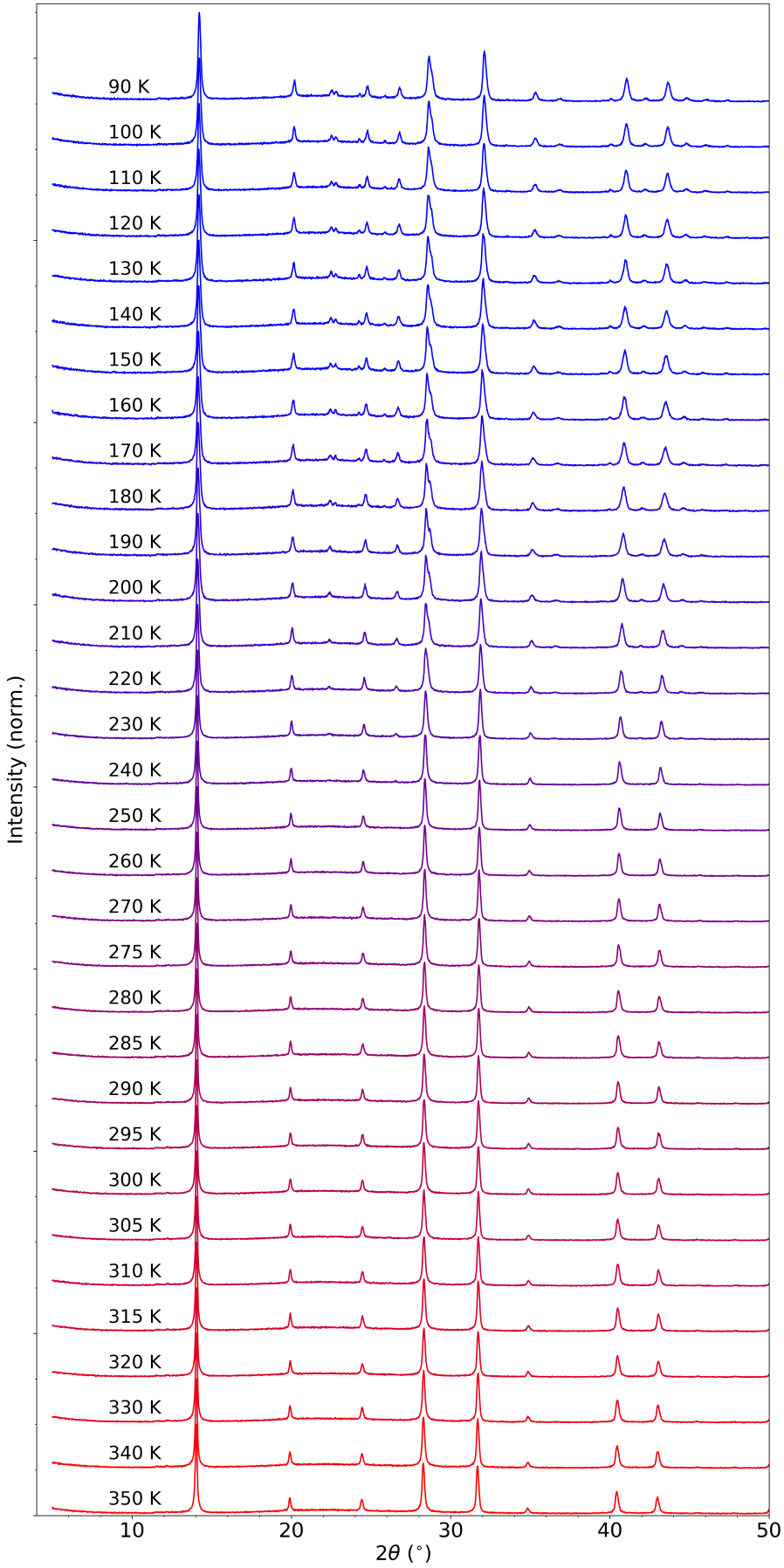

Figure C.3: XRD patterns as collected at a series of temperatures while heating the sample from 90 K to 350 K.

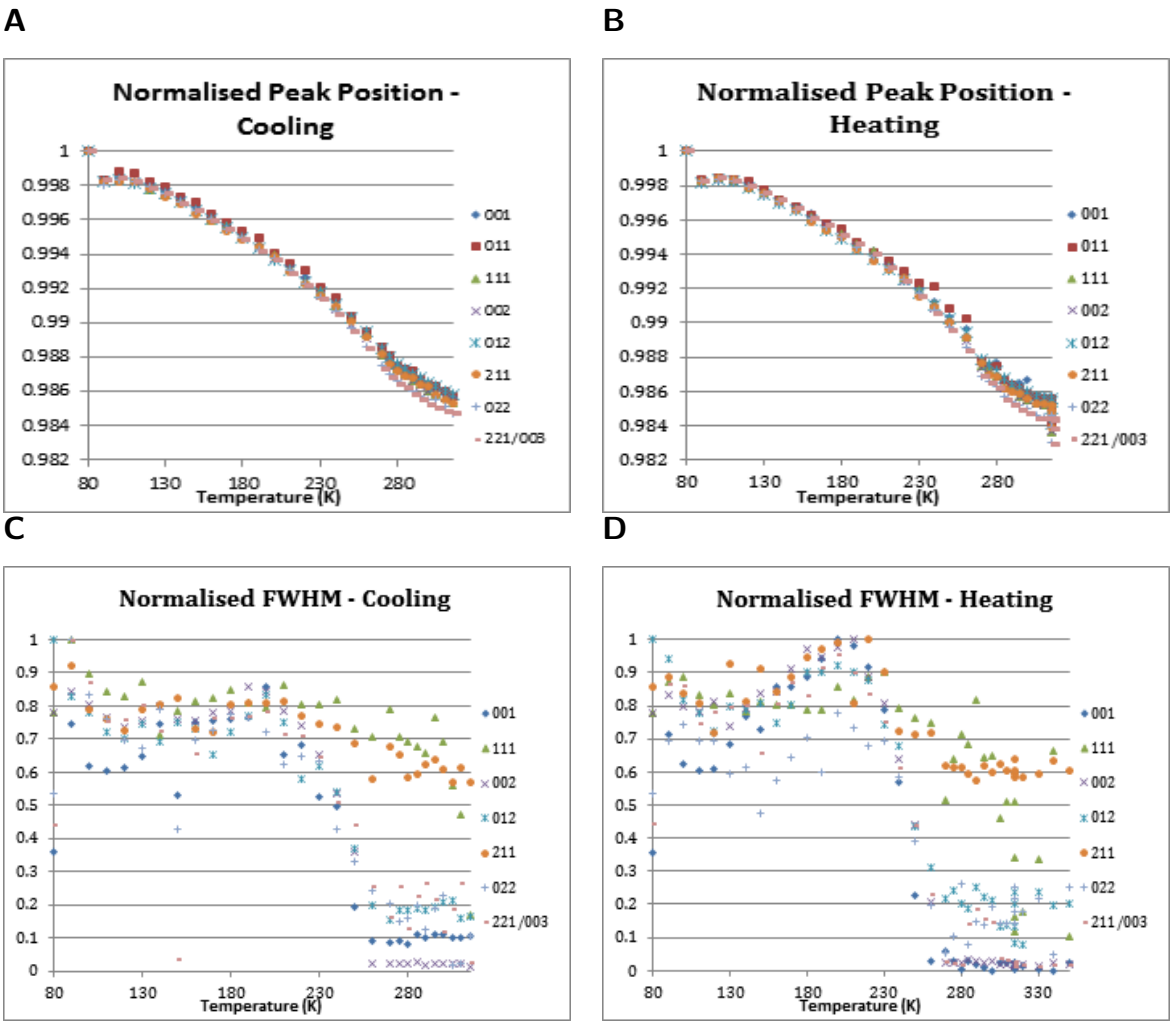

Figure C.4: PXRD peak parameters extracted from the Pearson VII fits. **A** Normalised peak positions as a function of temperature on cooling. **B** Normalised peak positions as a function of temperature on heating. **C** Normalised FWHM of key peaks as a function of temperature on cooling. **D** Normalised FWHM of key peaks as a function of temperature on heating.

C.1 Supplementary Note 1: Structural Modelling

Pearson VII Fits

To extract some minimally convoluted information a selection of peaks were modelled sequentially using a Pearson VII analytical peak fitting with TOPAS V5.0 across the VT-PXRD data. From this we observe a broadening in the distribution of peak position changes above 270 K. Considering the peak positions are normalised by their maximum, this is consistent with the relative elongation of an axis during the α/β phase transition. Between 210 and 270 K during heating the FWHM of many peaks broadens with decreasing temperature. The equivalent is observed during cooling only in a narrower range

between 230 and 270 K, on cooling the 111 and 211 peaks experience no change of the same magnitude. While on heating the 111 peak is narrower at 315 K and above. Much of the broadening of peaks is attributed crystallographic planes becoming inequivalent as the symmetry of the unit cell changes leading the splitting of peaks such as where 100, 010, and 001 become inequivalent on cooling. A δ phase is suspected at 80 K where there is a sudden increase in the lattice parameters as seen in Figure C.4**A**,**B** by the shift of the peaks to higher angles.

Rietvield Structure Refinements

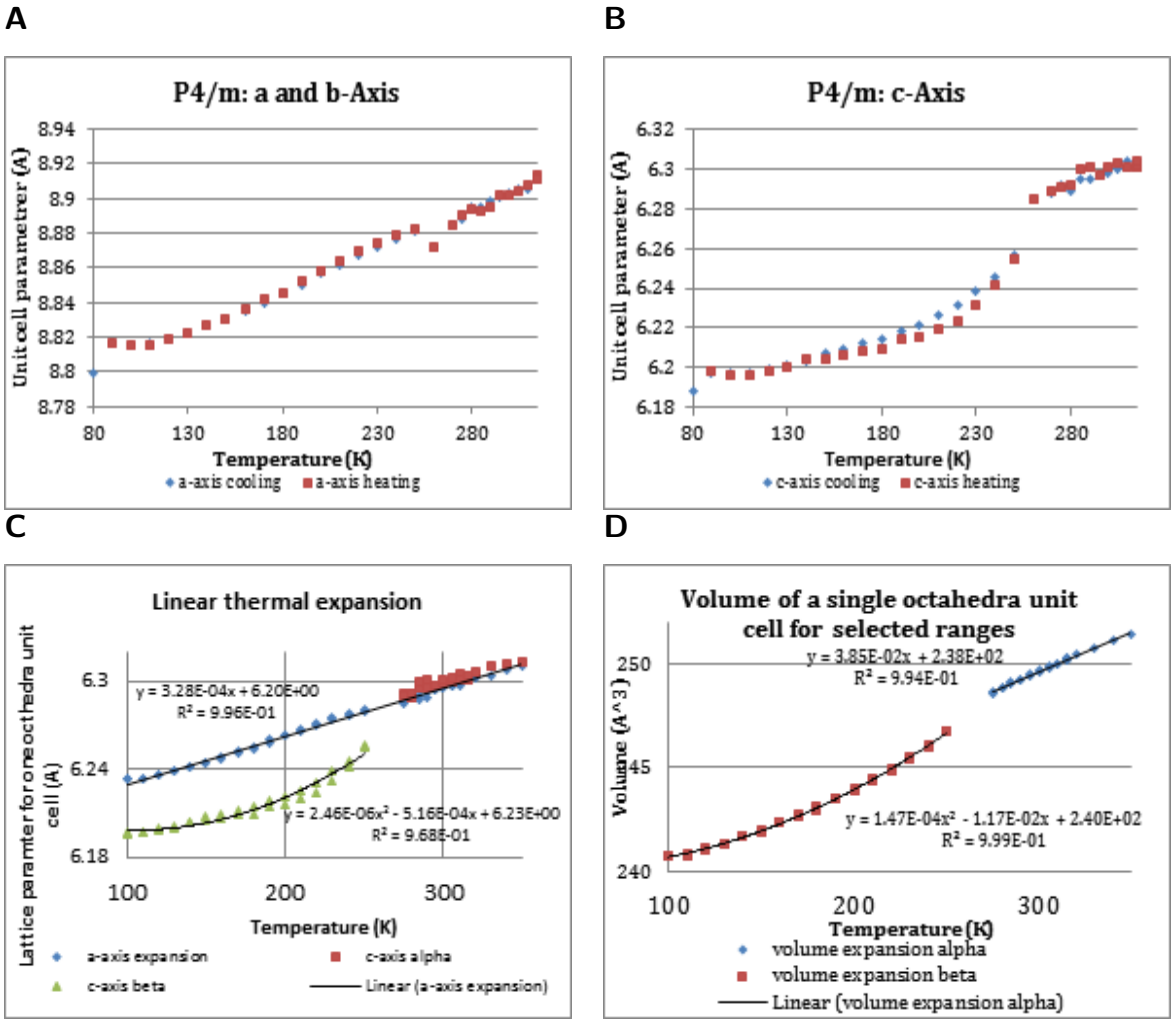

Figure C.5: PXRD peak parameters extracted from the Rietveld structure refinements. **A** Evolution of the *a*/*b*-axis parameter with temperature, assuming a *P*4/*m* space group. **B** Evolution of the *c*-axis parameter with temperature, assuming a *P*4/*m* space group. **C** Volumetric thermal expansion of the octahedral unit cell for the α and β phases. **D** Linear thermal expansion of the *a*- and *c*-axis parameters of the unit cell for the α and β phases.

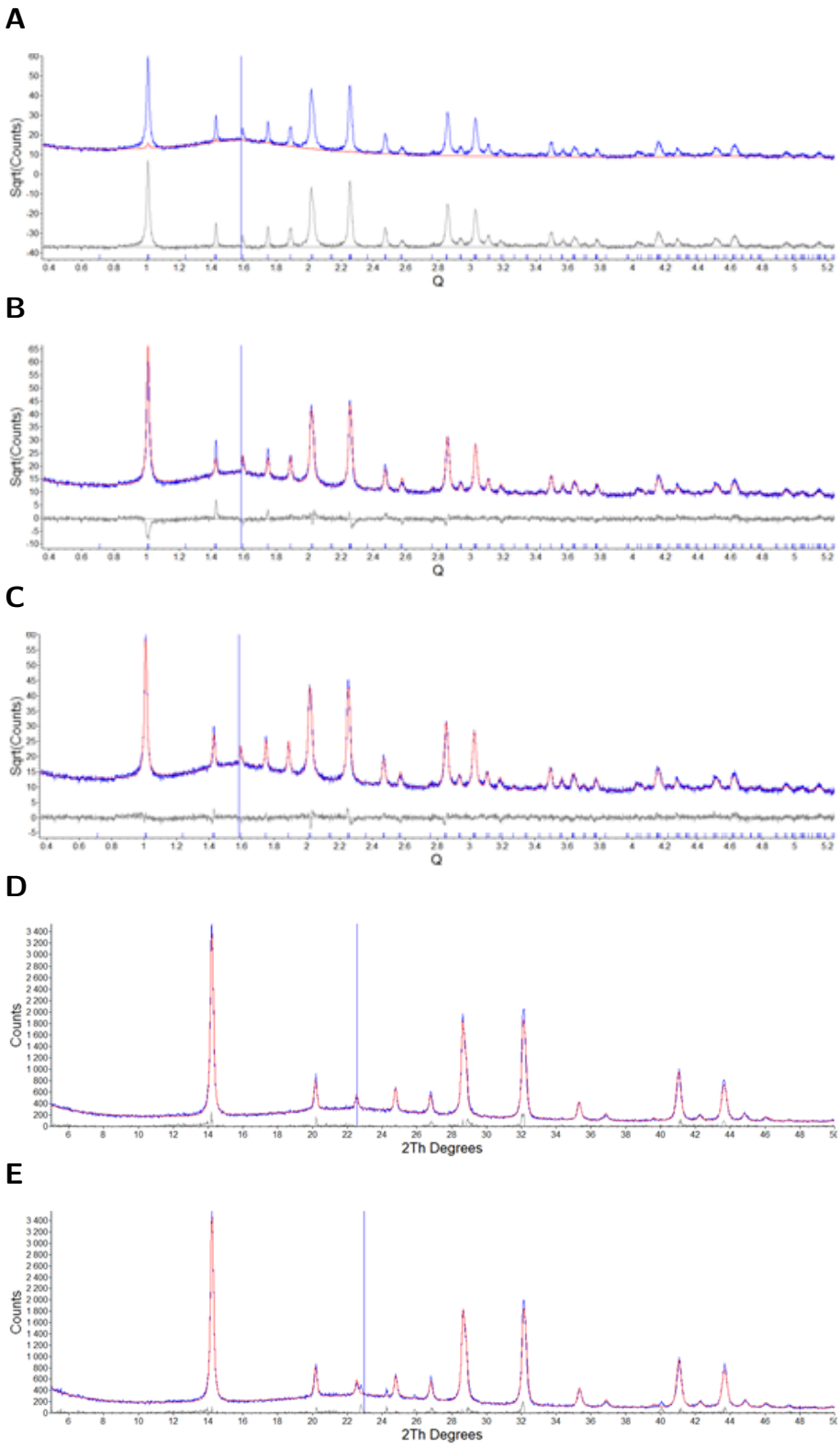

Figure C.6: **A** Blue line: raw data taken at 150 K on cooling of the sample. Red line: calculated fit from the Rietveld structure refinements. Grey line: difference between the raw data and calculated fit. **B** Blue line: raw data taken at 150 K on cooling of the sample. Red line: contribution of the FA cation to the calculated fit from the Rietveld structure refinements. Grey line: difference between the raw data and the FA contribution. **C** Blue line: raw data taken at 150 K on cooling of the sample. Red line: contribution of the PbX anion to the calculated fit from the Rietveld structure refinements. Grey line: difference between the raw data and the PbX contribution. **D** Blue line: raw data taken at 120 K on cooling of the sample. Red line: calculated fit from the Rietvield refinement. **E** Blue line: raw data taken at 100 K on re-heating of the sample. Red line: calculated fit from the Rietvield refinement.

The Pb cations are positioned on the 001 plane of the unit cell while the FA cations are roughly on the 002 plane. The interaction between the cation then results in destructive interference when scattering from the 001 and near equivalent planes as seen by the negative counts in the difference curve for the contribution of PbX.

In Figure C.6**D**,**E** we see unidentified extra peaks on the heating cycle that are not present during the cooling of the perovskite. These peaks disappear between 210 and 220 K, and are proposed as a derivative or component separating from the original structure.

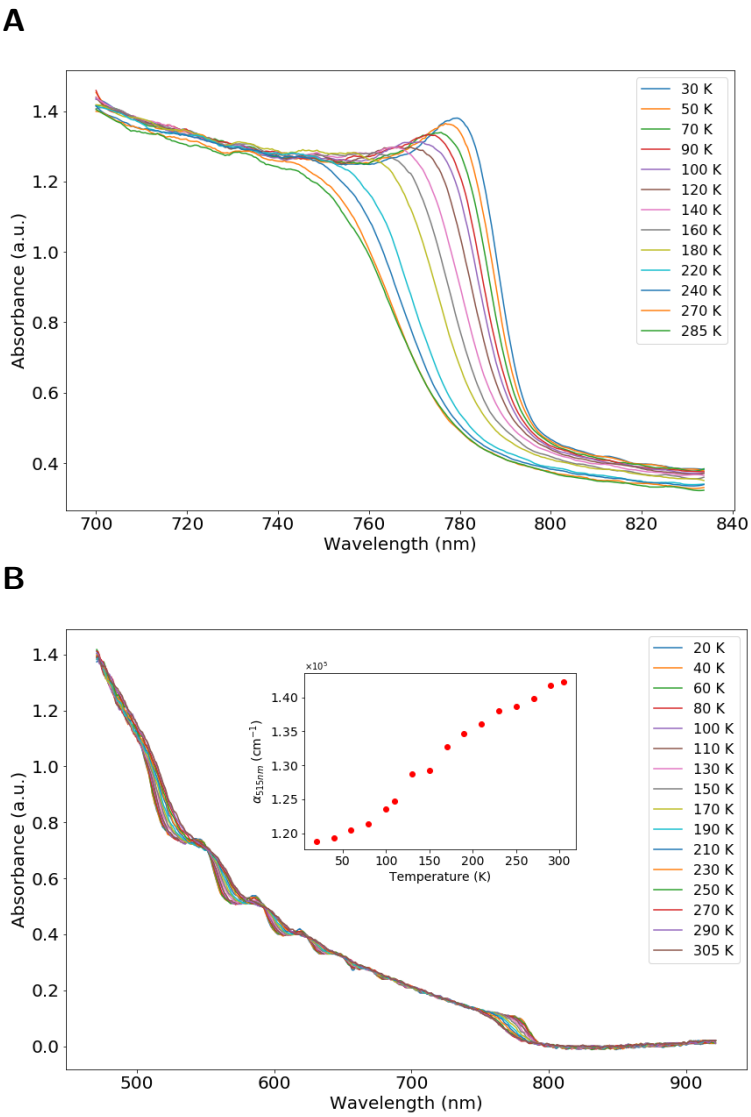

Figure C.7: **A** Temperature-dependence of the absorbance spectra at selected temperatures on a film of thickness 769 nm, showing the emergence of an excitonic absorption peak upon cooling to around 150 K. **B** Temperature-dependence of the absorbance spectra at selected temperatures on a film of thickness 125 nm.

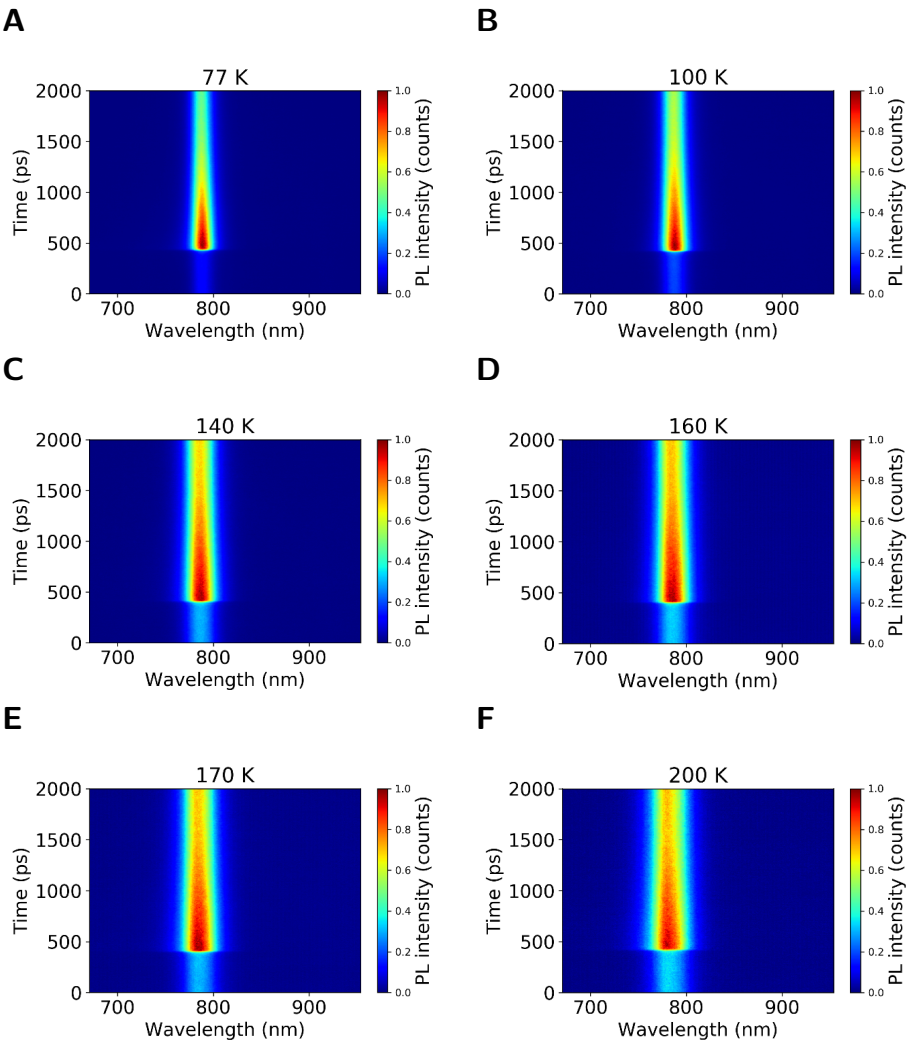

Figure C.8: Time-resolved photoluminescence colormaps from streak camera at a range of temperatures from **A** 77 K to **F** 200 K, at an excitation fluence of 3.1 μJcm^{-2}.

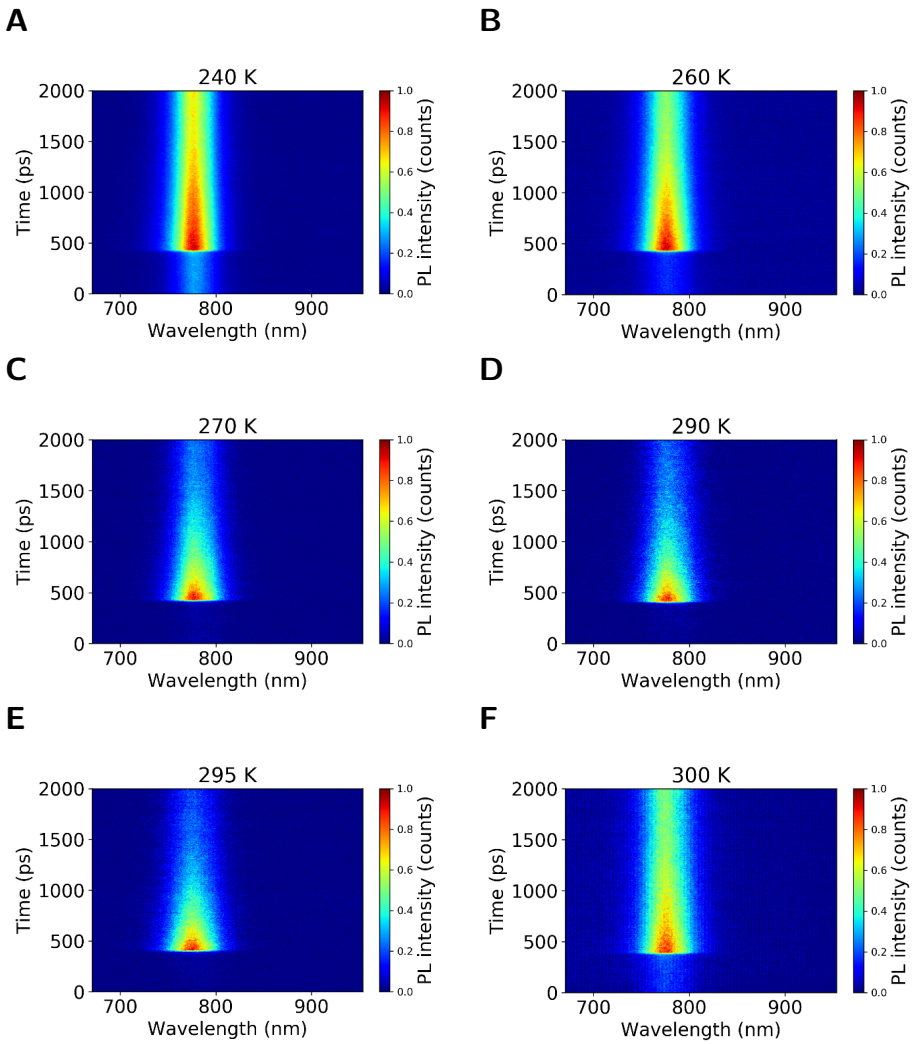

Figure C.9: Time-resolved photoluminescence colormaps from streak camera at a range of temperatures from **A** 240 K to **F** 300 K, at an excitation fluence of 3.1 μJcm^{-2}.

C.2 Supplementary Note 2: Temperature dependent PLQY

Temperature-dependent values of PLQY were calculated according to the following relation:

$$PLQY(T) = PLQY_{295K}\frac{PL(T)}{PL_{295K}}\frac{\exp^{-\alpha_{295K}L}}{\exp^{-\alpha(T)L}} \tag{C.1}$$

where $PLQY_{295K}$ is the value of PLQY as measured at 295 K (room temperature), PL_{295K} is the integrated photoluminescence at 295 K as determined from time-integrated PL measurements, $PL(T)$ is the integrated PL at temperature T. α_{295K} and $\alpha(T)$ are the absorption coefficients at 295 K and temperature T respectively, as determined from absorption measurements on $(FAPbI_3)_{0.85}(MAPbBr_3)_{0.15}$ thin films at the incident wavelength ($\lambda = 515$ nm).

The initial charge carrier density in the films was estimated using the following relation:

$$n_0(T) = \frac{E\lambda}{hc}\frac{1 - e^{-\alpha(T)L}}{L} \tag{C.2}$$

where E is the excitation density of the incident laser light, λ is the laser wavelength, L is the average thickness of the film, and $\alpha(T)$ is the absorption coefficient in the material at temperature T. The factor $1 - e^{-\alpha(T)L}$ accounts for the fraction of incident light absorbed by the film.

Alternative values of the initial charge carrier density were also estimated using:

$$n_0(T) = \frac{a(T)P}{E_{ph}f}\frac{1}{AL} \tag{C.3}$$

where $a(T)$ is the absorbance in the film at the excitation wavelength ($\lambda = 515$ nm) at temperature T, P is the laser power, E_{ph} is the energy of incident photons, f is the laser pulse frequency, A is the laser spot area and L is the average film thickness.

Values of $n_0(T)$ were used to calculate approximate values for $k_2(T)$ from the radiative recombination rate $k_r(T)$ using the relation $k_2(T) \approx k_r(T)/n_0(T)$.

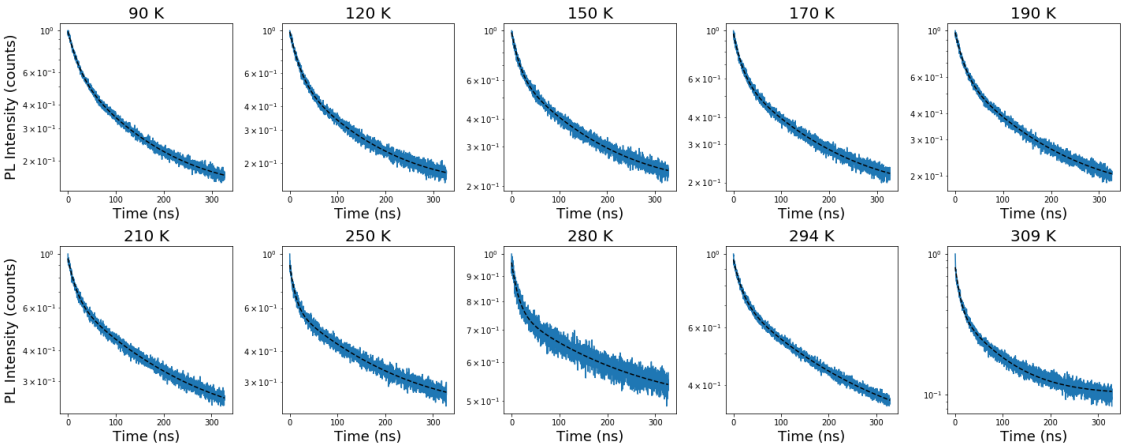

Figure C.10: Examples of TRPL decay traces obtained from low fluence (∼30 nJ/cm^2) TCSPC measurements, from which approximate values of k_1 were determined by fitting the PL decay curve to a double exponential fit.

C.3 Supplementary Note 3: Low fluence TCSPC measurements

We can see from Figure S8 that, despite the low excitation fluence of approx. 30 nJ/cm2, the TRPL decay traces are not monoexponential. This behaviour has been observed previously in low fluence TRPL measurements and has been attributed to localised recombination at grain boundaries and interfaces.[2] To obtain an estimate for k_1, we have therefore fitted the data with a double exponential of the form:

$$y(t) = A_1 e^{-\frac{t}{\tau_1}} + A_2 e^{-\frac{t}{\tau_2}} \tag{C.4}$$

where A_1 and A_2 are the amplitudes and τ_1 and τ_2 are the corresponding time constants of the fast and slow components of the decay, respectively. Values of these parameters for all temperatures are shown in Table S1. We took k_1 to be $1/\tau_2$, because it is the slow decay component τ_2 which describes the slow monomolecular behaviour associated with k_1. This allowed us to implement the fitting model based on a modified rate equation, as described in the main paper (Chapter 5).

Table C.1: Fitting parameters for a double exponential fit to low fluence (∼30 nJ/cm^2) TRPL data, at a series of temperatures from 90 K to 309 K.

Temperature (K)	A_1	τ_1 **(ns)**	A_2	τ_2 **(ns)**
90	0.384	19.82	0.471	117.94
120	0.421	18.96	0.419	122.94
150	0.343	15.86	0.444	134.49
170	0.356	17.55	0.439	141.72
190	0.368	18.25	0.453	139.69
210	0.304	16.61	0.465	164.07
250	0.300	11.27	0.382	161.68
280	0.198	14.46	0.288	217.83
294	0.234	18.95	0.462	205.39
309	0.416	9.59	0.293	79.26

Appendix D

Supporting Information for Chapter 7

Effect of Caesium Incorporation on the Phase Behaviour and Emission Properties of Triple Cation Perovskite Thin Films: Supporting Information

All data presented in this section was collected on triple cation perovskites of the form $Cs_zFA_xMA_yPb(I_{0.85}Br_{0.15})_3$ where $x = 4y$ and z is varied between 0.03 and 0.15, with these inclusions referred to as e.g. 3% Cs, 15% Cs etc.

Table D.1: Average film thicknesses for a typical thin film of triple cation perovskites of the form $Cs_zFA_xMA_yPb(I_{0.85}Br_{0.15})_3$, of varying values of z, where $x = 4y$. The average has been calculated from measurements on 3 different areas of the film, with the error calculated as the standard deviation of the 3 values.

Cs content (%)	Average film thickness (nm)
3	459.68 ± 13.22
5	495.14 ± 29.90
8	478.51 ± 7.32
10	456.87 ± 30.53
15	566.60 ± 26.97

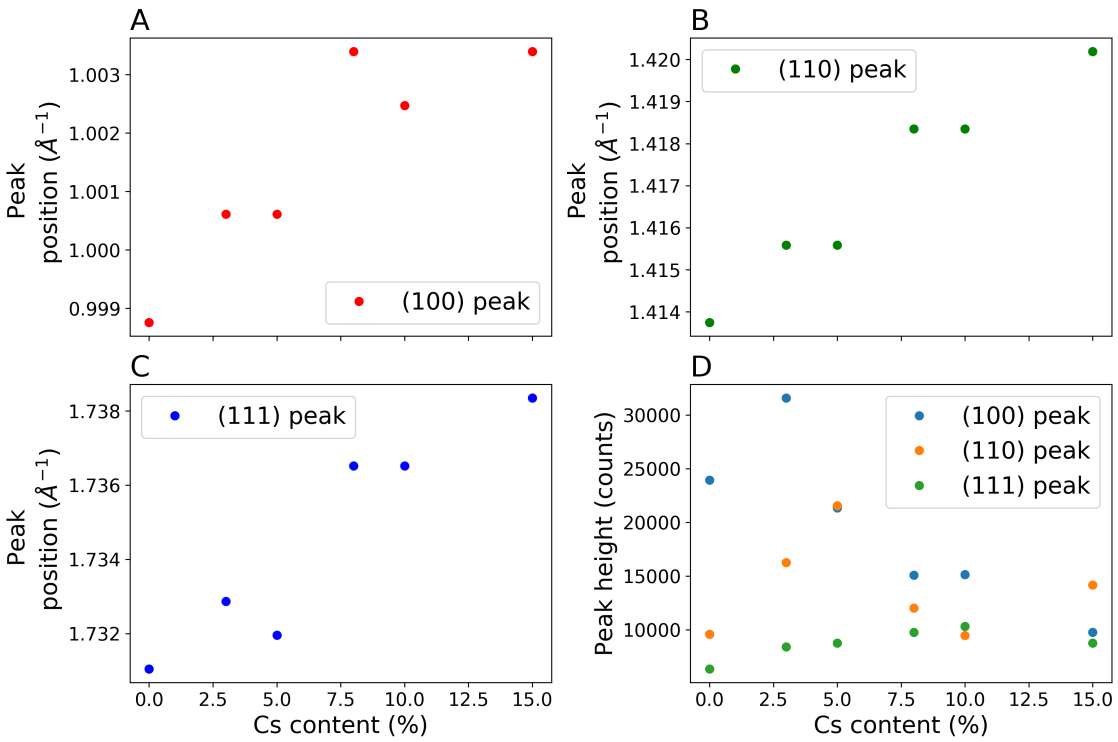

Figure D.1: Position of peaks corresponding to **A** the (100) plane, **B** the (110) plane and **C** the (111) plane, as a function of Cs content in Cs-containing triple cation perovskites. **D** Height of peaks corresponding to the (100), (110) and (111) planes as a function of Cs content.

D.1 Excitonic Effects

From the temperature-dependent absorbance spectra in Figure 7.3, the absorption coefficient as a function of photon energy was calculated for each temperature, and in Figure D.2 this quantity is plotted at selected temperatures for thin films of 5%, 8% and 10% Cs blends.

Here it can be seen that, for all compositions, there is a sharp peak in the absorption coefficient directly above the absorption edge at 4 K. This peak gradually flattens and disappears as each film is heated. This peak can be attributed to excitonic absorption effects in the film.[1] Upon closer inspection, it appears that the temperature dependence of the height of the excitonic peak varies depending on the Cs content of the film. The excitonic peak begins to flatten at ~170-180 K for the 5% Cs blend, whereas for the 8% blend it does not begin to flatten until ~200 K. For the 10% blend, the flattening of the excitonic peak appears to occur at ~180-190 K. This evidence suggests that the exciton binding energy for the 8% Cs blend is the highest of the 3 compositions.

D.2 Pseudo-Voigt Fitting Function

A pseudo-Voigt distribution function $y(E)$ can be defined as a linear combination of a Lorentzian distribution $L(E)$ and a Gaussian distribution $G(E)$:

$$y(E) = fL(E) + (1 - f)G(E) \quad \text{(D.1)}$$

where f is the fractional Lorentzian character of the curve (i.e. a Lorentzian distribution would be recovered for $f = 1$), and where

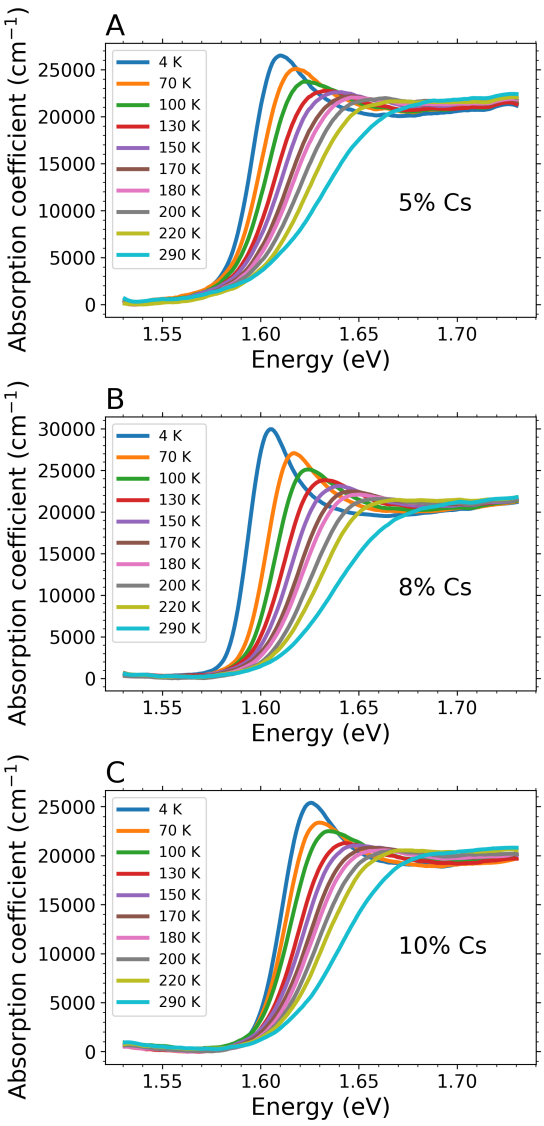

Figure D.2: Absorption coefficient as a function of photon energy at a series of selected temperatures for triple cation perovskites with varying Cs content: **A** 5%; **B** 10%; and **C** 10% Cs.

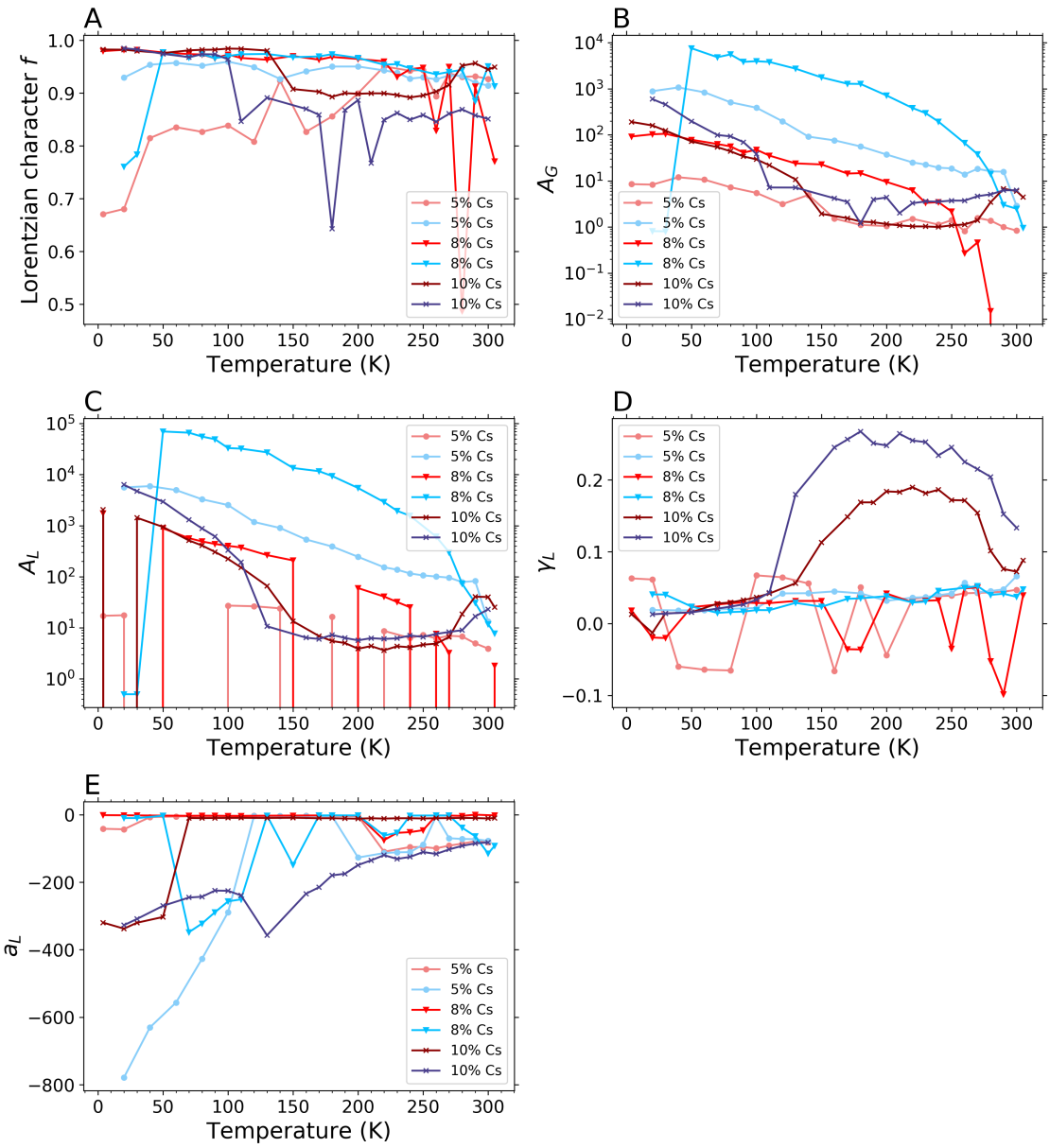

Figure D.3: Temperature dependence of a series of parameters extracted from asymmetric pseudo-Voigt fits to PL data collected for the 5% Cs blend on both cooling and heating of the film: **A** Lorentzian character f, which represents the fraction of the data exhibiting Lorentzian behaviour; **B** A_G, the area under the Gaussian component of the curve; **C** A_L, the area under the Gaussian component of the curve; **D** γ_L; and **E** L, the asymmetry parameter for the Lorentzian component.

$$G(E) = \frac{A}{\gamma(E)}\sqrt{\frac{4\ln 2}{\pi}}\exp\left(-4\ln 2\frac{E-\mu}{\gamma(E)}\right) \tag{D.2}$$

and

$$L(E) = \frac{2A/\pi\gamma(E)}{1 + 4[(E-\mu)/\gamma(E)]^2} \tag{D.3}$$

where E is photon energy, $\gamma(E)$ is the full-width at half-maximum (FWHM), μ is the mean of the Voigt distribution, and both functions are normalised such that A is the area under the curve.

In order to introduce asymmetry into the distribution, we allow γ to vary sigmoidally with respect to energy as follows, therefore defining a distribution of linewidths as follows:

$$\gamma(E) = \frac{2\gamma_0}{1 + \exp[a(x-\mu)]} \tag{D.4}$$

where a is an asymmetry parameter which determines the skew of the data. Negative values of a denote data which is skewed towards higher values of energy, and positive values of a denote data which is skewed towards lower values of energy.

D.3 Temperature Dependence of Mean Emission Energy

Figure 7.6**B** in Section 7.2.1 shows that the mean emission energy, μ, varies with temperature in a similar way to the PL peak energy (Figure 7.6**A**), with slightly lower values as expected due to the skew of the PL data. For the 10% Cs sample on the cooling cycle, in the temperature range ~200-270 K (when the material is in the tetragonal phase), μ diverges more from the PL peak energy than in any other temperature range or composition. If the low energy tail in the PL data which leads to a difference between μ and the peak energy is a band tail, a lower mean emission energy (μ) would suggest a broader band tail. As discussed earlier, band tails have been observed in hybrid perovskites and been attributed to dynamic disorder in the lattice in the tetragonal and cubic phases. A broader band tail suggests a greater degree of dynamic disorder in the lattice. Therefore the anomalously large divergence of μ from the peak energy may suggest a larger degree of dynamic disorder in the 10% Cs blend in the tetragonal crystal phase as compared

to the other two compositions. However, this only applies to the cooling cycle, and it is unlikely that this greater degree of disorder only occurs when the material is being cooled, therefore it is much more likely that this behaviour stems from fitting errors in this series of datasets.

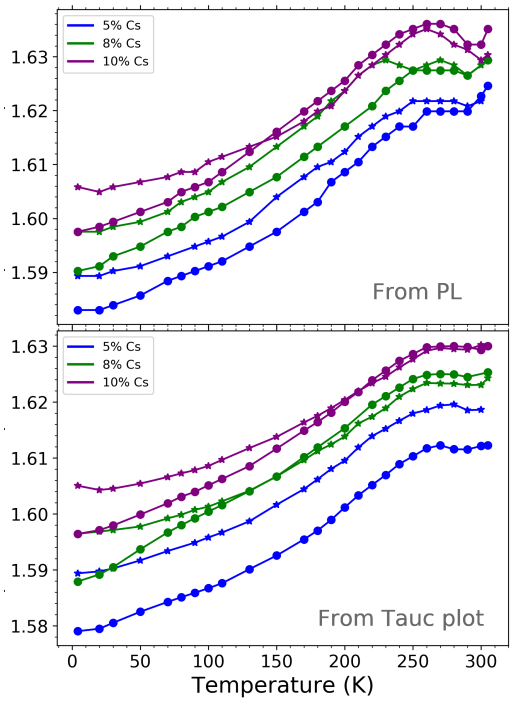

Figure D.4: Temperature dependence of the optical band gap as determined from PL and absorbance spectra, collected on heating cycles carried out on triple cation perovskite thin films with 5, 8 and 10% Cs content.

Table D.2: Peak position Q (Å^{-1}) of the (100), (110) and (111) diffraction peaks at $T = 310$ K, for triple cation perovskite compositions of varying Cs content.

	Q-value		
Cs content (%)	(100) peak	(110) peak	(111) peak
5	0.999906	1.412605	1.732041
8	0.999906	1.412605	1.732041
10	0.997738	1.414757	1.732041

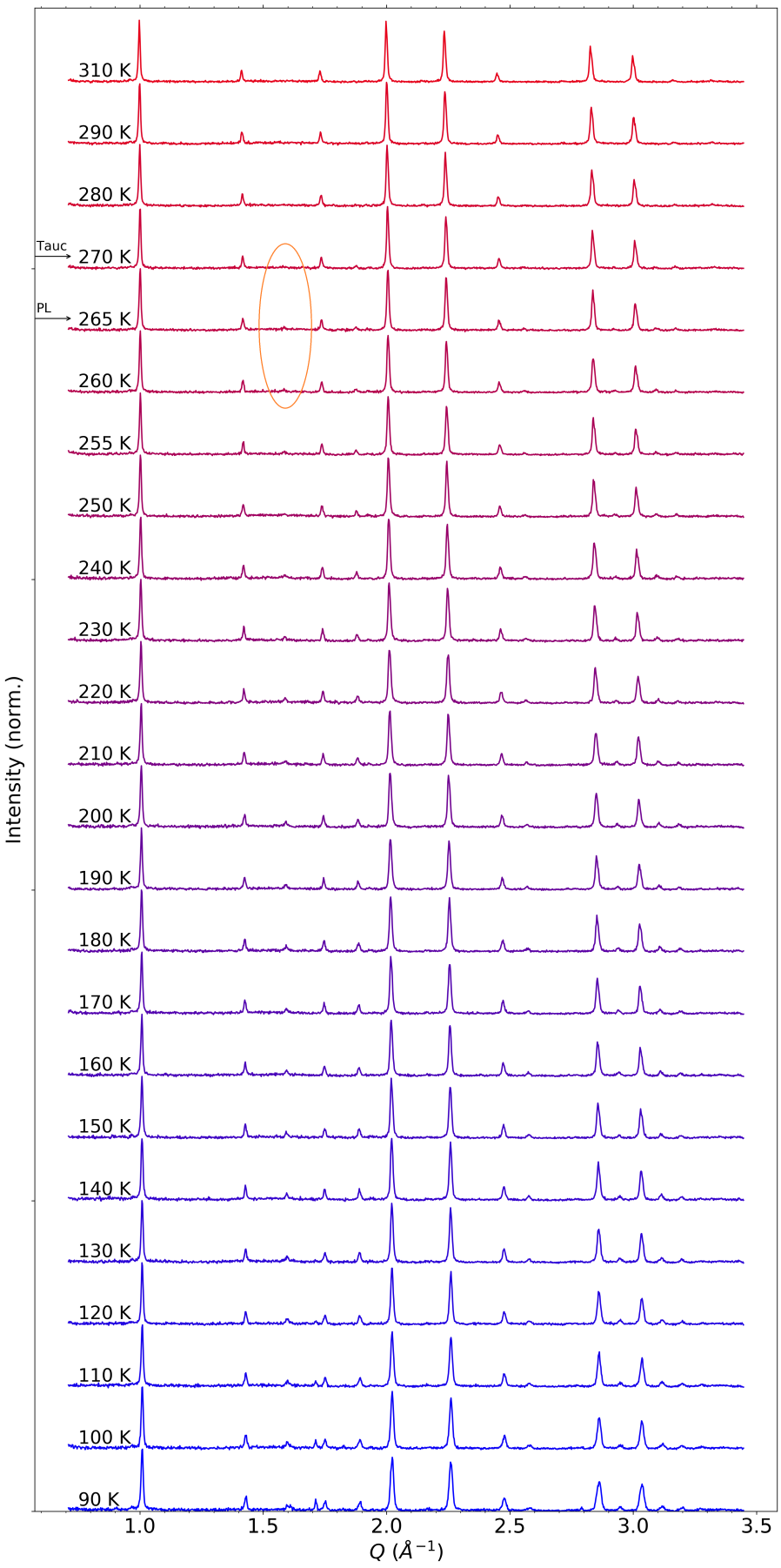

Figure D.5: XRD patterns as collected at a series of temperatures while cooling the powder sample of 8% Cs triple cation perovskite from 310 K to 90 K. The orange circle highlights the appearance of the peaks associated with the β phase.

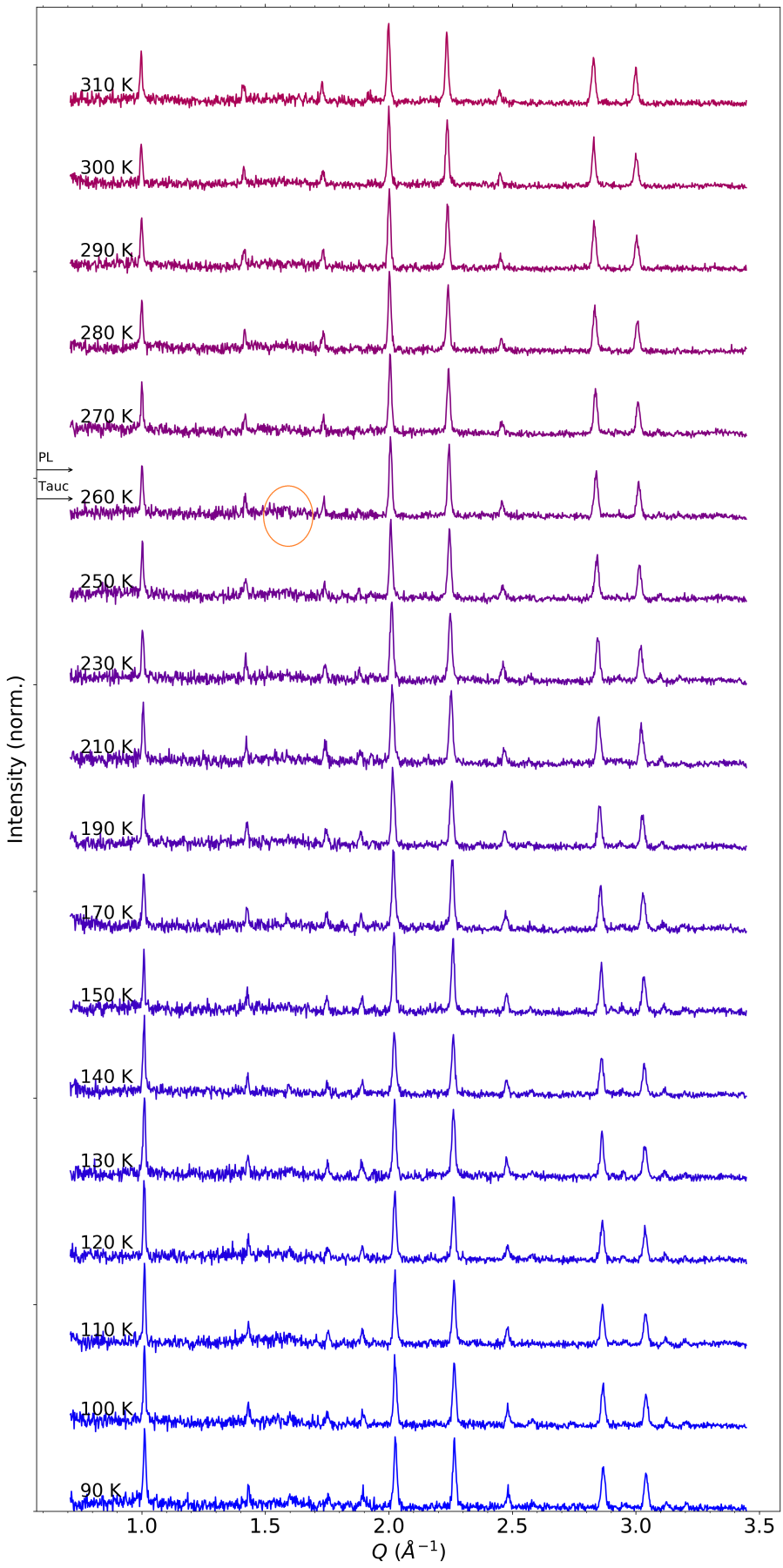

Figure D.6: XRD patterns as collected at a series of temperatures while cooling the powder sample of 10% Cs triple cation perovskite from 310 K to 90 K. The orange circle highlights the appearance of the peaks associated with the β phase.

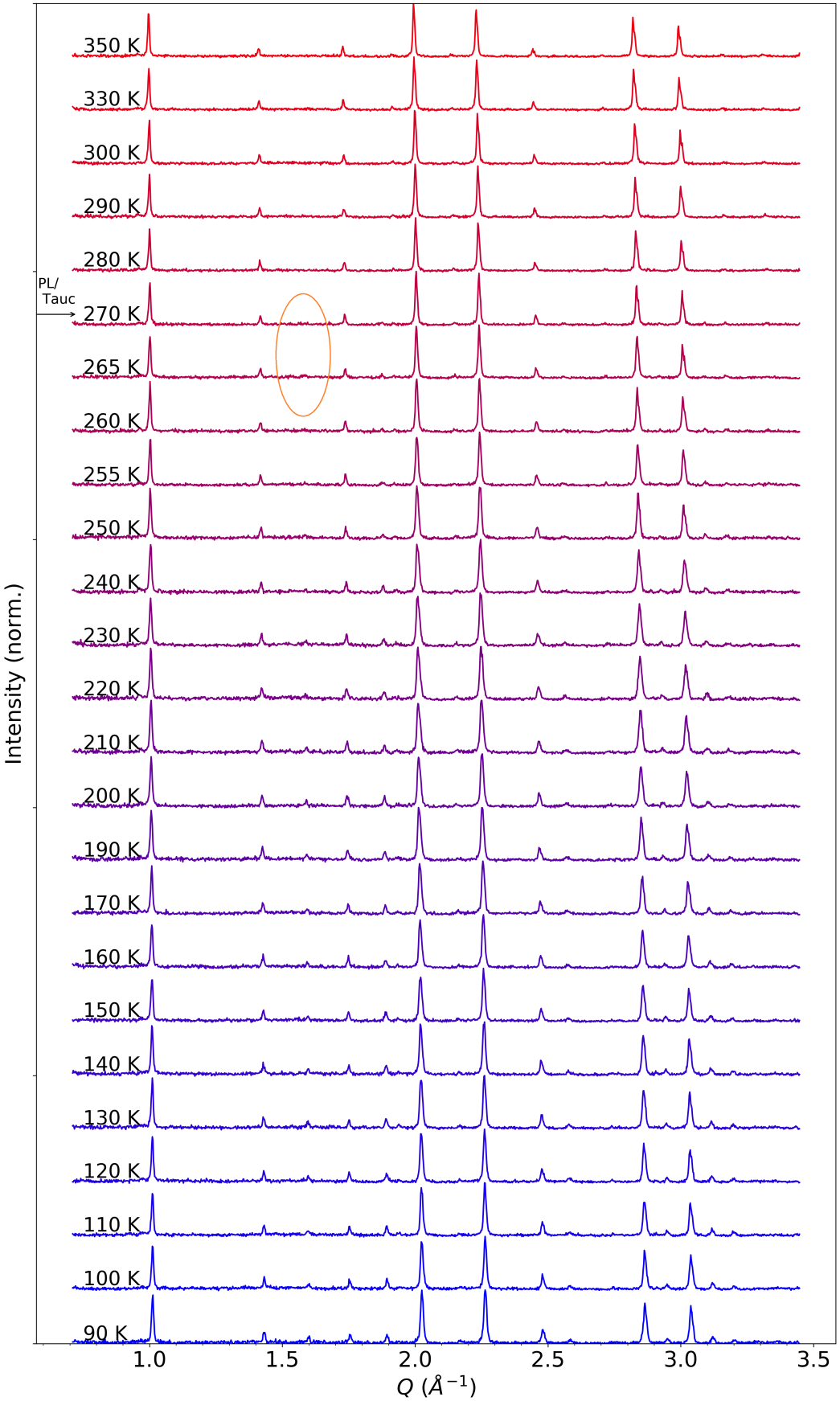

Figure D.7: XRD patterns as collected at a series of temperatures while heating the powder sample of 5% Cs triple cation perovskite from 90 K to 350 K. The orange circle highlights the appearance of the peaks associated with the β phase.

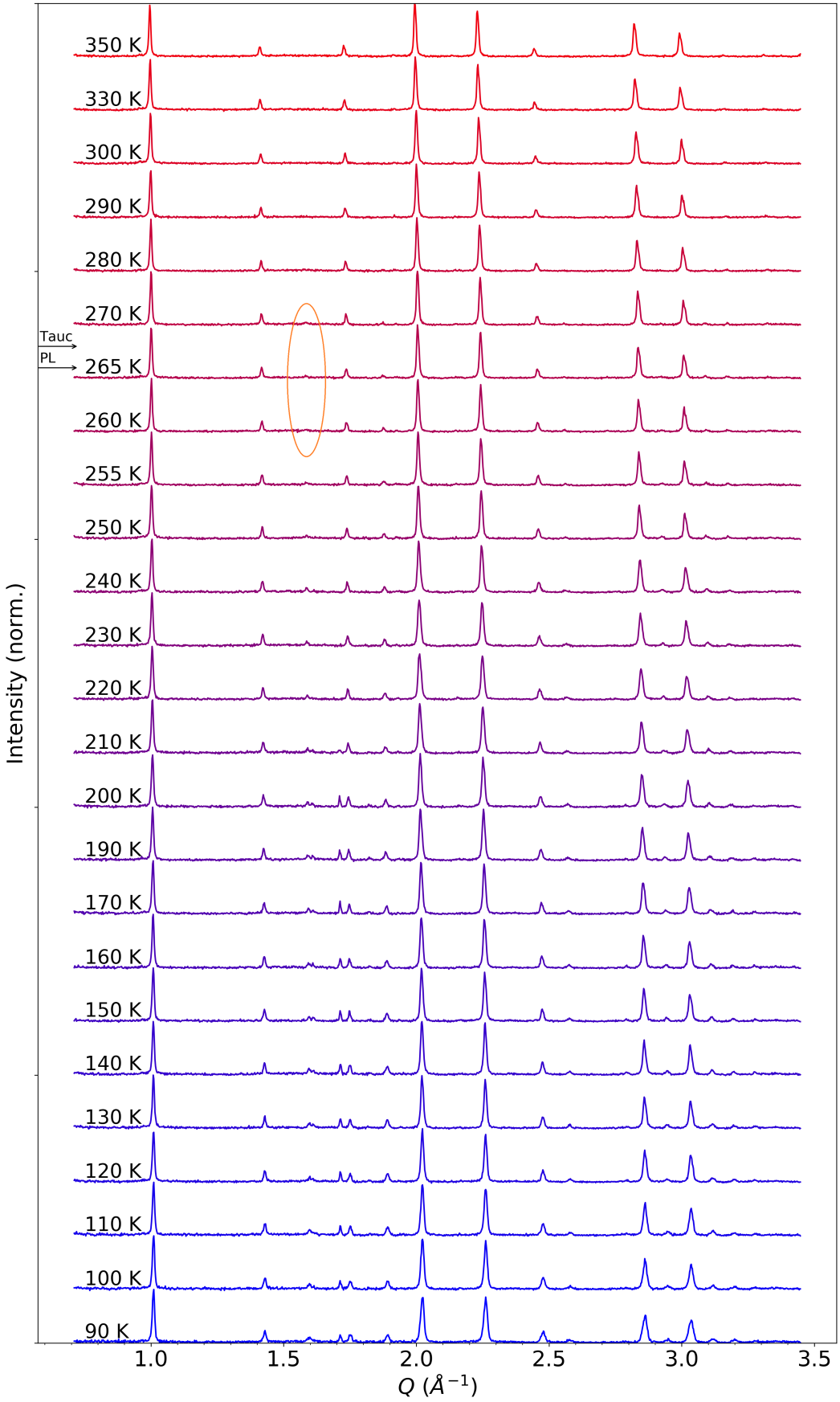

Figure D.8: XRD patterns as collected at a series of temperatures while heating the powder sample of 8% Cs triple cation perovskite from 90 K to 310 K. The orange circle highlights the appearance of the peaks associated with the β phase.

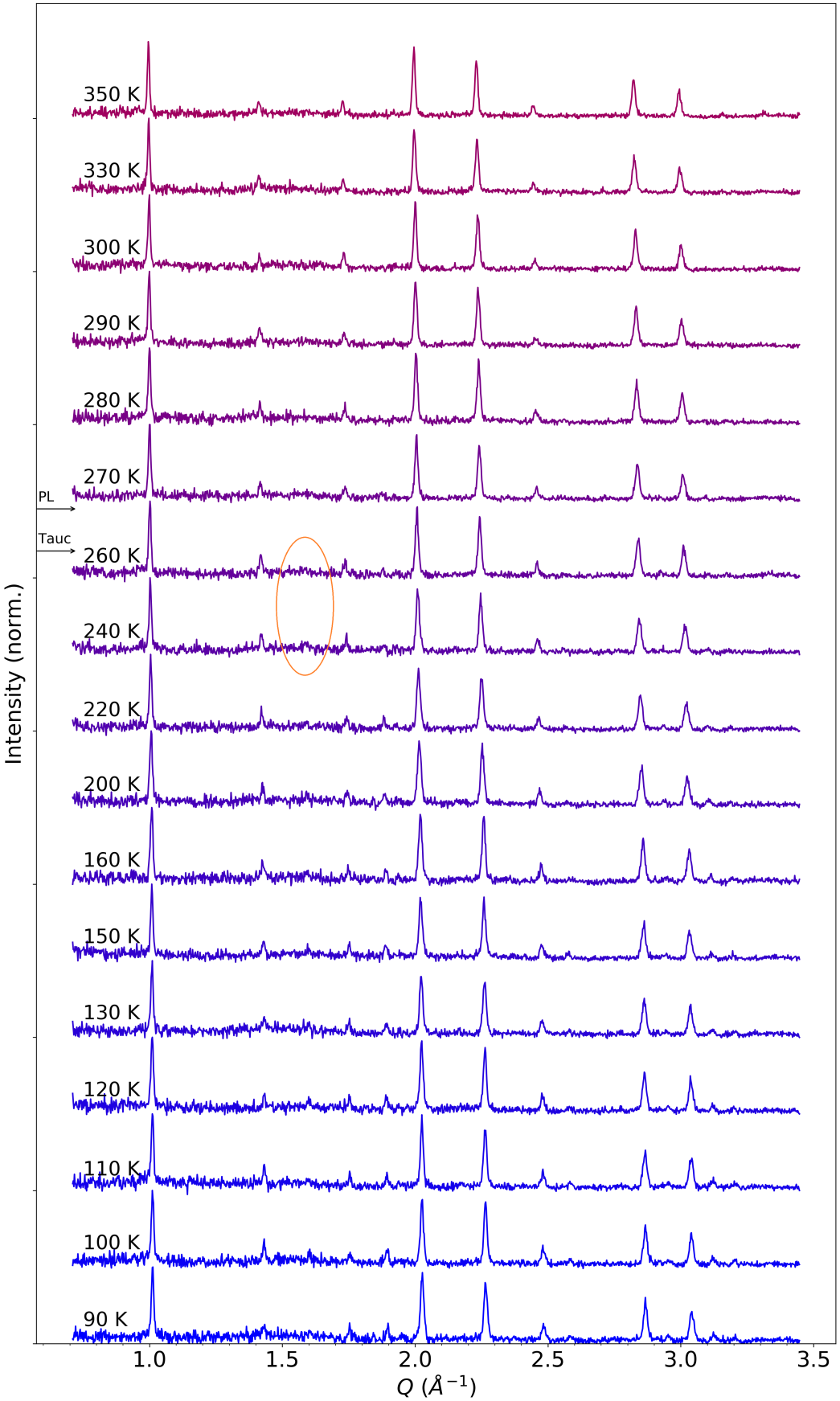

Figure D.9: XRD patterns as collected at a series of temperatures while heating the powder sample of 10% Cs triple cation perovskite from 90 K to 310 K. The orange circle highlights the appearance of the peaks associated with the β phase.

References

[1] V. D'Innocenzo, *Nature Commun.* **2014**, *5*.